The Production of Negative Carbon Ions from Volume-Cusp Ion Sources

by

Stéphane Melanson

M.Sc., Université Laval, 2014

B.Sc., Université de Moncton, 2012

A THESIS SUBMITTED IN PARTIAL FULFILLMENT

OF THE REQUIREMENTS FOR THE DEGREE OF

Doctor of Philosophy

in

THE FACULTY OF GRADUATE AND POSTDOCTORAL

STUDIES

(Physics)

The University of British Columbia

(Vancouver)

August 2020

The following individuals certify that they have read, and recommend to the Faculty of Graduate and Postdoctoral Studies for acceptance, the dissertation entitled:

The Production of Negative Carbon Ions from Volume-Cusp Ion Sources

submitted by **Stéphane Melanson** in partial fulfillment of the requirements for the degree of **Doctor of Philosophy** in **Physics**.

Examining Committee:

Richard Johnson, Department of Physics
Supervisor

Jong Seo Chai, Sungkyunkwan University, South Korea
External Examiner

Morgan Dehnel, D-Pace
Supervisory Committee Member

Janis McKenna, Department of Physics
University Examiner

David Chen, Department of Chemistry
University Examiner

Additional Supervisory Committee Members:

Jeff Young, Department of Physics
Supervisory Committee Member

Micheal Hasinoff, Department of Physics
Supervisory Committee Member

David Jack, Department of Chemistry
Supervisory Committee Member

Abstract

The goal of this Thesis work is to develop and study high current negative carbon ion sources, that do not require the use of alkali metals, with the volume-cusp technology. Very few other ions other than H^- and D^- have been studied with this technology, and to the best of our knowledge, the production of negative carbon ions has never been investigated even though there are industrial advantages. Along with the industrial interest in the development of an alkali free, negative carbon ion source for ion implantation, there is a great opportunity to learn about the production of negative carbon ions in carbon rich plasmas. A test facility was developed for the purpose of this study, and the characteristics of the facility and the performance of the baseline filament-powered H^- volume-cusp ion source are first presented. A radio frequency (RF) powered ion source was developed and the results of this new ion source with H^- are presented. The performance of the extraction of negative carbon ions from the ion sources with various gases was studied. The plasma inside the ion source has been studied to determine how the ion source's tuning parameters affect the species populations, the electron temperature and the electron density inside the different regions of the ion source. Finally, the ion source's stability was improved.

Lay Summary

The production of modern semi-conductors used in electronic devices is done through ion implantation, which is the process by which an ion beam of the doping material is implanted in a wafer. The ion beam is created by an ion source and is accelerated to the desired energy with a particle accelerator. Commonly, positive ions are generated, but some implantation systems require the use of negative ions to reach higher beam energies. There are some disadvantages in present negative ion implanters, which are mostly due to inefficient ion sources that sometimes contaminates the wafer. The development of negatively charged carbon ion beams through the direct extraction of carbon rich plasmas is thought to be a good alternative to the present system utilized. The Thesis presents the negative carbon ion source technology that was developed.

Preface

All of the work presented henceforth was conducted at Buckley Systems in Auckland, New Zealand and at D-Pace Inc in Nelson, British Columbia.

Information in Chapter 3 has been published as a poster presentation for the International Particle Accelerator Conference 2016 (IPAC2016) [Melanson, Stephane, et al. "The Production of Negative Carbon Ions with a Volume Cusp Ion Source." (2016): WEPMY031]. I was the lead investigator, responsible for all major areas of concept formation, data collection and analysis, as well as the majority of manuscript composition. The main contribution of the other co-authors was mostly in helping with the manuscript composition, H. McDonald helped with data collection.

Information in Chapter 4 has been published as an oral presentation at the Negative Ion Beams and Source 2016 (NIBS2016) [Melanson, Stephane, et al. "The extraction of negative carbon ions from a volume cusp ion source." AIP Conference Proceedings. Vol. 1869. No. 1. AIP Publishing, 2017] as well as a poster presentation at IPAC 2017 [Melanson, Stephane, et al. "H-, D-, C2-: A Comparison of RF and Filament Powered Volume-Cusp Ion Sources." (2017): TUPIK002] and at a poster presentation ICIS 2017 [Melanson, Stephane, et al. "Improvements to a 13.56 MHz RF powered H^- ion source." AIP Conference Proceedings. Vol. 2011. No. 1. AIP Publishing, 2018]. I was the lead investigator, responsible for all major areas of concept formation, data collection and analysis, as well as the majority of manuscript composition. The main contribution of the other co-authors was mostly in helping in the manuscript composition. The main contribution of the other co-authors was mostly in helping with the manuscript composition, H. McDonald helped with magnetic simulations, while A. George helped with data

collection.

Information in Chapter 5 has been published as a poster presentation at the NIBS 2018 [Melanson, Stephane, et al. "Beam current stability improvements of negative carbon ions extraction from a multi-cusp ion source." AIP Conference Proceedings. Vol. 2052. No. 1. AIP Publishing, 2018]. I was the lead investigator, responsible for all major areas of concept formation, data collection and analysis, as well as the majority of manuscript composition. The main contribution of the other co-authors was mostly in helping with the manuscript composition.

Information in Appendix A has been published as part of the International Conference on Ion Source 2015 [Melanson S, Dehnel M, Potkins D, Theroux J, Hollinger C, Martin J, Philpott C, Stewart T, Jackle P, Williams P, Brown S. A negative ion source test facility. Review of Scientific Instruments. 2016 Feb 13;87(2):02B109]. I was the lead investigator, responsible for all major areas of concept formation, data collection and analysis, as well as manuscripts composition. The main contribution of the other co-authors was mostly in helping with the manuscript composition as well as in the design phase of the project.

Table of Contents

List of Tables

List of Figures

xvii

xviii

xxii

Acknowledgments

I'd first like to thank my supervisors. Dr. Richard Johnson, thank you for taking on this role even though you are no longer a full time professor at UBC. I'm very grateful for the time you put into this project, through organizing and leading the committee meetings to reviewing many documents. Morgan, thank you for allowing me to join your team, and for your support and guidance throughout this project. You're the one that brought this project to me and without you this would have never happened.

I'd like to thank the entire staff at D-Pace. Thank you for the technical and the scientific support throughout the project. Most notably, I'd like to thank Dave for his ongoing technical help and problem solving skills, Thomas and Joe for their mechanical assistance, Jeff for his software and IT support, Craig for his electrical expertise, Phil for his beamline and magnet design knowledge and Meghan for her administrative help. I'd also like to thank the D-Pace owners, Morgan, Dave, Thomas, Kurt, Kent and Buckley Systems for the financial support throughout the project.

I'd like to thank the staff at Buckley Systems. You welcomed me to NZ from day one and made me feel right at home. I'm thankful for your support and for your friendship. Specifically, I'd like to thank Paul for his ongoing support at the ISTF and his technical knowledge. Dominic and Ales (Juice) for their technical assistance that went above and beyond what was expected from the maintenance team. Chris, Tobin and Hamish, for their fruitful discussions, modeling assistance and for the occasional psychological support. Anand for his ongoing support and for his patience. And many more, the entire staff at BSL has been the most helpful.

I'd like to thank the NSERC and UBC's physics department for the funding,

À mes parents

Chapter 1

Introduction

Particle accelerators have played a major role in many of the big discoveries in physics over the past century [1]. The cathode ray tube was used to study the properties of the electron in 1897, while the Higgs boson was recently discovered at the Large Hadron Collider (LHC) [2]. Particle accelerators are now used in many fields of research including materials science, nuclear astrophysics, biology, nuclear medicine and many more. In 2000, it was estimated that there were about 15 000 particle accelerators in operation around the world, with an estimated 15% yearly increase in their numbers [3]. There are many industrial applications using particle accelerators, which accounts for the largest proportion of particle accelerators used today. The applications include the polymerization of plastics [4], the sterilization of food [5], cancer therapy [6] and ion implantation for semi-conductor manufacturing [7], among many others.

Ion implantation for semi-conductor manufacturing represents the most popular use of particle accelerators, with estimated yearly global revenues of US$1.5 B [7]. Using this technique, specific ions can be introduced to dope a substrate at a precise depth [8–10]. Usually, a positive ion is extracted from an ion source, the ion is accelerated to the desired energy and the ion is implanted into the substrate. Positive ion sources are thus commonly used with ion implanters, however, certain classes of implanters use tandem accelerators, which require the use of negative ions, to double the energy of the accelerated ions [11–13]. A schematic of a common ion implanter system that uses a tandem accelerator, such as the
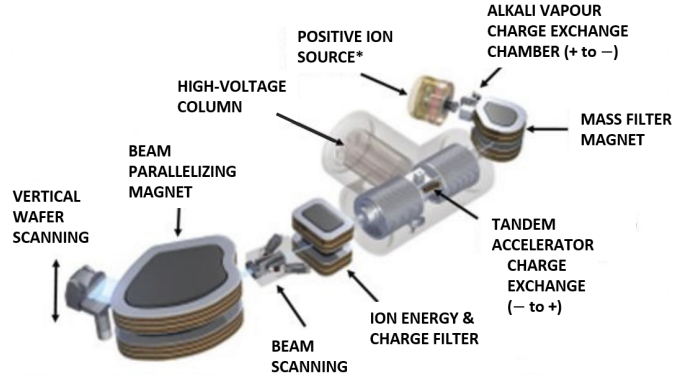
Figure 1.1: Schematic of the Varian 3000XP^{TM} showing the positive ion source and the charge exchange chamber. Taken from [19].

Varian 3000XP^{TM} [7, 14], is presented in Figure 1.1. For the case of the Varian 3000XP^{TM}, positive ions are first extracted from the ion source, are focused down the beamline, and are converted to negative ions by passing through a charge exchange alkali vapour chamber [15], with a transmission of less than 2% [16, 17]. The negative ions are then filtered by mass through an analyzer magnet before they enter the tandem accelerator. A tandem accelerator is composed of three stages, the negative ions are first accelerated by a positive potential, then the ions are stripped of at least two electrons by a stripping foil or gas, forming positive ions. The positive ions are then accelerated back to ground potential by the positive bias on the stripping chamber, enabling them to reach twice the energy of the voltage used in the accelerator [18]. As a final step, the particles are scanned across the wafer being implanted to increase the uniformity of the deposition.

There are a few significant problems associated with current tandem implanter systems. Firstly, the charge exchange chamber used to convert the positive ions extracted from the ion source to negative ions is very inefficient, with an efficiency of charge exchange from positive ion to negative ion of typically less than 2% [16, 17]. A schematic of a charge exchange chamber using a positive microwave-powered ion source is presented in Figure 1.2. With only a 2% conversion rate, the total beam current through the accelerator is low, slowing the implanting process, which reduces wafer and chip throughput, a serious financial impediment. More impor-
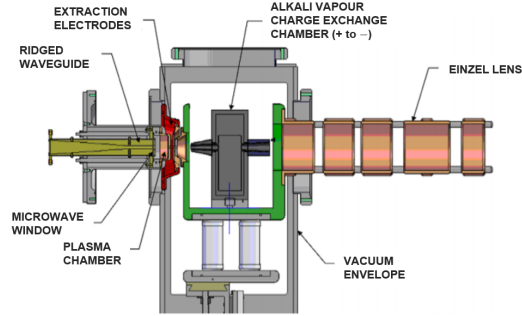
Figure 1.2: Schematic of a positive ion source and a charge exchange chamber, which are presented in Figure 1.1 as *, taken from [21].

tantly, alkali vapours used in the charge exchange chamber will migrate through the system and contaminate the wafers, which is detrimental to the performance of the semi-conductor [20]. The implanter manufacturer utilizes differential pumping, and sophisticated baffle systems to contain and limit alkali metal contamination, but this is not entirely effective particularly with modern high precision and extremely small scale semi-conductors. Ion inplanter manufacturers are thus highly motivated to eliminate alkali vapour from their implanter system [20]. The development of a negative ion source that extracts the negative ions directly from the ion source, eliminating the charge exchange chamber and the alkali vapours would significantly reduce wafer damage by alkali metal contamination, reducing chip rejection rates and improving throughput of viable chips and profitability.

D-Pace [22] has licensed a volume-cusp filament-powered ion source technology designed to directly produce negative ions from TRIUMF [23]. D-Pace desires to develop equipment beneficial to the ion implanter industry by research on its baseline 15 mA negative hydrogen ion filament-powered volume-cusp technology licensed from TRIUMF for the purpose of producing relevant negative ions to this community, such as: C^-, B^-, P^-, As^-. It is clear that such an ion source would reduce implanter manufacturer costs by eliminating the charge exchange chamber, in addition an even more important value added aspect would be the elimination of alkali vapour and concomitant wafer contamination risk. As outlined, this would increase yields of viable chips, be a more efficient use of resources, and increase profitability. Common ions implanted for the production of semi-conductors in-

3

clude boron, phosphorous, arsenic and carbon [7–10]. However, the feed gases used for boron, arsenic and phosphorus are extremely toxic and corrosive, and require very special and costly infrastructure. The focus of this study will; thus, be on negative carbon ions since the feed gases needed are non-toxic and non-corrosive. Carbon ions are used as a getter sink layer in silicon wafers with the purpose of reducing the concentration of metal impurities, which cause white defects in solid state imaging devices, by gathering the metallic ions in the getter layer [24]. In addition to the potential commercial benefits, the production of negative ions heavier than H^- and D^- is very rare by way of the volume-cusp technique, and, in particular, C^- production by this technique is absent in the literature. This constitutes a scientific first and all key parameters related to C^- production by the direct volume-cusp ion source technique, in particular the plasma parameters, are important to measure, assess and publish for the scientific record for future research. This is the first proof of principle step to provide boron, arsenic and phosphorus beams for the purpose of ion implantation.

The goals for the negative carbon ion source to be developed are determined by the ion implanter application for which this ion source is targeted. A high beam current is needed since the beam current is directly proportional to the implanted dose, so increasing the beam current above the 51 μA level currently achievable by the charge exchange mechanism [25] is necessary to achieve shorter implanting times. More specifically, a goal of 1 particle·mA of carbon (1 mA of C^- or 0.5 mA of C_2^-) was set. In addition, since the target application is for high energy beam implants (>1 MeV), the beam energy out of the ion source can be set between 10 keV and 30 keV, as the ion source energy is negligible compared to the final beam energy, and these energies are achievable by the baseline TRIUMF technology [23]. The beam current stability is another important criterion of the ion source. A high stability is needed since this ensures a uniform implanted dose on the wafers, a goal of stability of $\pm$0.5% was set. Moreover, the rapid changes in beam current caused by voltage breakdowns on the ion source's extraction electrodes should be minimized. A goal of less than 10 glitches per hour has been set (a typical maximum glitch rate permissible in the industry), where a glitch is defined as any beam current variation of more than $\pm$5% of the nominal beam current [26]. To ensure maximum transmission through the beamline, a normalized 4 RMS

4

emittance lower than 1 mm·mrad is required. Finally, one of the main goals of the project is to develop an ion source that does not have any metallic contaminants in the plasma, since metal impurities can drift through the implanter system and contaminate the wafers, similar to the alkali vapour problem that is to be eliminated. To summarize, the requirements needed for a negative carbon ion source for ion implanters utilizing a tandem accelerator for which the standard charge exchange ion source infrastructure is to be replaced are as follows:

Parameter	Value
Beam Current	1 particle· mA of carbon (1 mA of C^- or 0.5 mA of C_2^-)
Beam Kinetic Energy	10-30 keV
Normalized 4 RMS Emittance	<1.0 mm·mrad
Beam Current Stability	$< \pm 0.5\%$
Glitch Rate	< 10/hour
Metal Vapour Contamination	Undetectable

Table 1.1: Goals for the negative carbon volume-cusp ion source to be developed.

The purpose of this Thesis is to describe the work that was done to research and develop a metal contaminant free negative carbon ion source that meets the goals outlined above, to illustrate the significant discovery science results achieved, and to present several key applied science breakthroughs accomplished. The work done included assisting D-Pace with the design and implementation of an Ion Source Test Facility (ISTF) and its commissioning. It also includes proving out the baseline TRIUMF licensed 15 mA H^- configuration, research and the development of special plasma diagnostic tools as well as the study of the extraction of negative carbon ions from a baseline filament-powered volume cusp ion source. The final part of the work done included the development of a new RF-powered volume-cusp ion source for the production of negative ion beams and the study of the extraction of negative carbon ions from the newly developed RF-powered ion source.

The new RF-powered ion source developed was also extensively studied with H^- as part of this Thesis work. The ion source developed is a great alternative to the filament-powered ion source since it has no consumable parts. This ion source

is thus a valid option for applications that require high current H$^-$ beams, such as cyclotrons. The development of the ion source up to the performance of the filament-powered ion source thus serves as a secondary goal for the project.

The Thesis has been organized as follows.

i. The second chapter presents the background theory and practice. It includes notions of plasma physics, as well as ion-optics and ion source theory. Special attention is paid to negative ion source theory.

ii. The third chapter presents the production of negative carbon ions from the baseline TRIUMF licensed filament-powered volume-cusp ion source. This technology is ultimately inappropriate for the negative carbon ion source that is to be developed because sputtered metallic filament material contaminates the plasma and could contaminate implanted wafers. Nevertheless, this ion source is the baseline provided by D-Pace at the ISTF and the measurement of the extraction of negative carbon ions yields important new discovery science [27, 28] and provides a useful reference test from which improved systems described in subsequent chapters. This ion source was used to establish which carbon based gas gives the best negative carbon production results, it also revealed how the beam current stability is affected by the extraction of negative carbon ions.

iii. The fourth chapter reports on the extraction of negative carbon ions from the RADIS RF-powered volume-cusp ion source licensed by D-Pace from the University of Jyväskylä [29, 30]. This ion source has an external RF antenna, so is a good candidate for the target negative carbon ion source because it does not have sputtered metallic filament material in the plasma which would present a contamination risk to the implanted wafers. However, it is known to produce only about 1 mA of H$^-$ current [29], so was likely not the final solution for the production of negative carbon ions. In spite of this, it is important to investigate how the negative carbon ions are affected by the RF heating, and provides a new baseline negative carbon ion system that is closer to the final solution. The second section of the fifth chapter presents the development of a new hybrid ion source design as a key part of this Thesis

6

which consists of the RF heating capabilities of the RADIS ion source from the University of Jyväskylä [29, 30] combined with the body and extraction system of the TRIUMF licensed filament-powered ion source [23]. This new design is a good candidate for the final ion source design for the extraction of high current negative carbon ion beams since it rids the ion source of any metallic contaminants in the plasma chamber by using the external antenna of the RADIS ion source (i.e. no sputtered metallic filament material). In addition, it uses the TRIUMF licensed ion source body and extraction system that are known to produce high currents, so it could potentially be used to produce high negative carbon ion currents. The performance of the hybrid RF-powered volume-cusp ion source with H^- is presented in this chapter as it establishes a baseline to compare the performance with the TRIUMF licensed filament-powered volume-cups ion source, since the ion source is much more stable with a hydrogen plasma, facilitating the comparison of the technologies. This new hybrid ion source has been well received by the negative ion community for H^-/D^- [31, 32]. It yields beam currents approaching those of the TRIUMF licensed filament based technology but with no consumable filaments (350-500 hours at maximum filament power), and thus eliminating a costly and lengthy maintenance operation.

iv. The fifth chapter describes the negative carbon ion measurements with the hybrid RF-powered ion source presented in chapter five. The performance of the ion source is presented and the plasma parameters are measured as a function of the different ion source parameters. Strong efforts were made to improve the stability of the beam current by reducing the sparking between the electrodes through a wide range of experiments and assessments. The data and analysis yields important insight into negative carbon ion production and extraction through the RF-powered volume-cusp technique [27, 28, 33].

v. The final chapter summarizes the main achievements of this Thesis work. It also compares the final ion source performance results to the goals established in Table 1.1.

Chapter 2

Background Theory and Practice

The ultimate goal of this Thesis is to directly produce negative carbon ions (i.e. not via alkali metal vapour charge exchange mechanisms) using the volume-cusp technique to a standard that would be commercially viable in an ion implanter system, as described in the introduction. This chapter covers important background theory relevant to the Thesis topic and the theory presented is heavily based on past work [34–36]. Plasma physics is covered first, and then techniques for plasma generation and plasma confinement are described in general. This is followed by a section on basic ion source theory and a short review of negative ion source techniques is then covered. Lastly, extraction techniques, and charge particle transport theory is covered followed by a comprehensive section on beam quality, space charge (as it applies to charged particle beams) and space charge compensation.

2.1 Basic Plasma Parameters

A plasma is a charged gas state, and it is often called the fourth state of matter [37]. The main difference between a gas and a plasma is that in a plasma some of the electrons are stripped from the gas molecules, creating the partially charged state. There are four main types of particles in plasmas: neutrals, electrons, positive ions and negative ions, with the negative ion density often much lower than the other densities. Since, when a gas is ionized there is the creation of a positive and a negative particle, a plasma is quasi-neutral.

Plasmas can be created and appear in day-to-day life, notably in fluorescent lamps and in neon signs. In nature, plasmas are present in the sun, in the ionosphere and in lightning. Plasma physics also plays an important role in many fields of research, notably fusion [38], ion sources [35] and semiconductor processing [39].

2.1.1 Density, Degree of Ionization and Temperature

The density of the different species in a plasma, given in particles per meter cubed, will be given by n_n, n_+, n_e and n_- for the neutrals, the positive ions, the electrons and the negative ions, respectively. Plasmas are electrically neutral in a large volume. This is more generally stated as *quasi neutrality* [37] and is described as a situation where the positive and negative charge densities are equal in a large volume for a substantial amount of time. This can be stated mathematically as

$$n_e + n_- \approx \sum_i q_i \cdot n_{i+},$$

(2.1)

where n_{i+} represents the different positive ion species densities and q_i is the charge state of the positive ion species. Here it is assumed that the negative ions in the plasma all have a charge state of -1 and are all of the same species. The quasi neutrality of the plasma comes from the fact that when a neutral particle is ionized, the total charge remains zero since both a positive and a negative particle are created (positive ion and electron in most ionization interactions). Furthermore, the high electrical conductivity of plasmas prevents a net motion of charges out of the plasma since a net migration of charges in the plasma would cause an increase in the space charge of the opposite charge sign being created. The resulting electric field that is created will then oppose the flow of the charged particles, preserving the quasi-neutrality of the plasma.

The electron density is often used as a measure of the plasma density, due to the quasi neutrality of plasmas and the low negative ion densities. Laboratory plasmas, including plasmas seen in volume-cusp ion sources, commonly have a density of between 10^{14} m^{-3} and 10^{18} m^{-3} [40]. Knowing the gas pressure in the plasma

chamber, the *degree of ionization* [37], D_i, of the plasma can be defined as

$$D_i = \frac{n_+}{n_+ + n_n},$$ (2.2)

where n_n is the neutral density. Multiply charged ions and negative ions are neglected in 2.2. A plasma is said to be highly ionized if $D_i > 10\%$. Typical plasmas seen in volume-cusp ion sources have a degree of ionization of less than 1% [40].

Most laboratory plasmas have an electron and ion energy distribution that follows a Maxwell-Boltzmann distribution [34]. It is thus possible to define a characteristic temperature for these distributions. The distribution $f(v)$ is a probability distribution that is a function of the particle's velocity v, and is described by

$$f(v) = \sqrt{\left(\frac{m}{2\pi kT}\right)^3} 4\pi v^2 \exp\left(-\frac{mv^2}{2kT}\right),$$ (2.3)

with m the particle's mass, k the Boltzmann constant and T the characteristic temperature of the distribution. It's common practice to express the temperature in eV since kT has the units of energy and typical temperature values encountered in plasmas are on the order of a few electron-volts. One eV corresponds to the energy of an electron accelerated by 1 V,

$$T = \frac{eV}{k},$$ (2.4)

and for $V = 1$ V, this gives $T = 11594$ K. Figure 2.1 presents the velocity distribution for various temperatures.
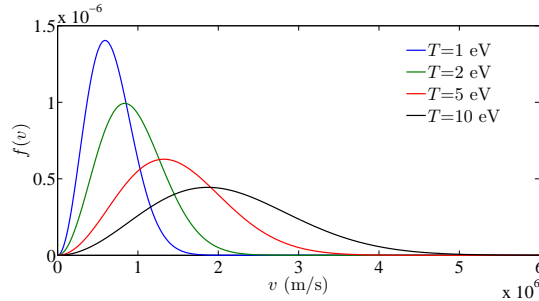
Figure 2.1: Maxwell-Boltzmann distribution for various temperatures.

The electron temperature T_e, the neutral temperature T_n and the ion temperature T_i are often very different from one another, with the T_e usually being the largest since the electrons are the most mobile in the plasma, being much lighter than the other particles. The temperature of the particles in the plasma depends on several parameters, such as the plasma generation method, the magnetic field and the pressure in the plasma chamber. For example, plasmas produced by an arc discharge have electron temperatures on the order of 1 eV, while Electron Cyclotron Resonance (ECR) discharges can have electron temperatures of more than 1 keV, with an ion temperature as low as 1 eV [41]. Additional information about the general movement of particles in a plasma can be found in Appendix A.

2.2 Plasma Interactions

There are various types of interaction between the different particles in the plasma, with ionization being the most important process for the plasma formation. Ionization is the process in which a neutral particle loses one or more electrons through an ionization process, becoming an ion. There are several ionization processes, including electron impact ionization, field ionization, ion impact ionization and photoionization. Furthermore, a particle can be multiply ionized, which is often the goal of Electron Cyclotron Resonance (ECR) ion sources [35]. The theory behind multiple ionization is presented in Appendix A.

2.2.1 Electron Impact Ionization

Electron impact ionization is the most common ionization process observed in most laboratory plasmas [37]. The ionization occurs when an electron interacts with a neutral, removing an electron from the neutral. The free electrons in the plasma are often accelerated by an electric field, giving them enough energy to ionize the neutrals. The extra electron created is subsequently accelerated by the electric field and can thus ionize more neutrals, which leads to even more free electrons. The energy of the free electrons in the process must exceed the ionization potential of the neutral, $E_e > e\phi_i$, where ϕ_i is the ionization potential.

The probability of ionization will be highly dependent on the electron energy. The probability is zero below the ionization potential and will rise and saturate to

a maximum at about three or four times the ionization potential [42, 43]. If the energy distribution of the electrons in the plasma follows a Maxwell-Boltzmann distribution with temperature T_e (i.e. Figure 2.1), the mean electron temperature is thus $\frac{3}{2}kT$, and most laboratory plasmas have an electron temperature on the order of 1-10 eV [37]. The ionization potential of common gases used in ion sources is on the order of 15 eV, which means that the electrons responsible for the ionization in these plasmas come from the high energy end of the distribution. Figure 2.2 presents the ionization cross section for hydrogen and helium.
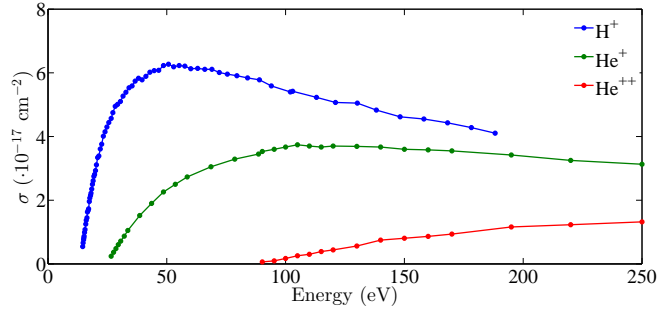
Figure 2.2: Ionization cross section for hydrogen [42] and single and double ionization of He [43].

The fast electrons in the plasma that are responsible for the ionization are often referred to as the primary electrons, while the electrons created from the ionization are referred to as the secondary electrons. The power input into the plasma must compensate for the power loss of the primary electrons from the ionization. The ionization efficiency can be greatly improved by confining the electrons with magnetic or electric fields, thus recycling the primary electrons by preventing them from reaching the plasma chamber walls and prolonging their time in the plasma. Volume-cusp and ECR ion sources use magnetic confinement to prolong the lifetime of the electrons in the plasma, while Penning ion sources use electric fields along with magnetic confinement to reflect the electrons back into the plasma [40].

2.2.2 Other Ionization Techniques

Ionization can also occur on surfaces, such a process is known as surface ionization. This process is most efficient for low work function alkali metals and alkali earths

(Li, Na, K, Rb Cs, Ca, etc.) on refractory metal hot plates (Ta, W, Re, Ir, Pt, etc.) [40].

Ion impact ionization is an ionization technique that involves the charge exchange with another ion. This includes the charge exchange interaction between a fast ion with a slow neutral, forming a slow ion and a fast neutral. If the ion and the neutral are of the same species, the ionization potential is the same for both particles, and the process is known as resonant charge exchange [40]. The energy required for the ion is high compared to electron impact ionization, therefore the process is not an important ionization mechanism in most laboratory plasmas.

Photoionization is the process of ionization by a photon [40]. The photon's energy has to be higher than the ionization potential. This can be written as $E = h\nu > e\phi_i$, where h is Planck's constant and ν is the photon's frequency. For ionization potentials between 5 eV and 15 eV, the wavelength ($\lambda = \frac{c}{\nu}$) of the photon will be between 80 nm and 250 nm, which spans from soft X-Rays to the ultraviolet regions.

2.2.3 Excited States

The interaction between a gas molecule and an electron can lead to the formation of an excited molecular state. Excited states are due to the discretization of the energy of the vibrational modes of the molecule. As the number of atoms in the molecule increases, so does the number of vibrational and rotational modes, which results in an increase in the number of excited states.

As an example, the volume production of H^- involves the interaction with ro-vibrationally excited states of hydrogen molecules $H_2^*(\nu'')$ [44]. It was found that the cross section for the production of $H_2^*(\nu'')$ by electron collisional excitation had a threshold of about 20 eV [45].

2.2.4 Negative Ions

Negative ions are also produced through interactions in the plasma. Charge exchange of positive and neutral species with another neutral can lead to the formation of negative ions. The probabilities associated with these processes are low and is greatly improved if the neutral has a low electron affinity. For a single step

13

process from positive ion to negative ion, alkaline earth vapors are used (Mg, Ca, Sr, Ba) while a two step process will be favored with alkali metals such as Na, K, Rb,Cs.

Direct production of negative ions in the plasma can also occur through dissociative attachment of electrons to vibrationally or rationally excited molecules. This is an important process in many H^- ion sources [46].

Finally, negative ions can also be formed on the surfaces of the plasma chamber. Positive ions interact with the surface and two electrons are captured by the ions, forming negative ions. The process is greatly improved by the addition of a low electron affinity material, such as Cs, on the surface [47].

2.3 Plasma Potential

Electrons are much more mobile in the plasma since the velocity of a particle is inversely proportional to the square root of the mass, so an electron would have a velocity that's about 43 times higher than a proton with the same energy. Also, most plasmas have an ion temperature that is smaller than the electron temperature, which results in an even higher electron velocity than the proton. The result of this difference in particle velocity will lead to a difference in the particle flux to the walls of the plasma chamber and thus the walls will have a negative potential relative to the bulk of the plasma [48]. Since the plasma chamber walls are often grounded, the net result will be a positive potential for the bulk of the plasma. This is known as the *plasma potential*, ϕ_p, and the transition region between the wall and the bulk of the plasma is known as the plasma sheath and is on the order of the Debye Length [34]. More information on the plasma sheath and the Debye Length can be found in Appendix A.

A value for the plasma potential can be found by examining the particle movement close to the plasma chamber walls. As a positive potential is established between the bulk of the plasma and the walls, the resulting electric field will reduce the flux of electrons to the wall until an equilibrium is established when the flux of electrons and the flux of ions to the walls is equal.

The wall potential will be negative relative to the bulk of the plasma. For the analysis, it is assumed that the potential will be higher than the ion temperature and

that positive ions will flow to the wall regardless of their initial velocity. It is also assumed that the particles are absorbed at the wall and are not reflected. The flux of ions to the wall, J_i, can be written as

$$J_i = e n_i v_B, \tag{2.5}$$

where e is the electron charge, n_i is the ion density and v_B is the Bohm velocity, $v_B = \sqrt{\frac{kT_e}{m_i}}$, as described in Appendix A. The electron flux to the wall will depend on the energy of the individual particles. In the plasma sheath description in Appendix A it was found that the electron distribution, n_e, can be written as

$$n_e = n_{ep} \exp\left(\frac{e\phi_w}{kT_e}\right), \tag{2.6}$$

where $n_{ep} \approx n_i$ is the electron density in the bulk plasma, ϕ_w is the potential of the wall relative to the bulk of the plasma, k is the Boltzmann constant and T_e is the electron temperature. The flux of electrons to the wall, J_e, will be given by [34]

$$J_e = -e\frac{n_e \bar{v}_e}{4}, \tag{2.7}$$

where n_e is the electron density close to the wall and $\bar{v}_e$ is the mean thermal velocity of the electrons, assuming a Maxwell-Boltzmann distribution, is given by

$$\bar{v}_e = \sqrt{\frac{8kT_e}{\pi m_e}}. \tag{2.8}$$

The $\frac{1}{4}$ factor in equation 2.7 comes from averaging over a solid angle. At equilibrium, the fluxes are equal ($J_e = J_i$); ϕ_w can thus be calculated:

$$\phi_w \approx \frac{kT_e}{e} \ln \sqrt{\frac{2\pi m_e}{m_i}}. \tag{2.9}$$

The plasma potential is given by $\phi_p = -\phi_w$, which is an approximation for the plasma potential. For a hydrogen plasma with $T_e = 1$ eV and assuming the only positive ions in the plasma are protons, the plasma potential will be about 2.84 V.

2.4 Plasma Generation

The following section will focus on the generation of plasmas. Most plasmas originate from the ionization of the gas by hot electrons. If the electrons have an energy that is higher than the ionization energy of the gas, there will be a non-zero probability that the electrons will ionize the gas. This will in turn generate more free electrons, that will ionize more gas and then generate more free electrons, and so forth. This avalanche effect is known as a Townsend discharge [49]. There are several techniques used to generate hot electrons, common techniques include thermionic emission from hot or cold cathodes and radio frequency or microwave heating.

2.4.1 Thermionic Emission

Thermionic emission occurs when valence electrons in metals have enough energy to escape. Usually the electrons in the tail end of the energy distribution are the ones with enough energy to overcome the potential barrier at the surface of the metal. The higher the temperature of the metal, the greater the electron flow will be. If the metal is biased at a lower potential than a neighbouring surface, forming a cathode and an anode, the electrons will be accelerated by the electric field and the electron current can be measured. The electron flux, J_e, as a function of the temperature, T, is known as the Richardson-Dushman law [50] and is written

$$J_e = A_R T^2 \exp\left(-\frac{W}{kT_e} \right), \tag{2.10}$$

where A_R is Richardson's constant and W is the work function of the metal. Both Richardson's constant and the work function are material dependent.

High melting point materials, such as tantalum, tungsten, thoriated tungsten and lanthanum hexaboride are used as resistively heated cathodes for thermionic emission. Thoriated tungsten and lanthanum hexaboride are known as dispenser cathode. They maintain a thin layer of emitting material out of a reservoir or a porous carrier. The material is commonly shaped into a filament and is heated with either DC or AC current or the cathode can be heated externally. Heating the cathode to generate hot electrons is known as the hot cathode method.

The filament lifetime in hot cathodes is mostly limited by sputtering of the filament material by positive ions in the plasma. Since the cathode is biased negatively with respect to the body of the plasma chamber, the positive ions will be accelerated to the filament and sputter the material. The filaments also evaporate, with a larger evaporation rate seen at higher temperatures [40]. The limited filament lifetime is an important drawback in cathode based plasma chambers.

Hot electrons can also be generated with high electric fields created by biasing the cathode at a high voltage relative to the anode. Once the electric field is high enough to cause a discharge between the electrodes, hot electrons will be emitted from the cathode and ionize the gas. If the arc can be sustained, positive ions in the plasma will be accelerated to the cathodes which will result in heating of the cathodes. The cathode will then start to emit electrons through thermionic emission and the plasma will be sustained with a lower voltage on the cathode. Such a configuration is seen in Penning and Magnetron ion sources [40]. This plasma heating technique is known as a cold cathode since the cathodes are not directly heated, but are indirectly heated by the ions in the plasma.

2.4.2 RF Heating

Radio Frequency (RF) heating is a popular plasma generation technique since it does not require the use of consumable cathodes to operate. There are two methods used to heat a plasma with RF electromagnetic fields. The simplest method is to have two parallel plates immersed in the plasma and applying a time varying electric field between the plates to accelerate the free electrons and ionize the gas. Such a scheme is known as capacitively coupled plasma heating. Alternatively, inductively coupled heating can also be used by applying the RF signal to a circular antenna which creates an alternating magnetic field, which in turn creates a time varying electric field that accelerates the electrons in the plasma. The antenna can be immersed in the plasma chamber, or outside the outer body of the plasma chamber. The varying magnetic field induces an electric field which accelerates the electrons. Additional heating is sometimes needed in these RF heating methods to generate the free electrons needed to start the Townsend discharge.

Static magnetic fields can be used with RF heating methods to create an Elec-

tron Cyclotron Resonance (ECR) condition. The magnetic field strength B must be chosen so that

$$B = \frac{\omega m_e}{e},$$ (2.11)

where ω is the angular frequency of the RF or microwave input, m_e is the mass of the electron and e is the electron charge. Magnetic field strength up to about 1 T can be achieved with non-superconducting electro-magnets, which means that the frequency needed to get the ECR condition is on the order of 10 GHz, which falls into the microwave frequency range. ECR ion sources are known to produce high charge states due to the high electron temperatures in the plasma. The electron density scales with the square of the frequency [40], but as the frequency increases, so does the magnetic field required. The current state of the art is a 28 GHz ECR ion source that require 4 T superconducting magnets to operate [51].

2.5 Magnetic Confinement

A charged particle traveling perpendicular to a uniform magnetic field will follow a circular trajectory in the plane perpendicular to the magnetic field. If the magnetic field is not uniform or the velocity of the particle is not perpendicular to the magnetic field the trajectory will be more complicated. The description of the motion of charged particles in a magnetic field is presented in Appendix A.

Magnetic fields are often used in plasma chambers because they can increase the electron confinement and thus increase the electron temperature and density in the plasma. This thus reduces the power consumption by recycling energetic electrons. Magnetic confinement in plasmas used for ion sources relies on the magnetic mirror phenomenon. Two common magnetic confinement configurations used are the multicusp array and the magnetic bottle, which are presented in Figure 2.3.
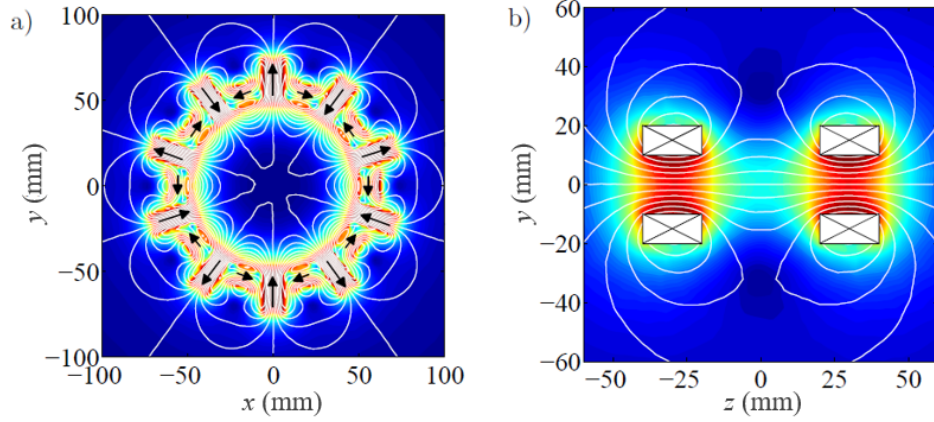
Figure 2.3: a) Schematic of the cross section of a multicusp magnet configuration with a Halbach array of permanent magnets and b) schematic of a magnetic bottle formed by two solenoids. The field lines are presented in white while the field strength is colored.

The magnetic mirror effect occurs when there is an increase in the magnetic field strength along the particle's trajectory, as in along the z axis in Figure 2.3b. A charged particle with a velocity under a certain threshold will be reflected back as the magnetic field strength increases. A particle with a velocity above the threshold will fly through the magnetic bottle.

The magnetic mirror effect can be understood by calculating the forces acting on the particle. If a charged particle is traveling along z in the magnetic bottle, because of Gauss' Law, $\vec{\nabla} \cdot \vec{B} = 0$, there is a non-zero component to the B_y field, which will lead to a force in the z direction given by

$$F_z = -\frac{qv_\perp r}{2} \frac{\partial B_z}{\partial z},$$

(2.12)

where r is the Larmor radius of curvature of the particle [34]. Mathematically, an easier method is to examine the energy of the particle. If there is no electric field and the magnetic field is constant in time, the total energy of the particle, E_{tot}, will be constant and is given by

$$E_{tot} = \frac{mv_\parallel^2}{2} + \mu B,$$

(2.13)

19

where $v_\parallel$ is the particle's velocity along the magnetic field and μ is the magnetic dipole moment of the particle, given by

$$\mu = \frac{mv_\perp^2}{2B}. \tag{2.14}$$

μ is conserved if the variation in the magnetic field is small compared to the Larmor radius, which it is in this example [34]. If there is an increase in the magnetic field along the particles motion, $v_\parallel$ will decrease since E_{tot} is constant. If the variation in the magnetic field is large enough, the particle's motion along the field reaches zero and the particle will be reflected back in the opposite direction.

If the field has a strength of B_0 at $z = 0$ and B_s at the solenoid ($z = 30$) in Figure 2.3b, then the maximum $v_\parallel$ for a particle to be trapped in the magnetic bottle will be

$$v_\parallel = \sqrt{\frac{2\mu}{m}\left(B_s - B_0\right)}. \tag{2.15}$$

For a plasma without any collisions, any particle with $v_\parallel$ under this value will oscillate along the z axis in the magnetic bottle, while a particle with $v_\parallel$ above this value will escape. However, plasmas include collisions, which causes particles to diffuse across the field lines and this will skew the analysis.

For the case of a multicusp magnetic configuration, as in Figure 2.3a, the magnetic field configuration isn't as simple but the concept of the magnetic mirror still applies. Electrons will follow the magnetic field lines and will oscillate if their velocity parallel to the magnetic field is lower than the escape velocity. The particles' oscillations will thus be curved and will oscillate between opposite facing poles as presented in Figure 2.4. The result is particle losses along the cusp lines, which can be seen as burn marks in the plasma chamber.
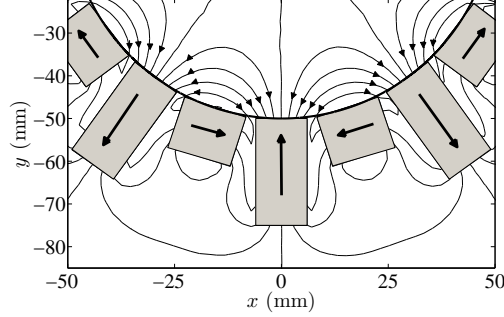
Figure 2.4: Schematic of the magnetic mirror effect in a multicusp magnet configuration with a Halbach array [52] around a plasma chamber with a radius of 50 mm. The electrons oscillate along the field lines, as presented by the arrows.

2.6 Ion Sources

The next section of the chapter focuses on ion sources and particle accelerator concepts. Ion sources are used to create and inject ions into every ion accelerator. There are various types of ion sources and various types of ions can be created, depending on the application. The most common ion source is probably the H^+ ion source. For example, a proton ion source is used in the highest energy accelerator found on earth, the Large Hadron Collider (LHC) [53], however, after the upgrade to the front end of the LHC, the ion source will be updated to a H^- ion source. Negative ion sources are advantageous over positive ion sources because two electrons can be stripped from the negative ions to create a positive ion and this leads to greater injection efficiency into the accelerator [54]. In addition to negative ions, high charge state ion sources [55] and rare isotope ion sources [56] have also received attention recently. This section will present basic ion source theory with a focus on negative ion sources and volume-cusp ion sources, which are the main ion sources studied for this Thesis work.

21

2.6.1 Basic Ion Source Theory

An ion source is commonly made of two main sections, the first being a plasma chamber or an area where ions are formed, the second being the extraction area, where the ions are extracted to form a beam. The most common technique used to create an ion beam is to first produce the desired ions on a floating high voltage platform that has the polarity of the ions so that the ions will be extracted to ground. A schematic of an ion source and its extraction system is presented in Figure 2.5.
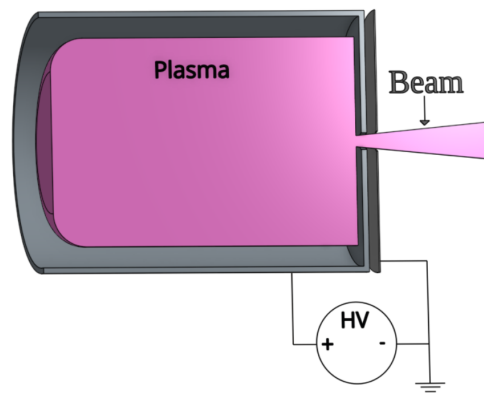
Figure 2.5: Schematic of a positive ion source.

As seen in section 2.4, there are several methods that can be used to generate a plasma. The method chosen for the ion source depends on the beam current, beam quality and ions required, as well as the power available. To generate a beam out of the plasma, an aperture is added to one end of the plasma chamber. This aperture can be a single circular hole, which is the case for most ion sources used for high energy accelerators, a slit, which is commonly used in ion implantation applications or a grid of circular apertures, which is the case for neutral particle injectors used in fusion. Additional electrodes can be added at different voltages to change the beam characteristics before the beam is transferred to the low energy beamline.

2.6.2 Negative Ion Sources

Negative hydrogen ions are the most studied negative ion due to their many applications. They are used in cyclotrons for variable energy stripping [46]. A cyclotron accelerates particles in a spiral pattern, particles start near the center of a circular dipole magnet and orbit around the center. The particles are accelerated at every turn which increases the radius of their orbit, giving a spiral shape to their trajectory. Extracting positive ions from a cyclotron is difficult because at higher energies the orbits of the different energy ions becomes tighter and eventually they overlap, so there isn't any clearance between orbits for a magnetic septum to bend the beam out of the cyclotron. Therefore, some beam hits the septum, which is beam loss and makes the septum highly radioactive. When one uses H^- ions, a thin sheet of carbon is used to strip the electrons from the nucleus creating positive ions that curve out of the cyclotron with an opposite radius of curvature to that of H^-. This allows for efficient extraction of the positive ions from the cyclotron. Negative hydrogen ions are also used for neutral beam heating in fusion applications [57]. Fusion devices use strong magnetic fields to confine the plasma, and these magnetic fields prevent the injection of charged particles into the plasma, thus requiring the use of neutral beams to heat the plasma. The neutral beams are created by stripping one electron from H^- ions, which is more effective than neutralizing H^+ at the energies used (1 MeV). These are two of the most popular applications for negative ions, in addition H^- ions are also used in storage rings [58–60] and in tandem accelerators [61, 62].

Tandem accelerators are the main targeted application for the negative carbon ion source that is being developed in this Thesis work. In a tandem accelerator, a beam of negatively charged particles is accelerated by a positive electrostatic potential, then the electrons are stripped from the negative ions by either a stripping foil or a gas stripper. The positive ions formed are then accelerated back to ground potential. The particle at the end of the tandem will thus have been accelerated twice, and will have acquired an energy of $E = qV_0 + (n-1)qV_0$, where V_0 is the voltage of the tandem's electrostatic electrode, q is the charge of the electron and n is the number of electrons that were stripped from the negative ion. The main advantage of tandem accelerators is the kinetic energy doubling for a given cost.

Another advantage is that a Direct Current (DC) beam can be accelerated and only the electrodes are biased at a high potential. However, tandem accelerators are limited to the voltage that can be applied to the electrodes, which is commonly on the order of 10 MV, which limits the energy of the accelerated beam to about 20 MeV.

The electron affinity of an element or a species is described as the amount of energy needed to separate an electron from the negative ion formed. Species with a higher electron affinity will thus be more stable since more energy is required to strip the electron. Hydrogen has an electron affinity of 0.75 eV, which is lower than carbon at 1.26 eV [63]. Some elements, such as helium, form negative ions that aren't stable, other elements, such as nitrogen, do not form negative ions.

There three main type of negative ion sources commonly used, which are charge exchange ion sources, surface ion sources and volume-cusp ion sources. Charge exchange and surface ion sources are presented in Appendix A. Volume-cusp ion sources are the focus of this study and are presented in the following section.

2.6.3 Volume-Cusp Ion Sources

An important type of ion source used for the production of negative ions is the volume-cusp ion source. An extensive literature review was done and very little research has been made on the production of negative ions heavier than H^-/D^- with volume-cusp sources. These ion sources are the focus of the project and will serve as the baseline technology that the industrial collaborator, D-Pace, wishes to test and potentially implement as a direct negative ion source without metallic contaminants as per the specifications stated in Table 1.1 in the Introduction.

The most common negative ions extracted from volume-cusp ion sources are H^- and D^- ions [46, 64–66], with a few heavier ions in the literature, such as Cl^- [67], Na^- [68], Li^- [69], O^-, O_2^-, F^- and BF_x^- [70]. There is no evidence of volume-cusp ion sources being used to extract negative carbon ions.

Volume-cusp ion sources are characterized by the magnetic configuration around the plasma chamber. The cylindrical plasma chamber has an array of alternating North and South facing magnets, as can be seen in Figure 2.6.
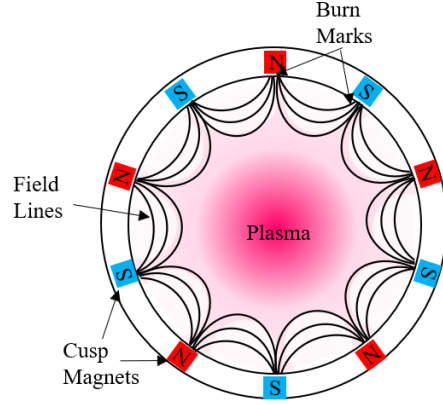
Figure 2.6: Schematic of the cross section of a volume-cusp ion source, showing the array of permanent magnets and the magnetic field lines.

The magnetic field lines created by such an array form the cusps for which the ion source is named. This magnetic configuration is known to increase the confinement of the plasma because of the magnetic mirror effect seen along the cusp lines, as described in section 2.5.

The main production characteristic of the volume-cusp ion source for negative ions is that, for the case of H^-, most negative ions are produced in the plasma volume, without the use of any alkali metal to transfer the extra electrons to the hydrogen. H^- ions are produced in the plasma volume by a succession of two distinct interactions in the plasma chamber [46, 47]. Firstly, the H_2 molecule interacts with a fast electron (> 20 eV) and is brought to an excited vibrational state $H_2^*(v'')$,

$$H_2 + e_{\text{fast}} \longrightarrow H_2^*(v''). \tag{2.16}$$

This excited molecule then interacts with a *cold* electron ($\sim$1-2 eV) to produce a negative ion and a hydrogen atom through dissociative electron attachment.

$$H_2^*(v'') + e_{\text{slow}} \longrightarrow H^- + H^+ \tag{2.17}$$
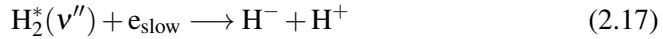
The cross section for reaction 2.17 is highly dependent on the internal energy of the molecule, and increases by more than 5 orders of magnitude if $v'' \geq 5$ [71].

The production of negative hydrogen thus requires a plasma that contains two electron populations to optimize the two reactions necessary for the production of H^- through the volume process. To achieve this, a magnetic dipole at the extraction end of the plasma chamber acts as a filter for fast electrons by trapping the fast electrons in the magnetic mirror created by the magnetic dipole. Collisional diffusion across the magnetic filter will reduce the average energy of the electron at the extraction end of the plasma chamber. Two distinct plasma regions are thus present in the plasma chamber. Furthermore, there are several interactions that can strip the H^- of its extra electron. One of them being the interaction with fast electrons. The dipole filter field is positioned close to the extraction aperture so that the negative ions produced can be extracted and there is a lower probability that they are going to get stripped from their electron in the *cold* plasma region. A schematic of an H^- ion source is presented in Figure 2.7.
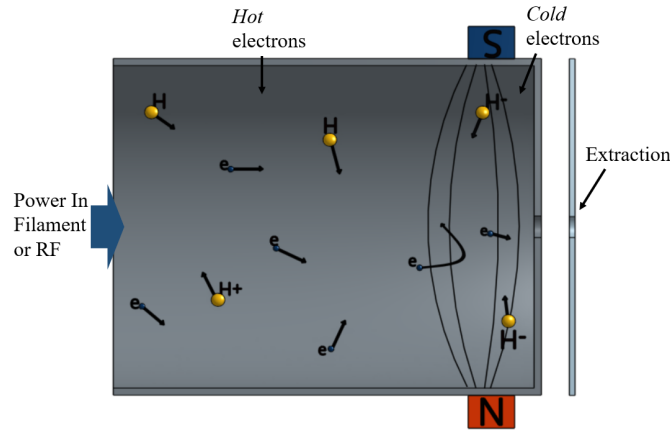
Figure 2.7: Schematic of an H^- volume-cusp ion source with a magnetic dipole filter separating the plasma into two regions. The hot plasma region is to the left of the magnetic dipole, and the cold plasma region is to the right of the magnetic dipole.

The wall material of the plasma chamber also plays an important role in the production of H^- ions in volume-cusp ion sources [72]. By changing the filament material from tungsten to tantalum, a significant improvement in beam current can be seen. This happens because the filaments in the ion source get sputtered by the positive ions in the plasma and the material coats the inner housing of the plasma

chamber. When tantalum is used on the plasma chamber walls, there's an increase in the vibrationally excited $H_2^*(v'')$, which leads to a higher H^- production rate in the plasma volume [72].

There are various methods used to generated plasmas, as discussed in section 2.4. The easiest method used to generate a plasma in a volume-cusp ion source is with a hot cathode, such as a filament. The plasma can also be generated with RF, with two methods commonly used to couple the RF power into the plasma. The first method consists of using a flat spiral antenna attached to the back of the plasma chamber and using a back plate with a low loss tangent to allow the power to couple through. The second method consists of wrapping a solenoid shaped antenna around the body of the plasma chamber. In this implementation, the plasma chamber must be transparent to the RF.

2.6.4 H^- Stripping

Along with the production of H^- ions, the destruction of the ions in the plasma and in the extraction region will contribute to the total H^- ion current extracted out of the ion source. There are multiple processes that lead to the stripping of H^- ions [71]. These include the mutual neutralization with the positive ions in the plasma (H^+, H_2^+ and H_3^+). There is also stripping from interactions with electrons, such as detachment in collisions with fast electrons, as well associative and non-associative electron detachment interactions, written as

$$H^- + H \rightarrow H_2 + e, \tag{2.18}$$

$$H^- + H \rightarrow 2H + e. \tag{2.19}$$

Finally, the H^- ions can be stripped in collisions with neutral molecules, however this process requires ion temperatures of a few eVs to become probable. This destruction interaction can thus be an important interaction within the first stage of the extraction system, where the pressure will be higher than the rest of the beamline. For example, in a study done at the National Institute for Fusion Science in Nagoya, Japan [73] they estimated that they were getting stripping losses of 24% over 2.3 meters for an ion source pressure of 0.9 Pa, but the beamline pressure is

not measured. They estimate that 20% of the loss was in the extraction area, before the beam reaches its final energy. In another study completed at TRIUMF [74], they found that their 12 keV H⁻ beam was being stripped at a rate of 50% per meter at a pressure of 0.016 Pa.

2.7 Extraction

Once a plasma is generated inside the ion source plasma chamber, there needs to be an extraction region for the beam to be created. The extraction system is composed of apertures at varying electric potentials. The potential difference between the electrodes creates the electric field that accelerates the beam.

The beam is first formed when the ions exit the plasma chamber through the front plate of the ion source, hereafter referred to as the plasma electrode. Most ion sources usually have at least one extra electrode before the ground electrode. For negative ion sources, the extra electrode is often used as an electron dump, preventing the co-extracted electrons from reaching the full ion source energy. For positive ion sources, an extra electrode is commonly biased at a few kilovolts below ground. It acts as a suppressor, preventing secondary electrons to back stream into the ion source. Figure 2.8 presents schematics of the extraction of H⁻ and H⁺ from a plasma.
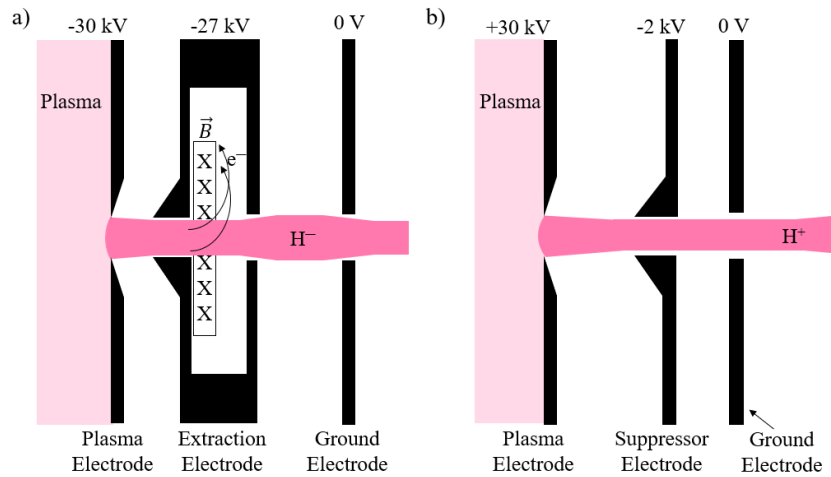
Figure 2.8: Schematic of a) an H^- and b) a H^+ extraction system.

28

Regardless of the number of electrodes used, the beam is always extracted with a kinetic energy, E_k, of

$$E_k = q(\phi_{\text{source}} - \phi_{\text{plasma}}). \tag{2.20}$$

Here q is the charge of the particles, ϕ_{source} is the potential of the ion source and ϕ_{plasma} is the plasma potential. As stated earlier, the plasma potential is usually on the order of a few volts, thus the kinetic energy of the beam is approximately given by $E_k = q\phi_{\text{source}}$. Typical ion source potentials are in the range of 40 kV to 80 kV.

The quality of the beam exiting the plasma chamber depends on multiple factors, which includes the shape of the electrodes and the voltage on the electrodes as well as the plasma parameters. The ions are accelerated by the electric field created by the electrodes, the electric field in the plasma is zero and the potential in the plasma is at the plasma potential (ϕ_{plasma}). There are thus two distinct regions, the field free plasma and the beam where the electric field is usually high and the particles are accelerated. The intersection of the two regions where the potential is zero is often referred to as the *plasma meniscus*, however this isn't a clear boundary between the two regions. One can define the plasma meniscus as the surface where $\phi = 0$, which can be simulated with particle tracking codes that have plasma models included [75–78]. The shape of the plasma meniscus will determine the quality of the beam extracted from the ion source [77]. Furthermore, there is limit to the total current density that can be extracted from an ion source geometry due to the inherent electric potential of the beam. This is known as the Child-Langmuir law [79] and the theory behind it is found in Appendix A.

There are several codes that simulate the extraction of ions from a plasma [75–78], and for these, the main parameters that will affect the shape of the plasma meniscus are the electron and ion densities in the plasma. The plasma shielding increases with the charged particle densities in the plasma, so a larger electric field is needed with a larger plasma density to preserve the shape of the plasma meniscus. If the second electrode in the extraction system is at a fixed location, the potential on this electrode is expected to increase as the ion density is increased in the plasma.

There is an important difference between the extraction of positive and negative ions from a plasma. Since the plasma potential is positive relative to the walls

of the plasma chamber, the potential along the beam axis will be monotonically decreasing at the extraction of a positive ion source because a negative potential is needed in the extraction region to extract the ions. From the plasma boundary analysis presented earlier, the potential falls off exponentially on the order of the Debye Length between the main plasma body and the plasma chamber wall. The electron density also falls off exponentially and will compensate the space charge of the positive ion beam as the particles exit the plasma.

The situation is different for negative ions. A potential well will form between the plasma and the extraction region because a positive potential is needed to extract the negative ions. If it is assumed that the negative ions are generated at the plasma potential, they'll have to overcome the potential barrier created by the plasma potential to be extracted from the plasma. Furthermore, the electric potential well will trap thermal positive ions that have an energy lower than the plasma potential. Faster positive ions will be accelerated by the plasma potential but will be reflected back into the plasma by the large electric field between the electrodes. Both positive ion species need to be considered in the extraction of negative ions from a plasma. In addition to the space charge of the positive ions, the space charge of the electrons also needs to be considered in the analysis. Electrons that have enough energy to overcome the potential barrier of the plasma potential will be extracted from the plasma along with the negative ions. Figure 2.9 presents a schematic of the electric potential along the beam axis.
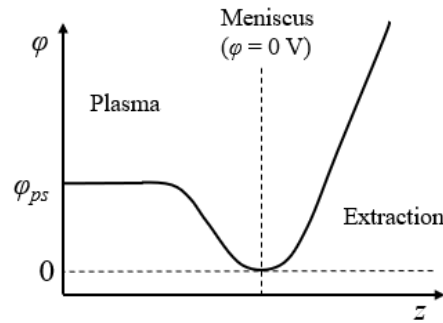
Figure 2.9: Schematic of the electric potential along the beam axis for the extraction of negative ions.

The complexity of the problem requires the use of numerical methods to accurately predict the extraction of the ions. In spite of this, some theoretical concepts can be derived about the extraction of positive and negative ions between electrodes.

2.8 Basic Ion-Optics

Particles are transported through an accelerator system using either electric or magnetic fields, however the only force that can accelerate charges is the electric force. The magnetic field acts perpendicularly to the particle's motion and does not cause any change in energy. Focusing of a beam of particles can either be done with electric or magnetic fields. For electrostatic focusing, the voltage needs to be on the order of the beam energy in volts. Therefore, for higher beam energies ($E_k > 1$ MeV) the electric field requirements are too high to be practical, so magnetic elements are most commonly used. Beam steering can be done with electric and magnetic fields, but electrostatic steering is only practical with low energy beams. Magnetic fields can also be used as a spectrometer as the bending radius of a charged particle depends on the ratio of its mass over its charge ($\frac{m}{q}$). More details on beam steering are presented in Appendix A.

It is common practice to use the same mathematical formulation used in light optics to describe the propagation of an ion beam. In fact, it's a convenient analogy when comparing a single photon with a single particle. However, more sophisticated models are needed to describe real particle beams since there is a distribution of particles and the beam has some space charge that will affect the electric potential.

2.8.1 Particle Tracking

To obtain a better description of the beam propagation through the beamline, individual particle tracking codes, such as IBSimu [77], IGUN [75], PBGUN [76] or KOBRA [78], can be utilized. In these codes, the beam is separated into individual particles with each particle representing an ensemble of particles of charge q. Each particle has a unique state vector and the sum of all the particles replicates the whole beam with the correct current. The beamline is divided into a grid, then the

electric and the magnetic fields are calculated at every point on the grid. The particle trajectories through the system are determined by calculating the force on the particles as they propagate. Computer codes are needed to make the calculations, and the process can be very time and memory consuming. One can accelerate the process by using coarser grids, larger time steps and less particles at the expense of a loss in precision.

2.9 Beam Quality

This section will present the charged particle beam emittance, which is a measure of the beam quality.

2.9.1 Emittance

It is common practice to define the beam axis of an ion source as the z axis. Alternatively, one can introduce the s coordinate, which follows the central trajectory of the beam. The x and y axis will always be transverse axes of the beam, with the x axis often chosen as being parallel to the laboratory floor and the y pointing in the vertical direction relative to the laboratory. The transverse velocities of the particles will be much smaller than the longitudinal velocity ($v_z \gg v_x$ and $v_z \gg v_y$) for standard ion source extraction energies (~ 5 keV-80 keV). A 6 dimensional space, known as the phase space, is introduced to describe the distribution of particles forming the beam. This distribution will be written as

$$n(x, x', y, y', z, \tfrac{\Delta p}{p}), \tag{2.21}$$

with $x' = \frac{dx}{dz} = \frac{v_x}{v_z}$, $y' = \frac{dy}{dz} = \frac{v_y}{v_z}$ and p defined as the momentum of the particles in the beam, with Δp the variation in momentum from the reference trajectory.

Liouville's theorem states that the phase space density for non-interacting particles is conserved for a system that can be described by a Hamiltonian [40]. Mathematically, this can be written as

$$\iint d\vec{r} d\vec{p} = \text{const}, \tag{2.22}$$

with $\vec{r}$ corresponding to the position of the particle, $\vec{r} = (x, y, z)$, and $\vec{p}$ correspond-

ing to the momentum of the particle, $\vec{p} = (p_x, p_y, p_z)$. This means that the volume in 6-D space occupied by the beam remains constant, and thus the phase space volume extracted out of the ion source will not vary as the beam is transported through the beamline.

It is convenient to introduce 2-D projections of the phase space, notably in (x, x'), (y, y') and $(z, \frac{\Delta p}{p})$, to help with the visualisation of the beam quality. $(z, \frac{\Delta p}{p})$ is mostly used with pulsed beams and can be used to measure the energy dispersion of DC beams; however, the dispersion of the beam was not measure as part of this Thesis work, therefore the focus will be on the transverse phase spaces $((x, x')$ and $(y, y'))$. The two-dimensional transverse phase spaces are introduced by first reducing the 6-D phase space to a 4-D phase space as $n(x, x', y, y')$. The (x, x') and (y, y') distributions thus can be found by

$$n_x(x, x') = \iint\limits_{-\infty}^{\infty} n(x, x', y, y') dy dy', \qquad (2.23)$$

$$n_y(y, y') = \iint\limits_{-\infty}^{\infty} n(x, x', y, y') dx dx'. \qquad (2.24)$$

Liouville's theorem holds true in 2-D phase spaces as well. This means that the phase space area will remain constant under conservative forces.

To quantify the quality of the beam in transverse phase spaces, it is common practice to describe the phase space occupied by the beam as an ellipse. Most beams produced by ion sources with single apertures, especially volume-cusp ion sources, produce beams that have an elliptical shape in (x, x') and (y, y') phase spaces. The equation used to represent the ellipse is chosen as

$$\gamma x^2 + 2\alpha x x' + \beta x'^2 = \varepsilon, \qquad (2.25)$$

with γ, α and β are the Twiss parameters and ε is defined as the emittance [36]. Figure 2.10 presents how the emittance and the Twiss parameters are related to the beam envelop ellipse.
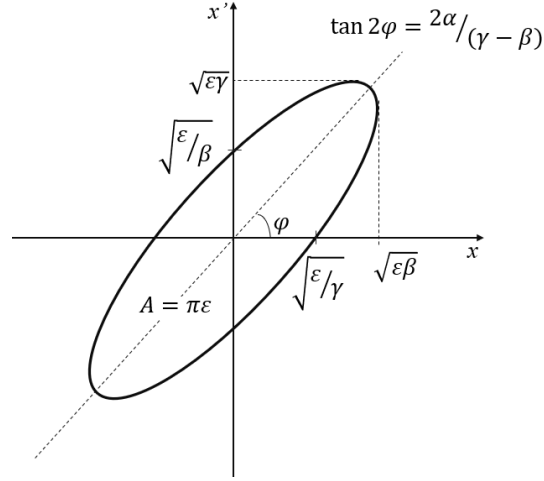
Figure 2.10: Schematic of the transverse beam envelope with the emittance and the Twiss parameters relations to the ellipse.

The Twiss parameters respect the relation

$$\beta\gamma - \alpha^2 = 1. \tag{2.26}$$

The area A of the ellipse in Figure 2.10 is given by

$$A = \pi\varepsilon. \tag{2.27}$$

The emittance will be used as the measure of the quality of the ion beam as it is a representation of the phase space area. To show how the emittance affects the beam size, the beam envelope size is calculated as the beam travels through a beamline. The Courant-Snyder envelop equation dictates the size of the beam envelope in a periodic beamline system [80], as described by

$$x_m'' + \kappa x_m - \frac{\varepsilon_x^2}{x_m^3} = 0, \tag{2.28}$$

where x_m is the size of the beam envelope, x_m'' is the second derivative of the size of the beam envelope with respect to z, κ is a constant related to the beamline and ε_x is the x emittance. Figure 2.11 plots x_m as a function of z for various emittances. An

initial beam radius of 10 mm with an initial divergence of -10 mrad was selected, and the results are plotted with $\kappa = 0$. This represents a converging beam drifting in free space.
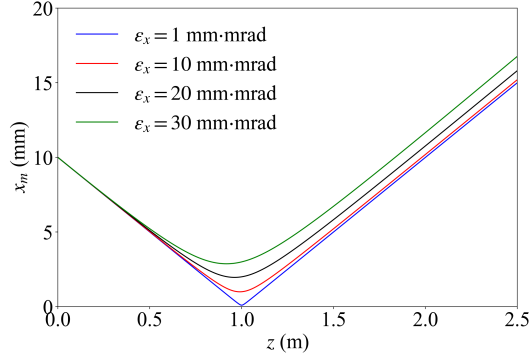
Figure 2.11: Dependence of the beam envelope size for various emittance. A value of $\kappa = 0$ was chosen along with an initial beam radius of 10 mm and an initial divergence of -10 mrad.

From Figure 2.11, the emittance limits the minimum size of the beam envelope at the waist location. The minimum beam size is related to the emittance by $x_{\min} = \frac{\varepsilon_x}{x'}$ [81], which can be seen in Figure 2.11.

The emittance corresponds to the area of the ellipse of the beam envelope divided by π. Commonly two different emittances are measured to describe the transverse quality of the beam, ε_x and ε_y, corresponding to both transverse directions of the beam. The longitudinal emittance can also be introduced and is useful to describe pulsed beams and the energy spread of the beam, but it isn't as relevant for the DC extraction that is utilized for this study.

From the ellipse shape, it's possible to learn valuable information about the beam propagation. Figure 2.12 presents a schematic of particles for a beam drifting along the z axis. The tilt of the ellipse shifts as the beam is converging, focused at a waist or diverging. Also, because of Liouville's theorem, the area of the ellipse doesn't change as the beam propagates.

35
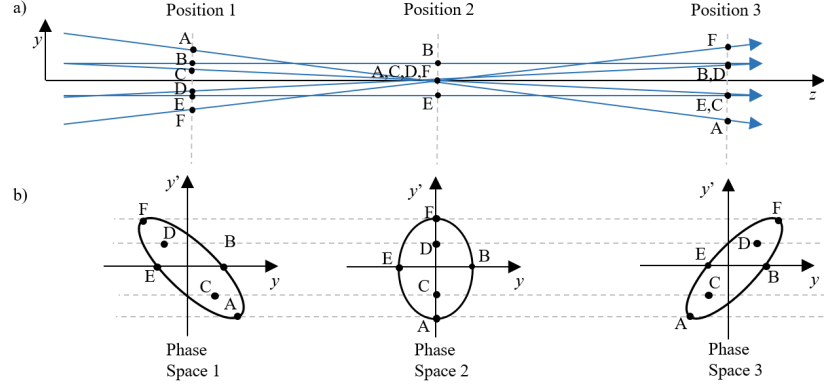
Figure 2.12: a) Schematic of beam particles along different points on the y axis. b) Corresponding phase space ellipse of the beam in (y, y') at three different positions.

2.9.2 RMS Emittance

To calculate the emittance experimentally, the phase space area can be calculated by measuring the distribution in transverse phase space, and then divide the result by π, as described by equation 2.27. However, by doing so the Twiss parameters are not obtained, which are often used as the input of beam tracking simulations. The concept of the RMS emittance is therefore introduced to obtain the Twiss parameters of any beam. It is described as

$$\varepsilon_{RMS} = \sqrt{\langle x'^2 \rangle \langle x^2 \rangle - \langle xx' \rangle^2},$$
(2.29)

with

$$\langle x^2 \rangle = \frac{\iint x^2 I(x, x') dx dx'}{\iint I(x, x') dx dx'},$$
(2.30)

$$\langle x'^2 \rangle = \frac{\iint x'^2 I(x, x') dx dx'}{\iint I(x, x') dx dx'},$$
(2.31)

$$\langle xx' \rangle = \frac{\iint xx' I(x, x') dx dx'}{\iint I(x, x') dx dx'},$$
(2.32)

where $I(x, x')$ is the distribution of beam current as a function of (x, x'). The Twiss parameters can be calculated from the RMS emittance as $\alpha = -\frac{\langle xx' \rangle}{\varepsilon}$, $\beta = \frac{\langle x^2 \rangle}{\varepsilon}$ and

$\gamma = \frac{\langle x'^2 \rangle}{\varepsilon}$, if $\langle x \rangle = 0$ and $\langle x' \rangle = 0$. Equations 2.29 to 2.32 apply to the (y, y') phase space as well.

2.9.3 Normalized Emittance

As a particle beam is accelerated, the divergence $x' = \frac{p_x}{p_z}$ and $y' = \frac{p_y}{p_z}$ decreases since the longitudinal momentum (p_z) increases but the transverse momenta do not. Thus, the emittance decreases as the beam energy increases. It is, however, possible to define an invariant emittance known as the normalized emittance, defined as

$$\varepsilon_n = \varepsilon \beta_r \gamma, \tag{2.33}$$

where β_r and γ are the relativistic parameters,

$$\beta_r = \frac{v_z}{c} \quad \text{and} \quad \gamma = \frac{1}{\sqrt{1 - \beta^2}}. \tag{2.34}$$

2.10   Space Charge

A charged off-axis particle within a charged particle beam will have a radial force acting on it, since all the particles in the beam have the same electric polarity and there is mutual repulsion of the particles. This is known as the space charge effect and it has adverse effects on charged particle beams.

2.10.1   Effect on a Beam

Gauss' law can be used to find the electric field created by a uniformly charged beam of radius r_b and current I with velocity v_z. Figure 2.13 presents a cylindrical Gauss surface of radius r and length l inside a beam.
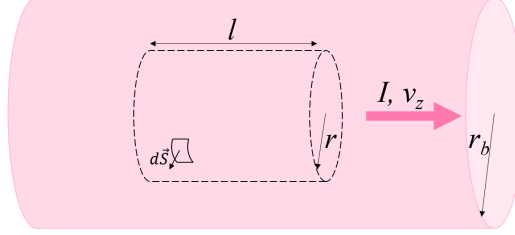
Figure 2.13: Schematic of a cylindrical Gauss surface inside a beam of current I, radius r_b and velocity v_z.

Gauss' law states that

$$\frac{Q}{\varepsilon_0} = \iint \vec{E} \cdot d\vec{S},$$ (2.35)

where Q is the total charge inside the volume, $\vec{E}$ is the electric field and $\vec{S}$ represents the surface of the Gauss surface and pointing perpendicularly to the surface.

For the case of $r \geq r_b$ the charge inside the Gauss surface is found by multiplying the surface volume ($l\pi r^2$) by the charge density ($\rho = \frac{I}{\pi r_b^2 v_z}$). If one assumes radial symmetry, there will only be a radial component for the electric field, E_r. Using Gauss' law for the surface presented in Figure 2.13,

$$l\pi r^2 \frac{I}{\varepsilon_0 \pi r_b^2 v_z} = 2\pi l r E_r.$$ (2.36)

From equation 2.36, E_r can be calculated,

$$E_r = \frac{I}{2\pi\varepsilon_0 v_z} \frac{r}{r_b^2}.$$ (2.37)

The same process can be done to find the electric field at $r_b \leq r \leq r_p$, with r_p the radius of the beam pipe. In this case the surface can be chosen with $r = r_b$ so the charge will be $Q = \frac{Il}{v_z}$.

$$E_r = \frac{I}{2\pi\varepsilon_0 v_z} \frac{1}{r}.$$ (2.38)

38

Adding the boundary condition $\phi(r_p) = 0$, the space charge potential is given by

$$\phi(r) = \begin{cases} \frac{I}{2\pi\varepsilon_0 v_z}\left(\frac{1}{2} + \ln\frac{r_p}{r_b} - \frac{r^2}{2r_b^2}\right), & \text{for } r \le r_b \\ \frac{I}{2\pi\varepsilon_0 v_z}\ln\frac{r_p}{r}, & \text{for } r_b \le r \le r_p. \end{cases} \quad (2.39)$$

The electric potential created by a 30 keV H^- beam with a 20 mm radius traveling through a beam pipe with a 100 mm radius is presented in Figure 2.14 for various beam currents.
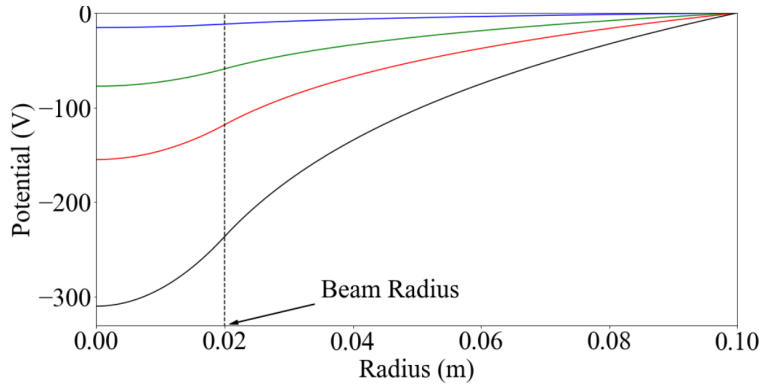
Figure 2.14: Electric potential due to beam space charge along the cross section of 30 keV H^- beam with a 20 mm radius in a beam pipe with a 100 mm radius.

Furthermore, the increase in size of H^- beams due to space charge was simulated. This is done through particle tracking simulations since the size of the beam, and thus the electric potential due to the space charge, changes as the beam drifts. To simulate the effect of space charge, IBSimu [77] was used. IBSimu calculates the potential created by the beam after tracking the particle through the simulation space and then recalculates the trajectories with the space charge potential added to the simulation space. The code then repeats the previous steps until the calculated trajectories converge to a solution. The initial beam simulated had a un-normalized 1-RMS emittance of 10 mm·mrad with Twiss parameters of $\alpha = 0.4$, $\beta = 2.4$ m/rad and $\gamma = 0.48$ rad/m at $z = 0$. The dependence of the beam size on the beam current and on the beam energy are presented in Figure 2.15.
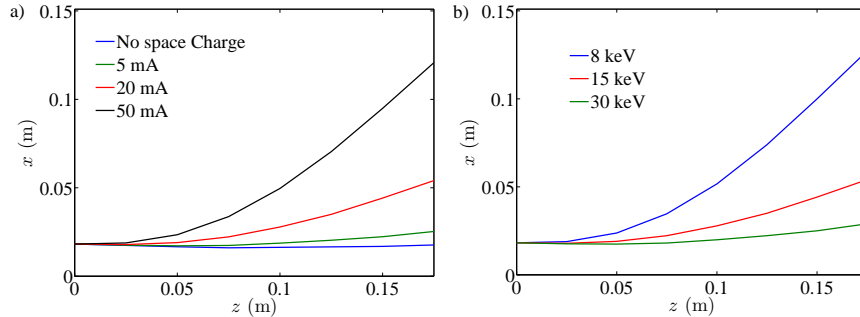
Figure 2.15: Simulation of a H$^-$ beam drifting with and without space charge, the beam has a un-normalized 1-RMS emittance of 10 mm·mrad with Twiss parameters of $\alpha = 0.4$, $\beta = 2.4$ m/rad and $\gamma = 0.48$ rad/m. a) Dependence of the beam envelop size on the beam current, the beam energy was set at 15 keV. b) Dependence of the beam envelop size on the beam energy, the beam current was set at 20 mA.

From Figure 2.15, the space charge is both highly dependent on the beam current and the beam energy. The effect of beam current is obvious, since there are more charged particles in the beam, the repulsing potential will be higher, resulting in a larger beam. The larger effect at lower beam energies is due to the slower velocity of the beam. It takes longer for the beam to travel through the 170 mm of the system, allowing the beam size to further increase. The baseline ion source used for this Thesis study has a maximum beam energy of 30 keV and the maximum H$^-$ beam current achieved was about 18 mA, so the space charge effect is a concern for such beam parameters. With a goal of 1 mA of C$^-$ or 0.5 mA of C$_2^-$, the space charge effect is not as important, however it could become an issue if the ion source is operated at the minimum allowable energy of 10 keV.

Since space charge is a linear effect, Liouville's theorem still holds. This means that the total area of the beam in phase space will remain constant. However, the un-normalized 1-RMS emittance can increase as a result of space charge because the fitted ellipse will be larger since the phase space will no longer be elliptical. Such an example is presented in Figure 2.16, where the phase space of a beam propagating 150 mm is simulated. The non-linear effect causes the beam to transform from an elliptical shape to one with more of an *S* shape. The RMS emittance

40

of the beam more than doubles, but the total area of the phase space remains constant, in accordance to Liouville's theorem. From the point of charged particle ion-optics, the emittance has grown and this increase must be accommodated by the ion-optical elements and apertures in the ion-optical system to reduce beam losses.
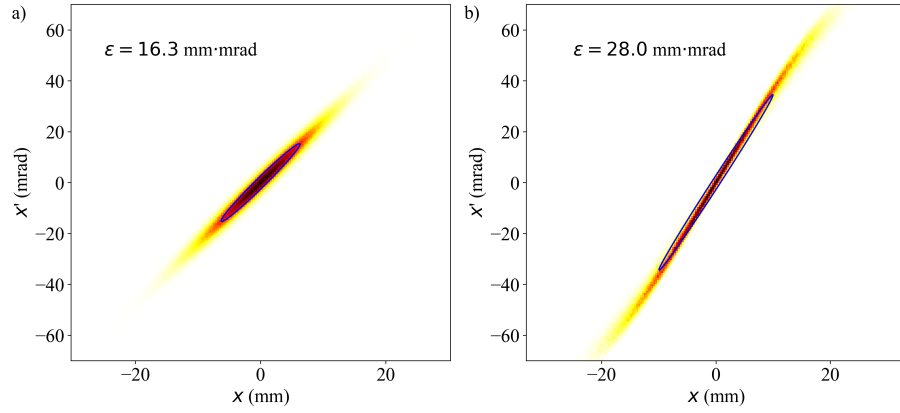
Figure 2.16: Phase space of a 30 keV Gaussian beam of 200 mA of H^+ a) initially and b) after drifting 150 mm. The RMS emittance ellipse is illustrated in blue and the RMS emittance value is presented in the upper left corner of the plots.

2.10.2 Space Charge Compensation

As the beam interacts with the residual gas in the beamline, ionization and charge exchange of the gas particles occurs. The result is positive ions and electrons are created in the beamline as per the two following equations:

$$A^+ + X \longrightarrow A^+ + X^+ + e^-, \qquad (2.40)$$

$$A^+ + X \longrightarrow A + X^+, \qquad (2.41)$$
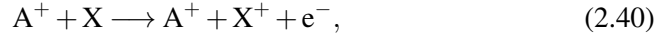
for a +1 charged beam, where A represents the beam and X represents the gas molecule. The cross sections for both reactions will dictate the electron and ion densities created by the beam, with the electron density only dependent on the

ionization of the gas and the ion density dependent on both the ionization and the charge exchange.

For negative ions, the most common interactions are the stripping of the negative ion in the beam by the residual gas and the ionization of the residual gas in the beamline. These interactions can be described by

$$A^- + X \longrightarrow A + X + e^-. \tag{2.42}$$

$$A^- + X \longrightarrow A^- + X^+ + e^-, \tag{2.43}$$
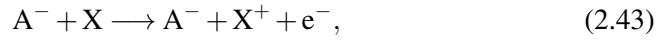
The space charge potential of the beam will either attract or repel the charged particles, depending on the polarity of the beam. For example, if the beam is composed of negative ions, the positive ions created by the ionization or the charge exchange will be attracted by the potential well created by the beam, as presented in Figure 2.14, while the electrons will be repelled towards the beam tube. The opposite will occur for a positively charged beam. This migration of charges in the potential well created by the beam will lead to compensation of the space charge of the beam.

A simple model that includes the space charge compensation to describe the electric potential across the beam can be written as

$$\phi(r) = (1 - f_e) \begin{cases} \frac{I}{2\pi\varepsilon_0 v_z} \left(\frac{1}{2} + \ln \frac{r_p}{r_b} - \frac{r^2}{2r_b^2} \right) & \text{for } r \leq r_b, \\ \frac{I}{2\pi\varepsilon_0 v_z} \ln \frac{r_p}{r} & \text{for } r_b \leq r \leq r_p, \end{cases} \tag{2.44}$$

with f_e the degree of compensation which corresponds to the ratio of space charge compensating particles to the beam density. Figure 2.17 presents the effect of 50% space charge compensation on the phase space. The S shape that comes from the non-linear space charge effect is reduced with the 50% space charge compensation.
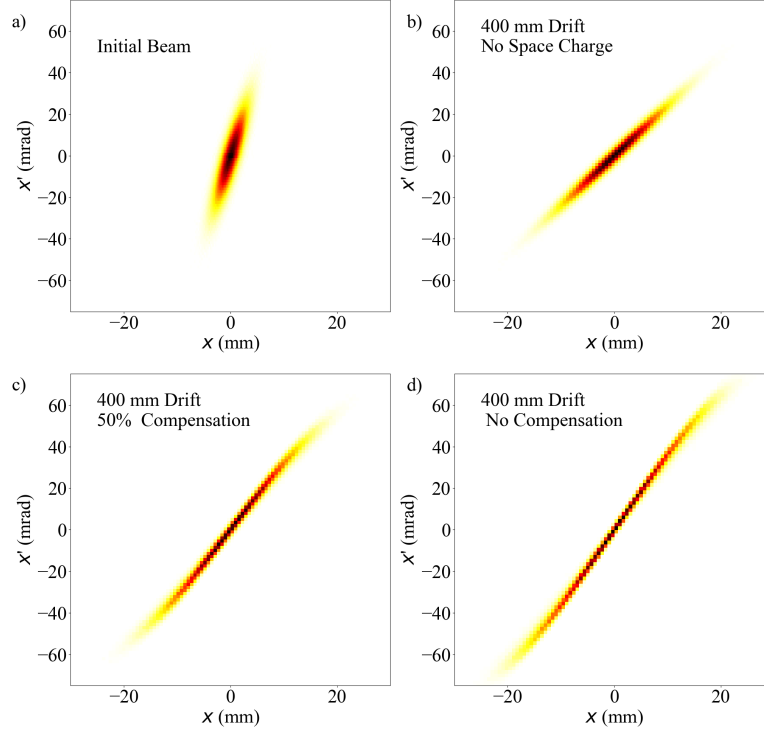
Figure 2.17: Simulation of a 10 mA H$^-$ beam with IBSimu [77]. a) Initial
phase space, b) after a 400 mm drift with no space charge, c) with 50%
space charge compensation and d) with no space charge compensation.

The degree of space charge compensation depends on multiple factors, such as
the type of gas particles present, the pressure in the beam pipe and the energy and
current of the beam. The effect is also time dependent which becomes important
for pulsed beams. Furthermore, the use of electrostatic components in the beamline
will greatly affect the space charge compensation since the potential created by
these components will create areas with variable charge densities.

As an example, Baartman and Yuan [74] found that they could achieve a space
charge compensation factor of 95.6% at a vacuum pressure of $1.1 \cdot 10^{-6}$ Torr with
their 12 keV, 1 mA H$^-$ beam. The compensation factor increased to 96.0% at

$5 \cdot 10^{-6}$ Torr and 97% at $1.4 \cdot 10^{-5}$ Torr. They saw an over-compensation effect at $1.2 \cdot 10^{-4}$ Torr, where the beam was self focusing. However, at this pressure they saw a H$^-$ stripping rate of more than 50% per meter.

2.11 Conclusion

This chapter presented important background theory relevant to the Thesis topic. Basic plasma physics, plasma generation and plasma confinement were first presented. Basic ion source theory, with an emphasis on negative ion sources, was then covered. Finally, ion optics notions relevant to ion sources were introduced.

The next chapter will describe the extraction of negative carbon ions from the baseline filament-powered volume-cusp ion source.

Chapter 3

Extraction of Negative Carbon Ions from the Filament-Powered Ion Source

All the experimental work done as part of this Thesis was conducted at the Ion Source Test Facility (ISTF). Appendix B presents the ISTF, the baseline ion source used as part of this Thesis work and the commissioning of the test facility with H^-. The baseline ion source is a filament-powered volume-cusp ion source that was licensed from TRIUMF [23]. Up to 18 mA of H^- was extracted out of the ion source during the commissioning.

This chapter will present an experimental study of negative carbon extraction out of the filament-powered ion source as it could be a good candidate for an ion source capable of producing the required negative carbon ion beam. Furthermore, since there is a lack of published data on direct negative carbon ion extraction out of volume-cusp ion sources, this will be important for the scientific record.

The first part of the chapter will focus on analyzing the performance of the ion source with different carbon rich injection gases, such as acetylene, carbon dioxide and methane. The chapter then focuses on the performance of the ion source with acetylene as the injection gas, as it was found that the highest C_2^- beam currents obtained were with acetylene. The beam current, co-extracted electron current, beam composition and phase space are analyzed as a function of the different ion source

parameters and are also compared to results obtained with hydrogen in Appendix B. Plasma parameters are then measured with the Langmuir probe as a function of the ion source parameters and the results are compared to those obtained with hydrogen. Finally, issues that arise from using acetylene as the feed gas in the ion source are presented.

3.1 Injection Gases

There are multiple gases that contain carbon, which creates multiple options to use as the injection gas. The injection gases tested as part of this Thesis work include acetylene, methane and carbon dioxide. Testing the TRIUMF licensed filament-powered volume-cusp ion source with different gases will give insight into which gas should be used for the final ion source design. It will also illustrate any potential ion source issue relating to the gas used.

3.1.1 Acetylene

Acetylene (C_2H_2) has been used in ion sources to produce carbon beams, notably it can be used in Electron Cyclotron Resonance (ECR) ion source to produce high charge states of carbon beams for carbon therapy [82]. However, no evidence was found of acetylene being used for the dedicated production of negative carbon ions.

The production of negative ions from electron interactions with acetylene gas was previously investigated by several groups [83–86]. Their results show that C_2^- and C_2H^- are the two main negative ions produced, with smaller amounts of C^-, CH^- and H^- also found. The authors note that the negative ions were produced by two main processes, which are Dissociative Electron Attachment (DEA) and Dipolar Dissociation (DD). DEA is described has the dissociation of a molecule and the attachment of the electron that it interacts with. It can be written as

$$AB + e^- \longrightarrow AB^{*-} \longrightarrow A^- + B, \qquad (3.1)$$
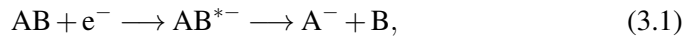
where AB is the gas molecule and AB^{*-} is an excited state of the molecule. For the case of acetylene, A can be C_2, C_2H, C, CH or H, since these are the negative ions that were shown to be produced.

For dipolar dissociation, there is no electron attachment, the dissociation produces a positive and a negative ion. DD can be represented as

$$AB + e^- \longrightarrow AB^* + e^- \longrightarrow A^- + B^+ + e^-, \qquad (3.2)$$
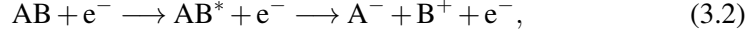
where A can be the same constituents as with DEA.

The DEA reactions have a higher cross section at lower electron temperatures, while DD has a threshold electron energy of more than 20 eV. Szymanska et al. [83] noted that DEA had several optimum electron temperatures for the production of the various ions below 20 eV of incoming electron energy. As can be seen in Figure 3.1, they found peaks for the production of C_2^- and C_2H^- at 2.5 eV, 7.3 eV and 12.7 eV of electron energy, as well as a peak for the production of H^- at 7.3 eV.
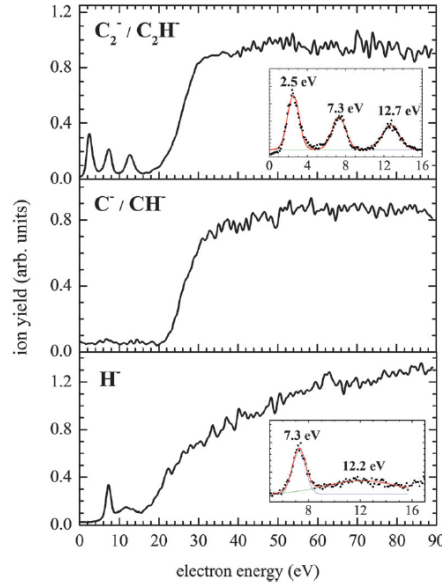
Figure 3.1: Negative ion yield for acetylene as a function of the electron energy. This figure was taken from [83].

From these studies, the prediction is that acetylene would be a good option for the production of C_2^- since it was found to be produced with one of the highest yields. Furthermore, the cross-section for the production of C_2^- has peaks at

electron energies of less than 10 eV, and thus it is expected that the low electron temperature seen in volume-cusp ion sources should be well suited for the volume production of C_2^- through dissociative electron attachment. The electron temperature in the TRIUMF licensed filament-powered volume-cusp ion source is much lower than the energy threshold needed for dipolar dissociation, as was seen with the Langmuir probe analysis done with H^-, so it is expected that the C_2^- ion yields for dipolar dissociation in the ion source will be lower than DEA.

The use of acetylene in the TRIUMF licensed filament-powered ion source was tested at the ISTF. An acetylene plasma was generated in the TRIUMF licensed filament-powered volume-cusp ion source with about 375 A of filament current in the four tantalum filament configuration presented in the Appendix B. This current is significantly larger than the 260 A to 280 A that is needed to start a plasma with hydrogen. Furthermore, the filament lifetime was considerably lower with acetylene due to the increased sputtering of the filaments caused by the heavier ions in the plasma. To reduce the total current needed, only the two outer filaments were used to operate the ion source which reduced the current needed to start the plasma to about 190 A.

A total maximum current of 0.33 mA was extracted from the ion source with a considerably larger co-extracted electron current than was seen with H^-. The beam current was measured with the Faraday cup located 480 mm from the plasma electrode and it includes all of the beam species extracted, before they were separated by the mass spectrometer system. The ion source parameters for the 0.33 mA tune are presented in Table 3.1. The mass spectrometer system with the entrance and exit slits set at 1 mm was used to analyze the beam composition. A typical spectrometer scan obtained is presented in Figure 3.2.

Parameter	Value
Total Beam Current	0.33 ± 0.02 mA
Arc Current	3.3 ± 0.1 A
Arc Voltage	120.0 ± 0.1 V
Bias Current	0.70 ± 0.04 mA
Bias Voltage	25.0 ± 0.1 kV
Extraction Electrode Current	24.5 ± 0.5 mA
Extraction Electrode Voltage	2.9 ± 0.1 kV
Plasma Electrode Current	3.0 ± 0.1 A
Plasma Electrode Voltage	20.0 ± 0.1 V
Gas Flow	5.0 ± 0.2 sccm
Filament Current	163 ± 1 A
Filament Voltage	5.1 ± 0.2 V
X Steering Current	0 ± 0.1 A
Y Steering Current	0 ± 0.1 A

Table 3.1: Ion source parameters for the maximum beam current obtained with C_2H_2.
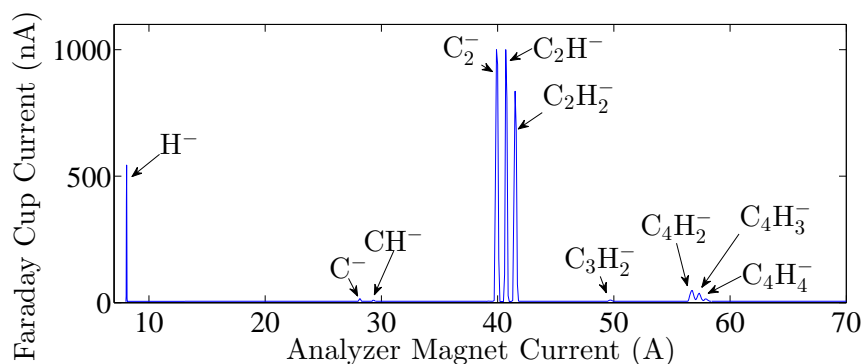
Figure 3.2: Spectrometer scan of a beam extracted by the TRIUMF licensed ion source with acetylene as the injection gas. The arc current was set at 1 A, the arc voltage was set at 120 V, the gas flow was set at 10 sccm and the beam energy was set at 30 keV.

As can be seen in Figure 3.2, the two largest negative ion species found were C_2^- and C_2H^-, which correlates well with previous studies on the production of negative ions with acetylene [83, 85, 87]. However, some of the ions obtained were not found in these previous studies, such as $C_2H_2^-$. Both Dipolar Dissocia-

tion and Dissociative Electron Attachment involve the dissociation of the molecule, and thus the production of $C_2H_2^-$ ions can't be through these processes. The production of this ion is through the surface production, where the molecule captures an electron when it interacts with the wall of the plasma chamber. Neutral C_2H_2 is the species that has the highest density in the plasma chamber (the degree of ionization is below 1% in volume cusp ion sources), so it's very likely that high $C_2H_2^-$ ion production rate would come from surface production. Surface production could also be responsible for the production of other species in the beam as well, including C_2^- and C_2H^-. Furthermore, the species which are heavier than C_2H_2 (such as $C_3H_2^-$, $C_4H_2^-$, $C_4H_3^-$ and $C_4H_4^-$) are probably the result of polymerisation of the molecules in the plasma [88].

The yields of H^-, C^-/CH^- and C_2^-/C_2H^- measured by Szymanska et al. [83] were done at electron temperatures of 80 eV and 8 eV. Their results are presented in Figure 3.3.
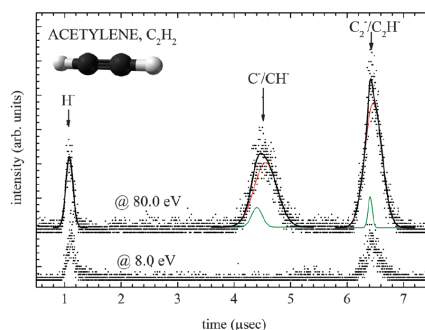
Figure 3.3: Mass spectra of acetylene at two incident electron energies. Data taken from [83].

The results at 80 eV show that the C^-/CH^- yields are similar to H^-. However, at 8 eV the C^-/CH^- is zero. Trace amounts of C^- and CH^- were extracted out of the ion source, which relates well with the results presented by [83] since the electron temperature in the TRIUMF licensed is less than 10 eV, as was seen with the Langmuir probe measurements of Appendix B.

As predicted, the large C_2^- ion yield seen with acetylene makes it a good candidate for a goal of 0.5 mA of C_2^-. However, the extraction was very unstable, with frequent sparking seen on the extraction electrode, causing interruptions in the

beam current. This led to glitch rates of more than 1000 glitches per hour. Furthermore, running the ion source with acetylene led to black deposits on the surfaces of the plasma chamber, as is presented in Figure 3.4. This could be problematic for the long term operation of the ion source if the insulators get contaminated.
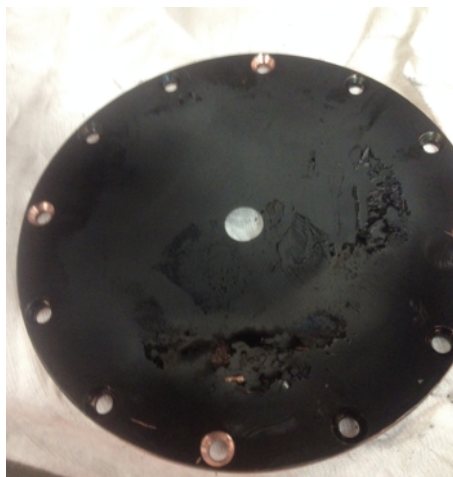
Figure 3.4: Photograph of the plasma electrode after running the filament powered ion source with acetylene for about 4 hours. A new plasma electrode is polished copper.

3.1.2 Carbon Dioxide

Carbon dioxide can be used to produce negative carbon ions in ion sources used for Accelerator Mass Spectrometry (AMS), where either charge exchange ion sources [89] or cesium sputter ion sources are used [90]. No evidence of an alkali metal free negative carbon ion source using CO_2 as the injection gas could be found in the literature.

Previous studies [91, 92] were done on the interaction of electrons with CO_2 and they found that O^- was the main ion produced with considerable yields of CO^- also found. In addition, it has been shown that the production of C^- by dissociative electron attachment in CO_2 only starts at electron energies above 15 eV and the maximum cross section of the reaction is on the order of $2 \cdot 10^{-21}$ cm^2 [93]. The prediction is thus that some C^- will be extracted from the ion source, but

the yield will be low.

Carbon dioxide was used in the TRIUMF licensed filament-powered volume-cusp ion source in an effort to produce C^- ions. Only two of the four filaments were used to reduce the total current needed to generate a plasma. The plasma was started with about 150 A of current in the filaments. Up to 0.2 mA of total beam current (all species combined) was measured on the Faraday cup with 850 W of arc power and 2.5 sccm of carbon dioxide gas flow. The ion source parameters used to obtain the maximum beam current are presented in Table 3.2.

Parameter	Value
Total Beam Current	0.22 ± 0.02 mA
Arc Current	8.5 ± 0.1 A
Arc Voltage	120.0 ± 0.1 V
Bias Current	2.8 ± 0.1 mA
Bias Voltage	25.0 ± 0.1 kV
Extraction Electrode Current	143.8 ± 0.5 mA
Extraction Electrode Voltage	3.3 ± 0.1 kV
Plasma Electrode Current	6.3 ± 0.1 A
Plasma Electrode Voltage	20.0 ± 0.1 V
Gas Flow	2.5 ± 0.2 sccm
Filament Current	153 ± 1 A
Filament Voltage	4.0 ± 0.2 V
X Steering Current	0 ± 0.1 A
Y Steering Current	0 ± 0.1 A

Table 3.2: Ion source parameters for the maximum beam current obtained with CO_2.

The mass spectrometer system with the entrance and exit slits set at 1 mm was used to analyze the beam composition. A typical spectrometer scan with CO_2 is presented in Figure 3.5.
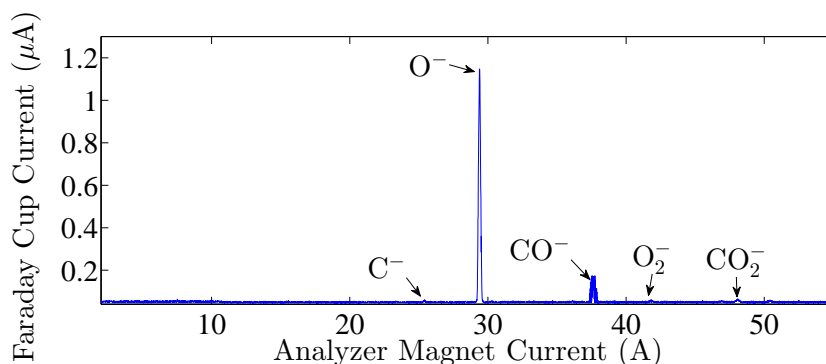
Figure 3.5: Spectrometer scan of a beam extracted by the TRIUMF licensed ion source with carbon dioxide as the injection gas. The arc current was set at 1 A, the arc voltage was set at 120 V, the gas flow was set at 10 sccm and the beam energy was set at 30 keV.

As can be seen in Figure 3.5, the main ion produced was O^- with small amounts of CO^- and trace amounts of C^-, O_2^- and CO_2^- also observed. The results compare well with the electron interaction studies presented earlier [91–93]. As was the case with the extraction of $C_2H_2^-$ from acetylene plasmas, the production of CO_2^- is through surface production as the volume production mechanisms involve the dissociation of the molecule.

The ion source's plasma chamber was much cleaner than with acetylene and the stability of the extraction was much better than with acetylene at about 100 glitches per hour. However, the C^- ion yield is too low which doesn't make carbon dioxide a viable injection gas for the production of negative carbon ions.

3.1.3 Methane

A previous study showed that the interaction of electrons with methane (CH_4) yields negative carbon ions through dissociative electron attachment [94]. C^- ions were found to be produced, however, the main negative ion found was H^- with a production rate of more than 13 times that of C^-. They also found that the minimum electron energy for the production of C^- was found to be of 26.7 eV, which is much higher than the average electron energy in the TRIUMF licensed filament-powered volume-cusp ion source. Other negative ions that were observed were

CH$^-$ and CH$_2^-$. It is predicted that methane will not be a good candidate for the production of C$^-$ with volume-cusp ion source but, it is important to measure the negative ions extracted with a methane plasma since it has a similar molecular geometry as phosphine (PH$_3$) and arsine (AsH$_3$), which are used in ion sources to implant phosphorus and arsenic respectively [95]. A positive result with methane would motivate the pursuit of experimenting with these gases for the production of P$^-$ and As$^-$ with volume-cusp ion sources for the purpose of ion implantation for semi-conductor production.

High purity methane (>99.9%) was used in the TRIUMF licensed ion source. Only two of the four filaments were used to reduce the total current needed to generate a plasma. The plasma was started with about 165 A of current in the filaments. A maximum total beam current of 0.28 mA was extracted with 4.4 sccm of methane gas flow and an arc power of about 600 W. The ion source parameters used to obtain the maximum beam current are presented in Table 3.3.

Parameter	Value
Total Beam Current	0.28±0.02 mA
Arc Current	4.9±0.1 A
Arc Voltage	120.0±0.1 V
Bias Current	1.43±0.08 mA
Bias Voltage	30.0±0.1 kV
Extraction Electrode Current	130.0±0.5 mA
Extraction Electrode Voltage	1.9±0.1 kV
Plasma Electrode Current	2.7±0.1 A
Plasma Electrode Voltage	20.0±0.1 V
Gas Flow	4.4±0.2 sccm
Filament Current	158±1 A
Filament Voltage	4.1±0.2 V
X Steering Current	0±0.1 A
Y Steering Current	0±0.1 A

Table 3.3: Ion source parameters for the maximum beam current obtained with CH$_4$.

The mass spectrometer system with the entrance and exit slits set at 1 mm was used to analyze the beam composition. A typical spectrometer scan obtained when methane was used as the injection gas is presented in Figure 3.6.
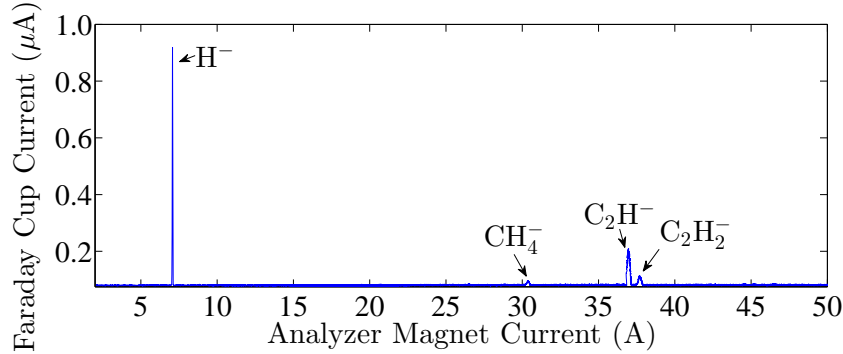
Figure 3.6: Spectrometer scan of a beam extracted with methane as the injection gas. The arc current was set at 1 A, the arc voltage was set at 120 V, the gas flow was set at 10 sccm and the beam energy was set at 30 keV.

From Figure 3.6, H^- composes most of the beam, with small contributions from CH_4^-, C_2H^- and $C_2H_2^-$. No C^- or C_2^- ions were detected in the beam. The hypothesis is that the C_2H^- and $C_2H_2^-$ ions come from contamination from previous tests with acetylene in the ion source. But, C_2 ions have been known to be present in methane plasmas [96], which could be an additional source of C_2H^- and $C_2H_2^-$ ions. From the results found by Smith [94], it was predicted that H^- was going to be the main negative ion produced in the methane plasma, which compares well with the extracted beam out of the ion source. Non-negligible amounts of CH_4^- were detected, which is due to surface production as dissociative electron attachment requires the molecule to split into two smaller entities. The C^-, CH^- and CH_2^- were also much lower than what was predicted. Since no C^- or C_2^- were extracted, methane is not a viable injection gas for the production of negative carbon ions.

3.2   Acetylene in the Filament Ion Source

Since the highest negative carbon current was extracted with acetylene as the injection gas in the plasma chamber, the remainder of the chapter will focus on the performance of the ion source with acetylene. This section will present how the negative beam current out of the TRIUMF licensed filament-powered volume-cusp ion source is affected by the different ion source parameters when acetylene is used

as the injection gas. The results obtained will be compared with the performance of the ion source for the production of H^-.

3.2.1 Gas Flow

Increasing the acetylene gas flow in the plasma chamber directly increases the pressure as was presented in the Section B.1.3. The total beam current, composed of all the species extracted out of the ion source and the co-extracted electron current as a function of the gas flow are presented in Figure 3.7. The extraction of the ion source with acetylene is unstable due to sparking on the extraction electrode and the frequency of the sparks observed is on the order of about 1000 glitches per hour. Due to these instabilities, the beam current values fluctuate and Figure 3.7 includes error bars which present a standard derivation of five consecutive measurements.
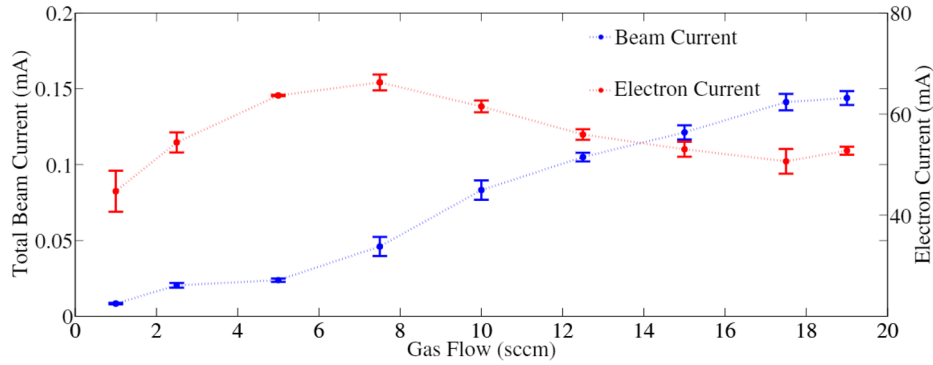
Figure 3.7: Total beam current and co-extracted electron current as a function of the gas flow. The arc current was set at 1 A, the arc voltage was set at 120 V, and the beam energy was set at 25 keV.

From Figure 3.7, there is an increase in beam current with an increase in gas flow. This is the opposite of what is seen with H^- at low arc currents, which was presented in the baseline H^- measurements in Figure B.22. Figure 3.8 presents the relative composition of the beam, measured with the mass spectrometer with the slits set at 1 mm, as a function of the gas flow for the data in Figure 3.7.
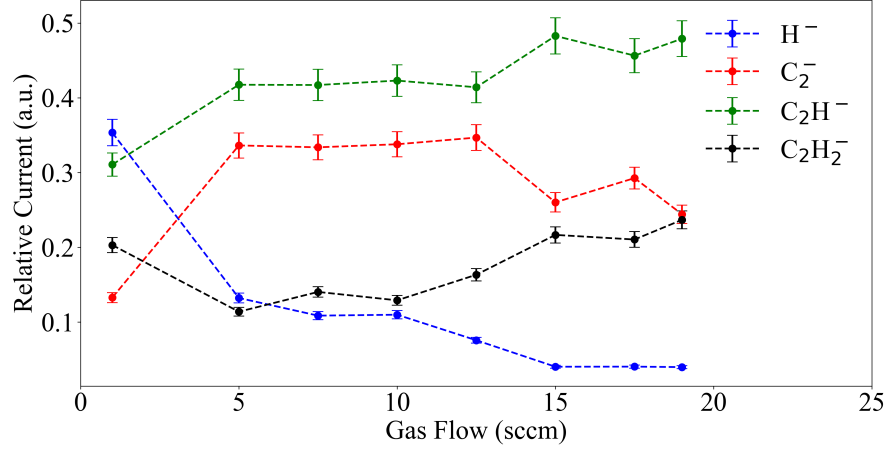
Figure 3.8: Relative current of the four main species as a function of the gas flow. The arc current was set at 1 A, the arc voltage was set at 120 V, and the beam energy was set at 25 keV.

From Figure 3.8, there is a decrease in the relative H^- current while there is a relative increase in beam current of the three main carbon species. The decrease in H^- current as a function of increasing gas flow is consistent with what is seen with the ion source operation with hydrogen. There is increased H^- stripping at the higher pressures which leads to a decrease in H^- beam current. The electron affinity of C_2H^- is 2.97 eV [97], that of C_2^- is 3.3 eV [98] and that of $C_2H_2^-$ is 2.21 eV [99], which are much higher than the electron affinity of hydrogen at 0.75 eV [100]. This means that the H^- is much more susceptible to stripping interactions than the negative carbon ion species.

There is also a net increase in the carbon species beam current with gas flow. This is due to an increase in production of these ions in the plasma, which can be caused by multiple factors including an increase in the neutral density in the plasma, an increase in the electron density or a change in the electron temperature. From Figure 3.7, there is no increase in co-extracted electron current as a function of gas flow, which indicates that there is no large change in the electron density close to the extraction of the ion source. Therefore, this eliminates an increase in the electron density as the cause of the increase in the total beam current. The

remaining factors for the total beam current increase as a function of the gas flow are thus related to either an increase in the neutral species density and/or an increase in the production cross section due to a change in the electron temperature in the plasma.

Increasing the gas flow in the ion source is thus a valid method to increase the negative carbon current extracted out of the ion source. The following section will focus on the effect of arc current on the beam current extracted.

3.2.2 Arc Current

From the baseline H^- measurements done in Figure B.22 the beam current generally increases with the arc power. This is due to an increase in the $H_2^*(v'')$ production rate in the plasma, which leads to an increase in H^- production through the dissociative electron attachment reaction. For acetylene, it is expected that increasing the arc current will increase the electron density in the plasma which should increase the negative ion production rate through dissociative electron attachment. Figure 3.9 presents the total beam current and the C_2^- current as a function of the arc current.
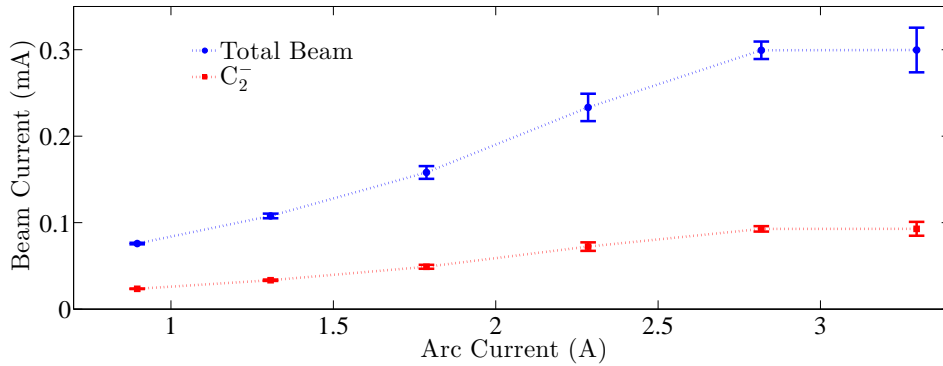
Figure 3.9: Total beam current and C_2^- beam current as a function of the arc current. The gas flow was set at 19 sccm, the arc voltage was set at 120 V, and the beam energy was set at 25 keV. The error bars correspond to the standard deviation of 5 consecutive measurements.

From Figure 3.9, there is an increase in both the total beam current and the

C_2^- beam current with arc current. The relative current of the different species stays constant as the arc current is increased which shows that the negative ion production rate increases uniformly for all of the negative ions, and suggests that the increase is due to an increase in the electron density in the plasma. There is also an increase in the frequency of the sparking on the extraction electrode when the arc current was increased, and this can be seen by the increase in the size of the error bars as the arc current is increased. The glitch rate increased from about 500-800 glitches per hour for arc currents of less than 2 A, to 2000-3000 glitches per hour for an arc current of 3 A. This restricts the operation at higher arc power, limiting the maximum beam current that could be extracted from the ion source.

Increasing the arc current is another valid method that could be used to increase the negative beam current extracted out of the ion source. However, with the increased power into the plasma there is also increased glitching on the extraction system, which limits the maximum power that can be applied into the plasma.

3.2.3 Plasma Electrode

For the operation of the ion source with H^-, there is a clear optimum in the plasma electrode potential, which was shown in Figure B.35 . The optimum plasma electrode voltage is usually close to the plasma potential because setting the electrode at this voltage eliminates the potential well created at the extraction, and increases the flux of H^- through the plasma sheath [46]. However, the extraction of negative carbon ions from an acetylene plasma was not influenced by the plasma electrode potential. Figure 3.10 presents the total beam current and the co-extracted electron current as a function of the plasma electrode voltage.
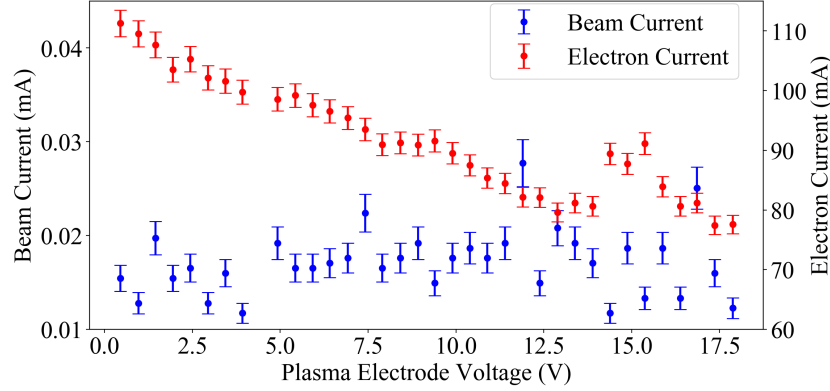
Figure 3.10: Total beam current and co-extracted electron current as a function of the plasma electrode voltage. The gas flow was set at 1 sccm, the extraction electrode was set at 2.9 kV, the arc current was set at 2 A and the arc voltage was set at 120 V and the beam energy was set at 25 keV.

From Figure 3.10, the plasma electrode voltage has no effect on the negative ion beam current extracted. The variation in the beam current seen is due to the instability of the extracted current caused by the frequent voltage breakdowns on the extraction system. The only effect the plasma electrode voltage had on the beam was on the co-extracted electron current, the increase in voltage on the plasma electrode reduces the co-extracted electron current, which is also seen with H^- (see Figure B.35). There is also an increase in the plasma electrode current as the electrode voltage is increased, which indicates that there is a depletion of the electron density in the plasma near the electrode, and the depletion increases with the plasma electrode voltage.

3.2.4 Emittance

A normalized 4-RMS emittance of less than 1 mm·mrad is required for the target ion implantation application. The emittance scanner at the ISTF is located upstream of the spectrometer system, so the phase space scans include all of the species that make up the total beam current and not just the desired C_2^- ions.

A normalized 4-RMS emittance value commonly between 0.5 mm·mrad and

60

0.9 mm·mrad for the total beam of all species was found, which is larger than what was commonly found with hydrogen, but is lower than the upper maximum limit of 1 mm·mrad desired for this Thesis work. The 4-RMS emittance of the C_2^- beam was not measured but is clearly less than 1 mm·mrad. The normalized 4-RMS emittance as a function of the acetylene gas flow is presented in Figure 3.11.
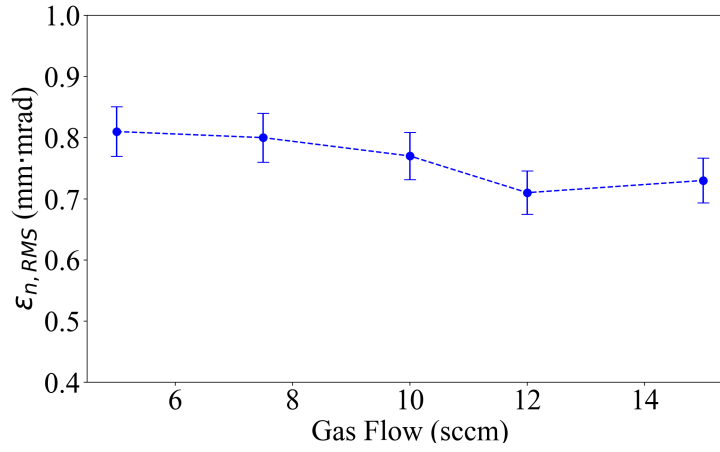
Figure 3.11: Normalized 4-RMS emittance as a function of the gas flow for the total (all species) negative ion beam extracted from an acetylene plasma and comprised of ions shown in Figure 3.2. The arc current was set at 2 A, the arc voltage was set at 120 V, the plasma electrode was set at 20 V, the extraction electrode was set at 2.8 kV and the bias voltage was set at 25 kV.

There is a slight decreases of the emittance as the acetylene gas flow increases. But, the 4-RMS emittance is also well below the desired upper limit of 1 mm·mrad. The phase space scans of the 5 sccm and 15 sccm tunes are presented in Figure 3.12.
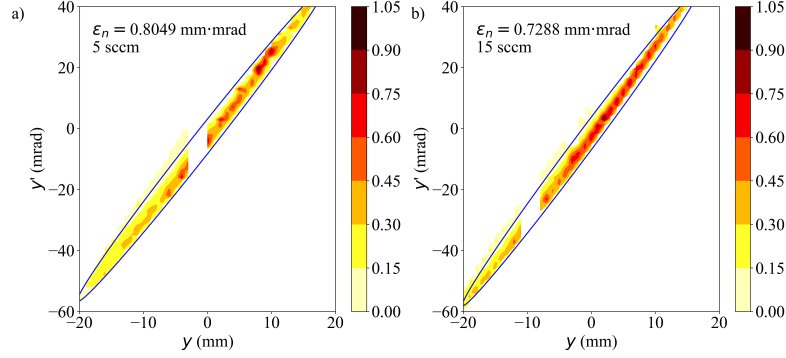
Figure 3.12: Phase space scan of a) the 5 sccm tune and b) the 15 sccm tune.

The ion source parameters for the phase space scans presented in Figure 3.12 are presented in Table 3.4.

	Tune a	Tune b
Total Beam Current	0.03 mA	0.13 mA
Arc Current	1.97 A	1.97 A
Arc Voltage	120 V	120 V
Bias Current	1.5 mA	1.4 mA
Bias Voltage	24.99 kV	24.99 kV
Extraction Electrode Current	54 mA	95 mA
Extraction Electrode Voltage	2.6 kV	2.52 kV
Plasma Electrode Current	0.31 A	0.31 A
Plasma Electrode Voltage	10 V	10 V
Gas Flow	5 sccm	15 sccm
Filament Current	370 A	367 A
Filament Voltage	4.3 V	4.4 V
X Steering Current	0 A	0 A
Y Steering Current	0 A	0 A

Table 3.4: Ion source parameters for the phase spaces presented in Figure 3.12.

From Figure 3.12, there are gaps in phase space due to large glitches that interrupt the beam and leave holes in the data as the emittance scanner is scanning. However, the emittance can still be properly calculated by judging how the emit-

tance ellipse overlaps the data.

To study the origin of the decrease of emittance with gas flow, the negative ion beam was simulated in IBSimu [77], as was presented in Section B.4.5. The beam parameters of Table 3.4 were used as well as the other IBSimu parameters used for the H^- study presented in Section B.4.5. The relative composition of the beams simulated were set to H^-:C_2^-/C_2H^-/C_2H2^- = 1:1 and 1:2. Figure 3.13 presents the phase spaces obtained at the location of the emittance scanner ($z = 368$ mm).
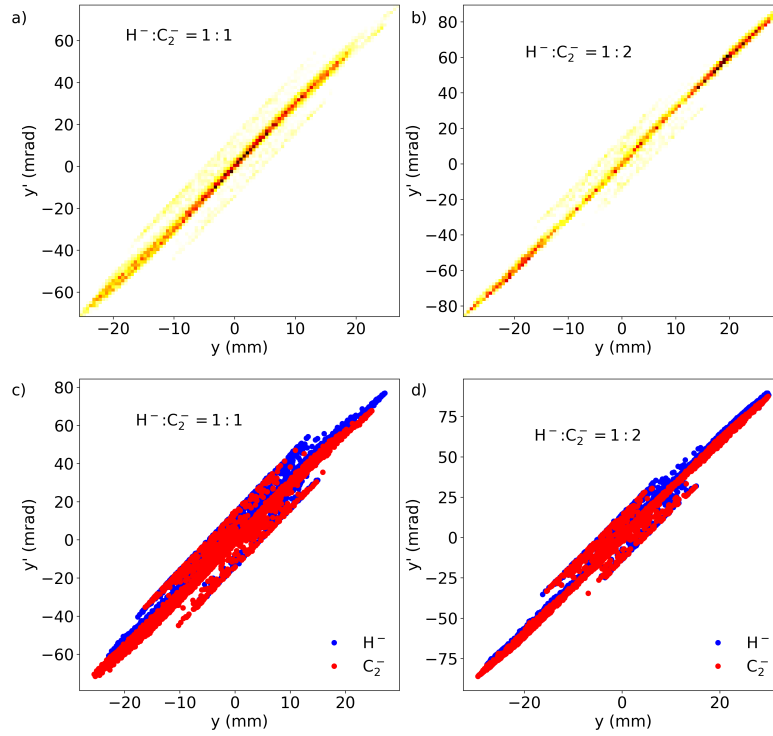
Figure 3.13: Phase space obtained in IBSimu for a relative H^-:C_2^- ratio of a) 1:1 and b) 1:2. c) and d) Scatter plots of the two simulated beam.

As can be seen in Figure 3.13, H^- and C_2^- beams produce different phase space

63

distributions and the difference between the two increases the RMS emittance. The reduction in emittance was due to a decrease in the relative H$^-$ current at higher gas flows.

The difference in the emittance as a function of gas flow is not due to the increased space charge compensation seen with the pressure in the vacuum chamber, as it was with hydrogen in Section B.4.5. This is due to the fact that the pressure in the vacuum chamber is much lower with the acetylene plasma compared to the hydrogen plasma and the pressure is too low for the space charge compensation to be effective. Upon igniting the acetylene plasma, there is a sharp drop in the pressure measured by the vacuum gauge in the upstream region of the vacuum box. The drop in pressure is likely explained by the formation of nanometer sized particles [101] that are deposited on the plasma chamber walls, as was presented in Figure 3.4. The pressure measured in the upstream region of the vacuum chamber as a function of gas flow for an acetylene plasma, a hydrogen plasma and acetylene gas flow but no plasma is presented in Figure 3.14. There is a clear drop in pressure when there is an acetylene plasma and the pressure is also much lower than it was with hydrogen plasmas.
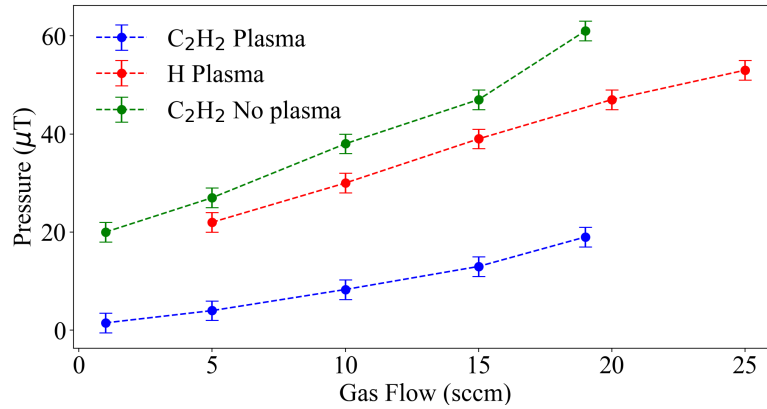
Figure 3.14: Pressure measured in the upstream region of the vacuum chamber as a function of the gas flow with an acetylene plasma, with a hydrogen plasma and with acetylene gas but without a plasma. The arc was set at 2 A and 120 V for the measurements with the plasma.

64

From Figure 3.14, the large drop in pressure between the case with and without the acetylene plasma can be seen. The pressure with the acetylene plasma is also much lower than the hydrogen plasma. Space charge compensation was only effective at hydrogen gas flows of more than 15 sccm, so the pressure with the acetylene plasma is too low for effective space charge compensation of the beam.

The emittance measurement as a function of the arc current could not be completed due to the higher glitch rates above 3 A of arc current (> 1000 glitches per hour) and the minimum time to take a phase space scan of the beam (about 2 minutes), which led to too much missing data to obtain valid emittance values.

The initial analysis of the extraction of negative carbon ions from an acetylene plasma presented in this section revealed that considerable C_2^- beam current (0.1 mA) can be extracted. This is the most negative carbon ion current extracted from a cesium free ion source that has been reported. There are, however, drawbacks to the use of acetylene in the ion source which include a high glitch rate and contamination of the plasma chamber. The following section will focus on the analysis of the acetylene plasma to determine which processes are involved in the production of the negative ions.

3.3   Plasma Parameters Analysis

To better understand why there is an increase in negative beam current as a function of gas flow, the acetylene plasma was analyzed with a Langmuir probe.

The Langmuir probe described in section B.4.9 was located 20 mm from the plasma electrode, upstream in the plasma chamber, on the central axis of the ion source. As with the hydrogen plasma, the probe was inserted through the extraction system, as in Figure B.20, preventing the application of a bias on the ion source and the electrodes. The same configuration was used to effectively measure the electron temperature and density in a hydrogen plasma, as was presented in Section B.4.9. Figure 3.15 presents an *IV* curve and obtained with the Langmuir probe in the acetylene plasma.
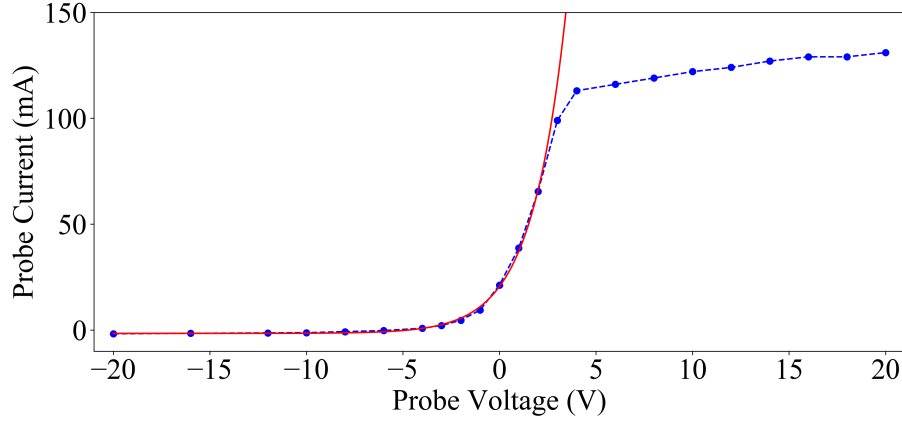
Figure 3.15: Langmuir probe *IV* curve with an exponential fit obtained with an acetylene plasma. The arc current was set at 1 A, the arc voltage was set at 120 V and the acetylene gas flow was set at 10 sccm.

From Figure 3.15, the plasma potential is very close to 0 V. Indeed, an important difference seen when comparing the acetylene and hydrogen plasma is that the plasma potential was lower with acetylene and even became negative for higher arc currents. This is explained by a reduced confinement of the positive ions in the acetylene plasma due to the heavier mass of the ions, which leads to a higher flow of positive ions to the walls of the plasma camber. When the total flow of positive ions to the wall is larger than the electron flow, the plasma potential becomes negative. The lower plasma potential explains why there is no optimum plasma electrode value with the extraction of negative ions with acetylene, as was seen in Figure 3.10. There is no potential well created by the plasma potential and the electric potential in the extraction region, thus the plasma electrode does not need to be biased to improve the flow of negative ions to the extraction region.

The electron temperature (T_e) and the electron density (n_e) were calculated as a function of the gas flow in the ion source using the theory presented in Section B.4.9. The results are presented in Figure 3.16. The error bars correspond to the 95% interval for the exponential fit to find T_e and by assuming ± 0.5 mA in the current measurement at the plasma potential to find n_e.

66
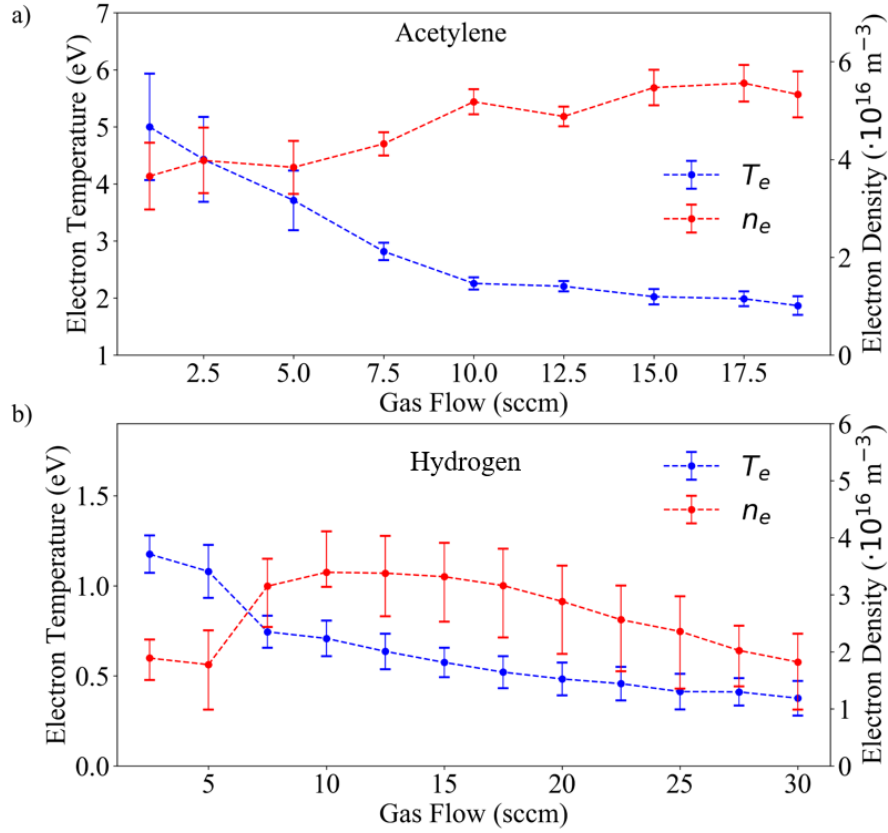
Figure 3.16: a) Langmuir probe measurements of electron temperature and density in an acetylene plasma as a function of the gas flow with the probe tip located 20 mm upstream from the plasma electrode, on the central axis of the ion source. The arc current was set at 1 A and the arc voltage was set at 120 V for the measurements. b) Measurements with hydrogen presented in Figure B.41.

From Figure 3.16, there is a considerable decrease in the electron temperature with the increase in gas flow, while the electron density remains relatively constant. The decrease in electron temperature places the electron energy distribution in a more favorable position for the production of C_2^- and C_2H^- with DEA in acetylene as was presented by Szymanska et al. [83]. They found that there was a peak in the DEA cross section at an energy of about 2.5 eV, which is slightly higher than the electron temperature at more than 10 sccm. The increased gas flow also leads

to an increase in the neutral density which would also lead to an increase in all the negative ion species. Both effects explain the increase in negative carbon beam seen with gas flow.

When comparing the plasma properties of acetylene and hydrogen, the electron density is comparable between the two plasmas at similar arc parameters however, the electron temperature is much higher in the acetylene plasma. The big difference seen in electron temperature is explained by a large pressure difference between the two plasmas, as was presented in Figure 3.14. The pressure in the ion source is much lower with acetylene due to the deposition of particles on the walls of the plasma chamber. The reduced density of neutral particles in the plasma means that the electron temperature will be higher since the collision frequency between the electrons and the neutrals will be lower. As is seen in Figure 3.16, the electron temperature is always lower at higher gas flows, which means that the electron temperature decreases with the pressure in the ion source since the gas flow and the pressure are directly related.

The plasma parameters as a function of the arc current for the acetylene and the hydrogen plasmas are presented in Figure 3.17.
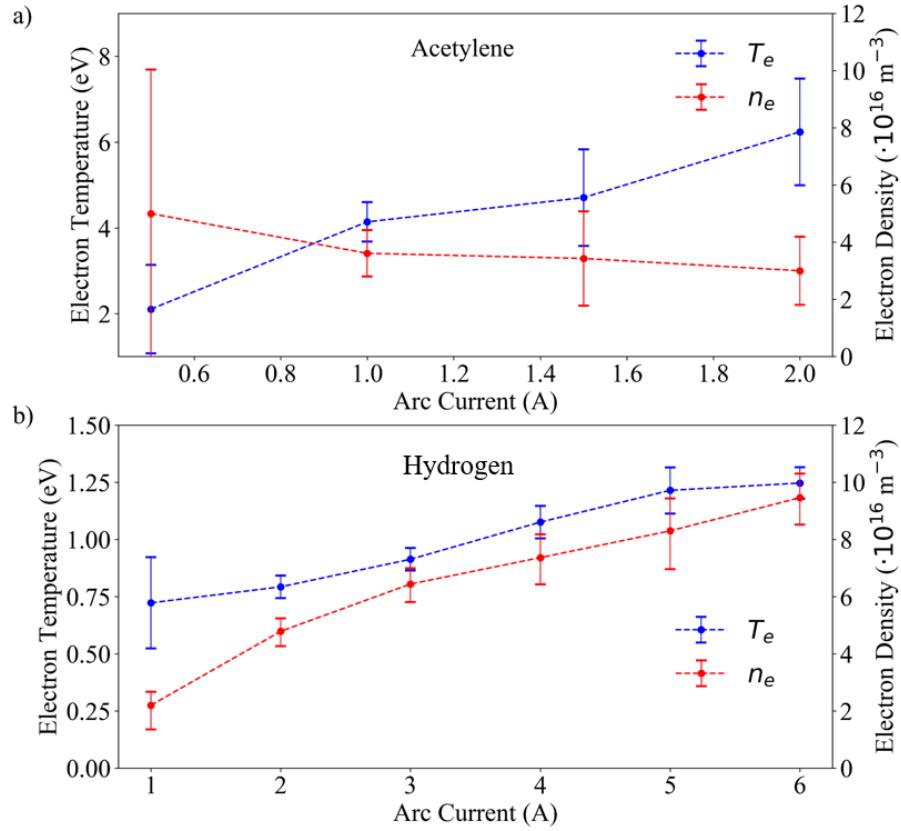
Figure 3.17: a) Langmuir probe measurement of the electron temperature and density in an acetylene plasma as a function of the arc current with the probe tip located 20 mm upstream from the plasma electrode, on the central axis of the ion source. The arc voltage was set at 120 V and the gas flow was set at 5 sccm for the measurements. b) Measurements with hydrogen presented in Figure B.40

.

From Figure 3.17, the electron temperature increases with the arc current, as it did with hydrogen. However, the electron density decreases slightly with the arc current unlike the case with hydrogen but, the error bars are large compared to the electron density values, which gives poor confidence in the results. Due to financial restrictions, the power supply used with the Langmuir probe is not a proper bi-polar power supply. When the arc current increases, the plasma potential becomes negative and the power supply can no longer supply the voltage needed

69

on the probe since the current is positive with a negative voltage. This increases the uncertainty in the measurements and prevents the measurement of the plasma properties at higher arc currents. The decrease of the plasma potential with arc current when acetylene is used in the TRIUMF licensed filament-powered volume cusp ion source is the opposite of what was seen with the hydrogen plasma, as presented in Figure B.36.

The Langmuir probe analysis completed allowed for the determination of the plasma parameters as a function of the gas flow and the arc current. From the analysis, it is clear that there is an important difference between hydrogen and acetylene plasmas.

3.4 Conclusion

The purpose of this chapter was to study the production and extraction of negative carbon ions with the TRIUMF licensed filament-powered volume-cusp ion source which was the baseline equipment defined by D-Pace for the ISTF. The four main constituents of the beam extracted out of the acetylene plasma include H^-, C_2^-, C_2H^- and $C_2H_2^-$. Up to 0.1 mA of C_2^- beam current can be extracted, which is more than any cesium free ion source reported in the literature, but it is short of the industrial goal of 0.5 mA. It was found that increasing the gas flow and the arc current led to an important increase in beam current. However, increasing the arc power also led to increased sparking on the extraction electrode, which leads to high glitch rates. Reducing the glitch rate would allow the ion source to be operated at higher powers and would lead to higher beam currents extracted out of the ion source. This will be part of the focus of Chapter 6. The analysis with the Langmuir probe revealed that the electron temperature is much higher with acetylene than with it was with hydrogen, and the main reason this is seen is because the pressure in the acetylene plasma is considerably lower than it is with hydrogen. Increasing the gas flow in the acetylene plasma led to a decrease of the electron temperature below 3 eV, which puts it in a more favorable region for the production of C_2^- through dissociative electron attachment. The results presented in this chapter led to the publication of two papers [27, 28].

The filament-powered ion source is ultimately not a commercially viable op-

tion for an ion implanter system because the tantalum filament material will get sputtered by the positive ions in the plasma and contaminate the system. The next two chapters of this Thesis will focus on volume-cusp ion sources with external RF antennas, which are ideal candidates for the target ion implanter application, since alkali metallic vapour and sputtered metallic filament material will be avoided altogether.

Chapter 4

RF-Powered Ion Source Development

Radio Frequency (RF) powered ion sources with external antenna would be a valid option for the ion source that is being developed for this Thesis work since there is no sputtered metallic filament material, thus no contaminants are introduced in the plasma. Furthermore, the filament is eliminated as a consumable item, so RF ion source lifetimes are estimated at greater than one year, regardless of the output beam current level. In the previous chapter it was shown that high C_2^- beam currents can be extracted from a filament-powered volume-cups ion source, but the filament material is sputtered into the plasma, adding an unwanted contaminant, there is thus an interest in RF-powered ion sources. This chapter will present the RF ion source development work that was completed as part of this Thesis work.

The first part of the chapter will present the RADIS ion design which is an RF-powered ion source that was licensed from the University of Jyväskylä [29, 30]. The focus will then be on the key contributions of this Thesis work which are the theory, implementation and performance of an impedance matching system, which is needed to efficiently couple RF power through an antenna. Finally, the extraction of negative ions from operating the RADIS ion source with acetylene was studied.

The second part of the chapter presents the development of a new hybrid RF-powered ion source that combines the RF window and antenna of the RADIS ion source with the body and extraction system of the TRIUMF licensed filament-

powered ion source. The design of the ion source and its performance with H$^-$ will first be presented. The ion source was commissioned with H$^-$ since it's known to be stable and the results can be easily compared with those obtained with the filament-powered ion source results that were presented in Appendix B. Finally, issues that arose from the development are presented and a few improvements to design are proposed.

4.1 RADIS Ion Source

To test whether an RF-powered ion source would be a suitable negative carbon ion source for an ion implanter system, the performance of the RADIS ion source [30] was measured with acetylene. This section will present the ion source in detail.

The RADIS ion source was developed by the University of Jyväskylä to replace their filament powered H$^-$ ion source [30]. The RADIS ion source is a volume-cusp ion source, similar in design to the TRIUMF licensed filament-powered volume-cusp ion source, it has a cylindrical plasma chamber with a diameter of 98 mm and a length of 130 mm. The plasma confinement is achieved with 16 rows of SmCo$_{26}$MGOe magnets around the circumference of the plasma chamber and an electromagnet is embedded into the plasma electrode to act as the electron filter that creates the *cold* plasma region. The electromagnet dipole allows for an adjustable magnetic dipole filter field while operating the ion source, it can be increased up to a maximum of about 670 G with the peak located about 15 mm from the plasma electrode. The RADIS ion source uses a flat 3.5 turn antenna located directly against an aluminum nitride (AlN) window to couple the power into the plasma. A cross section of a model of the RADIS ion source is presented in Figure 4.1.
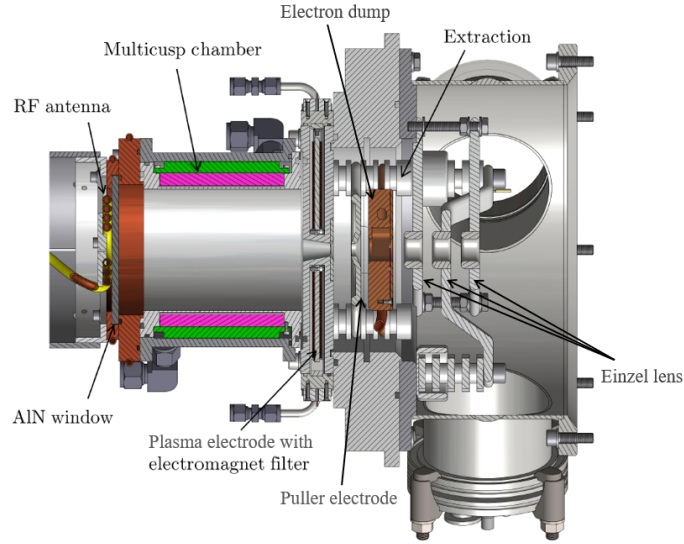
Figure 4.1: Cross-sectional view of the RADIS ion source. Figure taken from [30].

The extraction system is composed of 6 electrodes and consists of a plasma electrode, a puller electrode, an electron dump with two opposite direction magnetic dipoles and an Einzel lens. Table 4.1 presents the aperture diameters and the typical voltage on the electrodes.

Electrode	Aperture Diameter (mm)	Voltage (kV)
Plasma	7	-19
Puller	10	-9
Electron Dump	18	-13
Einzel (Upstream)	30	0
Einzel (Center)	30	$+20$
Einzel (Downstream)	30	0

Table 4.1: RADIS extraction system parameters.

The ion source is commonly biased at -19 kV and the plasma electrode can be biased at up to 40 V above the ion source potential. When comparing with the TRIUMF licensed ion source, two additional power supplies are needed for the added electrodes: i) a 13 kV, 8 mA power supply was used for the puller electrode

and ii) a +30 kV, 5 mA power supply was used for the Einzel lens. Figure 4.2 presents an IBSimu simulation of the extraction of the RADIS ion source as well as the magnetic field (B_y) on axis for various electromagnet currents [102].
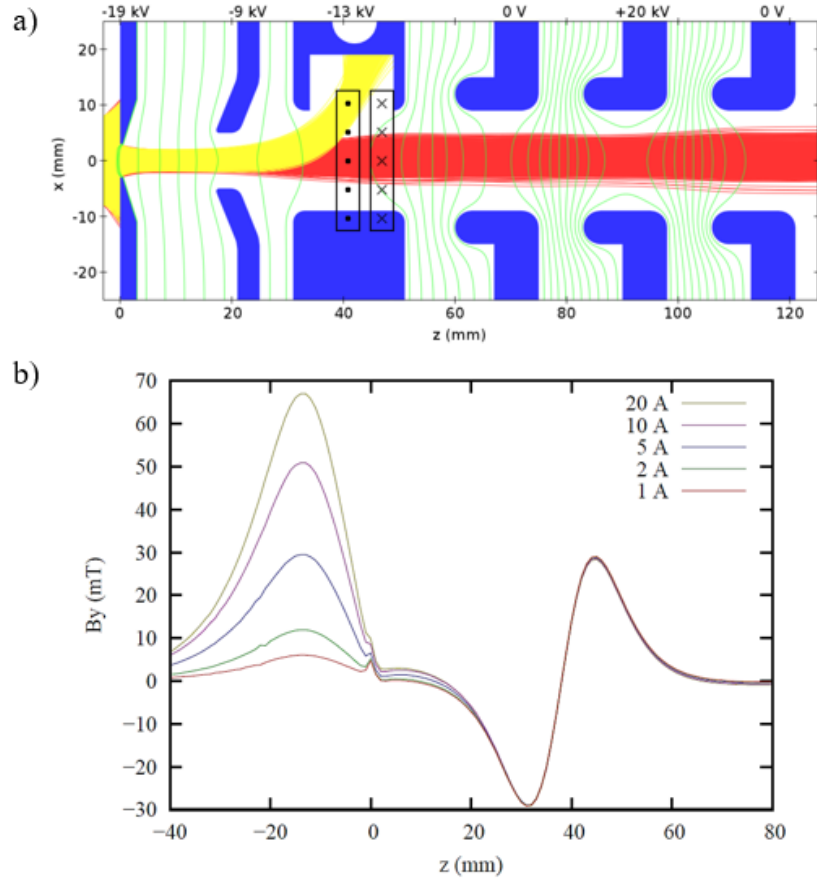
Figure 4.2: a) IBSimu simulation of the extraction of H$^-$ ions from the RADIS ion source. The electrodes are in blue, the equipotential lines are in green, the H$^-$ ions are presented in red and the co-extracted electrons are in yellow. b) Magnetic field on axis for various electromagnet currents. The plasma electrode is at $z = 0$ mm and the plasma chamber is represented by the negative axis. Taken from [102].

A copy of the RADIS ion source was manufactured and a custom mounting flange was designed so that it could be mounted at the ISTF. However, there was no impedance matching system on the baseline ISTF system since it is not needed to

operate the TRIUMF licensed filament-powered ion source. The following section will present the development of an impedance matching system which was part of the Thesis work, so that the RADIS ion source can be operated at the ISTF.

4.2   Impedance Matching

To maximize the power coupled through a system, the impedance of the system has to match the impedance of the power source. Such is the case for the RADIS ion source antenna and ion source system. Furthermore, the impedance of this system will be dependent on the plasma in the ion source, and thus the impedance will be time dependent when the plasma is first ignited in the ion source. An impedance matching system is therefore needed to operate the RADIS ion source.

To design a proper impedance matching system, the impedance of inductively coupled plasmas needs to be studied. This will be the first part of this section and the work is heavily based on previous work by Hopwood [103, 104]. An impedance matching circuit is then proposed and the capacitor values needed to efficiently couple power to the plasma for all of the operational settings are calculated. Finally, the implementation of the impedance matching circuit at the Ion Source Test Facility is presented.

4.2.1   RF Coupling with Plasma

To develop a proper impedance matching network system, the impedance of the plasma should be known, thus a study of the coupling of RF power into a plasma will be done. The antenna that sustains the plasma in RF ion sources generates decaying electromagnetic waves into the plasma [105]. As is discussed in Section A.1, the plasma frequency is given by $\omega^2 = \frac{ne^2}{\varepsilon_0 m}$ which gives an electron frequency of $1.3 \cdot 10^{13}$ Hz and a proton frequency of 294 MHz for densities of $5 \cdot 10^{16}$ m^{-3}. Thus there is now resonance between these frequencies and the RF frequency used (13.56 MHz).

For low pressure plasmas that are commonly seen with ion sources, the decay is exponential with decay constant given by [104]

$$\delta_{\mathrm{p}} \approx \frac{c}{\omega_p}. \tag{4.1}$$

where δ_p is known as the skin depth of the plasma, c is the speed of light, ω_p is the plasma frequency introduced in Section A.1.

There are two known modes for inductively coupled plasmas, the inductive and the capacitive modes [103]. In the capacitive mode, the plasma is sustained by the electric field created by the potential difference between the different turns in the antenna. For the planar coil used in the RADIS ion source, as presented in Figure 4.3, the electric field is mostly in the radial direction since there will be a potential difference between the turns of the antenna.
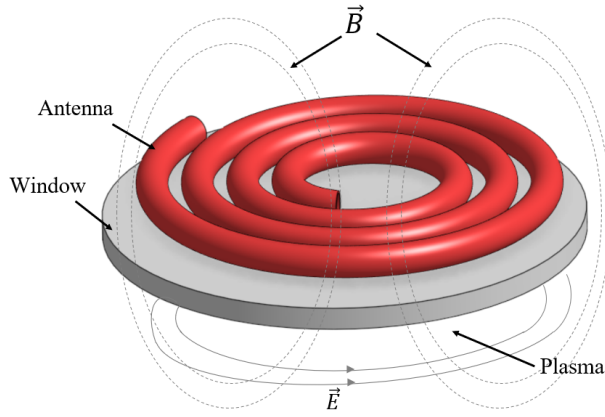
Figure 4.3: Schematic representation of the inductive RF coupling to a plasma with a flat coil antenna.

The capacitive mode is the dominant mode at lower RF powers and there is a threshold RF power for the coupling to be in the inductive mode. The capacitive mode is known to give a plasma with a lower electron density [106]. The inductive mode is the dominant mode above the threshold power and leads to higher electron densities. In the inductive mode, the electric field is mostly in the angular direction, as presented in Figure 4.3. This leads to a plasma current that follows the electric field lines and will thus circle in the same axis as the turns of the antenna at a distance δ_p inside the plasma chamber.

The goal is to predict the impedance seen by the RF amplifier for the inductive mode to be able to predict the impedance of the system, which will allow for a proper impedance matching system to be designed for the ion source. A schematic representation of the situation is presented in Figure 4.4.
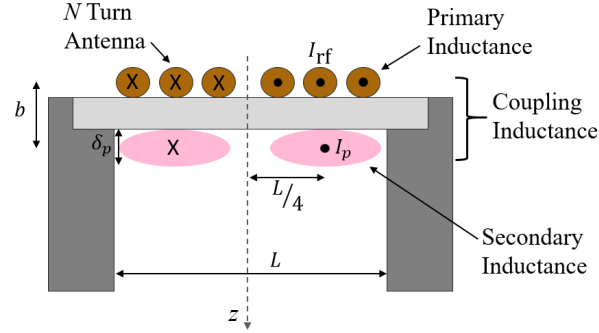
Figure 4.4: Schematic representation of the RF coupling to a plasma.

A cylindrical plasma chamber of diameter L, a plasma thickness of δ_p, which is the skin depth of the RF electromagnetic fields and a distance b between the antenna and the center of the plasma will be assumed for the analysis. The current generated by the plasma will be ring shaped with a radius of $L/4$ since this is where the electric field will be maximum. The electric field at $r = 0$ and at $r = L$ will be zero, where r is the radial coordinate of the plasma chamber. There is thus a ring of electron current in the plasma which is coupled to the antenna outside the plasma.

The coupling between the antenna and the plasma can be modeled as a transformer [107], as presented in Figure 4.5.
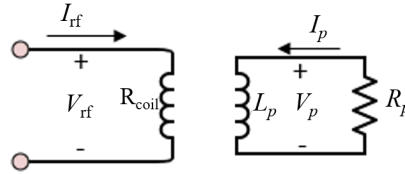
Figure 4.5: Schematic of the electrical representation of the RF coupling to a plasma.

I_{rf} and V_{rf} in Figure 4.5 represent the current and voltage from the RF generator, while I_p, V_p, R_p and L_p represent the current, voltage, resistance and inductance of the plasma. The plasma resistance R_p is inversely proportional to the plasma conductivity $\sigma_{dc} = \frac{e^2 n_e}{m_e v_e}$, where v_e is the collision frequency of the electrons in the plasma [103]. R_p will also be proportional to the ratio of the current circumference

to the cross-section of the current ring. R_p is thus

$$R_p \approx \frac{L}{2\sigma_{\text{dc}}\delta_p^2}.$$

(4.2)

The inductance of the plasma will be given by the magnetic flux produced by the plasma divided by the plasma current [103]. The magnetic flux from a ring of current I of radius R and length l is given by $B = \frac{\mu_0 \pi R^2 I}{l}$, where μ_0 is the vacuum permeability. Thus, the plasma inductance L_p will be given by

$$L_p \approx \frac{\mu_0 \pi L^2}{16\delta_p}.$$

(4.3)

The voltages in Figure 4.5 are given by the transformer equations:

$$V_{\text{rf}} = i\omega L_{11} I_{\text{rf}} + i\omega L_{12} I_{\text{p}}$$

(4.4)

and

$$V_{\text{p}} = i\omega L_{21} I_{\text{rf}} + i\omega L_{22} I_{\text{p}},$$

(4.5)

where ω is the angular frequency of the RF. Four induction terms were introduced in equations 4.4 and 4.5 [103]. L_{11} is the primary inductance of the coil, and by using the usual definition of the inductance, $L_{11} \approx \frac{\mu_0 \pi N L}{4}$. $L_{12} = L_{21}$ is the coupling inductance between the antenna and the plasma. It is given by the magnetic flux linking the plasma divided by the coil current, $L_{12} \approx \frac{\mu_0 \pi N L^2}{16b}$. Finally, $L_{22} = L_p$, which is the inductance of the plasma.

To simplify the analysis, the total impedance of the system ($Z_s = R_s + i\omega L_s$) will be considered and defined as $Z_s = \frac{V_{\text{rf}}}{I_{\text{rf}}}$. Ohm's law is used to describe the plasma potential, $V_{\text{p}} = -I_{\text{p}} R_{\text{p}}$. Using equations 4.4 and 4.5, one gets:

$$V_{\text{p}} = \frac{i\omega L_{12} I_{\text{rf}}}{1 + \frac{i\omega L_{22}}{R_{\text{p}}}},$$

(4.6)

and

$$Z_s = i\omega L_{11} + \frac{\omega^2 L_{12}^2}{R_{\text{p}} + i\omega L_{22}}.$$

(4.7)

79

Separating the real and the imaginary parts of Z_s and adding the impedance of the coil, $Z_{\text{coil}} = R_{\text{coil}} + i\omega L_{\text{coil}}$, in series, R_s becomes

$$R_{\text{s}} = R_{\text{p}}\frac{\omega^2 L_{12}^2}{R_{\text{p}}^2 + \omega^2 L_{22}^2} + R_{\text{coil}}, \tag{4.8}$$

and

$$L_{\text{s}} = \frac{L_{\text{coil}}(R_{\text{p}}^2 + \omega^2 L_{\text{p}}^2) - \omega^2 L_{12}^2 L_{\text{p}}}{R_{\text{p}}^2 + \omega^2 L_{\text{p}}^2}. \tag{4.9}$$

There are additional resistance and inductance components that come from the movement of the electrons in the plasma. The total resistance of the system is also highly dependent on the electron density. At higher electron densities, $\omega L_{22} \gg R_p$ and $R_s \approx R_p \propto \frac{1}{\sigma_{\text{dc}}\delta_p} \propto \frac{1}{\sqrt{n_e}}$. At lower densities, the plasma size is smaller than the skin depth and the resistance will be proportional to the number of electrons, $R_s \propto n_e$ [103]. This is important because the power absorbed by the plasma is given by

$$P = \tfrac{1}{2}|\tilde{I}_{\text{rf}}|^2 R_s. \tag{4.10}$$

The power loss in a plasma can be mostly attributed to particles hitting the plasma chamber walls, thus the power loss is proportional to the electron density ($P_{\text{loss}} \propto n_e$).

4.2.2 RF Coupling in the RADIS Ion Source

The following section will show how the power is absorbed and lost in a plasma generated by the flat antenna design of the RADIS ion source [30]. The antenna geometry is first introduced. The antenna is made of 3.5 turns of 6 mm diameter copper tubing. The outer diameter of the antenna is 90 mm and there is an inner diameter of 36 mm in the center. A schematic of the cross section of the antenna is presented in Figure 4.6.
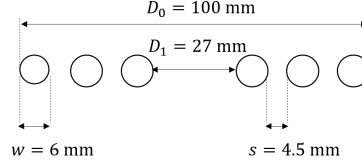
Figure 4.6: Schematic of the antenna used in the RADIS ion source.

The inductance of the antenna is given by [108]

$$L = \frac{N^2 A^2}{30A - 11D_1}. \tag{4.11}$$

with

$$A = \frac{D_1 + N(w+s)}{2}. \tag{4.12}$$

The parameters of equations 4.11 and 4.12 are presented in Figure 4.6. This gives an inductance $L_{\text{coil}} = 0.74\ \mu\text{H}$. Using this value and the theory presented in this section, the power absorbed by the plasma is calculated as a function of the electron density. This is represented in Figure 4.7, where the power absorbed is calculated by the plasma for two different currents in the antenna ($\tilde{I}_1$ and $\tilde{I}_2$).
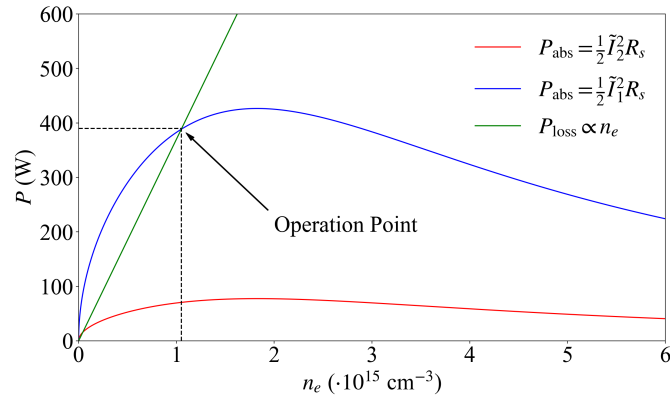
Figure 4.7: Power loss and absorbed for an inductively coupled plasma according to the transformer model and an antenna inductance of 0.74 μH.

Figure 4.7 is for illustrative purpose only since a model for the power loss

hasn't been introduced in this analysis. The operating condition is determined by the intersection of the absorbed power and the power loss curves. There's a minimum electron density to obtain an inductively coupled plasma, and the electron density increases with $\tilde{I}_{rf}$. Adding the capacitive mode to the model lowers the threshold in the low density part of the curve, making plasma generation possible at lower RF powers.

From this analysis, the impedance of the plasma that is coupled to an RF power source through a flat coil antenna was predicted. The next section will present the design of an adequate circuit to match the impedance of the system to the output impedance of the RF amplifier.

4.2.3 Impedance Matching Circuit

This section will present the impedance matching circuit that was developed to match the impedance of the system to the RF amplifier. As was presented in the previous section, the impedance of the system is highly dependent on the plasma parameters, thus an impedance matching system that can be tuned to accommodate changes in the plasma impedance is needed. Two common impedance matching circuits are presented in Figure 4.8.
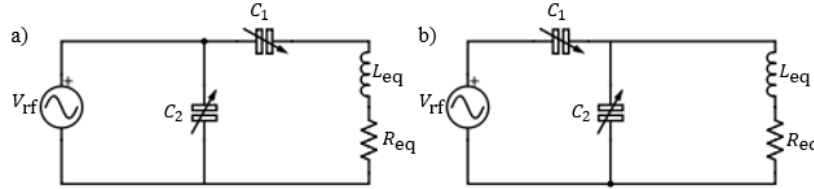
Figure 4.8: a) Reverse L-Network and b) L-Network impedance matching circuit.

The impedance matching networks presented in Figure 4.8 have variable capacitors so their impedance can be tuned with the varying plasma impedance as the plasma parameters change. An L-Network configuration has been chosen for the impedance matching system at the ISTF. The impedance, Z, of the L-Network circuit is given by

$$Z = \frac{1}{i\omega C_1} + Z_2, \tag{4.13}$$

where ω is the angular frequency of the RF, C_1 is the capacitance of the capacitor 1 and Z_2 is the impedance of C_2 and the plasma/antenna in parallel (L_{eq} and R_{eq}), as seen in Figure 4.8. Z_2 is given by

$$\frac{1}{Z_2} = i\omega C_2 + \frac{1}{R_{eq} + i\omega L_{eq}}. \tag{4.14}$$

Equation 4.13 then becomes

$$Z = \frac{-i}{\omega C_1} + \frac{R_{eq} + i\omega(L_{eq} - R_{eq}^2 C_2 - \omega^2 L_{eq}^2 C_2)}{(1 - \omega^2 L_{eq} C_2)^2 + \omega^2 C_2^2 R_{eq}^2}. \tag{4.15}$$

The impedance of the system has to match a load of 50 Ω of the RF amplifier. The C_1 and C_2 values needed are found using

$$\frac{R_{eq}}{(1 - \omega^2 L_{eq} C_2)^2 + \omega^2 C_2^2 R_{eq}^2} = 50 \ \Omega, \tag{4.16}$$

and

$$\frac{L_{eq} - R_{eq}^2 C_2 - \omega^2 L_{eq}^2 C_2}{(1 - \omega^2 L_{eq} C_2)^2 + \omega^2 C_2^2 R_{eq}^2} = \frac{1}{\omega^2 C_1}. \tag{4.17}$$

This is a quadratic system of equations with 2 variables and 2 equations. There are up to two solutions for a specific $Z_{eq} = R_{eq} + i\omega L_{eq}$. The positive solution will be used since the capacitance is a positive value. Z_{eq} is highly dependent on the plasma so C_1 and C_2 will have to be varied as the plasma conditions change.

A 3.5 turn antenna made of 6 mm diameter copper and with a total diameter of 90 mm is considered for the analysis. The inductance of the antenna is around 1 μH and the resistance is around 0.5 Ω. When the plasma isn't ignited $Z_{eq} \approx 0.5 + i85$ Ω at 13.56 MHz because the impedance is only determined by the geometry of the antenna. Solving for a match of 50 Ω, $C_1 = 13.8$ pF and $C_2 = 124$ pF. With the plasma ignited, R_{eq} increases and L_{eq} decreases. Assuming an electron density of $1 \cdot 10^{16}$ m^{-3}, $Z_{eq} \approx 1.5 + i59$ Ω. To match with a load of 50 Ω, $C_1 = 34$ pF and $C_2 = 163$ pF. C_2 will thus need to be higher than C_1 and C_2 will have to varied over a wider range than C_1.

The scattering parameter (S_{11}) of the system can be calculated to evaluate the

83

quality of the impedance matching [109]. The S_{11} parameter is given by

$$S_{11} = 10 \log \frac{P_r}{P_i}, \qquad (4.18)$$

where P_i is the forward power out of the RF amplifier and P_r is the reflected power. S_{11} is a measure of the quality of the match, if $S_{11} = -10$ dB, there's 10% reflected power. Figure 4.9 gives the S_{11} parameter for both configurations (without plasma and with plasma) as a function of the RF frequency. The data was obtained with an RF simulation software (RFSim) [110].
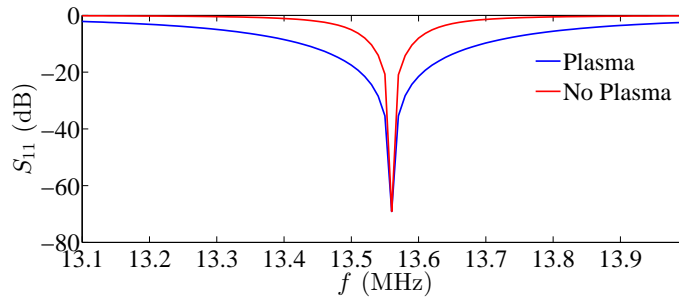
Figure 4.9: S_{11} parameter with and without a plasma for the RADIS ion source antenna design.

From Figure 4.9, the circuit is matched to the load at 13.56 MHz and the bandwidth is quite narrow ($\sim$40 kHz for a reflection of less than 50%) when the plasma is off and wider ($\sim$100 kHz) when the plasma is on. This increase in bandwidth is due to the added resistance that comes from the plasma.

The circuit chosen does, in theory, match the impedance of the system for the case without plasma and with plasma in the ion source. The next section will focus on the implementation of the impedance matching circuit presented herein.

4.2.4 Impedance Matching System Implementation

As described in the previous section, to efficiently couple the power from the RF amplifier to the antenna, an impedance matching system has to be implemented so that the impedance of the system can match the amplifier's 50 Ω output at 13.56 MHz. The implementation of the impedance matching network at the ISTF and the

performance of the circuit will be presented in this section.

An L-Network configuration, as described in Figure 4.8b, was chosen. From the analysis in the previous Section, Capacitor 1 (C_1) will need to be varied from about 13.8 pF to 34 pF, while Capacitor 2 (C_1) will need to be varied from about 124 pF to 163 pF. Thus, for Capacitor 1, a 10 pF to 100 pF motorized capacitor was purchased while a 25 pF to 250 pF capacitor was purchased for Capacitor 2. Both capacitors were purchased from Comet PCT [111] and have a maximum voltage capability of 5 kV. The capacitors are mounted in a box and the electrical RF connections are done with wide copper bars. The capacitors' capacitance are controlled by the PLC to allow for in situ control of the impedance. The antenna is mounted directly to the impedance matching box and the box sits on rails so that the antenna can be moved against the RF window on the ion source. The antenna and the capacitors are water cooled. A schematic model of the impedance matching system connected to the ion source as well as a photograph of the impedance matching system are presented in Figure 4.10.
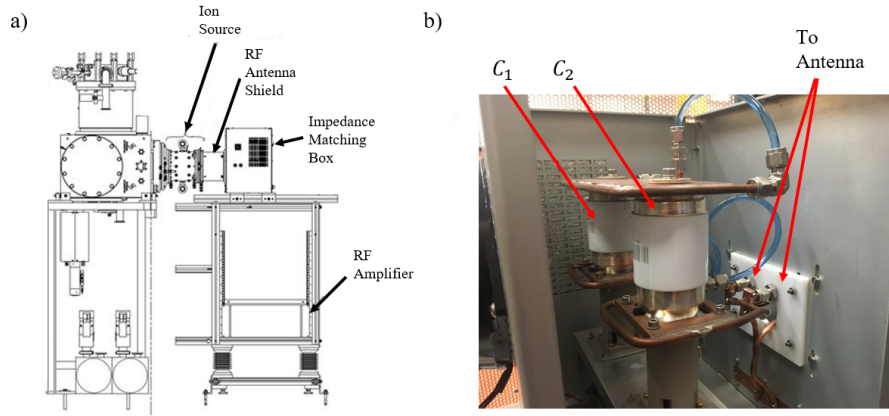
Figure 4.10: a) Model of the RF impedance matching system connected to the ion source. b) Photograph of the impedance matching system.

A 13.56 MHZ RF amplifier with a maximum forward power of 5 kW and a maximum reflected power of 500 W was purchased from Comet PCT [111]. A network analyzer is used to initially tune the capacitors to obtain as low a reflected power as possible at 13.56 MHz. An S_{11} value of less than -30 dB at 13.56 MHz

on the network analyzer can be achieved with the system, which corresponds to a reflected power of less than 0.1%. Once the plasma is ignited the impedance of the system changes; the total resistance increases while the total inductance decreases, as was presented in the previous section. The capacitance values need to be changed to accommodate this change in impedance. The values were changed manually while using the reflected power as feedback, which resulted in reflected power values of less than 1%. An automated system could be implemented to constantly monitor the reflected power and achieve as low a reflected power as possible at all times. Figure 4.11 presents the S_{11} parameter, as introduced in Equation 4.18, obtained as a function of the forward power through the antenna while the antenna was set against the RADIS ion source and hydrogen was used in the ion source.
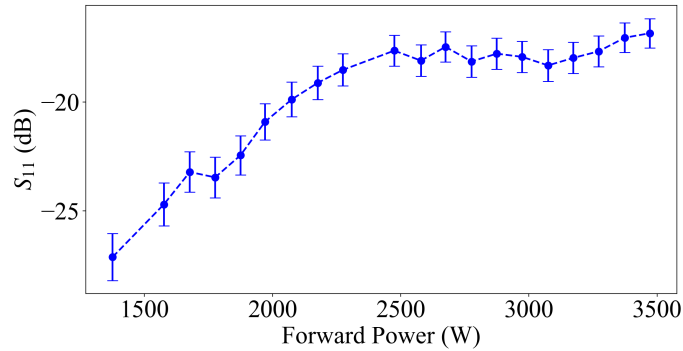
Figure 4.11: S_{11} parameter obtained with the RF ion source as a function of the forward RF power. The capacitors position was optimized to keep the reflected power as low as possible for every measurements and the hydrogen gas flow was set at 15 sccm for these measurements.

The increase in the reflected power seen at higher RF powers in Figure 4.11 is due to improper tuning of the capacitors. Improving the tuning with an automatic tuning system that uses the feedback of the RF amplifier to minimize the reflected power could potentially solve this problem. Nevertheless, if $S_{11} = -17$ dB at 3.5 kW, a reflected power of only 70 W is obtained, which is well below the RF amplifier's maximum of 500 W. Extrapolating to the maximum output power of 5 kW, this would give a reflected power of only 100 W. Thus, the conclusion is that the RF impedance matching network designed can properly match the impedance of

the RF amplifier.

4.3 Acetylene in the RADIS Ion Source

In Chapter 3, it was shown that acetylene gave the highest C_2^- yields in the TRI-UMF licensed filament-powered ion source, but this technology is ultimately not adequate for ion implanter applications due to the tantalum contamination. This section presents the negative carbon ion extraction performance of the RADIS ions when acetylene is used as the injection gas.

4.3.1 Initial Results

High purity acetylene ($> 99.99\%$) was used as the feed gas in RADIS ion source. The plasma was generated with as low as 400 W of RF power. As with the TRI-UMF licensed filament-powered volume-cusp ion source operation with acetylene, a black film was deposited on every surface of the plasma chamber. Figure 4.12 presents a photograph of the RADIS's plasma electrode after the ion source was operating for about two hours.
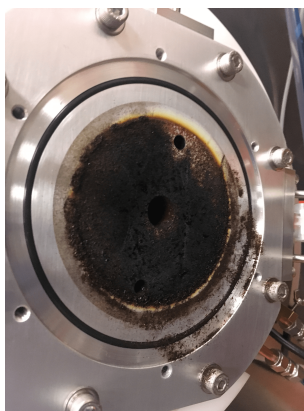
Figure 4.12: Photograph of the RADIS's plasma electrode after running with acetylene for about two hours.

The ion source was first set at -19 kV and could hold voltage on all the electrodes when there wasn't any plasma in the ion source's plasma chamber. However, there was significant sparking on the puller electrode when a plasma was generated

and a beam was being extracted. This is the same behavior that was seen with the TRIUMF licensed filament-powered ion source. The voltage on the ion source was reduced to -10 kV to improve the stability of the extraction system. Furthermore, the power supply that biases the puller electrode could not supply the required voltage as soon as there was plasma in the ion source as it became overloaded by current. This power supply has a maximum output current of only 8 mA. Thus, the puller electrode and the electron dump were connected together on the 150 mA power supply. The current on the electron dump estimates the co-extracted electron current since the electrons are dumped on the electron dump electrode. The same effect prevented the Einzel lens to be biased as well, so the Einzel lens voltage was set at 0 V for every measurement. This has a negative effect on the beam through-put, since, as can be seen in Fig. 4.2a, the Einzel lens is needed to properly focus the beam through the extraction system.

4.3.2   RF Power

To determine how much beam could be extracted from the RADIS ion source, the beam current and co-extracted electron current were measured as a function of the input RF power. A maximum total beam current, consisting of all the species in the beam, of 0.13 mA was measured on the Faraday cup. The tune values for the maximum beam current tune are presented in Table 4.2.

Parameter	Value
Total Beam Current	0.13 ± 0.02 mA
Forward RF Power	800 ± 5 W
Reflected RF Power	101 ± 5 W
Bias Current	0.41 ± 0.02 mA
Bias Voltage	10 ± 0.1 kV
Electron Dump/Puller Current	6.5 ± 0.2 mA
Electron Dump/Puller Voltage	2.5 ± 0.1 kV
Plasma Electrode Current	0 ± 0.1 A
Plasma Electrode Voltage	7.0 ± 0.1V
Gas Flow	20.0 ± 0.2 sccm
Electromagnet Filter Current	15 ± 0.1 A
Einzel Lens Voltage	0 ± 0.1 V
X Steering Current	0 ± 0.1 A
Y Steering Current	0 ± 0.1 A

Table 4.2: Maximum beam current tune obtained with the RADIS ion source.

The total negative ion beam current and the co-extracted electron current are presented as a function of the RF power in Figure 4.13.
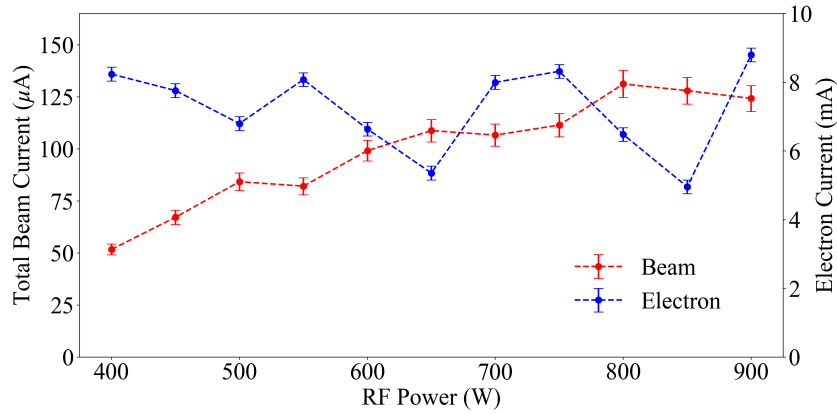
Figure 4.13: Total beam current (all species) and co-extracted electron current as a function of the RF power. The acetylene gas flow was set at 20 sccm, the electromagnet filter current was set at 15 A, the bias voltage was set at 10 kV, the plasma electrode voltage was set at 0 V and the puller/electron dump voltage was optimized at every measurement.

As can be seen in Figure 4.13, the beam current increases with the RF power but saturates above 800 W. Also, the co-extracted electron current does not increase with the RF power, while it increases with the arc power in the filament-powered ion source. This is due to the larger electron filter used in the RADIS ion source. As can be seen in Figure 4.2, at 15 A of electromagnet filter current, the peak magnetic field is around 550 Gauss, compared to about 150 Gauss in the TRIUMF licensed filament-powered ion source, as was presented in Figure B.30.

From spectrometer scans, about 30% of the beam current extracted is formed by C_2^- ions thus, the maximum C_2^- current extracted is only about 40 μA, which is well below the goal of 0.5 mA of C_2^-. In Chapter 3 it was shown that 100 μA of C_2^- can be extracted from the filament-powered ion source. This is not surprising since the maximum extracted H^- beam current extracted out of the RADIS ion source is a little more than 1 mA [30], which is much lower than the maximum H^- beam current that can be extracted out of the TRIUMF licensed filament-powered ion source (18 mA).

Finally, as with the TRIUMF licensed filament-powered ion source, the sparking seen in the extraction system increases with the power in the plasma, with glitch rates of more than 500 glitches per hour seen. The stability issue will have to be addressed as the glitch rate is much too high for the target industrial application. This will be one of the main focus of Chapter 6.

4.3.3   Emittance

The emittance of the beam is an important parameter to measure since it will ultimately dictate whether the beam can be transported through the beamline. The emittance of the beam extracted out of the RADIS ion source was measured with the emittance scanner in the *y* direction. Since the plasma electrode has a diameter of only 7 mm, the emittance was much smaller than the emittance obtained from the TRIUMF licensed filament-powered volume-cusp ion source, which has a plasma electrode aperture of 13 mm. The normalized RMS emittance was found to be of less than 0.3 mm·mrad for the different ion source tune parameters.

A typical phase space scan obtained is presented in Figure 4.14, where the normalized RMS emittance was measured to be 0.14 mm·mrad.
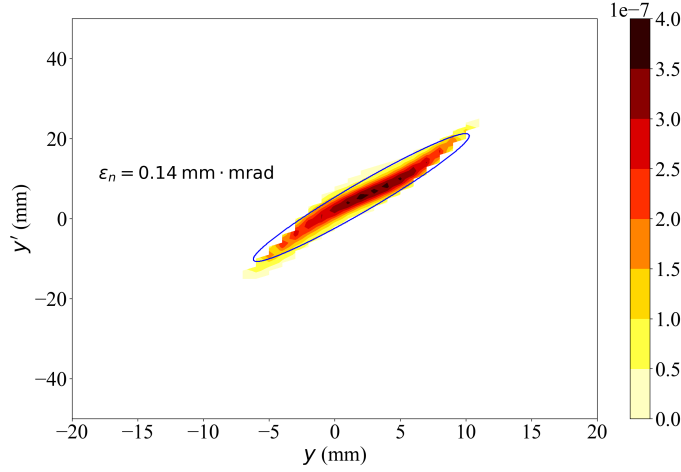
Figure 4.14: Phase space distribution obtained with the RADIS ion source, the normalized RMS emittance ellipse is presented in blue. The gas flow was set at 20 sccm, the RF power was set at 400 W, the bias voltage was set at 10 kV, the plasma electrode was set at 0 V and the puller/electron dumps were at 2.2 kV.

The emittance is much lower than the upper limit set of 1 mm·mrad.

4.3.4 Electron Filter

The RADIS ion source uses an electromagnet dipole to create an electron filter in the plasma. In the TRIUMF licensed filament-powered ion source, this filtering was done by a virtual dipole created by re-arranging the cusp magnets around the plasma chamber. The advantage of using an electromagnet system is that it adds another tuning parameter to the ion source, which is not easily varied with the TRIUMF licensed filament-powered volume-cusp ion source. The electromagnet filter current has an important effect on the extracted negative ion beam current, the co-extracted electron current and the glitch rate. Figure 4.15 presents the beam current and the co-extracted electron current as a function of the electromagnet filter current.
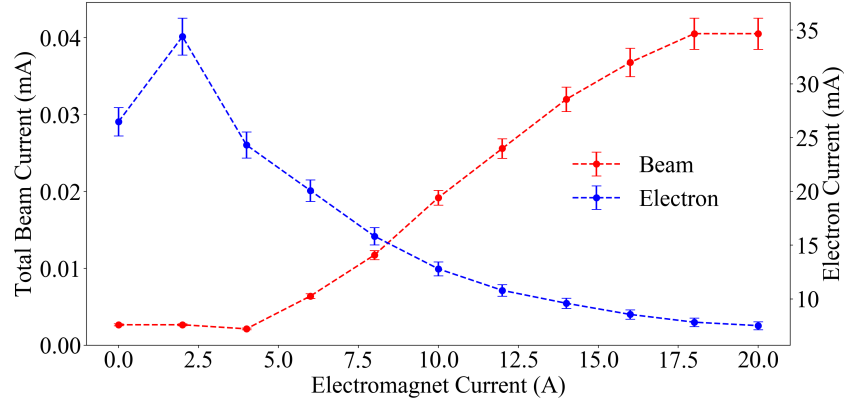
Figure 4.15: Total beam current and co-extracted electron current as a function of the electromagnetic filter current in the RADIS ion source. The bias voltage was set at 10 kV, the acetylene gas flow was set at 20 sccm, the RF power was set at 600 W, the plasma electrode voltage was set at 0 V and the puller/electron dump voltages were optimized at every measurement.

From Figure 4.15, the beam current increases and the co-extracted electron current decreases with the electromagnet filter current. The reduction of co-extracted electron current is expected since the larger filter magnetic field increases the confinement of the electrons along the magnetic field lines which will lead to a lower electron density close to the extraction area of the plasma. The increase in the negative ion current with the electromagnetic filter current can be explained by a variation of the electron temperature in the plasma, which affects the negative ion production rates which are highly dependent on the electron temperature [83].

The glitch rate was also highly dependent on the electromagnet current. The glitch rate as a function of the electromagnet filter current is presented in Figure 4.16.
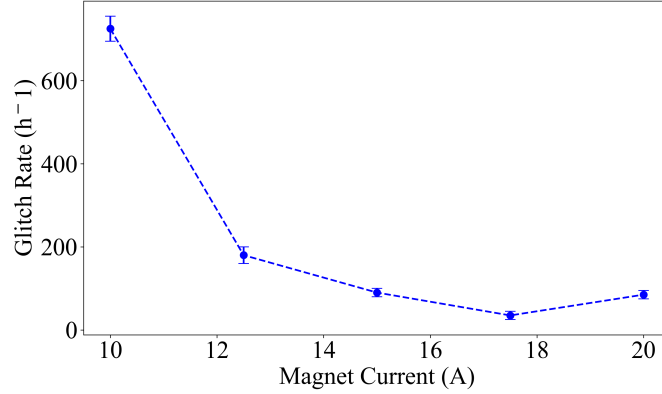
Figure 4.16: Glitch rate as a function of the electromagnet filter current in the RADIS ion source with acetylene. The RF power was set at 600 W, the bias voltage was set at 10 kV and the acetylene gas flow was set at 20 sccm.

From Figures 4.15 and 4.16, there is a clear advantage to using a stronger filter field in the plasma. It increases the total beam current extracted out of the ion source as well as it leads to a lower glitch rate in the extraction system.

To conclude this section on the RADIS ion source, the maximum C_2^- beam current that could be extracted ($\sim 40\,\mu A$) is much lower than the goal of 0.5 mA. Furthermore, there are known problems with the RADIS ion source's extraction system [29] and the glitch rate is too high for the targeted ion implanter application. The RADIS ion source is not the solution sought, a new RF-powered ion source is needed that can extract higher beam currents and that has a greater stability.

4.4   Hybrid Ion Source Design

As the negative carbon ion yield is low and there are problems with the extraction system of the RADIS ion source, a new RF-powered ion source design was pursued. The RADIS ion source serves as a good starting point since it utilizes an external RF antenna, which is needed for the targeted ion implanter application. Alternately, the TRIUMF licensed filament-powered volume-cusp ion source is known to produce high H^- beam currents and there are no problems with the

extraction system. This section will present the development of a new hybrid RF-powered ion source design that uses components of both technologies presented.

The performance of the ion source was first studied with H^- since the extraction of this ion is stable and because a high current H^- ion source that does not use consumable filaments would be highly valued by the accelerator community. The results obtained with the new RF-powered ion source will be compared to the RADIS ion source as well as to the TRIUMF licensed filament-powered H^- ion source performance since both ion sources use the same body and extraction system. Finally, the hydrogen plasma parameters will be compared in both ion sources.

4.4.1 Ion Source Description

The new RF-powered ion source design uses the ion source body and extraction system from the TRIUMF licensed filament-powered volume-cusp ion source, however the back plate is a modified back plate from the RADIS ion source, comprised of an AlN window. The antenna, impedance matching system and RF amplifier that were developed for the RADIS ion source as part of this Thesis work are used to couple power into the plasma. The new ion source developed thus uses an external RF antenna coupled to the body and extraction design from an ion source that is known to yield high negative ion beam currents.

Figure 4.17 presents a cross-sectional view of the TRIUMF licensed filament-powered volume-cusp ion source as well as the new RF-powered ion source that was developed.
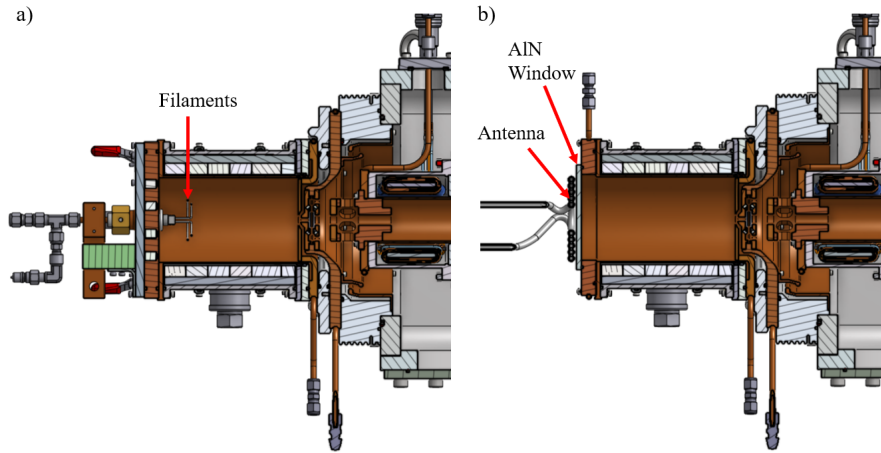
Figure 4.17: Schematic of a cross section of a) the TRIUMF licensed filament powered ion source and of b) the new hybrid design RF ion source.

Figure 4.18 shows a photograph of the new hybrid RF-powered ion source.
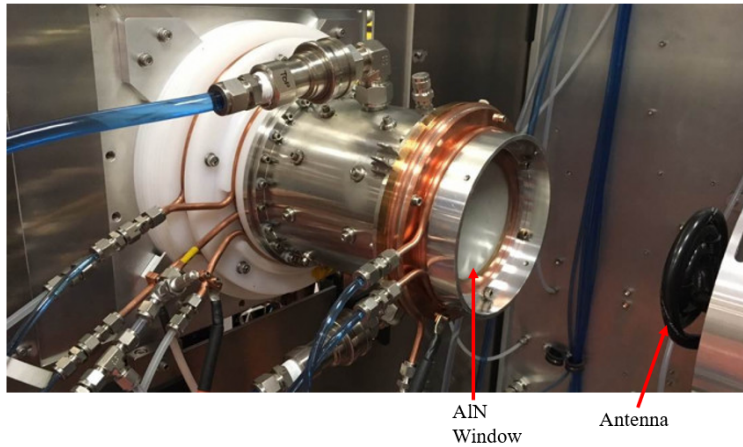
Figure 4.18: Photograph of the new RF-powered ion source installed at the ISTF.

4.4.2 Ion Source Performance

The new RF ion source design was first tested with H$^-$ since the performance of the TRIUMF licensed filament-powered volume-cusp ion source with H$^-$ is well

known, so it allows for an easy comparison between the two technologies. Furthermore, the new technology is also an interesting ion source for H^- applications since the RF-powered technology could drastically reduce the ion source maintenance, since the filaments have a limited lifetime but the RF antenna and window are not consumable parts. It is thus important to study the performance of the ion source with H^-. Also, along with the comparison to the filament-powered technology, the results obtained with the hybrid RF-powered ion source design can also be compared to the results obtained with the RADIS ion source [29, 30].

The ion source was tested with H_2 gas (> 99.999 % purity) to measure the H^- beam that could be extracted from the ion source. Since the ion source does not have an ignition system, it was often difficult to start the plasma in the ion source. Increasing the pressure in the ion source by rapidly opening the gas valve on the ion source helped to ignite the plasma. The pressure in the upstream region of the vacuum box would increase to about $5 \cdot 10^{-4}$ Torr and gradually fall back to normal levels ($5 \cdot 10^{-5}$ Torr) after about two minutes. RF powers of between 600 W and 1 kW were usually needed to ignite the plasma when the pressure was increased in the vacuum chamber. Once the plasma was ignited, the gas flow could be set to the desired value and the power could usually be reduced to about 400 W without extinguishing the plasma.

The procedure to tune the ion source for the extraction of the ions is similar to what is done with the filament-powered ion source. The plasma and extraction electrode voltages need to be tuned to maximize the beam current on the Faraday cup. The co-extracted electrons are dumped on the extraction electrode, so the extraction electrode current approximates the co-extracted electron current. The *XY* steerers are used to ensure that the beam is centered on the beamline. Figure 4.19 presents the beam current obtained as a function of the RF power for various hydrogen gas flows.
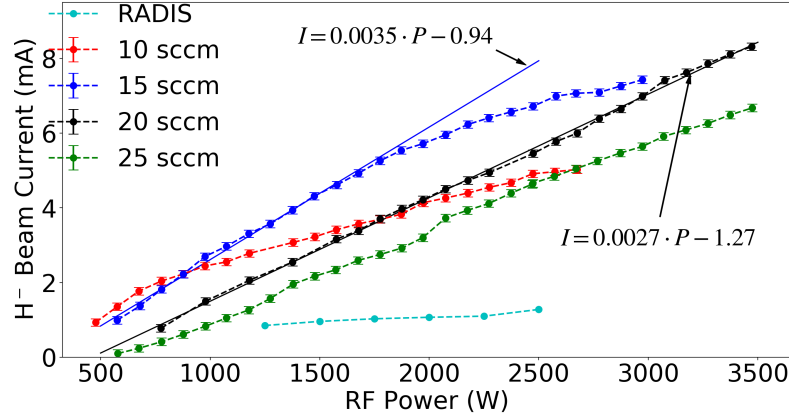
Figure 4.19: H^- beam current as a function of forward RF power for various gas flows and compare to RADIS ion source data from [29]. The beam energy was set at 30 keV for every measurement, and the plasma and extraction electrode voltages were tuned to maximize the beam current on the Faraday cup.

A maximum H^- beam current of 8.3 mA was obtained at an RF power of 3.5 kW and a gas flow of 20 sccm. The maximum power used was limited by a RF window temperature that got too high, which led to partial melting of the O-ring that seals the window. The H^- beam current extracted is considerably higher than what was extracted out of the RADIS ion source (1 mA). As presented in the previous section, the RADIS ion source uses a 7 mm plasma electrode aperture diameter, compared to the 13 mm plasma electrode diameter of the hybrid RF ion source presented in this Thesis. Therefore, the maximum current density extracted out of the RADIS is about 0.033 mA/mm^2 at 2.5 kW. At the same RF power, the hybrid ion source developed extracted about 0.050 mA/mm^2, which is still considerably higher. The RF ion source developed is thus an important improvement on the current RF-powered H^- ion source technology [31, 32].

As was seen with the filament-powered ion source, there seems to be saturation of the beam current above a certain power input and this is more evident at lower gas flows, where the saturation happens at lower RF powers. Lower beam currents at low RF power for higher gas flows were also observed, which is due to the higher

H$^-$ stripping rates at higher vacuum pressures. A linear fit to the data is plotted for the 15 sccm and 20 sccm curves, which clearly shows the saturation effect for the 15 sccm data.

The H$^-$ beam current is noticeably lower than with the filament powered ion source and the power efficiency is also lower. With the filament powered ion source, up to 18 mA of H$^-$ can be extracted with an efficiency of about 3.5 mA/kW of arc power, while the RF ion source achieved about 2.4 mA/kW of RF power.

The difference in power efficiency is due to three main reasons. Firstly, there are RF power losses to the outside of the ion source. Not all of the forward power in the RF circuit is coupled to the plasma, there is noticeable RF heating to the aluminum flanges and covers around the antenna, which accounts for some power loss. Secondly, the RF ion source does not have any confinement magnets on the back plate since this space is used for the AlN window. This is another cause of inefficiency since the electrons can travel directly to the back plate, dumping their energy. Finally, the RF ion source does not have a coat of tantalum on the plasma chamber walls as it does in the filament-powered ion source. Tantalum aids the production of H$^-$ through increasing the vibrationally excited hydrogen population (H$_2^*(v'')$) and through a reduction of the emission of H atoms from the walls, which leads to a decrease in H$^-$ stripping [112].

Along with the H$^-$ beam current measurements, it is also important to measure the co-extracted electron current out of the RF-powered ion source. The co-extracted electron to H$^-$ ratio for the various measurements of Figure 4.19 is presented in Figure 4.20.
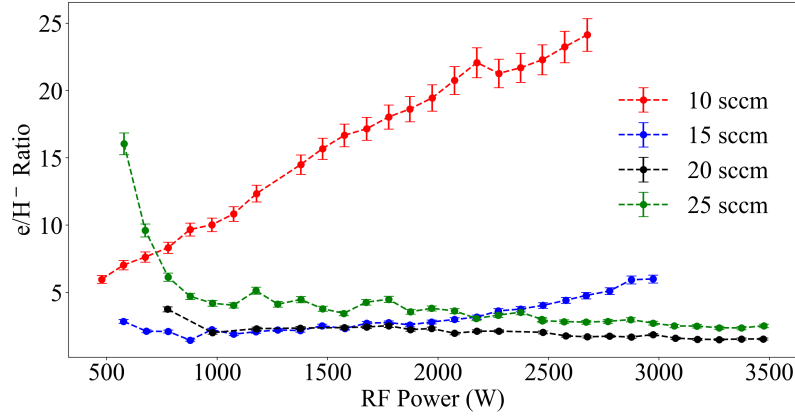
Figure 4.20: e/H⁻ ratio as a function of forward RF power for various gas flows. The beam energy was set at 30 keV for every measurement, and the plasma and extraction electrode voltages were optimized for each measurement.

The co-extracted electron to H⁻ ratio is on the same order of magnitude as with the filament powered ion source but, was a bit lower with the RF-powered ion source. A low of 1.5 e/H⁻ was achieved for multiple ion source tunes, which is lower than the 2.6 minimum ratio achieved for the filament-powered ion source. This is due to the higher plasma electrode voltage that is needed with the RF ion source for optimum ion source current extraction, which reduces the electron density close to the extraction aperture in the plasma. The study of the performance of the ion source as a function of the plasma electrode voltage will be presented in Section 5.4.4.

The H⁻ beam current and the e/H⁻ ratio can be directly compared for the TRIUMF licensed filament-powered and the new hybrid RF-powered ion sources. This is presented in Figure 4.21.
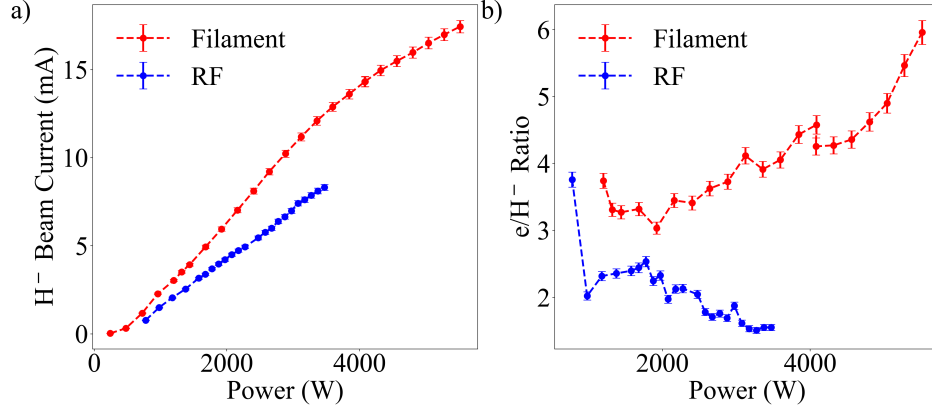
Figure 4.21: Comparison of a) the H$^-$ beam current and b) the e/H$^-$ ratio for the filament powered and the RF-powered ion sources. The gas flow was set at 20 sccm, the bias voltage was set at 30 kV, and the plasma and extraction electrode voltages were optimized for each measurement.

From Figure 4.21a, the H$^-$ beam current to power efficiency is considerably lower for the RF ion source. But the maximum power achieved with this ion source is also 2 kW lower than the maximum power of the filament ion source. As can clearly be seen in Figure 4.21a, there is an unexplored power area with the RF-powered ion source, which is predicted to yield more H$^-$ beam current than what is currently achieved. The maximum power is limited by the temperature of the RF window, as the RF amplifier at the ISTF can deliver up to 5 kW of forward power.

From Figure 4.21b, the electron to H$^-$ ratio is consistently lower with the RF ion source. This is due to the increased optimum plasma electrode voltage that depletes the electrons from the plasma region close to the extraction. High co-extracted electron currents at the extraction aperture increase the space charge, and thus the divergence of the beam, at the extraction.

Even though the H$^-$ current extracted out of the new RF-powered ion source is lower than the filament-powered ion source, there is a clear advantage in using an RF-powered ion source, being that there are no consumable parts. The ion source developed is an interesting option for many H$^-$ applications [31, 32].

4.4.3 Emittance

Since the extraction system of the new RF-powered ion source design is taken from the TRIUMF licensed filament powered ion source, the emittance of the beam extracted out of the new ion source is expected to be similar to the filament-powered version. Any difference between the phase space distributions will be attributed to differences in the plasmas in these ion sources.

The *y* emittance was measured with the emittance scanner located 368 mm downstream from the ion source's plasma electrode. The normalized RMS *y* emittance as a function of the RF power for various gas flows is presented in Figure 4.22.
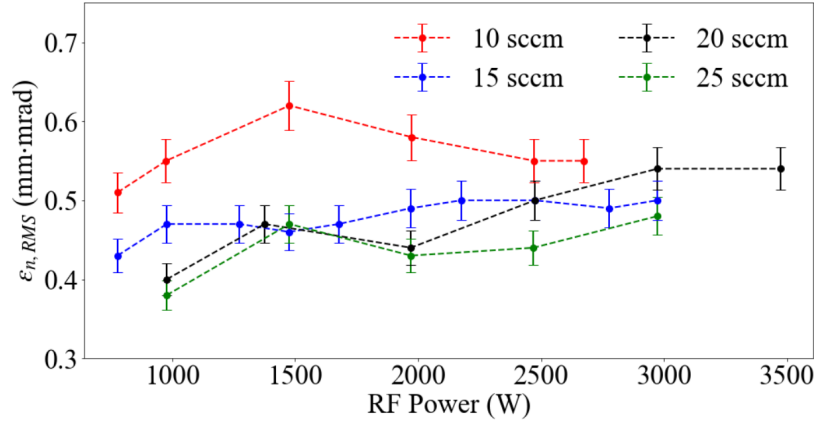
Figure 4.22: Normalized RMS emittance as a function of the RF power for various gas flows. The bias voltage was set at 30 kV, and the plasma and extraction electrode voltages were optimized for each measurement.

The emittance is constant to within 0.1 mm·mrad as a function of RF power but there is a slight decrease in emittance with gas flow. The same effect was seen with the TRIUMF licensed filament-powered volume-cusp H$^-$ ion source. In Section B.4.5, the lower emittance seen was due to an increase in the space charge compensation effect at the higher gas flows. The same effect causes the lower emittance with the RF-powered ion source as well.

Figure 4.23 compares the emittance values obtained for the TRIUMF licensed filament-powered volume-cusp ion source and the RF-powered hybrid ion source.

101
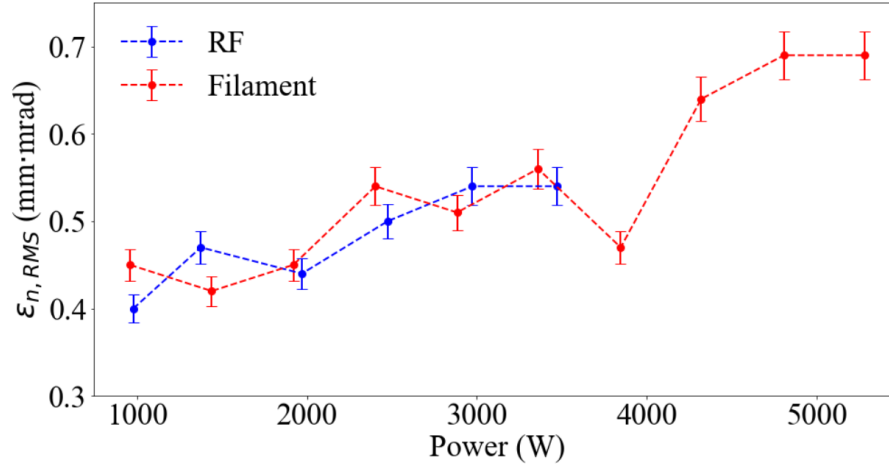
Figure 4.23: Normalized 4-RMS emittance as a function of the power for RF and the filament powered ion sources. The bias voltage was set at 30 kV, the gas flow was set at 20 sccm, and the plasma and extraction electrode voltages were optimized for each measurement.

As can be seen in Figure 4.23, the emittance values are almost equal between the two technologies because both ion sources use the same extraction system and plasma chamber.

4.4.4 Plasma Electrode

The plasma electrode voltage is an important component of H^- ion sources since increasing the voltage on the electrode reduces the co-extracted electron current and biasing the electrode close to the plasma potential is known to increase the extracted H^- current. The optimum plasma electrode bias was at a much higher voltage in the RF ion source than in the filament-powered ion source. Figure 4.24 presents the H^- beam current and co-extracted electron current as a function of the plasma electrode voltage with the RF-powered ion source.
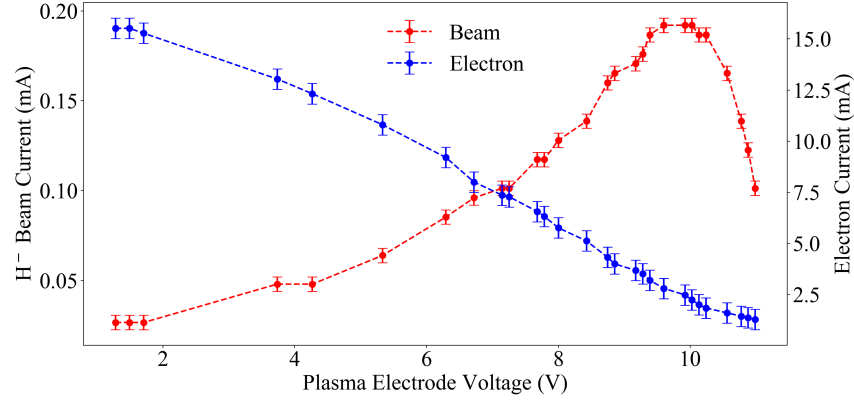
Figure 4.24: H$^-$ beam current and co-extracted electron current as a function of the plasma electrode voltage. The beam energy was set at 30 keV, the RF power was set at 576 W and the gas flow was set at 22 sccm.

As can be seen in Figure 4.24, the maximum beam current is at around 10 V, while the co-extracted electron current decreases with the plasma electrode voltage. This explains the lower e/H$^-$ ratios seen with the RF ion source, as was shown in Figure 4.21. The higher plasma electrode voltage needed leads to lower co-extracted electron currents, and lower e/H$^-$ ratios.

The optimum plasma electrode potential increases with the RF power. Figure 4.25 presents the optimum plasma electrode voltage as a function of the RF power for various gas flows.
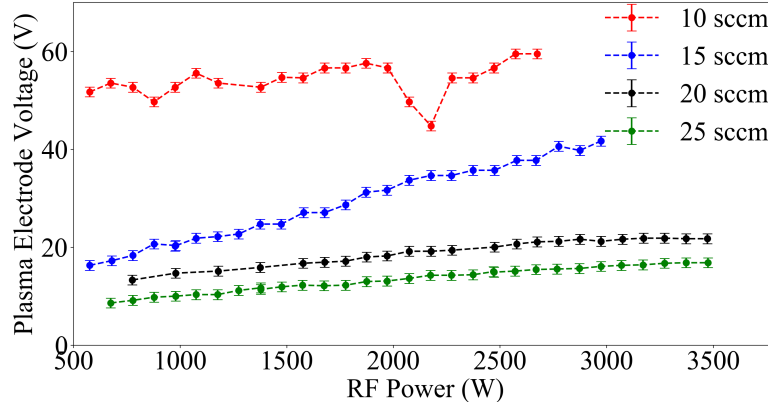
Figure 4.25: Optimum plasma electrode voltage as a function of the RF power for various hydrogen gas flows. The bias voltage was set at 30 kV and the extraction electrode voltage was optimized for every measurement.

As can be seen in Figure 4.25, the optimum plasma electrode voltage increases with the RF power and the optimum plasma electrode voltage decreases with gas flow. Both these trends were also seen with the TRIUMF licensed filament-powered volume-cusp ion source. The increase of the optimum plasma electrode potential with the RF power is due to an increase in the electron temperature in the plasma, which leads to a higher an increase in the plasma potential. The lowering of the optimum electrode potential with gas flow is caused by a lowering of the electron temperature with the gas flow, which leads to a lower plasma potential.

The optimum plasma electrode voltage is much higher with the RF-powered ion source than it was with the filament-powered ion source and this is due to a higher plasma potential in RF-powered ion sources, when compared to a similar filament powered ion source [113]. The high plasma electrode potential reduces the electron density close to the extraction region, leading to lower co-extracted electron currents with the RF-powered ion source when compared to the filament-powered ion source. The optimum plasma electrode voltage was not as prominent at higher RF powers, this explains the dip in the 10 sccm data curve.

4.5 Plasma Analysis

It is important to compare the plasma parameters of the new RF-powered hybrid ion source to the TRIUMF licensed filament-powered volume-cusp ion source because the cross section of the H^- volume production reactions are highly dependent on the electron temperature. The magnetic fields in the plasma chamber of H^- ion sources are highly optimized to maximize the production and minimize the destruction of H^-. Thus, it is interesting to see how the powering mechanism will affect the plasma parameters, and to verify if the magnetic configuration should be modified to accommodate this change.

The Langmuir probe system presented in Section B.4.9 was used with the RF ion source. An RF filter, following [114], was added between the power supply and the Langmuir probe. The Langmuir probe uses a 5 mm tantalum tip and was inserted in the plasma through the extraction aperture, as described in Section B.4.9.

The use of the Langmuir probe analysis made obvious the transition between the two different RF modes, the capacitive and the inductive modes, as described in Section 5.2.1. The capacitive mode is the dominant mode at low RF powers, and in this mode the trajectories of the electrons are mostly influenced by the radial electric field from the potential difference between the turns of the antenna. This leads to a radial oscillation of the electrons in the plasma. The inductive mode is the dominant mode at higher RF powers. The electron trajectories are governed by the electric field that comes from the varying magnetic field from the antenna's coils, which will be in the angular direction. The power transfer to the plasma is more efficient in the inductive mode, so it is expected that there will be a significant increase in electron density when the plasma switches between the two modes [106]. Figure 4.26 presents *IV* curves from the two modes.
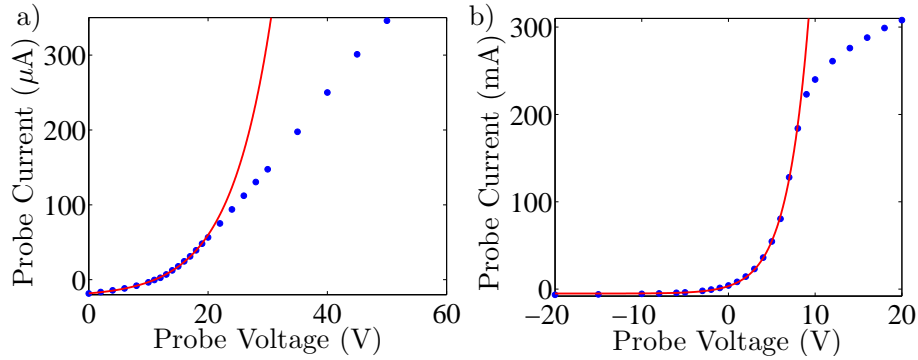
Figure 4.26: *IV* curves and exponential fits for an RF power of a) 500 W and b) 900 W. The gas flow was set at 15 sccm and the plasma electrode potential was at 0 V for both measurements. The Langmuir probe tip was located 20 mm from the plasma electrode.

The obvious difference between the two modes can be seen in Figure 4.26. The probe current is about three orders of magnitude higher in the inductive mode. The shape of the two curves is also much different, the inductive mode is characterized by the usual exponential increase followed by a saturation of the probe current, while the capacitive mode has a slight exponential increase but the current never saturates. The RF ion source is usually operated in the inductive mode, since the RF power used is commonly above 1 kW, so the Langmuir probe measurements will all be taken in the inductive mode.

Another important observation that can be made from Figure 4.26 is that the plasma potential is much higher with the RF-powered ion source. The plasma potential was between 5 V and 20 V for most Langmuir probe measurements, compared to 1-3 V with the filament powered ion source, as was shown in Figure 3.39. This explains the higher plasma electrode potential that was needed to optimize the H^- current in the RF ion source, as presented in Figure 4.24.

Figure 4.27 presents the electron density and the electron temperature as a function of the hydrogen gas flow for the new hybrid RF-powered ion source and for the TRIUMF licensed filament-powered volume-cusp ion source as was presented in Figure B.41.
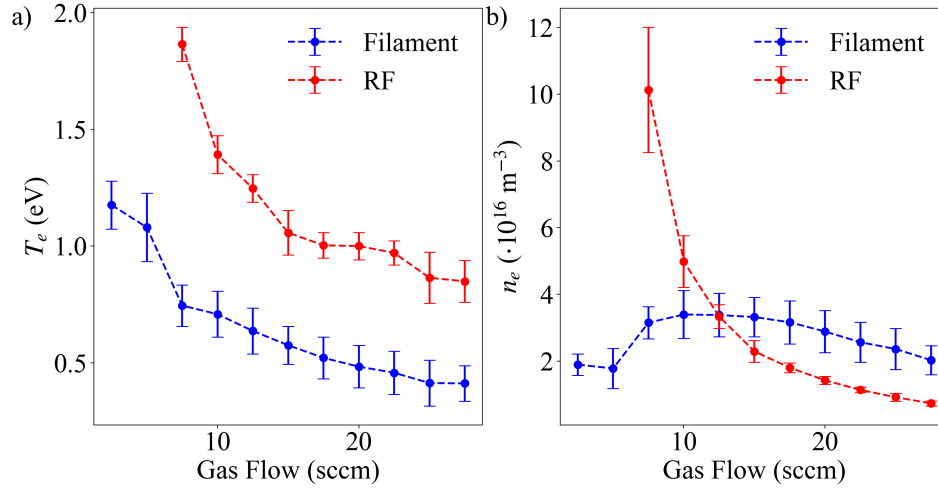
Figure 4.27: a) Electron temperature and b) density as a function of the hydrogen gas flow for the hybrid RF-powered and the filament powered ion sources. The arc voltage was set at 120 V, the arc current was set at 1 A and the probe tip was at 20 mm from the plasma electrode for the filament ion source. The RF power was set at 1 kW and the probe tip was at 10 mm from the plasma electrode for the RF ion source.

From Figure 4.27, both the electron temperature and the electron density decrease with the gas flow for the RF-powered ion source, while the electron density stayed relatively constant with gas flow for the filament ion source. Since the power in the filament powered ion source was much lower (120 W) than in the RF-powered ion source (1 kW), and the position of the probe in the plasma is slightly different in the two cases (10 mm and 20 mm from the plasma electrode), the absolute plasma parameter values cannot be compared between the two technologies. However, the electron density is similar in both cases, which points to the fact that the electron density is generally higher in filament powered plasmas for the same input power. This is explained by the direct injection of electrons in the filament powered ion source. Also, the theory predicts that in the RF generated plasma, the electron density falls off rapidly from the RF window [103], so it is expect that there will be a lower electron density close to the plasma electrode. Figure 4.28 presents the electron density and temperature as a function of the input power.
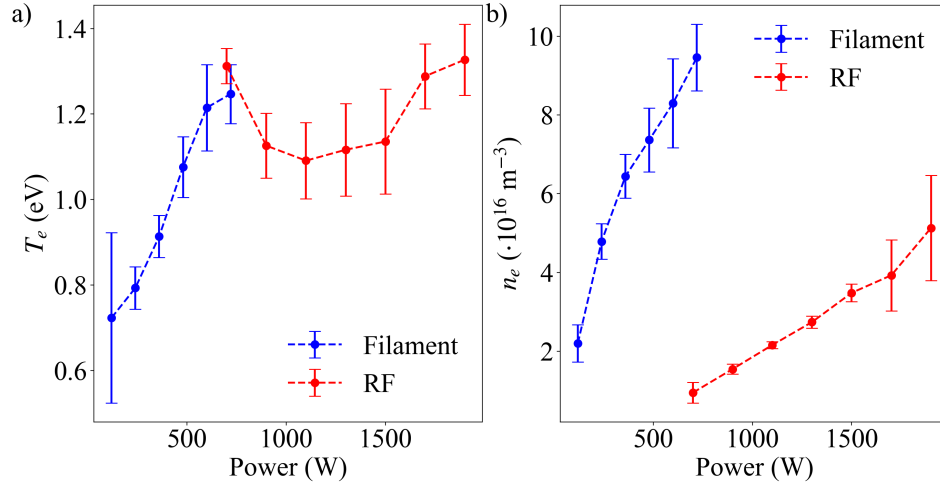
Figure 4.28: Electron density and temperature as a function of the power for the filament powered and the RF-powered ion sources. The arc voltage was set at 120 V, the gas flow was set at 10 sccm and the probe tip was at 20 mm from the plasma electrode for the filament ion source. The gas flow was set at 15 sccm and the probe tip was at 10 mm from the plasma electrode for the RF ion source.

From Figure 4.28, the electron density is much lower in the RF-powered ion source and the electron temperature stays relatively constant for the RF-powered ion source but increases for the filament powered ion source. This result is surprising since the both ion source have the same magnetic configuration and the probe tip is located in the *cold* plasma region for both ion sources. Furthermore, it was predicted that the electron temperature would be larger in the RF-powered ion source [113], but this is not the case in this region.

Figure 4.29 presents the electron temperature and density as a function of the gas flow with the Langmuir probe at various locations along the central axis of the ion source.
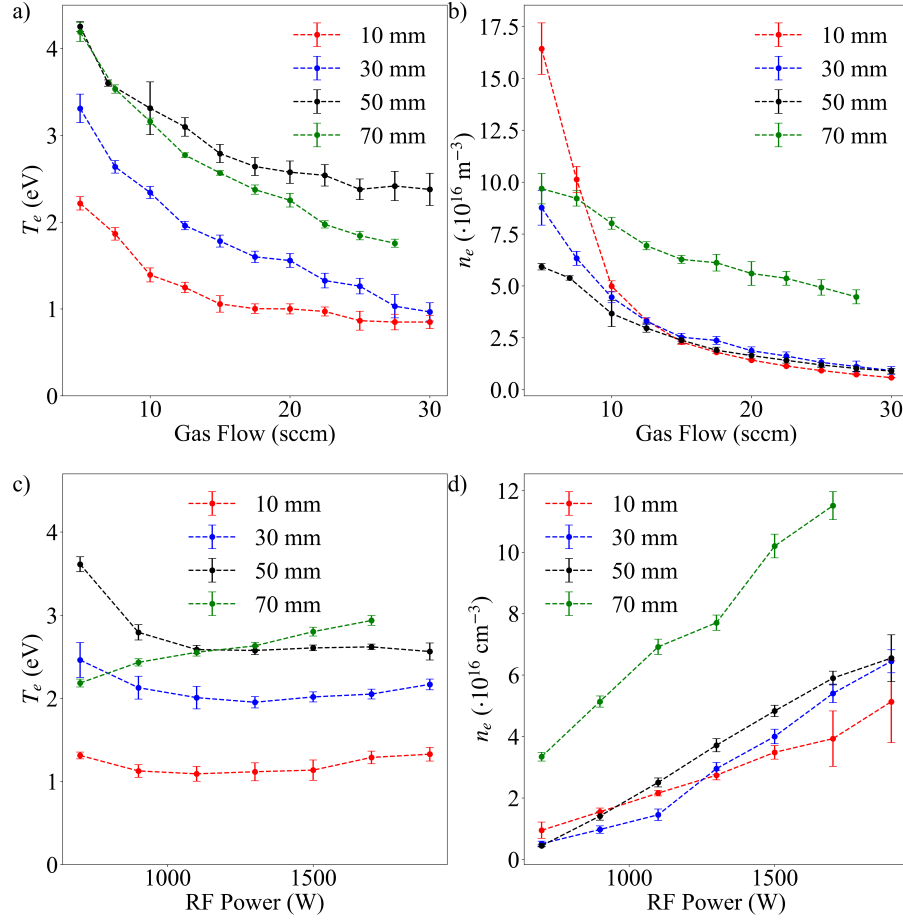
Figure 4.29: a) Electron temperature and b) density as a function of the gas flow as well as c) electron temperature and d) density as a function of the RF power with the Langmuir probe tip at various points along the central axis. The distance indicates the distance from the plasma electrode. The RF power was set at 1 kW and the plasma electrode potential was at 0 V.

From Figure 4.29, the dependence of the electron density on the position where the measurements were taken was not as expected. It was expected that the electron density would be lowest for the measurements closer to the plasma. However, there is a clear increase in the electron density for the 70 mm measurements, but the electron density is relatively constant for the 10 mm, 30 mm and 50 mm probe

locations. The reason for this constant electron density is unclear, as such an effect was not observed in the filament-powered ion source. It could indicate a small region of high electron density on the edge of the filter field region or it could also indicate that the electron density is much higher close to the RF window and falls rapidly closer to the plasma electrode. The increase in RF power also causes a linear increase in electron density, which was seen in the filament-powered ion source (Figure 4.28). However, there is a decrease in electron density with gas flow, while the density remained relatively constant with the gas flow in the filament powered ion source.

There is an increase in the electron temperature the further the measurements are taken from the plasma electrode, but the measurements at 50 mm and 70 mm are almost identical. This suggests that the plasma temperature is more uniform in the *hot* plasma region. The electron temperature is relatively constant as the RF power is increased for the measurements closest to the plasma electrode but increases slightly for the 70 mm measurements. This indicates that the magnetic dipole filter regulates the electron temperature close to the plasma electrode. The magnetic field at 70 mm is too weak to affect the electron temperature, so there is a stronger correlation between the RF power and the electron temperature. Also, the electron temperature in the *hot* plasma region is much higher than it was in the filament-powered ion source, as was presented in Figure B.42.

From the Langmuir probe analysis presented here, there are important differences between the plasma parameters in the filament-powered and the RF powered ion source. The main difference being the lower electron density in the RF-powered ion source, which partially explains the lower beam current power efficiency seen.

4.6   Ion Source Improvements

Since a high H$^-$ beam current can be achieved with the RF-powered ion source developed and it's an interesting ion source for many applications, work was done to further improve the performance of the ion source as a secondary goal of this Thesis work. The RF-powered ion source has a lower beam current power efficiency than the filament-powered ion source. Three main hypotheses were put forward

to explain this: (i) there are RF power losses to the outside of the vacuum chamber, (ii) the RF-powered ion source does not have a thin tantalum coating on its plasma chamber walls and (iii) there is no confinement on the back plate of the RF-powered ion source. This section will focus on improvements to the new hybrid RF-powered ion source design to increase the beam current efficiency, as well as the problems that were encountered during its development.

4.6.1 Tantalum

The filament-powered ion source uses negatively biased tantalum filaments which get sputtered by the positive ions in the plasma. The sputtered tantalum ends up on the plasma chamber walls, forming a thin tantalum layer and this tantalum layer plays an important role on the H^- production and stripping in the plasma [44]. Firstly, the coating reduces the emission of H atoms from the plasma electrode, which leads to a reduction in stripping of the H^- ions that are produced in the plasma volume. The second effect is the increase in the density of vibrationally excited hydrogen ($H_2^*(v'')$) by recombinative desorption on the chamber walls, which leads to a higher volume production of H^- ions through dissociative attachment. Figure 4.30 presents the H^- beam current with time starting with a clean plasma chamber in the TRIUMF licensed filament-powered volume-cusp ion source, which shows how the beam current is affected by the tantalum coating.
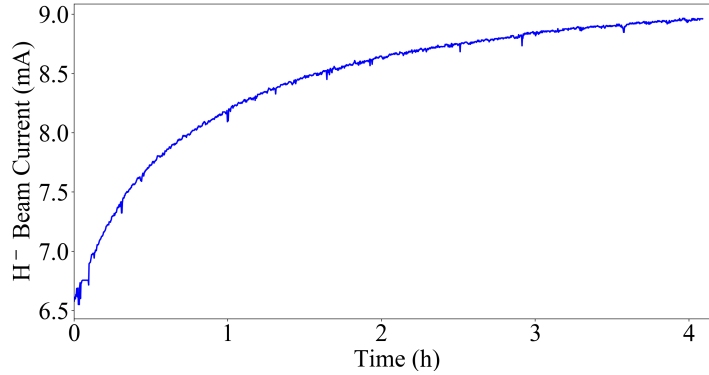
Figure 4.30: H$^-$ beam current extracted from the TRIUMF licensed filament-powered ion source with a clean plasma chamber. The arc current was set at 20 A, the arc voltage was set at 120 V, the gas flow was set at 15 sccm, the plasma electrode voltage was at 3.6 V, the extraction electrode voltage was at 3.08 kV and the beam energy was set at 30 keV.

From Figure 4.30, there is a clear increase in H$^-$ beam current for the first hour of operation due to the plating of the plasma chamber walls with tantalum. The increase in beam current then plateaus after about 3 hours. This shows that the H$^-$ beam current depends on the tantalum thickness and the effect is independent of the thickness above a certain value. The hybrid RF-powered ion source design does not have any tantalum on its plasma chamber walls and is thus one of the reasons why the beam current to power efficiency is lower with the RF-powered ion source than it is in the filament powered version.

To verify if the benefits of tantalum on the plasma chamber walls are still present with the RF-powered ion source, a tantalum coating was deposited on the plasma chamber walls of the hybrid RF-powered ion source. This was done by running the filament ion source at an arc current of 20 A, an arc voltage of 120 V and a H$_2$ gas flow of 15 sccm for two hours to deposit tantalum on all of the plasma chamber surfaces. The system was then vented to atmosphere and the back plate of the ion source was changed to the RF window. The system was pumped down again, with a total time under atmosphere of about 15 minutes.

Various tantalum coatings in the RF-powered ion source were tested. First,

the performance of the RF ion source with the tantalum coating the entire plasma chamber wall surfaces was tested to 3.5 kW of RF power. The ion source was then cleaned, the same tantalum coating was re-applied, but only the coating on the plasma electrode was kept, the coating on the rest of the plasma chamber body was removed. Finally, the performance of the ion source was also examined by running the ion source at an RF power of 2.5 kW for 10 hours with the same coating as applied earlier. Figure 4.31 presents the performance of the hybrid RF-powered ion source for i) a clean ion source without any Ta (Clean), ii) a new Ta coating in the ion source (Fresh) iii) an old Ta coating (Old) and iv) only the plasma electrode coated (Plasma).
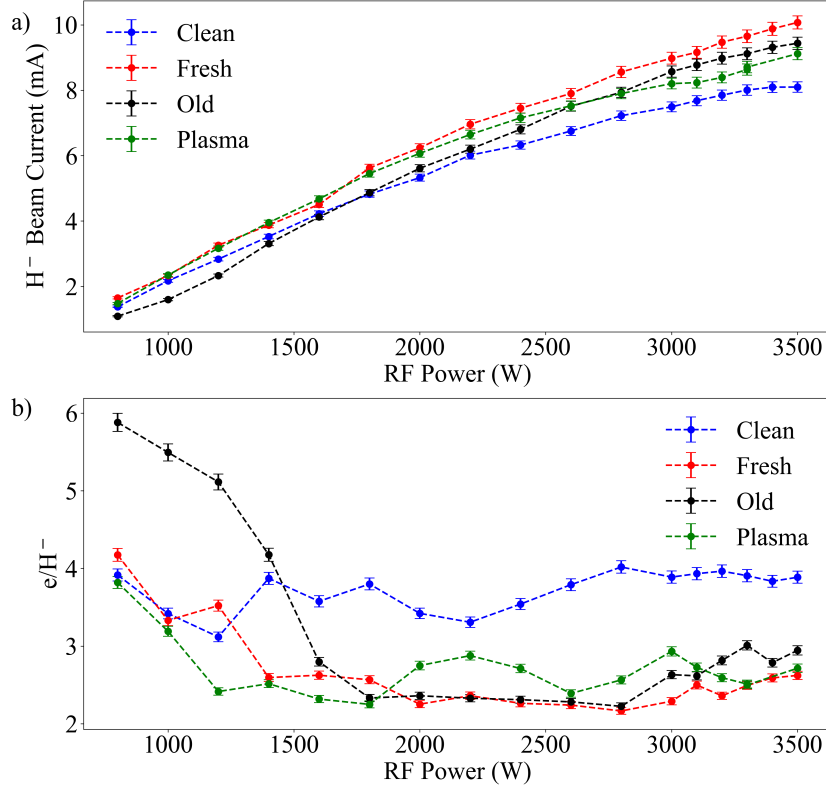
Figure 4.31: a) H^- beam current and b) e/H^- ratio as a function of the RF power for (i) a clean plasma chamber (Clean), (ii) one with a fresh Ta coating deposited on the entire plasma chamber (Fresh) (iii) one with a Ta that has been running with the RF power set at 2.5 kW for 10 hours (Old), and (iv) one with a Ta coating on the plasma electrode only (Plasma). The gas flow was set at 15 sccm and the beam energy was set at 30 keV.

The results clearly show the improvements resulting from the Ta coating (Fresh) versus no Ta coating (Clean). This is evident at 3.5 kW of RF power with 10,1 mA of H^- beam extracted for a fresh Ta coating, compared to only about 8.1 mA for the clean plasma chamber. The difference seen at lower RF power for the *Old* coating is thought to be due to improper tuning of the impedance matching network, leading to higher power losses in the tuning circuit. Every configuration with

114

some Ta coating saw improvements over the bare copper plasma chamber. Similar co-extracted electron currents were observed with a fully-coated chamber as with only the plasma electrode coated. This supports the theory that the Ta adsorbate helps reduce the stripping of the negative ions close to the plasma electrode, where it is thought that most of the ions are produced, since the lower H^- stripping rate in the plasma would also lead to a lower electron density. The difference in beam current between the fully coated and only the plasma electrode coated could be explained by a higher $H_2 * (v'')$ population from the larger Ta surface area seen in a fully coated plasma chamber and this is more evident at RF powers of more than 2 kW.

A decrease in beam current with the aging of the Ta adsorbate was observed. Figure 4.32 presents the beam current reduction over time, starting with a fresh Ta coating.
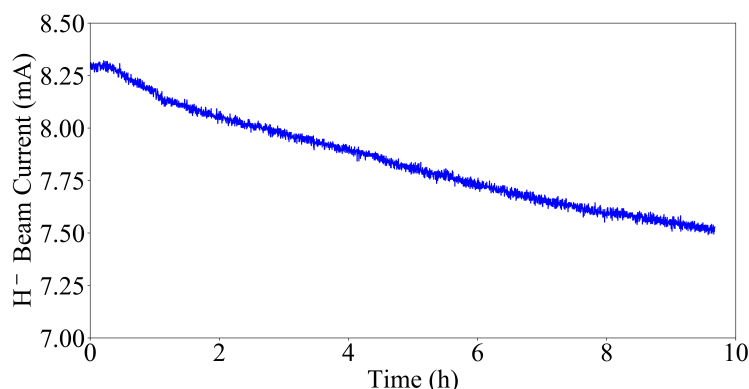
Figure 4.32: H^- beam current degradation with time after coating the RF ion source plasma chamber with a fresh coat of Ta. The RF power was set at 2.5 kW, gas flow was set at 15 sccm and the beam energy was set at 30 keV.

There are two potential explanations for the decrease seen. The erosion of the coating by the sputtering from the plasma particles could bring the Ta thickness under the minimum for optimum ion source performance and would lead to a decrease in the beam current. Or, it could be caused by a contamination of the coating by the hydrogen and impurities in the plasma. Further testing is required to deter-

mine if thicker Ta coatings would prevent the gradual beam current reductions, in order to utilize this RF-powered ion source for prolonged industrial applications.

From the analysis presented in this section, there is a clear advantage to have some tantalum on the plasma chamber walls. Tantalum filaments are chosen in the filament-powered ion source for this exact reason. The following section will focus on improving the magnetic confinement of the RF-powered ion source.

4.6.2 Magnetic Confinement

As stated previously, one of the reasons the hybrid RF-powered ion source is less efficient than the TRIUMF licensed filament-powered volume-cusp ion source is that the RF ion source does not have any confinement magnets on its back plate. Therefore, the electrons are free to flow to the back plate which results in some power loss. To improve the plasma confinement in the back of the ion source, Sm_2Co_{17} magnets were added to the back of the ion source as depicted in Figure 4.33. By adding 10 magnets a maximum dipole field in the center ring of about 50 G could be achieved, while about 30 G was achieved with 6 magnets. Figure 4.33 also presents the magnetic field obtained along the central axis of the ion source for the two configurations tested.
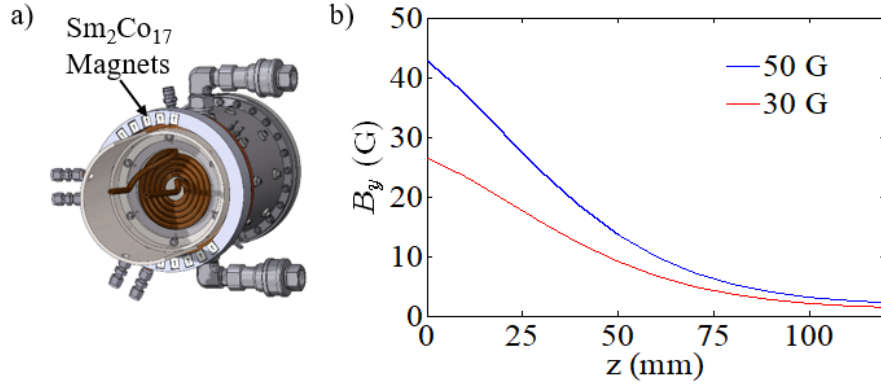
Figure 4.33: a) Schematic of the RF ion source with an added dipole made of
Sm$_2$Co$_{17}$ added 20 mm behind the RF window. b) Measured magnetic
field along the central axis for two configurations tested.

The hybrid RF-powered ion source was tested with the two magnet configurations presented in Figure 4.33. The results are presented with the results from the original configuration without any additional magnets in Figure 4.34.
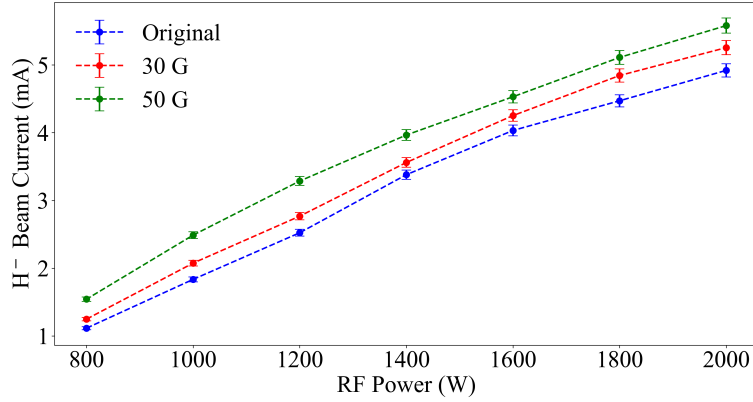
Figure 4.34: H$^-$ beam current for the various magnet configurations. The gas
flow was set at 15 sccm and the beam energy was set at 30 keV.

As can be seen in Figure 4.34, the addition of the dipole field causes an increase
in the extracted beam current and as the field strength is increased, there's an in-

crease in H$^-$ beam current. This is due to an increase in the plasma confinement in the back of the plasma chamber and thus an increase in the power efficiency of the ion source. Thus, the addition of the magnets on the back plate of the ion source is a simple and effective method to improve the power efficiency of the ion source and increase the beam current. The following section will present efforts that are made to remediate the RF window heating issues.

4.6.3 Window Temperature

The main setbacks in the development of the new hybrid RF-powered ion source were the fractures of the AlN RF window, which happened twice. The first fracture occurred when the new ion source was first brought above 2 kW, one week after the first RF ion source measurements were taken. The failure happened at 2.6 kW and caused a major vacuum breach which damaged the downstream turbo-molecular pump's inner housing. The window was replaced with a proper AlN window as the previous window was made of Macor, which is a machinable grade of AlN and has a lower thermal conductivity than pure AlN. But, there was a second failure of the window one year after the first incident. The ion source had more than 50 days of operation with this new window, including the 9 hour test at 2.5 kW that was presented in Figure 4.32. Figure 4.35 presents the AlN windows after the failures.
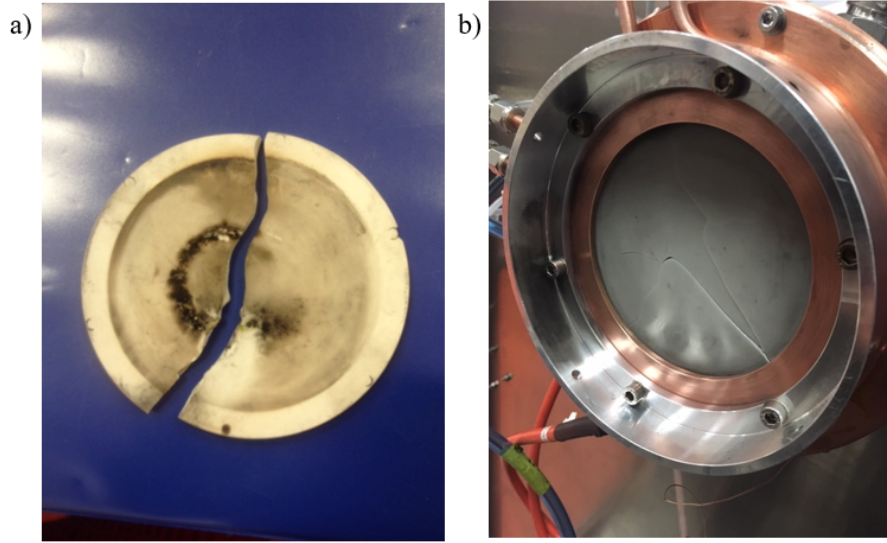
Figure 4.35: Photograph of the RF window after a) the first failure on August 8th, 2016 and b) the second failure on September 2nd, 2017.

Burn marks from sparking between the antenna turns can be seen in Figure 4.35a. One can also clearly see that the two windows are of different color, the first being made of Macor and the second out of pure AlN.

Along with the lack of confinement on the RF window, the current design doesn't include any cooling directly on the window. The window is only cooled via the cooled copper flange on which it is mounted. From the analysis of inductively coupled plasmas, the power deposited into the plasma falls off exponentially with a characteristic distance of the skin depth, which is only a few centimeters for most plasmas. For a planar configuration like the one used in the ion source, this means that most of the power will be deposited in the plasma close to the RF window, and this will thus cause the window to get hot.

Figure 4.36 presents the temperature of the window and of the O-ring around the edge of the window at various RF powers. The temperature was measured with thermocouples taped to the center and the edge of the window to obtain the *Window* and *O-Ring* temperatures respectively. The accuracy is poor since the thermocouples are not embedded into the material, so these measurements are used as an indication of the heat transferred to the RF window. Figure 4.36 also presents

119

the temperature profile of the window measured with an infrared (IR) camera. The temperature profile could only be taken after the ion source was turned off, so there is a delay of about 30 seconds between when the ion source was running and the temperature measurement. Furthermore, the temperature measurement profile was not calibrated with position.
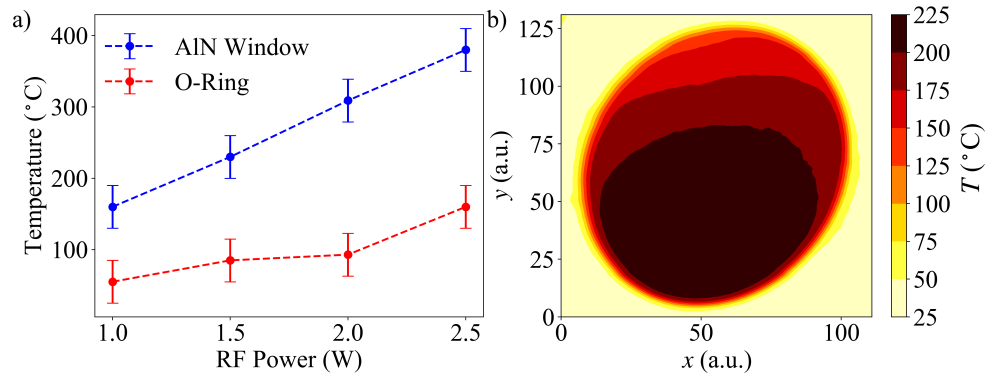
Figure 4.36: a) Measured window and O-ring temperature as a function of the RF power. b) Temperature profile measured with an infrared camera 30 seconds after the ion source had been running at 1.5 kW.

In Figure 4.36a, the temperature is linear with RF power and extrapolating to higher RF powers reveals that the center of the window would get to about 600 °C at 4 kW of RF power. The copper surrounding the window is cooled, so stays at a temperature of around 30 °C, which creates a large thermal gradient across the window. The temperature profile obtained gives a maximum temperature that's lower than the actual operation temperature since the IR photo was taken about 30 seconds after the ion source had been turned off. The temperature is maximum close to the center of the window, but there a slight offset towards the bottom. The reason for this is unknown, as the theoretical analysis of inductively coupled plasmas with planar antennas showed that the plasma should be concentrated in a ring centered in the middle of the window.

Thermal simulations of the ion source were completed in Solidworks [115]. A screenshot of the simulation results for an input power of 3 kW is shown in Figure 4.37.
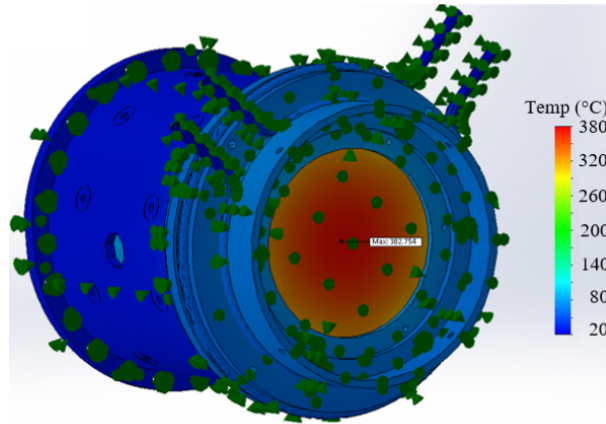
Figure 4.37: Thermal simulation results obtained with SolidWorks. The input power was set at 3 kW and the water temperature was set at 20°C.

From the thermal simulations, the maximum temperature obtained on the window was about 380 °C. The temperature profile also makes evident the large thermal gradient observed on the outer edge of the window. The measured stress measured on the window with the thermal simulation was at more than 500 MPa, while the flexural stress of AlN is around 200 MPa [116].

It is this therefore important to reduce the temperature gradient across the window. The vacuum seal is done with an O-ring, which cannot be at more than about 200°C, so the whole window will have to be cooled. A new cooling system has been designed with a water jacket surrounding the window, adding direct cooling to the aluminum nitride window. A model of the cooling jacket is shown in Figure 4.38.
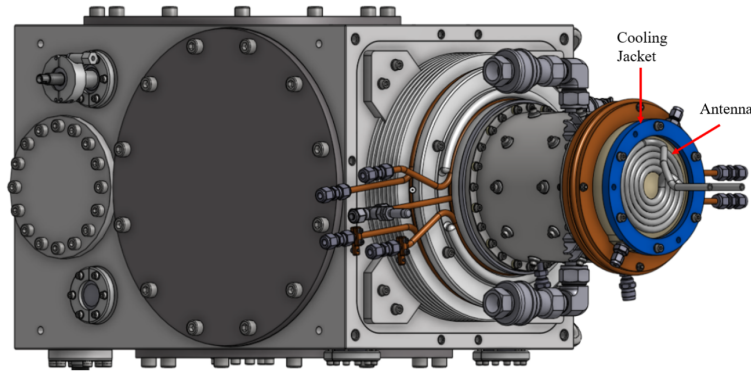
Figure 4.38: Model of the RF window water cooling water.

The new water cooling jacket has not yet been tested, but it is thought to allow for the ion source operation up to the full power of the RF amplifier (5 kW). This would lead to a more stable ion source operation without any window failures and which should lead to higher extracted H$^-$ beam current.

4.7   Conclusion

RF powered ion sources with external antennas are valid options for ion implanter applications because there are no contaminants added to the plasma chamber that could get sputtered by the positive ions in the plasma chamber, migrate through the vacuum system and contaminate the implanted wafers. The RADIS ion source, licensed from the University of Jyväskylä, was tested with acetylene as the injection gas for the extraction of negative carbon ions. The negative ion beam extracted from the RADIS ion source was too low for the goal of 1 mA C$^-$ or 0.5 mA C$_2^-$, however, these experiments gave insight into the nature of the sparking seen while extracting negative ions from an acetylene plasma, and confirmed that this RF powering technique can be used for a negative carbon ion source.

As a result of the RADIS ion source carbon experiments, a new RF-powered ion source was developed that uses the extraction system and ion source body of the TRIUMF licensed filament-powered ion source coupled to the back plate, RF antenna and impedance matching system of the RADIS ion source. Furthermore, when comparing the beam current density per RF power, the newly developed ion

source can still extract about 50% higher beam current densities. When comparing with the filament-powered ion source, the total H$^-$ beam current and the power efficiency were lower in the RF-powered ion source. The reason for the beam current differences were identified and improvements to the ion source design were proposed. The new RF-powered ion source developed is an interesting option for many H$^-$ applications, such as for cyclotrons and tandem accelerators since it has no consumable parts and it can achieve H$^-$ beam currents that are comparable to what can be extracted from the filament-powered ion source. The new RF-powered ion source was cited by two review publications on H$^-$ ion sources [31, 32], and led to two publications [117, 118].

The next chapter will present the performance of the new hybrid RF-powered ion source for the extraction of negative carbon ions. This ion source is a viable candidate to be used in ion implanter systems since no impurities are added to the plasma chamber.

Chapter 5

Extraction of Negative Carbon Ions with the RF-Powered Ion Source

Chapter 5 presented the development of a new hybrid design RF-powered H^- ion source which is an interesting ion source for H^- applications since high H^- currents can be extracted and the ion source does not have any consumable parts, leading to much longer operational lifetimes than filament-powered ion sources. Furthermore, the RF-powered ion source developed also does not add any contaminants to the plasma, so it is a valid option for ion implanter applications. This chapter describes the experiments and analysis that was undertaken with the new hybrid RF-powered ion source towards meeting the negative carbon ion beam production requirements for semiconductor ion implantation.

First, the performance of the RF-powered ion source with acetylene as the injection gas will be presented. This includes analyzing the negative ion current, the co-extracted electron current, the emittance and the beam composition as a function of the different ion source parameters and comparing the results with the filament-powered ion source to determine how the plasma generation technique affects the beam extracted out of the ion source. Then, optical emission spectrometry will be used to analyze the plasma species in the ion source as a function of the ion source parameters. Finally, the focus will be on improving the stability of

the extraction system to reduce the glitch rate, as the beam stability is the limiting factor in the performance of the ion source. Extraction geometry modifications, extraction simulation and magnetic configuration analysis will be included in this section.

5.1 Ion Source Performance

This section will focus on the analysis of the performance of the new hybrid RF-powered ion source for the extraction of negative carbon ions. The dependence of the beam current, the co-extracted electron current, the beam composition and the emittance on the gas flow and the RF power will be described. The beam properties will also be compared with results obtained in Chapter 3 with the filament-powered ion source.

Acetylene, purchased from Air Liquide with a purity of 99.99%, was used as the injection gas in the hybrid design RF-powered ion source. The ion source was as described in Section 4.4. A plasma could easily be generated with about 400 W of RF power, which is much lower than what was seen with hydrogen in the same ion source. At 11.4 eV [119], the ionization energy of acetylene is lower than hydrogen's ionization energy of 13.6 eV [120]. This means that the lower electric fields are needed to ionize the gas and start the plasma.

5.1.1 Beam Composition

This section studies the composition of the beam extracted out of the ion source by comparing it with results obtained with results with the filament-powered ion source, as was seen in Section 4.1.1. From the results in Chapter 3, it is expected that H^-, C_2^-, C_2H^- and $C_2H_2^-$ will be the main negative ions extracted from the hybrid RF-powered ion source when acetylene is used as the feed gas.

The beam composition was measured with the mass spectrometer presented in Section B.3.2. The entrance and exit slits of the mass spectrometer were set at 10 mm and a 3 mm circular aperture was positioned at the end of the ion source vacuum box to limit the beam current going through the spectrometer. A typical spectrometer scan obtained with the hybrid RF ion source is presented in Figure 5.1.
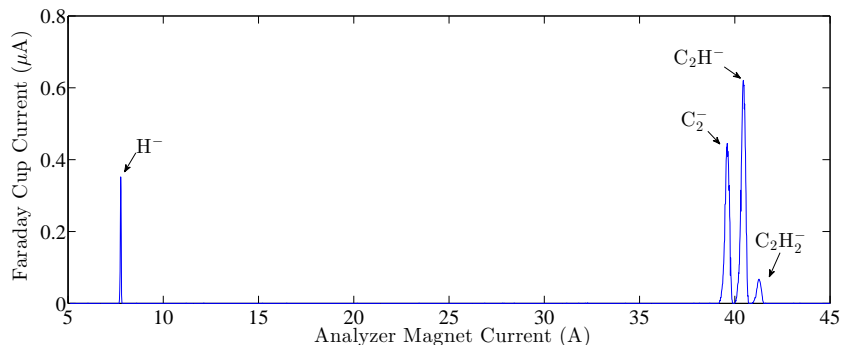
Figure 5.1: Spectrometer scan obtained with acetylene as the injection gas in the RF-powered ion source. The RF power was set at 500 W, the gas flow was set at 10 sccm, the beam energy was set at 30 keV, the plasma electrode was set at 0 V and the extraction electrode was set at 1.5 kV.

From Figure 5.1, there is a much lower $C_2H_2^-$ beam component with the RF-powered ion source than there is with the filament-powered ion source, as was seen in Figure 3.2. $C_2H_2^-$ ions are believed to come from surface production in the plasma since the volume production processes require the molecule to split when it produces a negative ion [83]. The main difference between the plasma wall surface of the filament-powered and the RF-powered ion sources is that there is no tantalum film on the plasma chamber walls of the RF-powered ion source. Tantalum has a lower work function (4.25 eV) than copper (4.65 eV) [121], but this is not enough of a difference to explain the difference in $C_2H_2^-$ current. There are other factors such as the sticking probability of the incident particle and the inhomogeneity of the surface that will influence the surface production of negative ions [122]. These factors explain why the relative $C_2H_2^-$ production is about three times larger in the filament-powered ion source.

The reduced $C_2H_2^-$ component obtained in the RF-powered ion source leads to an increased relative composition of C_2^- which is helpful for the negative carbon ion source goal. This is an additional advantage to using the RF-powered ion source for the production of negative carbon ion beam. The next section will present the maximum beam current that was extracted by increasing the RF power.

126

5.1.2 RF Power

In general, the beam current extracted out of the ion source increases with the input power, so the properties of the RF-powered ion source were measured as a function of the input RF power. Furthermore, it was shown in Chapters 3 and 4 that the glitch rate is dependent on the input power, with an increased glitch rate seen as the input power increases, so particular attention will also be paid to the glitch rate in this section.

The beam current extracted out of the hybrid RF-powered ion source was measured with the Faraday cup located 480 mm downstream of the plasma electrode. The total extracted beam current was found to increase with the RF power, with a greater relative increase seen with higher gas flows. As usual, the extraction was very unstable as there was frequent sparking on the extraction electrode, and the frequency of the sparking increased with the RF power to a rate of between 4000 and 5000 glitches per hour at 600 W of RF power. The total beam current as a function of the RF power for various gas flows is presented in Figure 5.2.
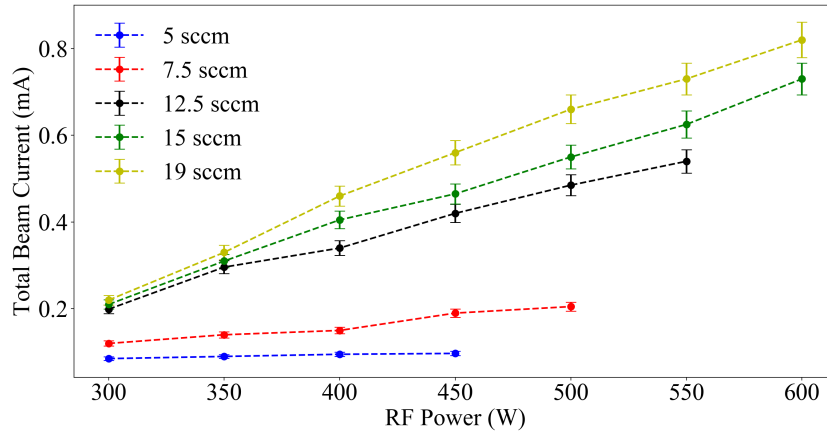
Figure 5.2: Total beam current (all species) as a function of the RF power for various gas flows. The bias voltage was set at 30 kV, the plasma electrode voltage was set at 0 V and the extraction electrode voltage was optimized at every measurement.

A maximum total beam current, consisting of all the species presented in Figure

5.1, of 0.82 mA was obtained at 600 W and 19 sccm of gas flow. This corresponds to a C_2^- beam current of about 0.27 mA, which is more than half of the goal of 0.5 mA and is considerably more than what was extracted out of the filament-powered ion source, which was 0.1 mA. The ion source parameters for this maximum current tune are presented in Table 5.1.

Parameter	Value
Total Beam Current	0.82 ± 0.04 mA
Forward RF Power	600 ± 5 W
Reflected RF Power	13 ± 5 W
Bias Current	2.6 ± 0.05 mA
Bias Voltage	30 ± 0.1 kV
Extraction Electrode Current	78 ± 4 mA
Extraction Electrode Voltage	1.8 ± 0.1 kV
Plasma Electrode Current	0 ± 0.1 A
Plasma Electrode Voltage	20.0 ± 0.1 V
Gas Flow	19.0 ± 0.2 sccm
X Steering Current	0 ± 0.1 A
Y Steering Current	0 ± 0.1 A

Table 5.1: Maximum beam current tune obtained with the hybrid ion source with acetylene.

From Figure 5.2, one can see that there is no saturation of the beam current up to 600 W, thus increasing the RF power even further would yield higher beam current. However, the maximum RF power that could be tested was limited by frequent sparking on the extraction electrode, which made the beam current measurement impossible. This was also seen in the TRIUMF licensed filament-powered ion source and in the RADIS ion source when acetylene is used as the injection gas. Improving the stability of the extraction system would allow the ion source to be operated to higher RF power and will lead to higher beam currents, this will be the focus of Section 5.3.

The gas flow into the ion source also had a large impact on the beam current extracted, with higher beam currents extracted with higher gas flows, which is the same effect that was seen with the filament-powered ion source. In the filament-powered ion source, this increase in beam current with gas flow was due to a lower-

ing of the electron temperature which led to higher negative carbon ion production rates through dissociative electron attachment of acetylene. Along with the negative ions, it is also interesting to study the co-extracted electrons. In the filament-powered ion source, the co-extracted electron current was much higher with acetylene than it was with hydrogen, and this was also the case with the RF-powered ion source, as can be seen in Figure 5.3.
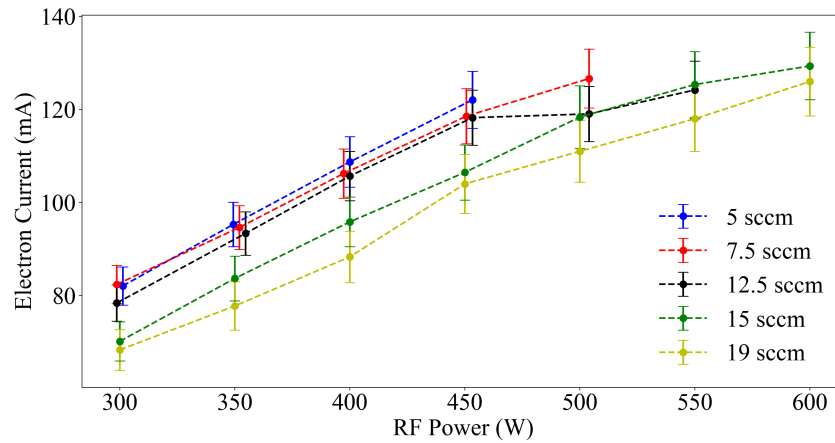
Figure 5.3: Co-extracted electron current as a function of RF power for various acetylene gas flows. The bias voltage was set at 30 kV, the plasma electrode voltage was set at 0 V and the extraction electrode voltage was optimized at every measurement.

From Figure 5.3, there is an increase in the co-extracted electron current with the RF power. This is due to an increase ionization rate in the plasma as the RF power is increased, which leads to an increase in the electron density in the plasma chamber. There is also a decrease in the electron current with gas flow. The same effect was seen in the filament-powered ion source, and the Langmuir probe study showed that the decrease was due to a decrease in the electron density in the plasma with the gas flow.

As presented in the previous section, there are four main negative ion components (H^-, C_2^-, C_2H^- and $C_2H_2^-$) in the beam extracted out of the RF-powered ion source when acetylene is used as the injection gas. The relative beam composition

for the four main constituents as a function of the RF power for a gas flow of 19 sccm is presented in Figure 5.4.
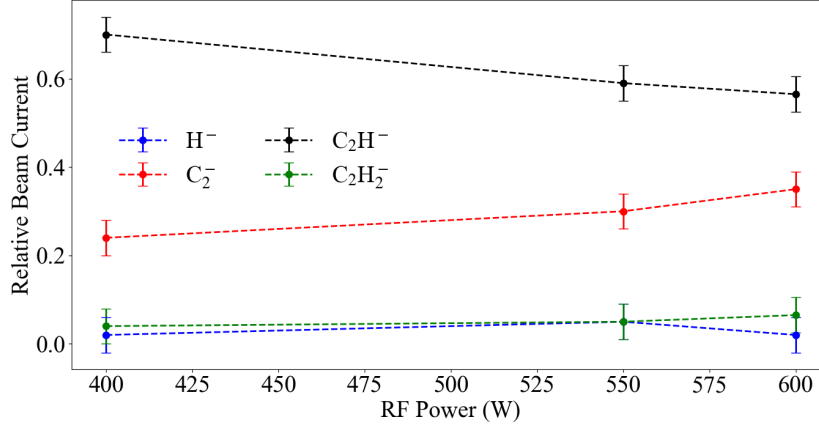
Figure 5.4: Relative beam composition as a function of the RF power for a gas flow of 19 sccm. The bias voltage was set at 30 kV, the plasma electrode voltage was set at 0 V and the extraction electrode voltage was optimized at every measurement.

From Figure 5.4, there is a slight increase in C_2^- and a decrease in C_2H^- as the RF power is increased. Previous studies [83] have showed that there is no large difference between the production cross sections of C_2^- and C_2H^-. Thus, the hypothesis is that the change in the relative population with the RF power is not due to change in the volume production through dissociative electron attachment, but it is due to the difference in surface production. The higher RF power leads to a higher dissociation of acetylene and a higher C_2 density in the plasma, which leads to higher C_2^- current.

The maximum C_2^- beam current extracted out of the ion source was of 0.27 mA at an RF power of 600 W and an acetylene gas flow of 19 sccm. However, at these settings, the beam stability was much worst than the goal of less than 10 glitches per hour, at more than 4000 glitches per hour. The maximum beam current extracted is not limited by the RF power but by the stability of the extraction system.

5.1.3   Gas Flow

This section will focus on the effect of gas flow on the properties of the beam extracted. As was seen in Figure 5.2, there is an increase in the total negative beam extracted with gas flow and this was also seen with the TRIUMF licensed filament-powered volume-cusp ion source. Figure 5.5 shows the effect of gas flow on the total beam current and on the beam composition for a constant RF power of 500 W.
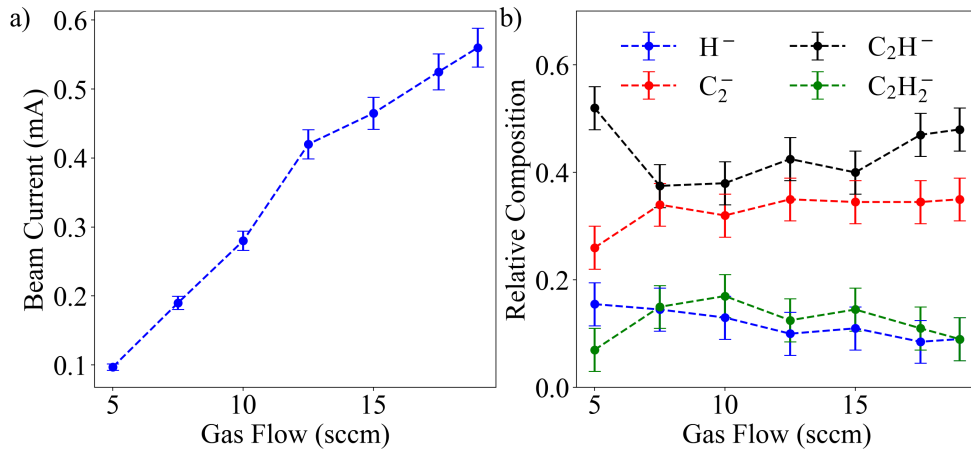
Figure 5.5: a) Total beam current for various acetylene gas flows and b) relative beam current of the four main component of the beam (H^-, C_2^-, C_2H^-, $C_2H_2^-$). The RF power was set at 500 W for the measurements, the bias voltage was set at 30 kV, the plasma electrode was set at 0 V and the extraction electrode voltage was optimized for every measurement.

The beam current is highly dependent on the gas flow, and in the filament-powered ion source this increase in beam current with gas flow was attributed to an increase in the production of the negative carbon ion species due a decrease in the electron temperature at these gas flows. From Figure 5.5b, there is also an increase in the C_2^- and C_2H^- currents with gas flow which suggests that the increase seen is due to an increase in the production of these ions in the plasma through dissociative electron attachment reactions from a lowering of the electron temperature and/or an increase in the neutral density.

From 5.5b, there's a slight decrease in the relative H^- current, which was also

seen in the filament-powered volume-cusp ion source. The decrease in H$^-$ current is due to higher H$^-$ stripping rates at the higher pressures, this is seen in the H$^-$ ion source.

One can conclude that higher gas flows are favorable for the production of negative carbon ions. This tendency was also seen in the filament-powered ion source.

5.1.4   Beam Emittance

The maximum normalized 4-RMS emittance for the target ion implanter application was set at 1 mm·mrad, and in Chapter 3 the emittance of the beam extracted out of the filament-powered ion source was shown to be between 0.6 mm·mrad and 0.9 mm·mrad. Since the RF-powered ion source uses the same body and extraction system as the filament-powered ion source, it is expected that the emittance will be similar. Any difference in the emittance can be attributed to differences in the plasma close to the extraction region of the ion source.

The emittance of the total beam (all species) was measured with the emittance scanner in Figure B.16 scanning in the y direction and located 368 mm downstream from the plasma electrode. An example of an yy' phase space of a beam extracted from an acetylene plasma with the RF-powered ion source is presented in Figure 5.6.
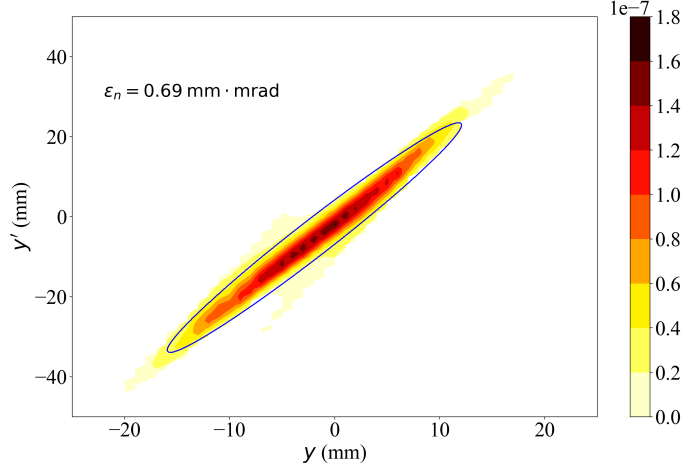
Figure 5.6: yy' phase space scan obtained with the RF power set at 400 W and the gas flow set at 19 sccm. The bias voltage was set at 30 kV, the plasma electrode was at 0 V and the extraction electrode voltage was set at 1.5 kV. The 4-RMS emittance ellipse is shown in blue.

Normalized 4-RMS emittance values between 0.6 mm·mrad and 1.0 mm·mrad were typically obtained, which is slightly higher than what was measured with the filament-powered ion source, but it is still below the goal of 1 mm·mrad.

The goal of having a C_2^- emittance of less than 1 mm·mrad is thus met with the hybrid RF-powered ion source.

5.2 Plasma Analysis

The production of negative ions in acetylene plasma is highly dependent on the plasma parameters [83]. Furthermore, when compared to hydrogen plasmas, there are many more species in the plasma that could influence the production and the destruction of the negative ions. It is thus important to study the composition of the plasma as a function of the ion source parameters to determine which configuration optimizes the production of C_2^- ions. Thus, optical emission spectroscopy was used to study the acetylene plasma generated by the RF-powered ion source.

This section will present the optical emission spectroscopy analysis that was done with the hybrid RF-powered ion source when acetylene was used as the injection gas. The different peaks that were identified will first be presented, then

these peaks will be used to compare the different species population inside the plasma as a function of the ion source parameters.

5.2.1 Optical Emission Spectroscopy

Optical emission spectroscopy was performed in the hybrid RF-powered ion source through the extraction aperture, using the configuration that was presented in Figure B.21.The fiber was attached to the end of the emittance scanner head and the head was moved in the beamline until a signal was observed on the spectrometer. The light was coupled in the fiber through an optical collimator, the fiber was connected to an optical vacuum feedthrough and the light was collect in the spectrometer via another fiber outside the vacuum chamber.

Figure 5.7 shows the observed spectrometer scan obtained at 5 sccm of acetylene gas flow and 400 W of RF power.
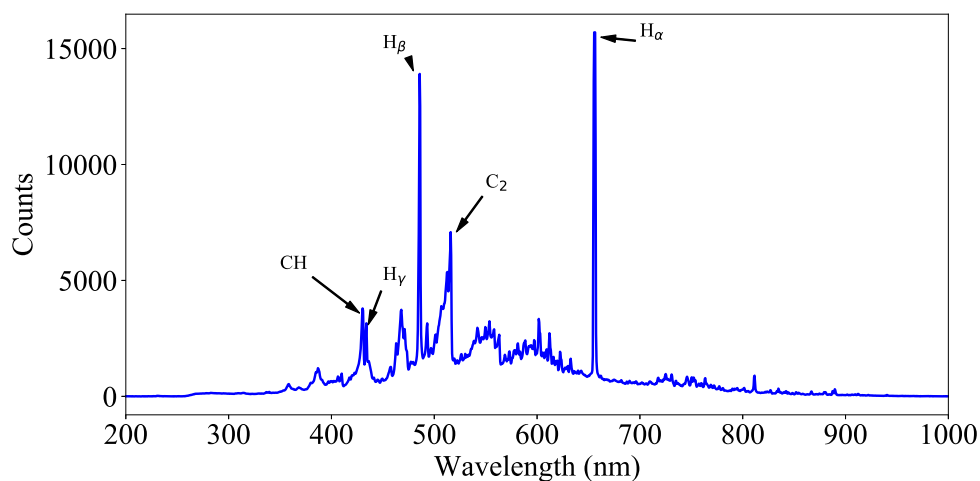
Figure 5.7: Optical emission from an acetylene plasma created with the RF-powered ion source with an RF power of 400 W and a gas flow of 5 sccm. The ion source and the electrodes were not biased for this experiment.

From Figure 5.7, the dominant peaks at 656 nm and 486 nm are the two first lines from the Balmer series of hydrogen [123], which indicates that there's a large density of atomic hydrogen in the plasma. The peak at 431 nm corresponds to the

A^2 $\Delta-$X^2 Π (0$\rightarrow$0) of CH [124]. The peak at 516 nm corresponds to one of the Swan peaks of the C_2 complex. The Swan system of C_2 constitutes multiple peaks between 400 and 650 nm [124]. Furthermore, there seems to be a continuum with a peak between 500 nm and 600 nm. When the integration time is increased and the dominant peaks are saturated, this continuum becomes more obvious, as can be seen in Figure 5.8.
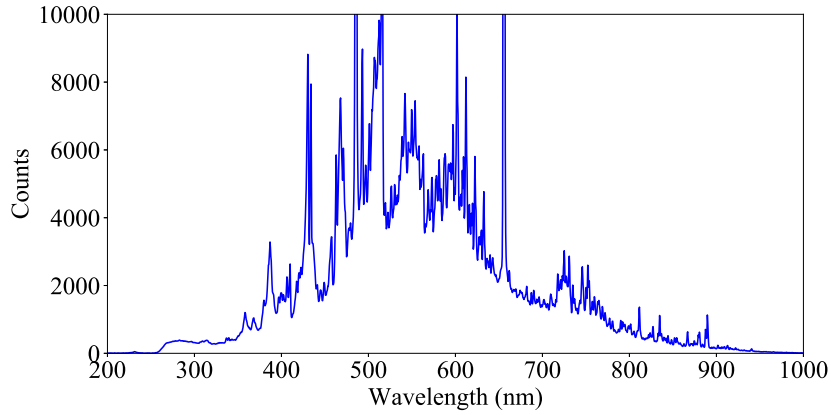
Figure 5.8: Spectrometer scan of figure 5.7 with a longer integration time, saturating the peaks and showing the continuum.

One possible explanation for this continuum is that it is from the hot incandescent carbon particles in the plasma [96], and thus should follow a blackbody radiation curve at the temperature of the gas particles. The blackbody radiation curve as a function of wavelength is given by

$$I(\lambda, T) = \frac{2hc}{\lambda^3} \frac{1}{\exp\left(\frac{hc}{\lambda kT}\right) - 1}, \tag{5.1}$$

where h is Planck's constant, c is the speed of light, λ is the wavelength, k is Boltzmann's constant and T is the temperature of the body. Equation 5.1 was fitted to the continuum region of Figure 5.8 and the resulting fit is plotted in Figure 5.9.

From Figure 5.9, the fit is poor since the curve has a much wider peak than what is seen in the plots. Furthermore, the temperature fitted of 8050 K is much higher than gas temperature values quoted in the literature for similar plasmas, where it
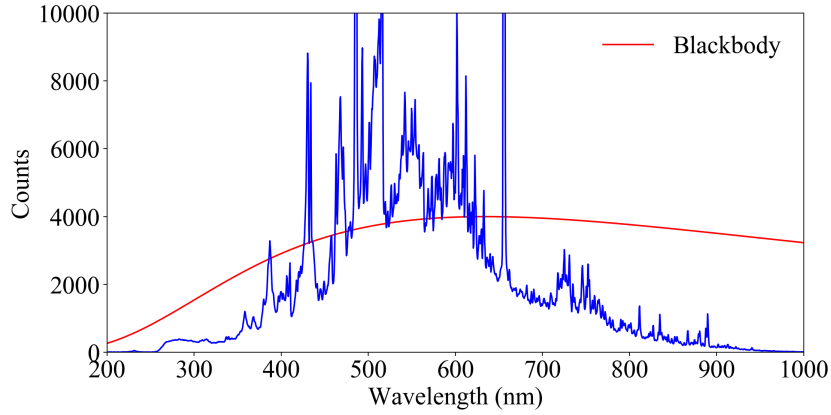
Figure 5.9: Blackbody radiation equation fitted to the continuum of the spectrum of Figure 5.8. A temperature of 8050 K was used for the fit.

is usually less than 4000 K [96]. The continuum is most likely due to the $\widetilde{B} - \widetilde{X}$ transition of C_2H as described by [125]. The continuum obtained resembles what is seen in the ion source, there's a quick increase between 430-470 nm and a slow drop at more than 550 nm.

From the analysis presented here, the relative population of different species in the plasma can be estimated by an optical emission spectroscopy analysis. The next section will describe how the species population are dependent on the different ion source parameters.

5.2.2 Species Analysis

By comparing the relative intensities of the different peaks, it's possible to compare the various populations in the plasma. The C_2, H and CH populations are monitored by comparing integral of the spectral lines at 516 nm, 486 nm and 431 nm respectively. The chosen peak was H_β instead of H_α since it's of comparable intensity to the other dominant peaks. The relative C_2H population is estimated by integrating a spline fit of the continuum. The relative peaks were measured as the gas flow and the RF power were varied. The results are presented in Figure 5.10. The values obtained are normalized, so the graphs are only used to show the trends in the population as the ion source parameters are changed, and not absolute

136

changes.
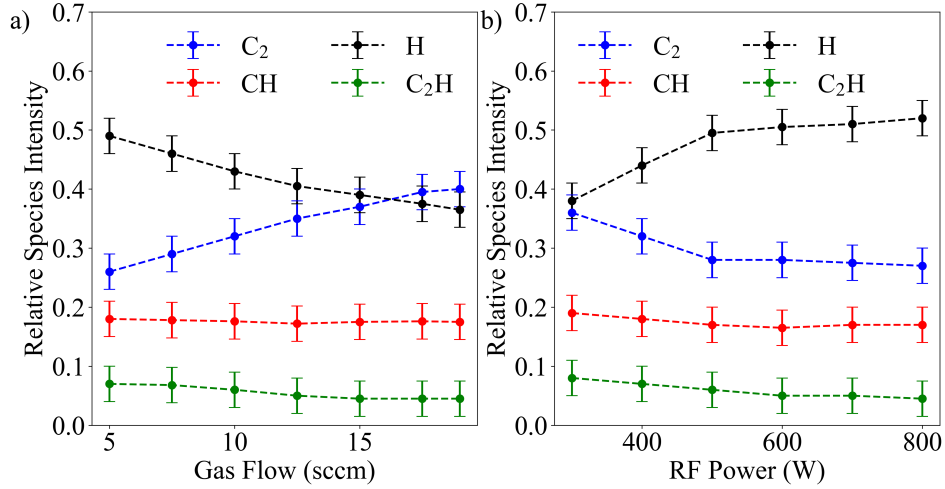
Figure 5.10: Relative intensity of various species for a) various gas flows and b) various RF powers. The RF power was set at 400 W in a), while the gas flow was set at 10 sccm in b).

From Figure 5.10, as the gas flow is increased, there is an increase in the C_2 signal and a decrease in the H signal. This decrease in the H population can also be seen in the beam composition presented in Figure 5.5, where there is a clear decrease in H^- current and an increase in $C_2H_x^-$ ions at higher gas flows. The CH population is constant at the various gas flows. Trace amounts of CH^- beam are detected out of the ion source.

There is an increase in the H population and a decrease in the C_2 population with increasing RF power. As the RF power increases, the increase in H can be explained by an increase in the dissociation of the acetylene molecule by the increase in electron density and temperature that is associated with the increase in RF power ($C_2H_2+e \rightarrow C_2H+H+e$). This would lead to an increase in the H population. It is expected that the C_2 population increases in a similar fashion, but the difference is due to the fact that two H atom would be produced for every dissociated acetylene molecule ($C_2H_2+e \rightarrow C_2+2H+e$).

From the analysis presented in this section, some of the populations follow the trends seen in the beam composition analysis. For example, the H^- current

decreases with the gas flow and increases with the RF power, and the same trend was seen with the H population with the optical emission spectroscopy analysis. However, the C_2 and C_2H populations seen in this analysis don't follow the beam composition values as well as the dependence with the RF power. The negative ions produced by surface production are expected to follow the population densities seen with optical emission spectroscopy, thus the C_2 and C_2H population differences seen are explained by the fact that the production of these ions is also dependent on the volume negative ion process.

The main problem associated with optical emission spectroscopy is that the signals obtained are averaged over the line of the sight through the plasma. This is problematic for the highly non-uniform plasma that's created in the ion source and adds to the uncertainty in the OES population density results.

5.3 Beam Stability

Ion implanters have stringent beam stability requirements since the dose implanted in the wafers is directly proportional to the beam current. Thus, to ensure that the implanted dose is uniform across the wafers, the beam current has to be stable. For this project, a goal of less than 10 glitches per hour was set, where a glitch consists of any beam current deviation of more than $\pm 5\%$ of the nominal beam current.

The stability of the extraction of negative ions with an acetylene plasma was first seen as an issue in Chapter 3 when the TRIUMF licensed filament-powered volume-cusp ion source was used with acetylene. Stability issues were also seen with the RADIS ion source in Chapter 4 and with the hybrid RF-powered ion source presented in this Chapter. The main issue stems from electrical breakdowns on the extraction electrode of the ion source. This section will present how the extraction system and the plasma were studied to reduce the glitch rate in the ion source. The original extraction system and how it performs will first be presented, then the effect of bias voltage and the aperture sizes on the glitch rate and the beam current will be shown. Finally, the magnetic filter field will be changed to reduce the co-extracted electron current and reduce the glitch rate.

5.3.1 Initial Beam Stability

Initial experiments with all three ion sources tested as part of this Thesis work showed that there were important instabilities in the beam current when acetylene was used. Figure 5.11 presents the beam current with time with acetylene used in the RF-powered hybrid ion source.
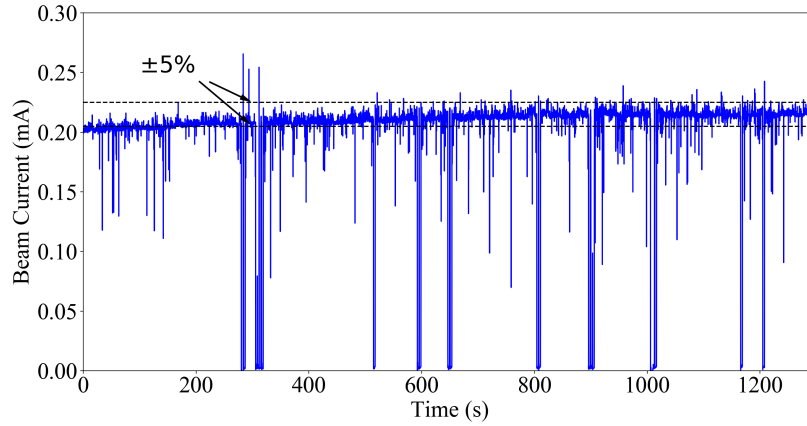
Figure 5.11: Beam current stability with acetylene in the RF-powered ion source. The RF power was set at 500 W, the gas flow was set at 10 sccm, the bias voltage was set at 30 kV, the plasma electrode was set at 0 V and the extraction electrode was set at 0.7 kV.

From Figure 5.11, it is evident that the glitch rate is much higher than what is acceptable for implantation applications. The glitch rate is close to 1000 glitches per hour. Furthermore, some of the glitches persist for more than a second and the beam current falls to zero.

The glitches in the beam current are caused by voltage breakdowns on the extraction electrode. The extraction electrode is commonly biased between 1 kV and 3 kV above the ion source potential. Figure 5.12 presents the extraction electrode voltage (V_{ext}) along with the beam current as a function of time when acetylene is used in the RF-powered ion source.
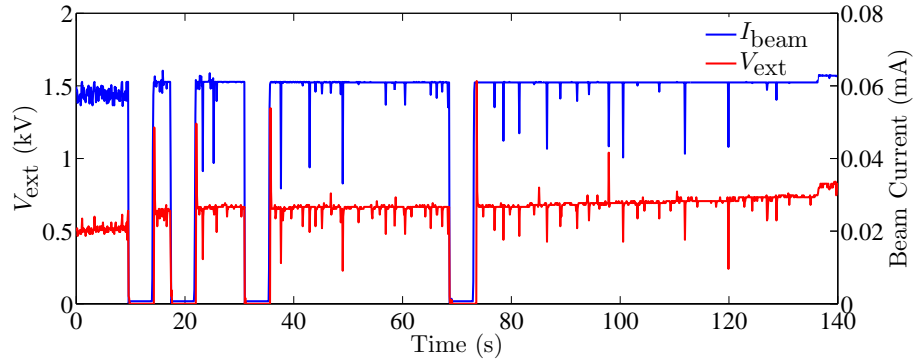
Figure 5.12: Beam current and extraction electrode voltage stability with acetylene in the RF-powered ion source. The RF power was set at 500 W, the gas flow was set at 10 sccm, the bias voltage was set at 30 kV, the plasma electrode was set at 0 V and the extraction electrode was set at 0.7 kV.

From Figure 5.12, the drop in beam current is caused by the extraction voltage instabilities and that some of the glitches seen in the extraction electrode voltage are not seen in the beam current. This is explained by the low sampling rate (10 Hz) of the PLC, which can not measure any fluctuations of less than 100 ms. Furthermore, some of the glitches in the extraction electrode voltage are positive, which indicates that the electrode was sparking to ground potential instead of the ion source potential.

These instabilities were not seen with H^-, as can be seen in Section B.2.2. Furthermore, there are no issues with the electrodes holding voltage when there is no plasma in the ion source and the purity of the gas used was at 99.99%, so the instability is most likely not due to impurities in the plasma. The issue must thus be caused by the acetylene plasma or the beam that's extracted from the plasma. The following sections will present experiments that were performed to determine how the glitch rate was reduced.

5.3.2 Extraction Geometry

The geometry of the extraction system will first be studied to determine where the electric field is maximum. The extraction system of the original ion source design

140

is composed of a plasma electrode, an extraction electrode and a ground electrode. The geometry of the extraction system is presented in Figure 5.13.
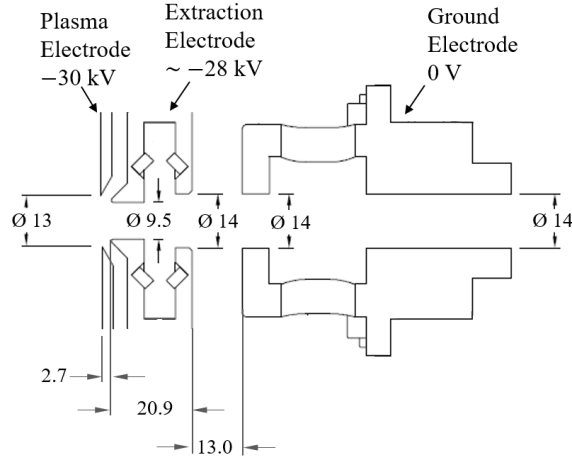
Figure 5.13: Schematic of the extraction system in the original ion source design. Taken from [23].

The protrusion of the extraction electrode and the short spacing between it and the plasma electrode (2.7 mm) creates a high electric field. IBSimu simulations were used to find the electric field in the extraction. The results are presented in figure 5.14.
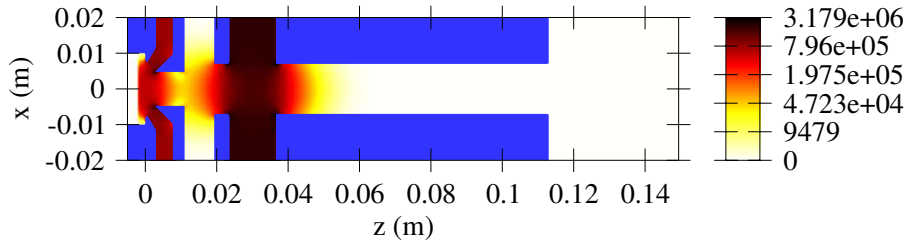
Figure 5.14: Magnitude of the electric field from a beam extraction simulation in IBSimu [77] of the extraction system. The electrodes are presented in blue, with the plasma electrode set at 30 kV, the extraction electrode set at 26.5 kV and the ground electrode set at 0 V.

A safe limit of 5 MV/m is often taken to ensure that the extraction system will hold the proper voltage [126], and from Figure 5.14 the electric field is below this value. Thus, the sparking is not caused by the high electric field alone, which is not surprising since H^- ions can safely be extracted with this extraction system.

142

However, the electric field is maximum on the tip of the extraction electrode, which makes this a high risk area for sparking.

The initial design of the ion source extraction system uses a 13 mm diameter plasma electrode aperture with a 9.5 mm extraction electrode aperture. This size difference places the extraction electrode in a vulnerable position for beam strike. When an ion strikes an electrode, there is a release of secondary electrons that will be accelerated by the strong electric field in the extraction system which could lead to avalanche discharges. Additionally, the striking of the extraction electrode could also produce positive ions which will be accelerated to the plasma electrode and start an avalanche discharge from this collision [127].

IBSimu simulations of the extraction system were done to examine whether there was any beam strike on the electrodes. For the simulations, 0.75 A/m^2 of C$_2^-$ ions were simulated, which corresponds to an extracted beam current of about 0.1 mA with a plasma electrode aperture diameter of 13 mm. Figure 5.15 presents the results of the simulation for two different extraction geometries.
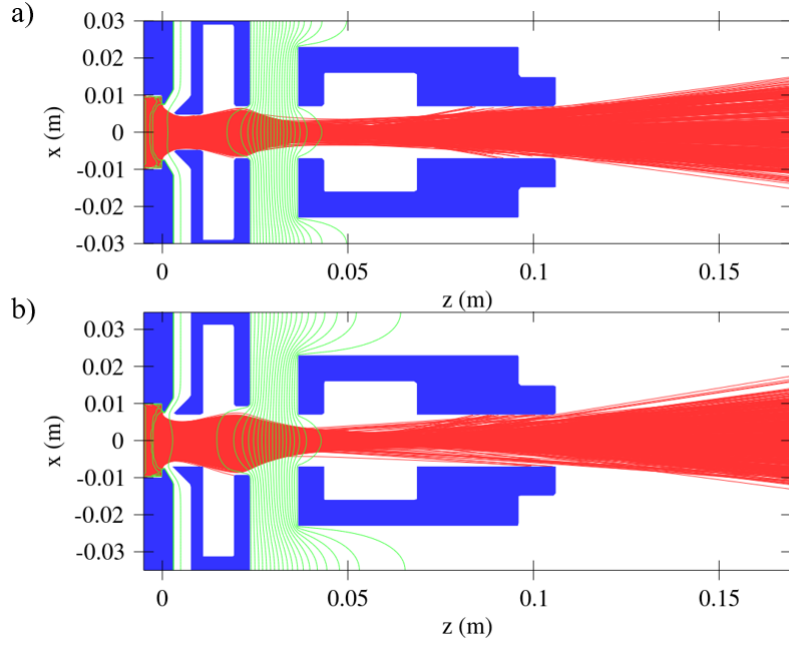
Figure 5.15: Beam extraction simulations for a) the original, 13 mm plasma and 9.5 mm extraction aperture, configuration and b) a 13 mm plasma and 14 mm extraction aperture configuration. 0.75 A/m^2 of C$_2^-$ is simulated with the ion source biased at -30 kV and the extraction electrode at 1 kV.

From Figure 5.15a, there is significant beam strike on the extraction electrode if the plasma meniscus is not optimized with the right highly concave curvature. When the size of the extraction aperture was increased to be larger than the plasma aperture, the simulations predict that the beam is extracted through the system without ever striking the extraction electrode, even if the plasma meniscus shape is not optimized.

The diameter of the extraction electrode aperture was increased and the diameter of the plasma electrode aperture was decreased to test whether this would lead to a reduced glitch rate. Several different configurations were tested experimentally with an RF power of 500 W and an acetylene gas flow of 30 sccm. The results are presented in the table 5.2.

$\varnothing_{\text{plasma}}$ (mm)	$\varnothing_{\text{extraction}}$ (mm)	V_{plasma} (V)	$V_{\text{extraction}}$ (kV)	Glitch Rate (h^{-1})	C_2^- Current (mA)
13	9.5	20	1.5	~1100	0.055
13	16	20	1.5	~700	0.057
8	14	20	1.5	~150	0.017
10.5	14	20	1.5	~390	0.060
10.5	16	20	1.5	~410	0.036

Table 5.2: Ion source stability for various electrode aperture sizes.

From Table 5.2, there is a decrease in the glitch rate when the ratio of the diameter of the plasma electrode over the extraction electrode aperture diameter decreases. The lowest glitch rate is observed when a 8 mm plasma electrode aperture is used with a 14 mm extraction electrode aperture. However, as the size of the plasma electrode decreases, so does the C_2^- beam current.

Figure 5.16 presents the relation between the glitch rate and the ratio of the aperture size of the plasma electrode and the extraction electrode.
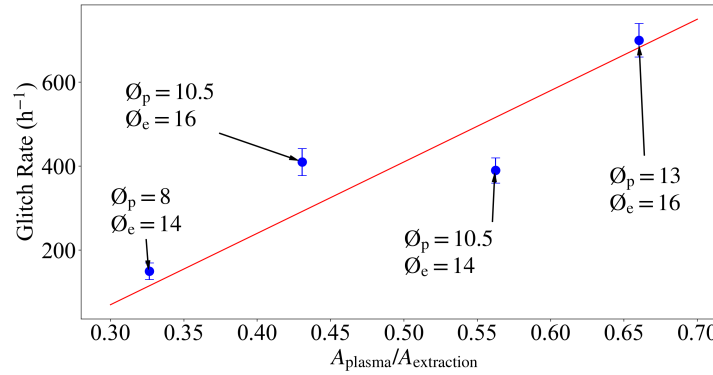
Figure 5.16: Glitch rate as a function of the ratio of the plasma electrode aperture over the extraction electrode aperture.

From Figure 5.16, there is a linear dependence when the ratio of the aperture size of the plasma electrode and the extraction electrode is less than 1.

With the larger extraction electrode aperture and smaller plasma electrode aperture the glitch rate is still high, even though the simulations show that the beam

145

does not strike the extraction electrode with these geometries. The sparking between the electrodes must thus be caused by additional phenomena. Furthermore, to maintain a higher beam current but still keeping the glitch rate low, a configuration with a 10.5 mm plasma electrode aperture diameter with an extraction electrode aperture diameter of 14 mm was identified as a good compromise. The next section will focus on how the bias voltage on the ion source affects the glitch rate.

5.3.3 Bias Voltage

From Figure 5.14, the highest electric field region is between the extraction and ground electrodes, as the electric field in this region is created by the bias voltage. It is thus expected that reducing the bias voltage will lead to lower glitch rates since it will reduce the electric field in the extraction region. For the target ion implanter application, a beam energy as low as 10 keV can be used, thus the performance of the ion source was studied at various bias voltages. Figure 5.17 presents the glitch rate and the beam current for various bias voltages with a 10.5 mm diameter plasma electrode aperture and a 14 mm diameter extraction electrode aperture.
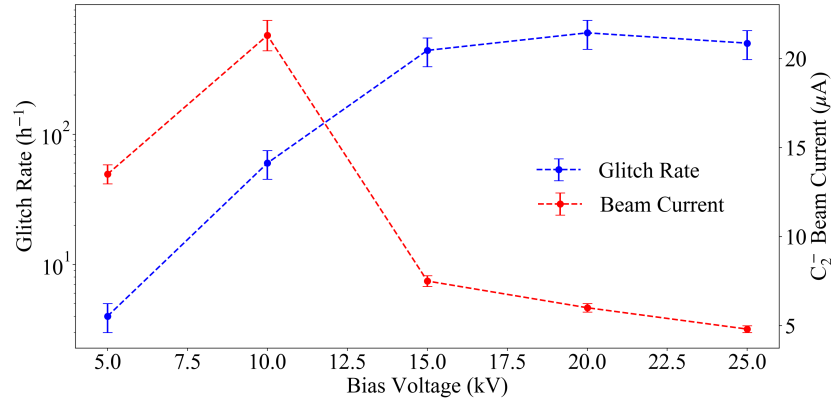
Figure 5.17: Glitch rate and total beam current extracted from the RF-powered source at various bias voltages. The RF power was set at 350 W, the gas flow was set at 15 sccm, the extraction electrode voltage was set at 2 kV and the plasma electrode was set at 20 V. The configuration with $\varnothing_{plasma} = 10.5$ mm and $\varnothing_{extraction} = 14$ mm was used.

Since the extraction electrode voltage was set to 2 kV for all the measurements in Figure 5.17, the extraction was not optimized for every bias voltage and the maximum beam current extracted was at 10 kV. The reason for the reduction in the glitch rates with the lower bias voltages is the reduced electric field seen between the extraction and the ground electrodes at the lower bias voltages. This suggests that some of the breakdowns occur between these two electrodes and explains why the glitch rates are still high when the risk of beam strike on the extraction electrode is eliminated.

By modifying the extraction geometry and reducing the bias voltage the glitch rate was dramatically reduced. However, it is still too high, especially at higher RF powers. The following section will present how the plasma parameters can be changed to further improve the beam current stability.

5.3.4 Gas Flow

Increasing the gas flow in the TRIUMF licensed filament-powered ion source lead to a lower electron density in the plasma, as was shown in Figure 3.16, which leads to lower co-extracted electron currents, as was shown in Figure 5.3. With the RADIS ion source, it was shown that increasing the electromagnetic dipole filter field in the plasma reduced the co-extracted electron current, and it also reduces the glitch rate. Thus, it is believed that the lower co-extracted electron currents seen at higher gas flows could lead to lower glitch rates.

Figure 5.18 presents the beam current, co-extracted electron current and glitch rate as a function of the RF power for various gas flows. The extraction configuration used a 10.5 mm diameter plasma electrode aperture and a 14 mm diameter extraction electrode aperture and the bias voltage was set at 10 kV.
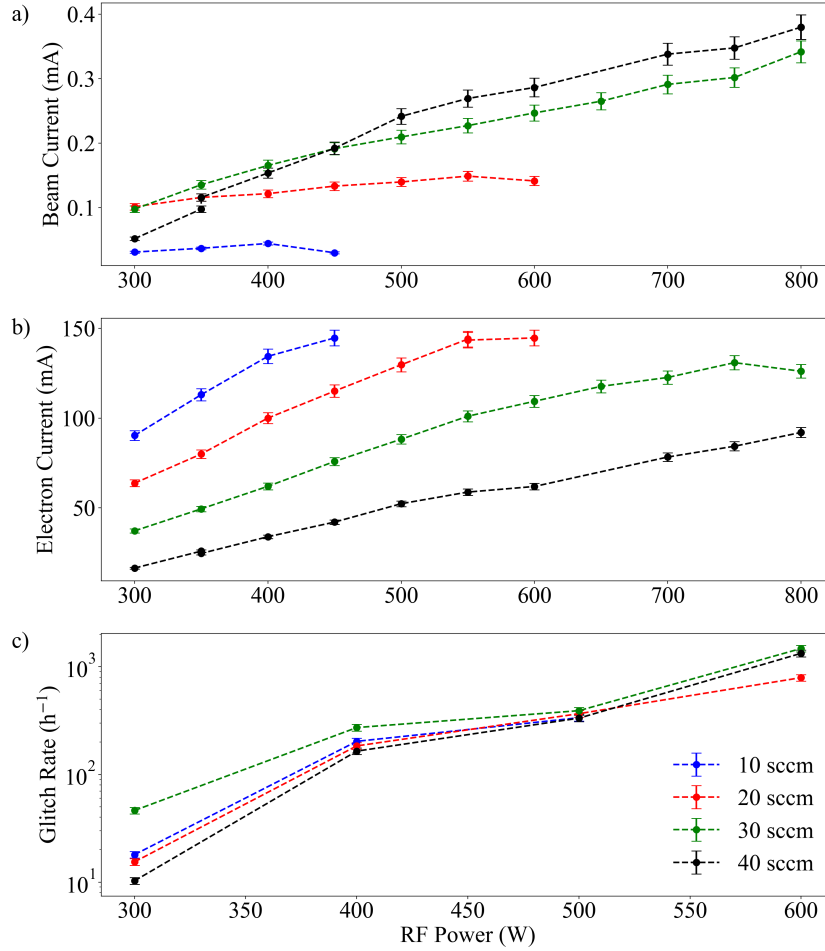
Figure 5.18: a) Beam current, b) co-extracted electron current and c) glitch rate as a function of the RF power for various gas flows. The bias voltage was set at 10 kV, the plasma voltage was set at 20 V, the extraction electrode was optimized for every measurement and the configuration with $\varnothing_{\text{plasma}} = 10.5$ mm and $\varnothing_{\text{extraction}} = 14$ mm was used.

From Figure 5.18, the difference in glitch rate with gas flow is small, but is noticeable at low RF power. The biggest change in glitch rate is seen with the RF power. However, from Figure 5.18 a, the greatest increase in beam current is seen

with an increase in the gas flow, as was noted in previous sections. Furthermore, the increased gas flow leads to an important reduction of the co-extracted electron current, which comes for a decrease in the electron density close the extraction region of the plasma chamber.

The co-extracted electron current has an effect on the glitch rate, and reducing the co-extracted electron current leads to lower glitch rates. The next section will thus focus on the dumping of the co-extracted electrons.

5.3.5   Extraction Simulations

As was seen with the RADIS ion source in Section 4.1 and in the previous section, higher co-extracted electron currents are correlates to higher glitch rates. The dumping of the electrons in the extraction system was thus studied to determine how the electron dumping could be improved to reduce the sparking on the extraction electrode.

IBSimu was used to model the extraction of the negative carbon ions and the dumping of the co-extracted electrons. The goal is to find a configuration that properly dumps the electrons between the two extraction electrode apertures while minimizing the negative ion beam losses along the extraction system. As seen in previous simulations (Figure B.31), the electrons are dumped on the front face of the extraction electrode, while the original ion source design has the electrons dumped between the two apertures of the extraction electrode. The reason for this difference is that the magnetic filter field in the plasma chamber extends into the extraction region, deflecting the co-extracted electrons before they reach the extraction electrode. To reduce the magnetic field between the plasma and extraction electrodes, the magnetic field in the ion source and the extraction system with the first set of dipoles in the extraction electrode removed was modeled in Opera [128]. The beam extraction simulation results for this configuration are shown in Figure 5.19.
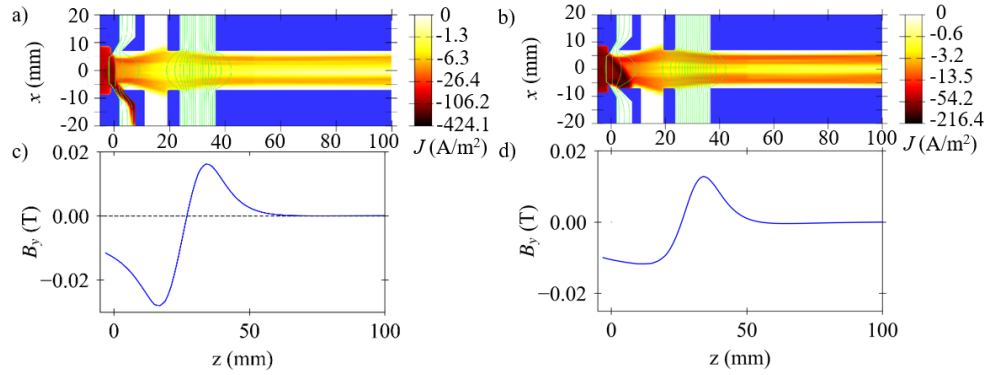
Figure 5.19: IBSimu simulations of a) the original extraction configuration and b) a modified extraction configuration with the first set of magnets removed from the extraction electrode aperture. The simulations were done at a bias voltage of 10 kV and an extraction electrode voltage of 1.5 kV. 0.1 mA of C_2^- and 30 mA of electrons were simulated. Magnetic field on the central axis for c) the original configuration and d) the modified configuration.

As can be seen in Figure 5.19, removing the first dipole from the extraction electrode prevents the electrons from being dumped on the front face of the extraction electrode, where the electric field is maximum. The new magnetic configuration was tested. The glitch rate and the beam current as a function of the RF power for various gas flows for the two magnetic configurations in Figure 5.19 is plotted in Figure 5.20.
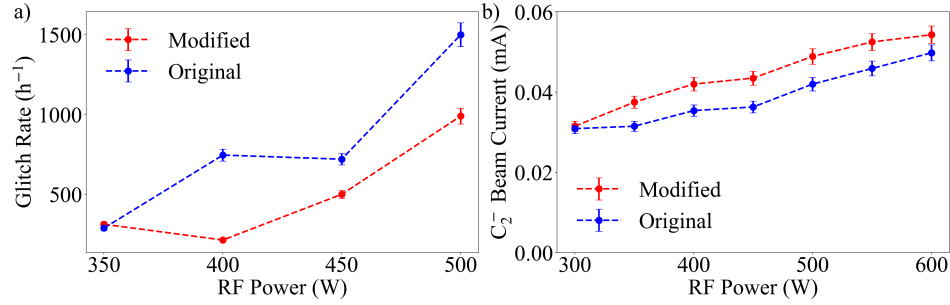
Figure 5.20: a) Glitch rate and b) C_2^- beam current measured with the original magnetic configuration and without the first set of magnets. The gas flow was set at 20 sccm, the bias voltage was set at 10 kV and aperture diameters of 10.5 mm and 14 mm were used for the plasma and extraction electrodes respectively.

From Figure 5.20, the glitch rate is lower with the modified magnetic configuration, while the beam current is almost unaffected. The glitch rates obtained are still higher than the goal, even for low RF powers. But, improving the electron dumping location leads to lower glitch rates, so the hypothesis is that reducing the total co-extracted electron current will also lead to a lower glitch rate. This will be studied in the following section.

5.3.6 Magnetic Filtering

The analysis with the RADIS ion source presented in Section 5.3.4 revealed that increasing the magnetic filter field strength leads to an important reduction in the glitch rate when the ion source was operated with acetylene. This section will focus on the study of the magnetic filter field in the RF-powered RF ion source. The goal is to understand how the electrons are affected by the magnetic filter field and to be able to predict which magnetic configuration will lead to the largest reduction in co-extracted electrons, while not affecting the total negative ion beam current out of the ion source.

The TRIUMF licensed volume-cusp ion source has a permanent magnet filter configuration, so the filter field can only be modified in discreet steps and the ion source has to be disassembled to modify the magnetic filter field. An example of how the magnetic field configuration can be modified to increase the magnetic filter

151

effect is presented in Figure 5.21.
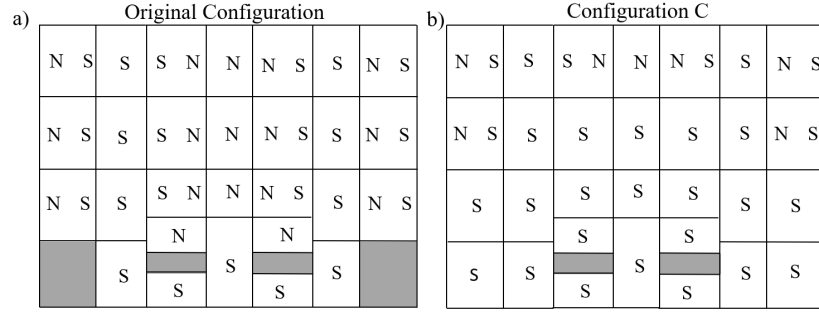
Figure 5.21: a) Schematic of the original and b) a modified permanent magnet configuration in the TRIUMF ion source. The schematic depicts only half of the circumference with the bottom of the schematic corresponding to the plasma electrode end. The opposite magnetic configuration is found on the opposite side of the plasma chamber, forming a dipole.

Several magnetic field configurations were simulated in Opera [129]. The y component of the magnetic field (B_y) along the central axis of the ion source was calculated and is presented in Figure 5.22 for the various configurations tested. The magnetic field configurations were later measured on a translation bench with a Hall probe, with good agreement between the simulations and the measurements.
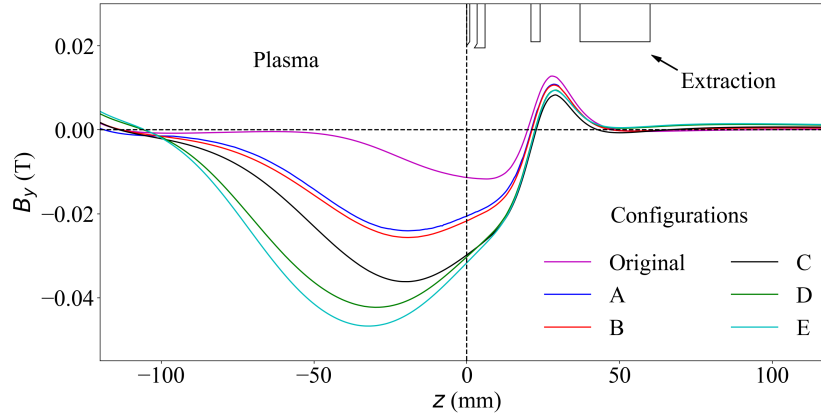
Figure 5.22: Measured B_y for the various magnetic configurations tested. The $z = 0$ corresponds to the location of the plasma electrode and the negative z represent the inside of the ion source while the positive z values depict the extraction region.

As can be seen, the configurations tested have an increasingly larger and longer magnetic dipole, which is expected will reduce the co-extracted electron current. The integral of B_y inside the plasma chamber ($z = 0$ mm to $z = -100$ mm) for the various configurations is presented in Table 5.3 to quantify the strength of the dipoles.

Configuration	Field Integral (T·mm)
Original	0.46
A	1.52
B	1.94
C	2.60
D	3.29
E	3.61

Table 5.3: Various magnetic configurations studied.

To study the effect of the magnetic field configuration on the electron trajectories, electron tracking simulations were undertaken to determine how the electrons are distributed in the plasma chamber and how the magnetic filter field affects the trajectories of the electrons. To simulate the trajectories of the electrons, 5000 electrons were generated randomly in the ion source's plasma chamber. The particles'

153

initial velocities were chosen to follow a Maxwell-Boltzmann distribution with a temperature of 3 eV, which is similar to the value obtained with Langmuir probe measurements in Figure 4.29, and the initial direction of travel was set randomly. The particles were tracked for 1 μs, or until the particles hit one of the plasma chamber's surfaces, and the time step was set at 1 ns. Figure 5.23 presents the location of the collisions on the outer surface of the ion source for a simulation with 5000 electrons in the original magnetic configuration. In Figure 5.23, the collision locations are compared to burn marks seen in the ion source.
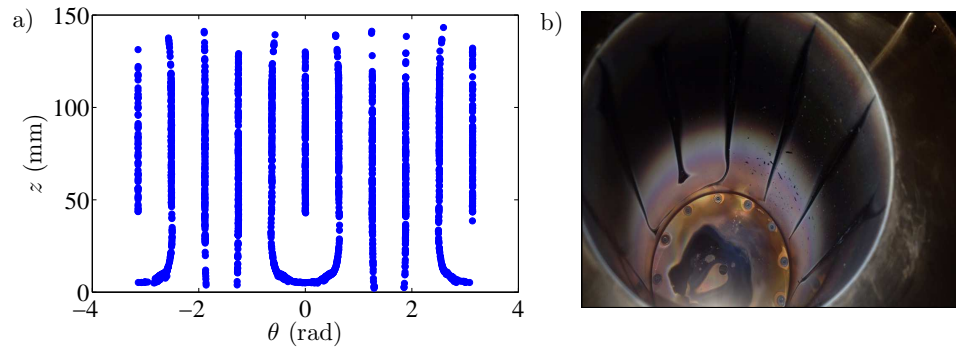
Figure 5.23: a) Simulated collision location on the cylindrical plasma chamber wall obtained with electron tracking through the standard configuration magnetic field. The angle $\theta = 0$ is chosen as the x axis. b) Photograph of the burn marks in the plasma chamber.

From Figure 5.23, the electron tracking simulations properly predict where the electrons collide with the plasma chamber walls. However, the simulation does not include collisions which have an important effect on the electron trajectories. Collisions allow electrons to drift across the magnetic field lines.

From the simulations, it is possible to obtain the electron density at various points in the ion source. The electron density was calculated along z by measuring the total number of intersections with planes along the central axis of the plasma chamber, giving a prediction of the electron density along the z axis of the ion source. This will give an indication of the effectiveness of the magnetic filter field at reducing the electron density in close to the plasma electrode. The results are

presented in Figure 5.24.
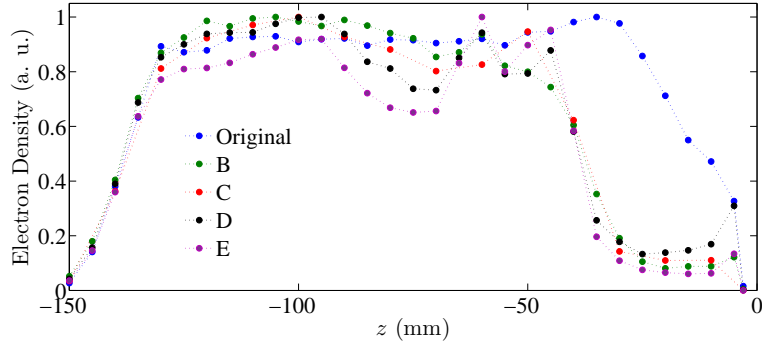
Figure 5.24: Electron density along the plasma chamber for various magnetic field configurations as calculated with electron tracking simulations. 5000 electrons with an initial temperature of 3 eV were used for the simulations, the plasma electrode is at $z = 0$ and the back plate is at $z = -150$.

From Figure 5.24, the increase in the magnetic filter field has a significant effect on the electron distribution close to the plasma electrode. For every configuration with a larger magnetic field integral than the original configuration there is large decrease in the electron density between 5 mm and 40 mm from the plasma electrode. The electron density at the plasma electrode is expected to be incrementally lower with every incremental increase in the magnetic field integral. However, the simulations predict that most of the configurations have a similar electron density distribution. When the motion of individual electrons in magnetic field configuration that have a larger filter field strength than the original configuration is analyzed, one sees that there is a strong magnetic mirror effect everywhere the field is above a threshold value of about 100 Gauss.

From Figure 5.22, there is a large increase in the distance in the magnetic field area away from the plasma electrode for configurations A to E. This can be seen by looking at a cross-sectional view of the electron density in the ion source. Figure 5.25 presents *zy* cross sections of the electron density for two magnetic configurations.

155
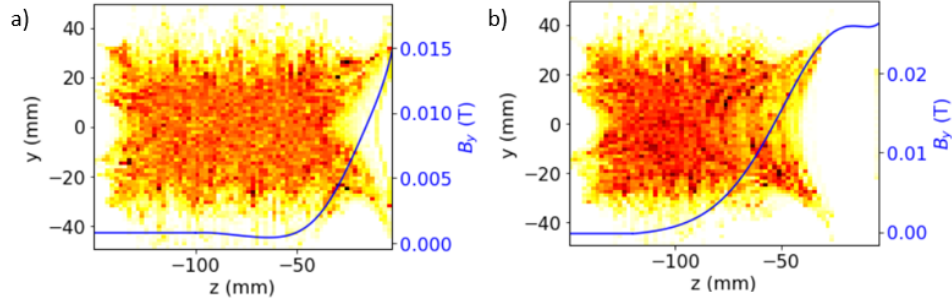
Figure 5.25: *zy* cross section of the simulated electron density with a) the original magnetic configuration and b) magnetic configuration B. The magnetic field on axis is overlaid on both plots. The plasma electrode is at $z = 0$ and the back plate is at $z = -150$.

From Figure 5.25, the electrons follow the magnetic filter field lines and this creates a low electron density area close to the plasma electrode. The low electron density region is larger when the filter field extends deeper into the plasma chamber ($z < -20$ mm). However, the analysis is incomplete since the simulation does not take into account the collisions between the particles. The multiple collisions would allow more electrons to drift across the magnetic filter and reach the plasma electrode. This would lead to a much higher electron density close to the plasma electrode for every magnetic configuration.

To test the simulations, magnetic field configurations were implemented in the ion source and the electron density was measured along z in the plasma chamber. To measure the electron density in the plasma, the Langmuir probe, as described in Section B.4.9, was used. A probe with a 5 mm tip length and 1.6 mm tip diameter was inserted in the plasma through the extraction aperture while the ion source and the electrodes were not biased. A plasma was generated in the plasma chamber with 600 W of RF power and with 20 sccm of gas flow. The results of the measurements are presented in Figure 5.26.

From Figure 5.26, for the original magnetic configuration, the electron density decreases slightly from the plasma electrode, while an increase in the electron density was expected from the simulations. For magnetic configurations B and D, the electron density is lower close to the plasma electrode than it was for the original configuration. The electron density is also relatively constant up to 40 mm for
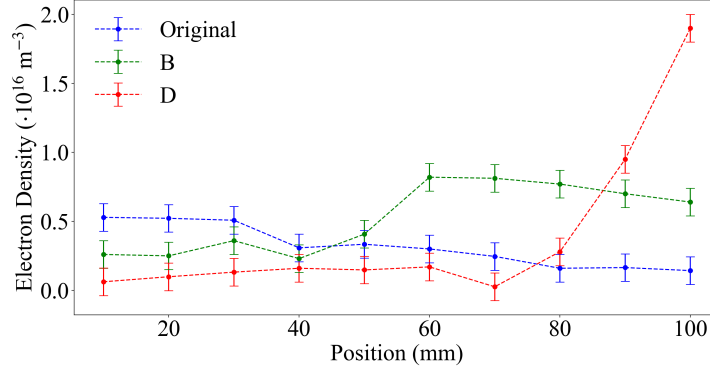
Figure 5.26: Electron density along the plasma chamber for various magnetic field configurations as measured with the Langmuir probe. The RF power was set at 600 W and the acetylene gas flow was set at 20 sccm. A position of 0 mm corresponds to the plasma electrode

configuration B and up to 70 mm for configuration D. From the simulation results presented in Figure 5.24, the electron density was expected to only be low up to about 40 mm for both configurations B and D. The difference between the Langmuir probe results and the simulation is explained by the lack of electron collisions in the simulations. Electron collisions allow the electrons to drift across the magnetic field lines, creating a higher electron density close to the plasma electrode.

From Figure 5.26, the larger magnetic filter field does indeed reduce the electron density close to the plasma electrode. This is what was to be achieved because a decrease in the co-extracted electron current is needed to achieve a lower glitch rate.

The performance of the ion source with acetylene was tested with the various magnetic fields of Figure 5.22. The total beam current, co-extracted electron current and glitch rate as a function of the RF power is presented in Figure 5.27.

From Figure 5.27b, the increased magnetic filter field reduces the co-extracted electron current as predicted and, from Figure 5.27c, the glitch rate is in general lower with the larger fields. The exception to this is configuration E, which has the lowest co-extracted electron current but does not have the lowest glitch rate. Further IBSimu simulations need to be performed to determine whether improper
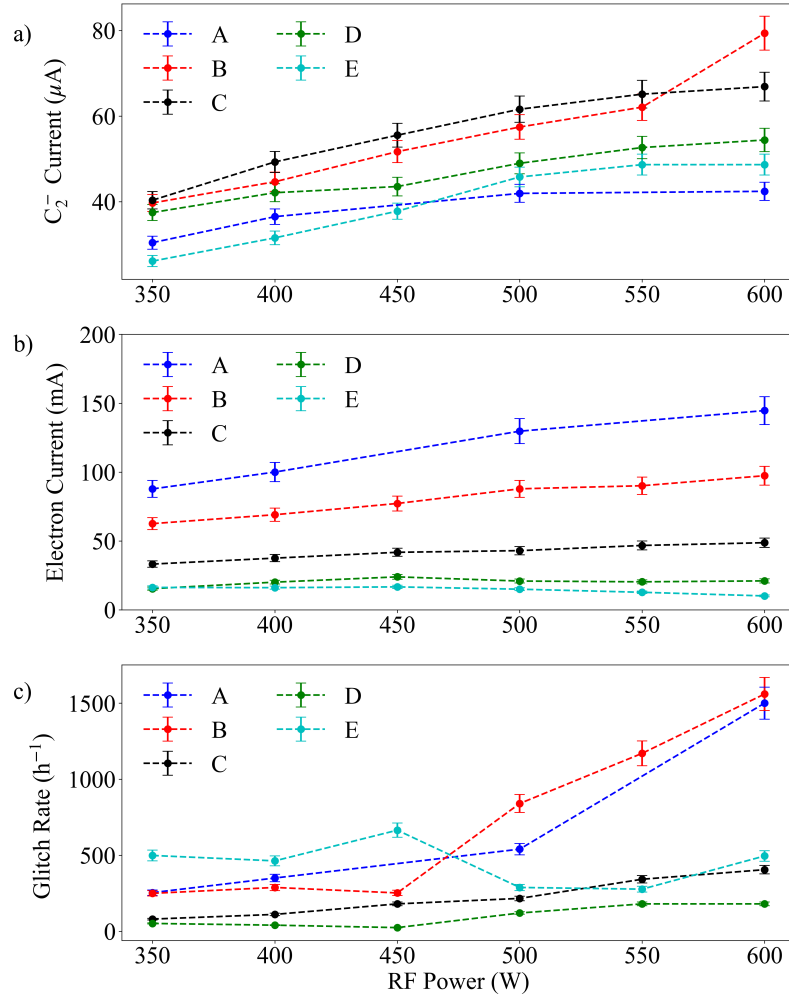
Figure 5.27: a) Total beam current, b) co-extracted electron current and c) glitch rate as a function of the RF power for various magnetic configurations. The bias was set at 10 kV and the gas flow was set at 20 sccm.

electron dumping is causing the high glitch rates seen. The optimum magnetic field configuration to reduce the glitch rate was configuration D. The field strength is large enough to reduce the co-extracted electron current, but not too strong as to impede the dumping of the electrons, as was seen with configuration E. The glitch rate was lowest for configuration D, with glitch rates of less than 50 glitches per

hour achieved for RF power of less than 500 W, which is the best glitch rate that could be achieved.

The C_2^- beam current is also highly affected by the magnetic filter field strength. There seems to be an optimum magnetic dipole field strength for configuration C. The optimum magnetic filter field strength for the production of negative carbon ions is combines the optimum electron temperature (about 2.5 eV [83]) while maximizing the electron density to maximize the frequency of negative ion production reactions. For configuration D, which is the optimum magnetic configuration to reduce the glitch rate, the production of C_2^- is not optimize, with a maximum C_2^- current of 48 μA obtained.

The study done to reduce the glitch rate led to a great decrease in the glitch rate seen. Unfortunately, the best glitch rate obtained is still higher than the goal of less than 10 glitches per hour, and the C_2^- beam current extracted with this configuration was of less than 50 μA, which is an order of magnitude from the semiconductor implantation goal of 0.5 mA of C_2^-.

5.4   Conclusion

The newly developed hybrid RF-powered ion source is a valid option for ion implantation application since it does not use any low affinity metals like cesium and it does not have any metal contamination from filaments. Acetylene was used in the RF-powered ion source and a maximum beam current of 0.27 mA of C_2^- was extracted. However, the stability of the extraction was poor, giving a glitch rate of more than 1500 glitches per hour. The stability of the ion source is the limiting factor in increasing the beam current, thus reducing the glitch rate is the most important aspect of the ion source.

Several experiments were completed to identify the nature of the voltage breakdowns seen on the extraction electrode and to determine how the glitch rate could be reduced. Increasing the aperture size of the extraction electrode and reducing the bias voltage on the ion source significantly reduces the glitch rate. Additionally, modifying the magnetic field in the ion source and in the extraction system reduced the co-extracted electron current and improved the dumping of the electrons, which led to a further reduction of the glitch rate. About 50 glitches per hour

159

could be achieved with the modifications to the ion source, which is higher than the goal but considerably lower than the initial results. Furthermore, the extracted C_2^- beam current was 50 μA with the new configuration, which is considerably lower than the goal set. The work done to improve the stability of the extraction of the negative carbon beam was the subject of a poster presentation at the Negative Ion Beams and Source conference in September 2018 [33].

Chapter 6

Conclusion

The purpose of this Thesis work was to develop a negative carbon ion source to be used for ion implantation in implanters that utilize tandem accelerators to accelerate the ions to their final energy. The main drawback of the ion sources currently used is that they rely on low affinity metals, such as cesium, to produce the negative ions. The use of these metals poses a contamination risk to the wafers that are implanted, as the metals can migrate through the system. Volume-cusp ion sources were identified as a good candidate to replace the current technology as these ion sources do not rely on the use of low electron affinity metals and reliably produce several milli-amperes of H^- ions. The Thesis work thus focused on the study of the production and the extraction of negative carbon ion beams from volume-cusp ion sources. The goal was to achieve up to 1 mA of C^- or 0.5 mA of C_2^-, with an energy between 10 keV and 30 keV, a beam stability of less than 10 glitches per hour and a normalized emittance of less than 1 mm·mrad.

To complete this study, a test facility that allows for the proper study of the beam characteristics and the plasma in the ion source had to be designed and developed. The Ion Source Test Facility (ISTF) was commissioned as a first step of the work. The facility allows for ion sources to be tested up to an energy of 30 keV, and the beam diagnostic devices include an emittance scanner, a mass spectrometer and a Faraday cup. To study the plasma in the ion source, a Langmuir probe system and an optical emission spectroscopy system were developed as part of this Thesis. The ISTF was commissioned with a filament-powered H^- volume-cusp ion source

licensed from TRIUMF, which was shown to produce up to 18 mA of H^- beam current.

The filament-powered ion source was the first ion source studied for the extraction of negative carbon ions. Multiple gases were identified as potential candidates to be used as the injection into the ion source to produce the high negative carbon ion current needed for the ion implanter application. Acetylene proved to yield the highest current of C_2^-, and no other gas yielded considerable amounts of C^- or C_2^-. Up to 0.1 mA of C_2^- current could be extracted out of the filament-powered ion source, which is 20% of the goal. The beam current was found to be limited by the beam stability and not the power into the plasma, which indicates that higher beam currents could be achieved if the beam stability can be improved. The beam stability issue arises from frequent electrical breakdowns on the extraction electrode which led to glitch rates of more than 1000 glitches per hour, which is more than 2 orders of magnitude higher than the Thesis goal of less than 10 glitches per hour. Furthermore, the filament-powered technology used is inadequate for the target ion implanter application as the filament introduces a metal impurity into the plasma chamber, as can be seen by the sputtered tantalum coating on the plasma chamber walls after operation.

The contamination issue seen with the filament-powered ion source led to the development of an RF-powered ion source that uses an external antenna, since there are no contaminants introduced into the plasma chamber with these ion sources. The RF-powered ion source developed is a hybrid design between the TRIUMF licensed volume-cusp ion source and the RADIS ion source developed by the University of Jyväskylä. The ion source uses the RF antenna and backplate system of the RADIS ion source coupled to the body and extraction system of the TRIUMF ion source. The development work was undertaken with H^-, and up to 8 mA were extracted at an RF power of 4 kW, which is a considerable increase in H^- beam current when compared to the 1.5 mA that was achieved with the RADIS ion source, upon which the new RF ion source design is based. The beam current to power efficiency of the RF-powered ion source is lower than the filament-powered version, and the difference is due to the lack of confinement in the back plate of the RF ion source, to the absence of a tantalum coating on the plasma chamber walls and to RF power losses outside of the plasma chamber. Modifications to the

162

RF-powered ion source showed that the addition of confinement on the back of the plasma chamber and the addition of a thin tantalum coating on the plasma chamber walls improved the performance of the ion source with more than 10 mA of H^- extracted from the ion source.

Since the RF-powered ion source developed does not use any consumable parts that could contaminate the system, the ion source is a good candidate for the extraction of negative ions for ion implantation applications. Up to 0.27 mA of C_2^- was extracted when the RF ion source was used with acetylene. As with the filament-powered ion source, the beam current was limited by beam stability and not by the input power into the plasma. There were frequent voltage breakdowns on the extraction electrode, which led to high glitch rates, so the study focused on reducing the glitch rate caused by the unstable extraction system. The glitch rate was significantly reduced by changing the size of the apertures, increasing the magnetic filter field to reduce the co-extracted electron current, reducing the bias voltage and improving the electron dumping. A glitch rate of less than 50 glitches per hour could be achieved, but the C_2^- current was of only 50 μA with this extraction configuration.

The final results obtained for the lowest glitch rate configuration are presented in Table 6.1 along with the initial goals.

Parameter	Value Desired	Value Obtained
Beam Current	1 particle· mA of carbon (1 mA of C^- or 0.5 mA of C_2^-)	0.05 mA of C_2^-
Beam Kinetic Energy	10-30 keV	10 keV
Normalized 4 RMS Emittance	<1.0 mm·mrad	0.71 mm·mrad
Beam Current Stability	$< \pm 0.5\%$	$\pm 0.1\%$
Glitch Rate	< 10/hour	$\sim$ 50/hour
Metal Vapour Contamination	0	0

Table 6.1: Goals and values achieved for the negative carbon volume-cusp ion source.

From Table 6.1, the goals for the negative carbon ion source that was developed were not all met. However, significant improvements to the stability of the ion source were made and important insights into the production of negative carbon

163

ions, such as the production mechanisms and the optimum ion source magnetic configuration, were gained through this Thesis work. Furthermore, the work led to the development of an RF-powered ion source that produces high H^- current densities and is a significant improvement to the ion source on which it was based. Since the ion source does not have any consumable parts, the lifetime of the ion source is substantially longer than filament-powered ion sources, and it is thus an interesting option for H^- applications, such as cyclotrons that use an external injection system and Boron Neutron Capture Therapy (BNCT) applications.

For the developed negative carbon ion source to be used for ion implantation, the stability of the extraction system will have to be further improved so the input power, and thus the beam current, can be increased. The extraction system should be re-designed using the findings of this study, which includes testing different materials, further increasing the size of the apertures and experimenting with the configuration of the insulators between the electrodes. Additionally, the materials used in the ion source would also have to be changed to further reduce the contamination risk in the ion implanter. The copper plasma chamber walls and electrodes should also be replaced to materials that are less prone to sputtering, such as tantalum or graphite. Finally, the long-term performance of the ion source should then be tested to determine how the carbon deposits in the plasma chamber affect the RF power transmission into the plasma chamber and how it influences the stability of the extraction system.

The most pressing development to the RF-powered H^- ion source is the cooling of the RF window to prevent window failures and increase the power to the full 5 kW of the RF amplifier and thus increase the beam current. In addition, further developments include experimenting with a tantalum plasma chamber and plasma electrode, as this study showed that tantalum sputtered onto copper led to a 25% increase in beam current. Using tantalum instead of copper could also lead to a reduction in the sputtered material on the AlN window, as the copper walls could be detrimental to the performance of the ion source after a prolonged period. Additionally, experiments on the dimensions of the ion source's plasma chamber should be undertaken, as the theoretical study of inductively heated plasmas showed that the power density in the plasma is concentrated close to the RF window. A shorter plasma chamber might lead to a more efficient production of H^- ions as the popu-

lation of vibrationally excited H_2 would be higher close to the extraction region of the ion source. Finally, long term tests with the RF ion source will also have to be completed before the ion source can be used for an industrial application.

Bibliography

[1] O. Barbalat, "Applications of particle accelerators," tech. rep., CERN, 1994. → page 1

[2] G. Aad, T. Abajyan, B. Abbott, J. Abdallah, S. A. Khalek, A. Abdelalim, O. Abdinov, R. Aben, B. Abi, M. Abolins, *et al.*, "Observation of a new particle in the search for the standard model higgs boson with the atlas detector at the lhc," *Physics Letters B*, vol. 716, no. 1, pp. 1–29, 2012. → page 1

[3] U. Amaldi, "The importance of particle accelerators," *europhysics news*, vol. 31, no. 6, pp. 5–9, 2000. → page 1

[4] S. Al-Salem, P. Lettieri, and J. Baeyens, "Recycling and recovery routes of plastic solid waste (psw): A review," *Waste management*, vol. 29, no. 10, pp. 2625–2643, 2009. → page 1

[5] B. P. Fairand, *Radiation sterilization for health care products: x-ray, gamma, and electron beam*. CRC Press, 2001. → page 1

[6] I. Kato, K. Ono, Y. Sakurai, M. Ohmae, A. Maruhashi, Y. Imahori, M. Kirihata, M. Nakazawa, and Y. Yura, "Effectiveness of bnct for recurrent head and neck malignancies," *Applied Radiation and Isotopes*, vol. 61, no. 5, pp. 1069–1073, 2004. → page 1

[7] S. Felch, M. Current, and M. Taylor, "Ion implantation for semiconductor devices: The largest use of industrial accelerators," in *Proceedings of the North American Particle Accelerator Conference*, p. 740, 2013. → pages 1, 2, 4

[8] J. F. Gibbons, "Ion implantation in semiconductors—part i: Range distribution theory and experiments," *Proceedings of the IEEE*, vol. 56, no. 3, pp. 295–319, 1968. → page 1

[9] P. K. Chu, S. Qin, C. Chan, N. W. Cheung, and L. A. Larson, "Plasma immersion ion implantation—a fledgling technique for semiconductor processing," *Materials Science and Engineering: R: Reports*, vol. 17, no. 6-7, pp. 207–280, 1996.

[10] J. Williams, "Ion implantation of semiconductors," *Materials Science and Engineering: A*, vol. 253, no. 1, pp. 8–15, 1998. → pages 1, 4

[11] J. Ishikawa, "Negative-ion sources for modification of materials," *Review of scientific instruments*, vol. 67, no. 3, pp. 1410–1415, 1996. → page 1

[12] E. Cottereau, J. Camplan, J. Chaumont, R. Meunier, and H. Bernas, "Aramis: An ambidextrous 2 mv accelerator for iba and mev implantation," *Nuclear Instruments and Methods in Physics Research Section B: Beam Interactions with Materials and Atoms*, vol. 45, no. 1-4, pp. 293–295, 1990.

[13] A. Taylor, J. R. Wallace, E. A. Ryan, A. Philippides, and J. R. Wrobel, "In situ implantation system in argonne national laboratory hvem-tandem facility," *Nuclear Instruments and Methods in Physics Research*, vol. 189, no. 1, pp. 211–217, 1981. → page 1

[14] S. Chang, V. Chavva, and F. Sinclair, "True zero degree incident implants on viista3000," in *AIP Conference Proceedings*, vol. 1321, pp. 357–360, AIP, 2011. → pages 2, 189

[15] K. Shinto, H. Sugawara, M. Takenaga, S. Takeuchi, N. Tanaka, A. Okamoto, S. Kitajima, M. Sasao, M. Nishiura, and M. Wada, "Optimization of a compact multicusp he+ ion source for double-charge-exchanged he- beam," *Review of scientific instruments*, vol. 77, no. 3, p. 03B512, 2006. → page 2

[16] E. Hooper Jr, P. Pincosy, P. Poulsen, C. Burrell, L. Grisham, and D. Post, "High current source of he- ions," *Review of Scientific Instruments*, vol. 51, no. 8, pp. 1066–1070, 1980. → page 2

[17] S. Chang, B. Gori, C. Norris, J. Klein, and K. Decker-Lucke, "High energy hydrogen and helium ion implanter," in *Ion Implantation Technology (IIT), 2014 20th International Conference on*, pp. 1–4, IEEE, 2014. → pages 2, 189

[18] R. Van de Graaff, "Tandem electrostatic accelerators," *Nuclear Instruments and Methods*, vol. 8, no. 2, pp. 195–202, 1960. → page 2

167

[19] M. I. Current, "Ion implantation for fabrication of semiconductor devices and materials," in *Industrial Accelerators and Their Applications*, pp. 9–56, World Scientific, 2012. $\rightarrow$ page 2

[20] J. F. Ziegler, *Handbook of ion implantation technology*. North-Holland, 1992. $\rightarrow$ page 3

[21] B. Han, K. Von Reden, M. L. Roberts, R. J. Schneider, J. M. Hayes, and W. Jenkins, "Electromagnetic field modeling and ion optics calculations for a continuous-flow ams system," *Nuclear Instruments and Methods in Physics Research Section B: Beam Interactions with Materials and Atoms*, vol. 259, no. 1, pp. 111–117, 2007. $\rightarrow$ page 3

[22] "D-Pace dehnel particle accelerator components and engineering." http://www.d-pace.com. $\rightarrow$ pages 3, 197

[23] T. Kuo, D. Yuan, K. Jayamanna, M. McDonald, R. Baartman, P. Schmor, and G. Dutto, "On the development of a 15 ma direct current h- multicusp source," *Review of scientific instruments*, vol. 67, no. 3, pp. 1314–1316, 1996. $\rightarrow$ pages 3, 4, 7, 45, 142, 197, 198, 203, 205, 206, 212, 213, 222, 231, 232, 233, 234, 236

[24] V. R. Chavva, K.-H. Shim, and T. Henry, "Dark current reduction in image sensors through metals gettering: A critical review of disruptive techniques," in *2013 International Image Sensor Workshop*, 2013. $\rightarrow$ page 4

[25] S. Kim, R. Schneider, K. Von Reden, J. Hayes, and J. Wills, "Test of negative ion beams from a microwave ion source with a charge exchange canal for accelerator mass spectrometry applications," *Review of scientific instruments*, vol. 73, no. 2, pp. 846–848, 2002. $\rightarrow$ page 4

[26] K. P. Regan, "Method and apparatus for arc suppression in scanned ion beam processing equipment," Mar. 18 2008. US Patent 7,345,856. $\rightarrow$ page 4

[27] S. Melanson, M. Dehnel, C. Hollinger, P. Jackle, T. Jones, J. Martin, H. McDonald, C. Philpott, D. Potkins, T. Stewart, *et al.*, "The production of negative carbon ions with a volume cusp ion source," in *7th International Particle Accelerator Conference (IPAC'16), Busan, Korea, May 8-13, 2016*, pp. 2620–2622, JACOW, Geneva, Switzerland, 2016. $\rightarrow$ pages 6, 7, 70

[28] S. Melanson, M. Dehnel, D. Potkins, H. McDonald, C. Hollinger, J. Theroux, J. Martin, T. Stewart, P. Jackle, C. Philpott, *et al.*, "The extraction of negative carbon ions from a volume cusp ion source," in *AIP Conference Proceedings*, vol. 1869, p. 040001, AIP Publishing, 2017. → pages 6, 7, 70

[29] T. Kalvas, O. Tarvainen, J. Komppula, H. Koivisto, J. Tuunanen, D. Potkins, T. Stewart, and M. Dehnel, "Power efficiency improvements with the radio frequency h- ion source," *Review of Scientific Instruments*, vol. 87, no. 2, p. 02B102, 2016. → pages 6, 7, 72, 93, 96, 97

[30] T. Kalvas, O. Tarvainen, J. Komppula, H. Koivisto, J. Tuunanen, D. Potkins, T. Stewart, and M. Dehnel, "A cw radiofrequency ion source for production of negative hydrogen ion beams for cyclotrons," in *AIP Conference Proceedings*, vol. 1655, p. 030015, AIP Publishing, 2015. → pages 6, 7, 72, 73, 74, 80, 90, 96

[31] D. Faircloth and S. Lawrie, "An overview of negative hydrogen ion sources for accelerators," *New Journal of Physics*, vol. 20, no. 2, p. 025007, 2018. → pages 7, 97, 100, 123

[32] O. Tarvainen and S. Peng, "Radiofrequency and 2.45 ghz electron cyclotron resonance h- volume production ion sources," *New Journal of Physics*, vol. 18, no. 10, p. 105008, 2016. → pages 7, 97, 100, 123

[33] S. Melanson, D. Potkins, H. McDonald, C. Philpott, , and M. Dehnel, "Beam current stability improvements of negative carbon ions extraction from a multi-cusp ion source," in *AIP Conference Proceedings*, AIP Publishing, 2019. → pages 7, 160

[34] R. J. Goldston and P. H. Rutherford, *Introduction to plasma physics*. CRC Press, 1995. → pages 8, 10, 14, 15, 19, 20, 181, 182, 183, 184, 188

[35] I. G. Brown, *The physics and technology of ion sources*. John Wiley & Sons, 2004. → pages 9, 11

[36] T. Kalvas, "Beam extraction and transport," *arXiv preprint arXiv:1401.3951*, 2014. → pages 8, 33

[37] H. Rucker, "Introduction to plasma physics," *Austria: Karl-Franzens-University Graz*, 2007. → pages 8, 9, 10, 11, 12

[38] R. Aymar, P. Barabaschi, and Y. Shimomura, "The iter design," *Plasma physics and controlled fusion*, vol. 44, no. 5, p. 519, 2002. → page 9

[39] D. B. Graves, "Plasma processing," *IEEE transactions on Plasma Science*, vol. 22, no. 1, pp. 31–42, 1994. → page 9

[40] B. Wolf, *Handbook of ion sources*. CRC press, 2017. → pages 9, 10, 12, 13, 17, 18, 32

[41] E. W. McDaniel, "Collision phenomena in ionized gases," 1964. → page 11

[42] M. Shah, D. Elliott, and H. Gilbody, "Pulsed crossed-beam study of the ionisation of atomic hydrogen by electron impact," *Journal of Physics B: Atomic and Molecular Physics*, vol. 20, no. 14, p. 3501, 1987. → page 12

[43] M. Shah, D. Elliott, P. McCallion, and H. Gilbody, "Single and double ionisation of helium by electron impact," *Journal of Physics B: Atomic, Molecular and Optical Physics*, vol. 21, no. 15, p. 2751, 1988. → pages 12, 190

[44] M. Bacal and M. Wada, "Negative hydrogen ion production mechanisms," *Applied physics reviews*, vol. 2, no. 2, p. 021305, 2015. → pages 13, 111, 190, 248, 249

[45] J. Hiskes, "Cross sections for the vibrational excitation of the h2 x 1σ+ g (v) levels generated by electron collisional excitation of the higher singlet states," *Journal of applied physics*, vol. 70, no. 7, pp. 3409–3417, 1991. → page 13

[46] M. Bacal, A. Hatayama, and J. Peters, "Volume production negative hydrogen ion sources," *IEEE Transactions on Plasma Science*, vol. 33, no. 6, pp. 1845–1871, 2005. → pages 14, 23, 24, 25, 59

[47] J. Hiskes, "Formation of hydrogen negative ions by surface and volume processes with application to negative ion sources," *Le Journal de Physique Colloques*, vol. 40, no. C7, pp. C7–179, 1979. → pages 14, 25, 190

[48] → pages 14, 186, 187

[49] J. W. Gewartowski and H. A. Watson, *Principles of electron tubes: including grid-controlled tubes, microwave tubes, and gas tubes*. van Nostrand, 1965. → page 16

[50] C. Crowell, "The richardson constant for thermionic emission in schottky barrier diodes," *Solid-State Electronics*, vol. 8, no. 4, pp. 395–399, 1965. → page 16

[51] D. Leitner, C. Lyneis, S. Abbott, D. Collins, R. Dwinell, M. Galloway, M. Leitner, and D. Todd, "Next generation ecr ion sources: First results of the superconducting 28 ghz ecris–venus," *Nuclear Instruments and Methods in Physics Research Section B: Beam Interactions with Materials and Atoms*, vol. 235, no. 1-4, pp. 486–493, 2005. → page 18

[52] K. Halbach, "Permanent magnets for production and use of high energy beams," in *Proceedings of the 8th International Workshop on Rare-earth Permanent Magnets*, pp. 123–136, 1985. → page 21

[53] F. Zimmermann, "Cern upgrade plans for the lhc and its injectors," tech. rep., CERN, 2009. → page 21

[54] A. W. Chao, K. H. Mess, M. Tigner, and F. Zimmermann, *Handbook of accelerator physics and engineering*. World Scientific, 1999. → page 21

[55] R. Geller, *Electron cyclotron resonance ion sources and ECR plasmas*. CRC Press, 1996. → page 21

[56] V. Mishin, V. Fedoseyev, H.-J. Kluge, V. Letokhov, H. Ravn, F. Scheerer, Y. Shirakabe, S. Sundell, O. Tengblad, I. Collaboration, *et al.*, "Chemically selective laser ion-source for the cern-isolde on-line mass separator facility," *Nuclear Instruments and Methods in Physics Research Section B: Beam Interactions with Materials and Atoms*, vol. 73, no. 4, pp. 550–560, 1993. → page 21

[57] P. Franzen, H. Falter, U. Fantz, W. Kraus, M. Berger, S. Christ-Koch, M. Fröschle, R. Gutser, B. Heinemann, S. Hilbert, *et al.*, "Progress of the development of the ipp rf negative ion source for the iter neutral beam system," *Nuclear fusion*, vol. 47, no. 4, p. 264, 2007. → page 23

[58] J. Lettry, D. Aguglia, Y. Coutron, E. Chaudet, A. Dallocchio, J. Gil Flores, J. Hansen, E. Mahner, S. Mathot, S. Mattei, *et al.*, "H- ion sources for cern's linac4," in *AIP Conference Proceedings*, vol. 1515, pp. 302–311, AIP, 2013. → page 23

[59] D. Findlay, "Isis-pulsed neutron and muon source," in *Particle Accelerator Conference, 2007. PAC. IEEE*, pp. 695–699, IEEE, 2007.

[60] T. Mason, D. Abernathy, I. Anderson, J. Ankner, T. Egami, G. Ehlers, A. Ekkebus, G. Granroth, M. Hagen, K. Herwig, *et al.*, "The spallation neutron source in oak ridge: A powerful tool for materials research," *Physica B: Condensed Matter*, vol. 385, pp. 955–960, 2006. → page 23

[61] W. Grüebler, V. König, and P. Schmelzbach, "Source of polarized negative hydrogen ions for a tandem accelerator," *Nuclear Instruments and Methods*, vol. 86, no. 1, pp. 127–139, 1970. → page 23

[62] L. Collins and A. Riviere, "A negative hydrogen ion injector for a tandem electrostatic accelerator," *Nuclear Instruments and Methods*, vol. 4, no. 3, pp. 121–128, 1959. → page 23

[63] T. Andersen, H. Haugen, and H. Hotop, "Binding energies in atomic negative ions: Iii," *Journal of Physical and Chemical Reference Data*, vol. 28, no. 6, pp. 1511–1533, 1999. → page 24

[64] K. Leung, C. Hauck, W. Kunkel, and S. Walther, "Optimization of h-production from a small multicusp ion source," *Review of Scientific Instruments*, vol. 60, no. 4, pp. 531–538, 1989. → page 24

[65] M. Stockli, "Volume and surface-enhanced volume negative ion sources," *arXiv preprint arXiv:1404.0943*, 2014.

[66] M. Hanada, T. Inoue, H. Kojima, Y. Matsuda, Y. Ohara, Y. Okumura, K. Watanabe, and M. Seki, "A 14 cm× 36 cm volume negative ion source producing multi-ampere h- ion beams," *Review of Scientific Instruments*, vol. 61, no. 1, pp. 499–501, 1990. → page 24

[67] S. Hahto, S. Hahto, J. Kwan, K. Leung, and L. Grisham, "Negative chlorine ions from multicusp radio frequency ion source for heavy ion fusion applications," *Review of scientific instruments*, vol. 74, no. 6, pp. 2987–2991, 2003. → page 24

[68] S. Walther, K. Leung, and W. Kunkel, "Volume production of li- in a small multicusp ion source," *Applied physics letters*, vol. 51, no. 8, pp. 566–568, 1987. → page 24

[69] M. Sasao, H. Yamaoka, M. Wada, and J. Fujita, "Direct extraction of a na- beam from a sodium plasma," *Nuclear Instruments and Methods in Physics Research Section B: Beam Interactions with Materials and Atoms*, vol. 55, no. 1-4, pp. 318–322, 1991. → page 24

[70] Q. Ji, T.-J. King, K.-N. Leung, and S. Wilde, "Production of various species of focused ion beam," *Review of scientific instruments*, vol. 73, no. 2, pp. 822–824, 2002. → page 24

[71] R. K. Janev, D. Reiter, and U. Samm, *Collision processes in low-temperature hydrogen plasmas*. Forschungszentrum Jülich, Zentralbibliothek, 2003. → pages 25, 27

[72] M. Bacal, A. Ivanov Jr, M. Glass-Maujean, Y. Matsumoto, M. Nishiura, M. Sasao, and M. Wada, "Contribution of wall material to the vibrational excitation and negative ion formation in hydrogen negative ion sources," *Review of scientific instruments*, vol. 75, no. 5, pp. 1699–1703, 2004. → pages 26, 27

[73] A. Ando, K. Tsumori, Y. Oka, O. Kaneko, Y. Takeiri, E. Asano, T. Kawamoto, R. Akiyama, and T. Kuroda, "Large current negative hydrogen ion beam production," *Physics of plasmas*, vol. 1, no. 9, pp. 2813–2815, 1994. → page 27

[74] R. A. Baartman and D. Yuan, "Space charge neutralization studies of an h-beam," tech. rep., Triumf, 1988. → pages 28, 43

[75] R. Becker and W. Herrmannsfeldt, "igun- a program for the simulation of positive ion extraction including magnetic fields," *Review of scientific instruments*, vol. 63, no. 4, pp. 2756–2758, 1992. → pages 29, 31

[76] J. E. Boers, "Pbguns: A digital computer program for the simulation of electron and ion beams on a pc," in *Plasma Science, 1993. IEEE Conference Record-Abstracts., 1993 IEEE International Conference on*, p. 213, IEEE, 1993. → page 31

[77] T. Kalvas, O. Tarvainen, T. Ropponen, O. Steczkiewicz, J. Ärje, and H. Clark, "ibsimu: A three-dimensional simulation software for charged particle optics a," *Review of Scientific Instruments*, vol. 81, no. 2, p. 02B703, 2010. → pages 29, 31, 39, 43, 63, 142, 218, 240, 242

[78] P. Spädtke, "Kobra3-inp user manual," *Windows version*, vol. 4, 2012. → pages 29, 31

[79] C. Child, "Discharge from hot cao," *Physical Review (Series I)*, vol. 32, no. 5, p. 492, 1911. → pages 29, 191, 192, 217

[80] E. D. Courant, M. S. Livingston, and H. S. Snyder, "The strong-focusing synchroton—a new high energy accelerator," *Physical Review*, vol. 88, no. 5, p. 1190, 1952. → page 34

[81] W. Joho, *Representation of beam ellipses for transport calculations*. Schweizerisches Institut für Nuklearforschung, 1980. → page 35

[82] A. Drentje, A. Kitagawa, and M. Muramatsu, "Experiments with fundamental aspects performed in a small ecr ion source for a new carbon therapy facility," *IEEE Transactions on Plasma Science*, vol. 36, no. 4, pp. 1502–1511, 2008. → page 46

[83] E. Szymańska, I. Čadež, E. Krishnakumar, and N. J. Mason, "Electron impact induced anion production in acetylene," *Physical Chemistry Chemical Physics*, vol. 16, no. 8, pp. 3425–3432, 2014. → pages 46, 47, 49, 50, 67, 92, 126, 130, 133, 159

[84] C. Melton and P. Rudolph, "Negative ion mass spectra of hydrocarbons and alcohols," *The Journal of Chemical Physics*, vol. 31, no. 6, pp. 1485–1488, 1959.

[85] L. Von Trepka, "L. von trepka and h. neuert, z. naturforsch. a 18, 1295 (1963).," *Z. Naturforsch. a*, vol. 18, p. 1295, 1963. → page 49

[86] J. T. Tate and P. Smith, "The efficiencies of ionization and ionization potentials of various gases under electron impact," *Physical Review*, vol. 39, no. 2, p. 270, 1932. → page 46

[87] R. Dressler and M. Allan, "A dissociative electron attachment, electron transmission, and electron energy-loss study of the temporary negative ion of acetylene," *The Journal of chemical physics*, vol. 87, no. 8, pp. 4510–4518, 1987. → page 49

[88] S. Stoykov, C. Eggs, and U. Kortshagen, "Plasma chemistry and growth of nanosized particles in a c2h2 rf discharge," *Journal of Physics D: Applied Physics*, vol. 34, no. 14, p. 2160, 2001. → page 50

[89] M. L. Roberts, R. J. Schneider, K. F. von Reden, J. Wills, B. Han, J. M. Hayes, B. E. Rosenheim, and W. J. Jenkins, "Progress on a gas-accepting ion source for continuous-flow accelerator mass spectrometry," *Nuclear Instruments and Methods in Physics Research Section B: Beam Interactions with Materials and Atoms*, vol. 259, no. 1, pp. 83–87, 2007. → page 51

[90] C. B. Ramsey, P. Ditchfield, and M. Humm, "Using a gas ion source for radiocarbon ams and gc-ams," *Radiocarbon*, vol. 46, no. 1, pp. 25–32, 2004. → page 51

[91] D. Rapp and D. D. Briglia, "Total cross sections for ionization and attachment in gases by electron impact. ii. negative-ion formation," *The Journal of Chemical Physics*, vol. 43, no. 5, pp. 1480–1489, 1965. → pages 51, 53

174

[92] J. Moruzzi and A. Phelps, "Survey of negative-ion—molecule reactions in o2, co2, h2o, co, and mixtures of these gases at high pressures," *The Journal of Chemical Physics*, vol. 45, no. 12, pp. 4617–4627, 1966. → page 51

[93] D. Spence and G. Schulz, "Cross sections for production of o 2- and c- by dissociative electron attachment in co2: An observation of the renner-teller effect," *The Journal of Chemical Physics*, vol. 60, no. 1, pp. 216–220, 1974. → pages 51, 53

[94] L. G. Smith, "Ionization and dissociation of polyatomic molecules by electron impact. i. methane," *Physical Review*, vol. 51, no. 4, p. 263, 1937. → pages 53, 55

[95] M. R. Shubaly, "Method and apparatus for generating ion beams," Dec. 22 1987. US Patent 4,714,834. → page 54

[96] M. Heintze and M. Magureanu, "Methane conversion into acetylene in a microwave plasma: optimization of the operating parameters," *Journal of applied physics*, vol. 92, no. 5, pp. 2276–2283, 2002. → pages 55, 135, 136

[97] L. A. Curtiss, P. C. Redfern, K. Raghavachari, and J. A. Pople, "Assessment of gaussian-2 and density functional theories for the computation of ionization potentials and electron affinities," *The Journal of chemical physics*, vol. 109, no. 1, pp. 42–55, 1998. → page 57

[98] S. Yang, K. Taylor, M. Craycraft, J. Conceicao, C. Pettiette, O. Cheshnovsky, and R. Smalley, "Ups of 2–30-atom carbon clusters: Chains and rings," *Chemical physics letters*, vol. 144, no. 5-6, pp. 431–436, 1988. → page 57

[99] B. Hughes, C. Lifshitz, and T. Tiernan, "Electron affinities from endothermic negative-ion charge-transfer reactions. iii. no, no2, so2, cs2, cl2, br2, i2, and c2h," *The Journal of Chemical Physics*, vol. 59, no. 6, pp. 3162–3181, 1973. → page 57

[100] R. A. Kendall, T. H. Dunning Jr, and R. J. Harrison, "Electron affinities of the first-row atoms revisited. systematic basis sets and wave functions," *The Journal of chemical physics*, vol. 96, no. 9, pp. 6796–6806, 1992. → page 57

[101] K. De Bleecker, A. Bogaerts, and W. Goedheer, "Detailed modeling of hydrocarbon nanoparticle nucleation in acetylene discharges," *Physical Review E*, vol. 73, no. 2, p. 026405, 2006. → page 64

[102] T. Kalvas, "Development and use of computational tools for modelling negative hydrogen ion source extraction systems," *Research report/Department of Physics, University of Jyväskylä no. 10/2013.*, 2013. → page 75

[103] J. Hopwood, "Planar rf induction plasma coupling efficiency," *Plasma Sources Science and Technology*, vol. 3, no. 4, p. 460, 1994. → pages 76, 77, 78, 79, 80, 107

[104] J. Hopwood, "Review of inductively coupled plasmas for plasma processing," *Plasma Sources Science and Technology*, vol. 1, no. 2, p. 109, 1992. → page 76

[105] J. D. Jackson, *Electrodynamics*. Wiley Online Library, 1975. → page 76

[106] K. Suzuki, K. Nakamura, H. Ohkubo, and H. Sugai, "Power transfer efficiency and mode jump in an inductive rf discharge," *Plasma Sources Science and Technology*, vol. 7, no. 1, p. 13, 1998. → pages 77, 105

[107] R. Piejak, V. Godyak, and B. Alexandrovich, "A simple analysis of an inductive rf discharge," *Plasma sources science and technology*, vol. 1, no. 3, p. 179, 1992. → page 78

[108] "Flat spiral coil." http://www.deepfriedneon.com/tesla_f_calcspiral.html. Accessed: 2018-10-23. → page 81

[109] T. T. Ha, "Solid-state microwave amplifier design," *New York, Wiley-Interscience, 1981. 338 p.*, 1981. → page 84

[110] S. Hyde, "Rfsim99." → page 84

[111] "Comet pct." https://www.comet-pct.com/home. → page 85

[112] M. Bacal and M. Wada, "Effect due to plasma electrode adsorbates upon the negative ion current and electron current extracted from a negative ion source," in *AIP Conference Proceedings*, vol. 1869, p. 030025, AIP Publishing, 2017. → pages 98, 255

[113] U. Fantz, H. Falter, P. Franzen, E. Speth, R. Hemsworth, D. Boilson, and A. Krylov, "Plasma diagnostic tools for optimizing negative hydrogen ion sources," *Review of scientific instruments*, vol. 77, no. 3, p. 03A516, 2006. → pages 104, 108

[114] A. E. Wendt, "Passive external radio frequency filter for langmuir probes," *Review of scientific instruments*, vol. 72, no. 7, pp. 2926–2930, 2001. → pages 105, 229

[115] M. Lombard, *SolidWorks 2013 bible*. John Wiley & Sons, 2013. → page 120

[116] G. R. Johnson, T. J. Holmquist, and S. R. Beissel, "Response of aluminum nitride (including a phase change) to large strains, high strain rates, and high pressures," *Journal of Applied Physics*, vol. 94, no. 3, pp. 1639–1646, 2003. → page 121

[117] S. Melanson, M. Dehnel, H. McDonald, C. Philpott, and D. Potkins, "H-, d-, c2-: A comparison of rf and filament-powered volume-cusp ion sources," in *8th Int. Particle Accelerator Conf.(IPAC'17), Copenhagen, Denmark, 14-19 May, 2017*, pp. 1685–1687, JACOW, Geneva, Switzerland, 2017. → page 123

[118] S. Melanson, A. George, H. McDonald, D. Potkins, C. Philpott, and M. Dehnel, "Improvements to a 13.56 mhz rf powered h- ion source," in *Int. Conf. on Ion Sources (ICIS'17), Geneva, Switzerland, 15-20 October, 2017*, 2017. → page 123

[119] P. Plessis and P. Marmet, "Electroionization study of acetylene and fragment ions," *International journal of mass spectrometry and ion processes*, vol. 70, no. 1, pp. 23–44, 1986. → page 125

[120] D. Shiner, J. Gilligan, B. Cook, and W. Lichten, "H 2, d 2, and hd ionization potentials by accurate calibration of several iodine lines," *Physical Review A*, vol. 47, no. 5, p. 4042, 1993. → page 125

[121] H. B. Michaelson, "The work function of the elements and its periodicity," *Journal of applied physics*, vol. 48, no. 11, pp. 4729–4733, 1977. → page 126

[122] H. Kawano and F. M. Page, "Experimental methods and techniques for negative-ion production by surface ionization. part i. fundamental aspects of surface ionization," *International Journal of Mass Spectrometry and Ion Physics*, vol. 50, no. 1-2, pp. 1–33, 1983. → page 126

[123] U. Fantz, H. Falter, P. Franzen, D. Wünderlich, M. Berger, A. Lorenz, W. Kraus, P. McNeely, R. Riedl, and E. Speth, "Spectroscopy—a powerful diagnostic tool in source development," *Nuclear fusion*, vol. 46, no. 6, p. S297, 2006. → pages 134, 228, 229

[124] J. Rabeau, P. John, J. Wilson, and Y. Fan, "The role of c 2 in nanocrystalline diamond growth," *Journal of Applied Physics*, vol. 96, no. 11, pp. 6724–6732, 2004. → page 135

[125] J. Han, C. Ye, M. Suto, and L. Lee, "Fluorescence from photoexcitation of c2h2 at 50–106 nm," *The Journal of Chemical Physics*, vol. 90, no. 8, pp. 4000–4007, 1989. → page 136

[126] D. Faircloth, "Technological aspects: High voltage," *arXiv preprint arXiv:1404.0952*, 2014. → page 142

[127] F. Kreuger, "Industrial high voltage: electric fields, dielectrics, constructions," *Delft University Press, Delft, The Netherlands*, 1991. → page 143

[128] *Opera-3D User Guide*. → page 149

[129] *3D Software*. → pages 152, 240

[130] T. A. Carlson, C. Nestor Jr, N. Wasserman, and J. McDowell, "Calculated ionization potentials for multiply charged ions," *Atomic Data and Nuclear Data Tables*, vol. 2, pp. 63–99, 1970. → page 183

[131] J. Ishikawa, Y. Takeiri, and T. Takagi, "Mass-separated negative-ion-beam deposition system," *Review of scientific instruments*, vol. 57, no. 8, pp. 1512–1518, 1986. → page 189

[132] L. Blau, R. Novick, and D. Weinflash, "Lifetimes and fine structure of the metastable autoionizing (1 s 2 s 2 p) p j 4 states of the negative helium ion," *Physical Review Letters*, vol. 24, no. 23, p. 1268, 1970. → page 190

[133] C. W. Schmidt and C. D. Curtis, "A 50-ma negative hydrogen-ion source," *IEEE Transactions on Nuclear Science*, vol. 26, no. 3, pp. 4120–4122, 1979. → page 190

[134] J. T. Tanabe, *Iron dominated electromagnets: design, fabrication, assembly and measurements*. World Scientific Publishing Company, 2005. → page 195

[135] T. Kuo, D. Yuan, K. Jayamanna, M. McDonald, R. Baartman, W. Gelbart, N. Stevenson, P. Schmor, and G. Dutto, "Further development for the triumf h-/d- multicusp source," *Review of scientific instruments*, vol. 69, no. 2, pp. 959–961, 1998. → pages 197, 206

[136] "BSL buckley systems." http://www.buckleysystems.co.nz. → page 198

[137] R. Kersevan, "Molflow user's guide," *available from one of the authors (RK)*, 1991. → pages xxi, 203, 204

[138] R. Kersevan and J.-L. Pons, "Introduction to molflow+: New graphical processing unit-based monte carlo code for simulating molecular flows and for calculating angular coefficients in the compute unified device architecture environment," *Journal of Vacuum Science & Technology A: Vacuum, Surfaces, and Films*, vol. 27, no. 4, pp. 1017–1023, 2009. → page 203

[139] K. Halbach, "Design of permanent multipole magnets with oriented rare earth cobalt material," *Nuclear instruments and methods*, vol. 169, no. 1, pp. 1–10, 1980. → page 206

[140] S. Melanson, M. Dehnel, C. Hollinger, J. Martin, C. Philpott, and D. Potkins, "A pid control algorithm for filament-powered volume-cusp ion sources," in *7th International Particle Accelerator Conference (IPAC'16), Busan, Korea, May 8-13, 2016*, pp. 2623–2624, JACOW, Geneva, Switzerland, 2016. → pages 208, 209, 210

[141] P. Svarnas, B. Annaratone, S. Béchu, J. Pelletier, and M. Bacal, "Study of hydrogen plasma in the negative-ion extraction region," *Plasma Sources Science and Technology*, vol. 18, no. 4, p. 045010, 2009. → page 217

[142] P. W. Allison, J. D. Sherman, and D. B. Holtkamp, "An emittance scanner for intense low-energy ion beams," *IEEE Transactions on Nuclear Science*, vol. 30, no. 4, pp. 2204–2206, 1983. → pages 219, 220

[143] M. Mao, J. Benedict, A. Consoli, and A. Bogaerts, "Investigation of negative ion growth mechanisms in acetylene dusty plasmas," *ESCAMPIG 2008*, 2008. → page 223

[144] C. Braams, "Edge effect in charged-particle analyzing magnets," *Nuclear Instruments and Methods*, vol. 26, pp. 83–89, 1964. → page 224

[145] "Langmuir's probe." http://www.physics.csbsju.edu/370/langmuir_probe.pdf. Accessed: 2010-09-30. → pages 225, 226

[146] R. L. Merlino, "Understanding langmuir probe current-voltage characteristics," *American Journal of Physics*, vol. 75, no. 12, pp. 1078–1085, 2007. → page 227

[147] *ADAS User Manual.* → page 229

[148] U. Fantz, "Basics of plasma spectroscopy," *Plasma sources science and technology*, vol. 15, no. 4, p. S137, 2006. → page 229

[149] J. C. Butcher, "The numerical analysis of ordinary differential equations: Runge-kutta and general linear methods," 1987. → page 243

[150] K. Leung, K. Ehlers, and M. Bacal, "Extraction of volume-produced h-ions from a multicusp source," *Review of Scientific Instruments*, vol. 54, no. 1, pp. 56–61, 1983. → page 243

[151] S. Lawrie, D. Faircloth, A. Letchford, M. Whitehead, and T. Wood, "Detailed beam and plasma measurements on the vessel for extraction and source plasma analyses (vespa) penning h- ion source," *Review of scientific instruments*, vol. 87, no. 2, p. 02B122, 2016. → page 251

[152] G. A. H. Bilheux, "Elementary theory for optimum extraction of space-charge-dominated ion beams from plasma boundaries," *High Energy Physics and Nuclear Physics*, p. S1, 2007. → page 251

[153] W. Wiese and J. Fuhr, "Nist atomic spectra database, lines data (1999)." → page 258

[154] D. B. Kinghorn and L. Adamowicz, "Electron affinity of hydrogen, deuterium, and tritium: A nonadiabatic variational calculation using explicitly correlated gaussian basis functions," *The Journal of chemical physics*, vol. 106, no. 11, pp. 4589–4595, 1997. → page 258

[155] M. Bacal and G. Hamilton, "H- and d- production in plasmas," *Physical Review Letters*, vol. 42, no. 23, p. 1538, 1979. → page 258

[156] Y. Takeiri, "Negative ion source development for fusion application," *Review of Scientific Instruments*, vol. 81, no. 2, p. 02B114, 2010. → pages 259, 260

[157] K. Leung and K. Ehlers, "Self-extraction negative ion source," *Review of Scientific Instruments*, vol. 53, no. 6, pp. 803–809, 1982.

[158] K. Jimbo, K. Ehlers, K. Leung, and R. Pyle, "Volume production of negative hydrogen and deuterium ions in a reflex-type ion source," *Nuclear Instruments and Methods in Physics Research Section A: Accelerators, Spectrometers, Detectors and Associated Equipment*, vol. 248, no. 2-3, pp. 282–286, 1986. → page 259

Appendix A

Additional Background Theory

A.1   Plasma Frequency

Oscillation of charges inside the plasma occurs when a particle is disturbed from its neutral position. If a group of charges displaced by a distance δx in the x direction is considered, the x component of the electric field (E_x) created by this charge movement will be described by

$$E_x = \frac{\rho}{\varepsilon_0} x = \frac{ne\delta x}{\varepsilon_0},\tag{A.1}$$

where ρ is the charge density, ε_0 is the permeability of free space, n is the particle density and e is the electric charge. Newton's third law is now used with the Lorentz force to predict the movement of the charged particles.

$$m\frac{d^2\delta x}{dt^2} = eE_x = \frac{ne^2}{\varepsilon_0}\delta x\tag{A.2}$$

Equation A.2 represents a simple harmonic motion. The *plasma frequency* [34] is introduced as $\omega_p^2 = \frac{ne^2}{\varepsilon_0 m}$, which represents the time scale of the plasma. It is species dependent and inversely proportional to the mass, so the electrons have the highest plasma frequency of all the different species in the plasma. In order to be able to use plasma physics to describe the behavior of the plasma, the average time between collisions must be larger than the plasma cycle time, this can be described

as

$$\omega_p \tau > 1, \tag{A.3}$$

where τ is the mean time between collisions.

A.2 Collisions

Various collision processes occur in a plasma including, but not limited to, electron-neutral, electron-ion and ion-neutral. The processes can be described with a random-walk concept, where the movement of the particles arises from the sum of a large number of small changes in momentum, resulting in a chaotic motion. Nevertheless, the collision frequency and the mean free path for each process can be loosely defined. The mean free path, λ, for a process is given by

$$\lambda = \frac{1}{n\sigma}, \tag{A.4}$$

where n is the particle density and σ is the cross section of the specific process. Each interaction possible has a specific cross section. The collision frequency, f_c, is given by

$$f_c = nv\sigma, \tag{A.5}$$

with v the particle's velocity. The different collision frequencies in the plasma vary greatly between the kind of interactions and can be on the order of kHz to GHz [34].

A.3 Multiple Ionization

More than one electron can be stripped from a neutral, forming a multiply charged ion. The ionization number can be as high as the number of electrons in the neutral particle. The ionization potential increases with the ionization degree since as the electrons are removed, the screening of the nucleus from the other electrons decreases. Thus, it takes more energy to ionize the ions further. Figure A.1 presents the ionization potential for degrees of ionization from 1 to 10 for every element up to copper.
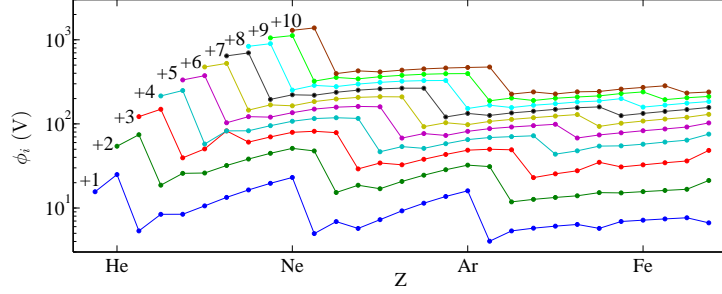
Figure A.1: Ionization potential for the first 10 charged states for elements up to copper [130].

From Figure A.1, as the atomic number increases, the ionization potential increases slightly, but there is an exception when the electrons form stable orbitals. For example, Li has the lowest ionization potential for the +1 ionization state, but the ionization potential greatly increases for the +2 state since Li^+ has a full 1s orbital. Furthermore, as the charge state of the ion increases, so does the ionization potential, with more than 100 V needed to ionize most atoms to a charge state of +6.

Multiply ionized ions can be created in two ways. Either the ion is created in one interaction with the electron, or the ion is created by multiple successive interactions with different electrons. Both mechanisms require higher electron temperatures than is required for singly charged ions. High temperature plasmas, such as the ones created in ECR ion sources, yield highly charged ion densities.

A.4 Debye Length

Plasmas can be considered uniform and quasi-neutral however, under a certain distance, the electric field from a single particle is not shielded by the bulk of the plasma and the quasi-neutrality condition is not established. The lower limit of quasi-neutrality is referred to as the *Debye Length* [34]. This value can be derived from basic electromagnetic and statistical physics. Poisson's equation states that the electric potential is related to the charge density by the Laplacian:

$$\nabla^2 \phi = -\frac{\rho}{\varepsilon_0},$$
(A.6)

where ϕ is the electric potential, ρ is the charge density ($\rho = q \cdot n$ with q being the charge of the species and n being the particle density) and ε_0 is the vacuum permeability. From basic statistical mechanics, an ensemble of n_0 charged particles in an electrical potential will follow a Maxwell-Boltzmann distribution [34]. Thus at position (x, y, z), the density will be given by:

$$n(x, y, z) = n_0 \exp\left(-\frac{e\phi(x, y, z)}{kT} \right), \tag{A.7}$$

where e is the elementary charge, k is the Boltzmann constant and T is the temperature. Applying this relation to A.6:

$$\nabla^2 \phi = \frac{-1}{\varepsilon_0} \left[-n_e e \exp\left(\frac{e\phi}{kT_e} \right) - n_n e \exp\left(\frac{e\phi}{kT_n} \right) + n_p e \exp\left(\frac{e\phi}{kT_p} \right) \right], \tag{A.8}$$

where T_e, T_n and T_p represent the electron, negative ion and positive ion temperatures and n_e, n_n and n_p denote the electron, negative ion and positive ion densities. For simplicity, one can assume that $n_e \gg n_n$ and $Z = 1$ for the positive ions, thus from quasi-neutrality, $n_e \approx n_p = n$. If it is assumed that $T_e = T_p$, Equation A.8 simplifies to

$$\nabla^2 \phi = \frac{ne}{\varepsilon_0} \left(\exp\left(\frac{e\phi}{kT} \right) - \exp\left(-\frac{e\phi}{kT} \right) \right) = \frac{2ne}{\varepsilon_0} \sinh\left(\frac{e\phi}{kT} \right). \tag{A.9}$$

Expanding in a Taylor Series and assuming that the potential is much smaller than the thermal energy of the particles ($\frac{e\phi}{kT} \ll 1$), Equation A.9 simplifies to

$$\nabla^2 \phi \approx \frac{2ne^2}{\varepsilon_0 kT} \phi. \tag{A.10}$$

This is a linear second order differential equation. The constant before the potential on the right hand side of the equation has the units of inverse distance squared. The Debye Length is thus introduced as $\lambda_D = \sqrt{\frac{\varepsilon_0 kT}{ne^2}}$ [34] and equation A.10 becomes

$$\nabla^2 \phi = 2\lambda_D^2 \phi. \tag{A.11}$$

Equation A.11 can be solved by assuming spherical symmetry in the solution, so that the equation is solved in spherical coordinates and the angular dependent terms are eliminated. The equation becomes

$$\frac{1}{r^2}\frac{\partial}{\partial r}\left(r^2\frac{\partial\phi}{\partial r}\right) = \frac{\partial^2\phi}{\partial r^2} + \frac{2}{r}\frac{\partial\phi}{\partial r} = 2\lambda_D^2\phi. \tag{A.12}$$

Solving equation A.12 with the initial conditions $\phi(\infty) = 0$ and $\phi(0) = \phi_0$,

$$\phi(r) = \phi_0\exp\left(-\frac{\sqrt{2}r}{\lambda_D}\right). \tag{A.13}$$

Equation A.13 indicates that the potential created by a single charge falls exponentially with a characteristic length of the Debye Length in a plasma. This effect is referred to as the plasma shielding. The Debye Length increases when the charge density decreases, since there are fewer particles to create the shielding effect, and the Debye Length increases with an increased particle temperature, since the particles are more mobile. For the quasi-neutrality of a plasma to be valid, the size of the area studied needs to be larger than the Debye Length of the plasma.

A.5 Plasma Sheath

The plasma sheath is the region between the bulk of the plasma and the chamber walls. The following section will present the development of the theory behind plasma sheaths.

The potential as a function of x close to the plasma chamber walls can be calculated. $x = 0$ is set in the bulk of the plasma, where $\phi = \phi_p = 0$ so that the wall is floating at a negative potential. It is assumed that the ions start at $x = 0$ with an initial velocity v_0 and collisions will be neglected for this analysis. Conservation of energy gives

$$\frac{m_i v(x)^2}{2} = \frac{m_i v_0^2}{2} - e\phi(x), \tag{A.14}$$

with $v(x)$ is the velocity and $\phi(x)$ is the potential. The conservation of ions gives $n_0 v_0 = n_i(x)v(x)$, where $n_i(x)$ is the ion density along x. Combining it with equation

A.14 leads to

$$n_i(x) = n_0 \left(1 - \frac{2e\phi}{m_i v_0^2} \right)^{-1/2}. \tag{A.15}$$

To obtain a relation for n_e, the fluid momentum equation is used and it is assumed that the magnetic field is in the x direction only [48],

$$\frac{\partial v_x}{\partial t} + (\vec{v} \cdot \vec{\nabla}) v_x = \frac{e}{m_e} E_x - \frac{kT_e}{m_e n_e} \frac{\partial n_e}{\partial x}, \tag{A.16}$$

where E_x is the electric field. Assuming the system is at equilibrium ($\vec{v} = const$, Equation A.16 becomes

$$\frac{e}{m_e} E_x = \frac{kT_e}{m_e n_e} \frac{\partial n_e}{\partial x}. \tag{A.17}$$

Using the relation $E_x = -\frac{\partial \phi}{\partial x}$ and integrating, an expression for n_e can be found:

$$n_e = n_0 \exp\left(\frac{e\phi}{kT_e} \right), \tag{A.18}$$

with n_0 the electron density in the bulk of the plasma. Using the particle densities calculated, Poisson's equation now reads

$$\frac{\partial^2 \phi}{\partial x^2} = \frac{e n_0}{\varepsilon_0} \left(\exp\left(\frac{e\phi}{kT_e} \right) - \left(1 - \frac{2e\phi}{m_i v_0^2} \right)^{-1/2} \right). \tag{A.19}$$

From equation A.19, which requires

$$\exp\left(\frac{e\phi}{kT_e} \right) < \left(1 - \frac{2e\phi}{m_i v_0^2} \right)^{-1/2} \tag{A.20}$$

to get a decreasing potential to the wall. This leads to the following condition:

$$v_0 > \sqrt{\frac{kT_e}{m_i}}. \tag{A.21}$$

The *Bohm velocity* [48] can be defined as $v_B = \sqrt{\frac{kT_e}{m_i}}$. Therefore, the ions initial velocity will be higher than the Bohm velocity at $x = 0$. The potential at $x = 0$ will be slightly below the plasma potential since the ions' velocities are above the

Bohm velocity. It will equate to

$$\phi(0) = \phi_{ps} = \frac{kT_e}{2e}, \tag{A.22}$$

which is half of the electron temperature in volts. This region is known as the pre-sheath [48].

Equation A.19 can be solved numerically to find the potential distribution along the wall and the different densities. The electron and ion densities are presented in Figure A.2 along with the electric potential.
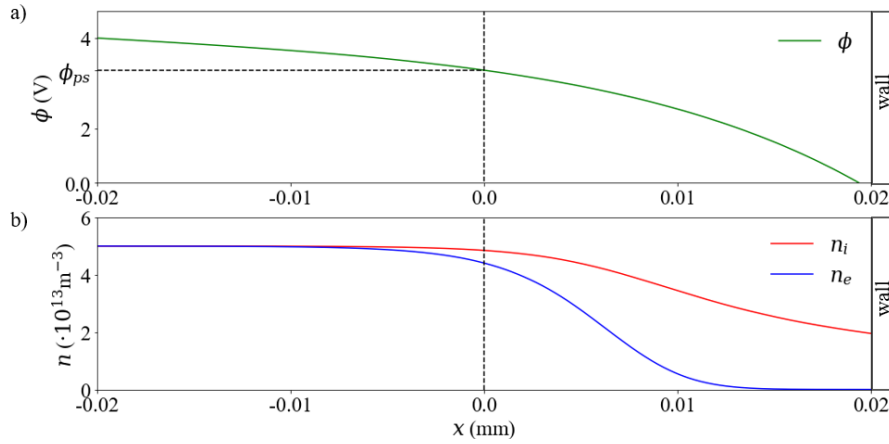
Figure A.2: Representation of a) the electric potential and b) the ion and electron density close to the wall of the plasma chamber.

A.6   Particle Motion in a Magnetic Field

The motion of individual particles in a magnetic field will be studied in this section. The magnetic force on a particle with velocity $\vec{v}$ in a magnetic field $\vec{B}$ is given by

$$\vec{F} = q\vec{v} \times \vec{B}. \tag{A.23}$$

The force is perpendicular to the particle's motion, which leads to a circular motion of radius

$$r = \frac{mv_\perp}{qB}, \tag{A.24}$$

where $v_\perp$ is the component of the velocity that's perpendicular to the magnetic field and B is the magnitude of the magnetic field. The angular frequency of the rotation of the particles, ω, is given by

$$\omega = \frac{qB}{m} \tag{A.25}$$

It is independent of the particle's velocity and is directly proportional to the magnetic field. The movement of the particle in the direction that is parallel to the magnetic field is unaffected, so the particle's motion will be a helix with the center of the helices following the magnetic field lines. The center of the rotation is known as the guiding center and it will travel parallel to the magnetic field at a velocity $v_{gc} = v_\parallel$, where $v_\parallel$ is the component of the velocity parallel to $\vec{B}$. A schematic of a particle's motion in a uniform magnetic field with $\vec{v} \cdot \vec{B} \neq 0$ is presented in Figure A.3.
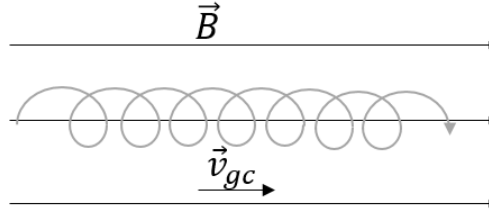
Figure A.3: Schematic of a particle motion in a uniform magnetic field without any electric field.

If there's an electric field in addition to the magnetic, there's an additional drifting term. The equation of motion becomes

$$m\frac{d\vec{v}}{dt} = q(\vec{E} + \vec{v} \times \vec{B}). \tag{A.26}$$

The analysis is simplified by defining the velocity $\vec{u} = \vec{v} - \frac{(\vec{E} \times \vec{B}) \times \vec{B}}{B^2}$ [34]. The guiding center will move at a velocity of

$$\vec{v}_{gc} = v_\parallel \hat{b} + \frac{\vec{E} \times \vec{B}}{B^2}, \tag{A.27}$$

where $\hat{b}$ is a unit vector in the direction of $\vec{B}$. The motion of an electron where

$\vec{E} \times \vec{B} \neq 0$ and $\vec{v} \cdot \vec{B} \neq 0$ is presented schematically in Figure A.4.
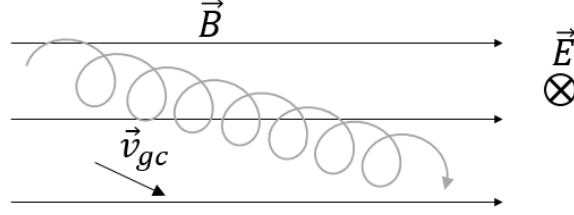
Figure A.4: Schematic of a particle motion when $\vec{E} \times \vec{B} \neq 0$.

If the magnetic field is not uniform, an additional drifting term that is proportional to the gradient of $\vec{B}$ arises. This comes from the fact that the radius of curvature of the helix will be smaller on the side of the orbit where the magnetic field is larger. There will be a net drift in the $\vec{B} \times \vec{\nabla} B$ direction. A schematic of the drift of a particle in a non-uniform magnetic field is presented in Figure A.5.
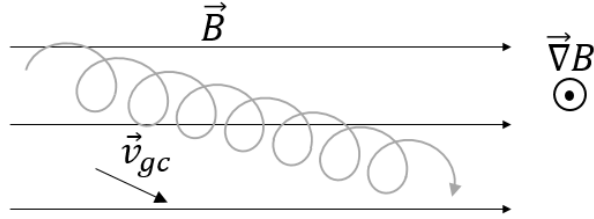
Figure A.5: Schematic of a particle motion in a non-uniform magnetic field.

A.7   Charge Exchange Ion Sources

Charge exchange ion sources are a common type of negative ion source that use low electron affinity vapour chambers to transfer electrons to a positive particle beam [14, 131]. Such an ion source is used in a certain class of ion implanter systems that use tandem accelerators [17]. The main disadvantage of using these ion sources in implanter systems is that they require alkali or alkaline earth vapours to create the negative ions. These vapours will migrate through the vacuum system and will contaminate the wafers in the implanter station.

This type of ion source first uses a positive ion source at the injection. The positive ion beam created is transported through a vapour comprised of low ionization energy molecules or atoms. The negative ions are formed either by a one or two step process. For the one-step process, alkaline earth vapours, such as magnesium, calcium, strontium or barium are used. Two electrons are transferred to the positive ions to form the negative ions, as described by

$$A^+ + Mg \rightarrow A^- + Mg^{2+}, \tag{A.28}$$
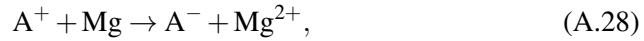
where A is the species that becomes the negative ion. Species with higher electron affinities, such as chlorine, are preferred for the production of negative ions with the one-step process. The two-step process sees the positive ion first be neutralized then transformed into a negative ion. Alkali metals, such as sodium, potassium, rubidium and cesium, are thus preferred for the two-step process. Negative helium, which has a lifetime of about 18 μs [132] can be produced using the two-step process with cesium [43]. The process is described by the following equations.

$$He^+ + Cs \rightarrow He + Cs^+, \tag{A.29}$$

$$He + Cs \rightarrow He^- + Cs^+. \tag{A.30}$$

A.8   Surface Ion Sources

Surface ion sources, such as Penning [47] or Magnetron [133] types, rely on the interaction between the wall of the plasma chamber and particles in the plasma to produce the negative ions. Negative hydrogen ions are often produced through this process. There is the direct transfer of electrons between the surface to the hydrogen atom leaving the surface. The work function of the metal surface is commonly more than 4 eV, so the transfer of the electron to the hydrogen is not efficient. However, as the hydrogen approaches the surface, its affinity level lowers to a level where the electron can tunnel to the hydrogen [44]. A low work function material, such as cesium, can be used on the walls to improve the transfer of the electrons to the hydrogen by lowering the work function of the surface.

A.9 Child-Langmuir Law

The following analysis will focus on the theoretical study of a beam being accelerated between two electrodes. The electric field created by the potential on the electrodes is responsible for the force accelerating the particles. As particles are accelerated between the electrodes, there is an opposing potential created by the charge of the particles. One would thus expect there to be an upper limit to the total beam that can be accelerated between the electrode at a certain potential. This space charge limited extraction is known as the Child-Langmuir Law [79].

A one-dimensional system of two electrodes separated by a distance d with an electric potential V between them, and a beam starting at $z = 0$ with no velocity ($\vec{v} = 0$) is considered. $\phi(z = 0) = 0$ and $\phi(z = d) = V$, where ϕ is the electric potential and z is the position along the beam axis. The continuity equation gives the current density of the beam, J, $J = \rho v = \text{const}$, where ρ is the charge density and v is the particle's velocity.

The velocity of the particles is found by considering the conservation of energy. The conservation of energy reads

$$\frac{mv^2}{2} = q\phi, \tag{A.31}$$

where m is the particle's mass and q is the particle's charge. The Poisson equation for the 1-D system is

$$\frac{d^2\phi}{dz^2} = -\frac{\rho}{\varepsilon_0} = -\frac{J}{\varepsilon_0}\sqrt{\frac{m}{2q\phi}}, \tag{A.32}$$

with ρ the charge density and J the current density.

With $J = 0$, the electric potential will be linear between the plates and the electric field will be constant, but as the current density increases, the electric field at $z = 0$ will decrease until it will be 0. This will be the maximum current, $J_{\max}$, that can be extracted between the plates. Equation A.32 can be solved by integration with the boundary conditions $\phi(z = 0) = 0$ and $\frac{d\phi}{dz}\big|_{z=0} = 0$ to yield

$$\phi(x) = \left(\frac{3}{2}\right)^{\frac{4}{3}}\left(\frac{J_{\max}}{\varepsilon_0}\right)^{\frac{2}{3}}\left(\frac{2q}{m}\right)^{-\frac{1}{3}}x^{\frac{4}{3}}. \tag{A.33}$$

Substituting $x = d$ so that $\phi(d) = V$, the maximum current density that can be extracted at voltage V is given by

$$J_{\text{max}} = \frac{4}{9}\varepsilon_0\sqrt{\frac{2q}{m}}\frac{V^{3/2}}{d^2}. \tag{A.34}$$

The extracted current is proportional to $V^{3/2}$. The perveance, P [79], can be define as

$$P = \frac{I}{V^{3/2}} = \frac{4}{9}\varepsilon_0\sqrt{\frac{2q}{m}}\frac{\pi a^2}{d^2}, \tag{A.35}$$

with a the radius of a circular aperture. The perveance is dependent only on the geometry of the system and on the properties of the particles accelerated.

Figure A.6 plots a schematic representation of the beam current as a function of the potential applied to the electrodes. For low voltages, the beam is extraction limited and will follow Eq. A.35 as the plasma density is high enough to enable the maximum current to be extracted. However, as the voltage on the electrode increases, there is a saturation of the beam current as the plasma cannot supply the particles needed to reach extraction limited extraction. Figure A.6 schematically presents the case with two different plasma powers (P_1 and P_2), leading to saturation of the beam current at different values.
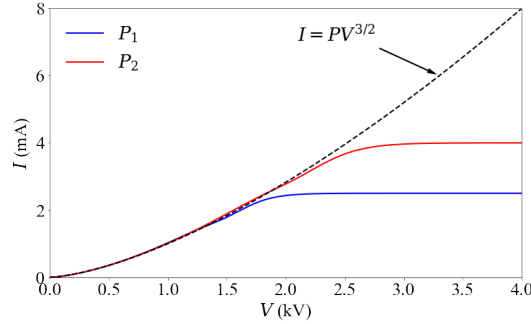
Figure A.6: Schematic representation of the Child-Langmuir law for a beam extracted from plasmas with two different powers.

As can be seen in Figure A.6, increasing the potential on the electrode will lead to an increase in the beam current, but there is a limit set by the density of ions in the plasma.

The Child-Langmuir law can be extended to include beams with 2 extracted species, such as the case of H^- ion sources where the extracted beam can include co-extracted electrons. If two species, m_1 and m_2, are extracted beam current given by $I_1 = \alpha I_{tot}$ and $I_2 = (1-\alpha)I_{tot}$, $0 < \alpha < 1$, then the Child-Langmuir law becomes

$$J_{tot} = \frac{4}{9}\varepsilon_0 \sqrt{\frac{2q}{m_{eff}}} \frac{V^{3/2}}{d^2},$$ (A.36)

with

$$m_{eff} = \left(\alpha\sqrt{m_1} + (1-\alpha)\sqrt{m_2}\right)^2.$$ (A.37)

A.10 Electrostatic Steering

For lower energy beams (< 1 MeV), electrostatic plates can be used to steer the beam. Figure A.7 represents a particle being deflected with electrostatic plates.
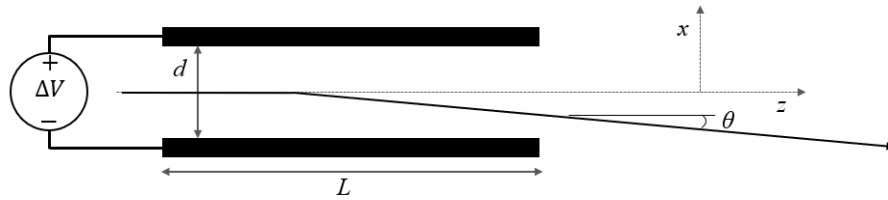
Figure A.7: Deviation of a particle with charge q, mass m and energy V_0 by a uniform electric field created by parallel plates of length L and separation d.

An effective length, L_{eff}, for the parallel plates is defined as

$$\int E dz = E_{max}L_{eff}.$$ (A.38)

Where E is the electric field along the z direction and E_{max} is the maximum electric field value, which will be the electric field in the center of the plates. The electric field created by the biased plates in Figure A.7 is given by $E_{max} = \frac{\Delta V}{d}$. Using Newton's third law, the acceleration in x is calculated from the electric force $F_x =$

193

$qE_{\max}$,

$$\frac{d^2x}{dt^2} = \frac{qE_{\max}}{m} = \frac{q\Delta V}{md}.$$ (A.39)

Since the particle's longitudinal velocity is constant through the plates, the variation in v_x is given by $\Delta v_x = \frac{a_x L_{\mathrm{eff}}}{v_z}$. $\theta = \frac{\Delta v_x}{v_z} = \frac{a_x L_{\mathrm{eff}}}{v_z^2}$ is to be calculated. Using equation A.39,

$$\theta = \frac{q\Delta V L_{\mathrm{eff}}}{dmv_z^2} = \frac{q\Delta V L_{\mathrm{eff}}}{2dE_k} = \frac{\Delta V L_{\mathrm{eff}}}{2V_0 d},$$ (A.40)

with the kinetic energy $E_k = \frac{1}{2}mv_z^2$ and V_0 which corresponds to the energy of the particle divided by the charge (from the conservation of energy, $qV_0 = E_k$).

From equation A.40, one sees the equation is independent of the mass of the particle. This is a useful result since it means that a beam of multiple species with different masses, but the same charge state, can be steered uniformly without any species separation. The main drawback seen with electrostatic steering is that the potential required to steer a beam becomes impractical if the beam energy is high. For example, for parallel plates with $L_{\mathrm{eff}} = 10$ cm separated by 5 cm, more than 1 MV would be needed to deviate a 10 MeV beam more than $10°$.

A.11 Magnetic Steering

An alternative to electrostatic steering is to use magnetic fields. A magnetic dipole that creates a uniform magnetic field $\vec{B}_0$, perpendicular to the particle's motion, as presented in Figure A.8, is considered.
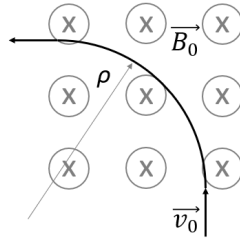
Figure A.8: Deviation of a particle with charge q, mass m and initial velocity $\vec{v}_0$ by a uniform magnetic field of strength B_0 (directed into the page). ρ is the radius of curvature of the particle.

The particle will have a circular motion in the plane perpendicular to the mag-

netic field. This can be seen by analyzing the forces on the particle. The magnetic force is given by

$$\vec{F} = q\vec{v}_0 \times \vec{B}_0, \tag{A.41}$$

with $\vec{F}$ the force acting on the particle, q the particle's charge, $\vec{v}_0$ the velocity of the particle and $\vec{B}_0$ the magnetic field. But since $\vec{v}_0$ and $\vec{B}_0$ are perpendicular, $|\vec{v}_0| = \text{const}$ and $|\vec{B}_0| = \text{const}$, the magnetic force will be a centripetal force ($\frac{mv_0^2}{\rho}$) and the motion will be circular. Equation A.41 can be written as

$$F = qv_0 B_0 = \frac{mv_0^2}{\rho}. \tag{A.42}$$

The magnetic field can be isolated,

$$B_0 = \frac{1}{\rho}\sqrt{\frac{2mV_0}{q}}, \tag{A.43}$$

where $V_0 = \frac{E_k}{q}$, as defined in Section A.10. From equation A.43, the magnetic field required to steer a beam is much more achievable than with the electrostatic case. In the example from the Section A.10, $L_{\text{eff}} = 10$ cm and $\theta = 10°$, which gives a radius of curvature of $\rho \approx \frac{L_{\text{eff}}}{\theta} = 57$ cm. Using equation A.43, a magnetic field of about 0.78 T is required to deviate a beam of 10 MeV protons at this radius of curvature. Iron magnets can easily achieve more than 1 T with copper conductor [134], so the magnetic field required could easily be achieved with a room temperature electromagnet.

Magnetic dipoles are also used as mass spectrometers since the radius of curvature of the particles is dependent on the mass-to-charge ratio ($\rho = \frac{m}{q}\frac{v}{B}$) of the particles. A schematic of a mass spectrometer with a dipole magnet is shown in Figure A.9.

The beam is first collimated by the entrance slit, it is then bent 90° by a dipole magnet through the second slit and into the Faraday cup. The current in the dipole magnet is increased so that the beam is swept through the system while separating and measuring the different components in the Faraday cup. Assuming the dipole magnet is not saturating, the magnetic field will be directly proportional to the current [134], and a plot of the Faraday cup current as a function of the magnet
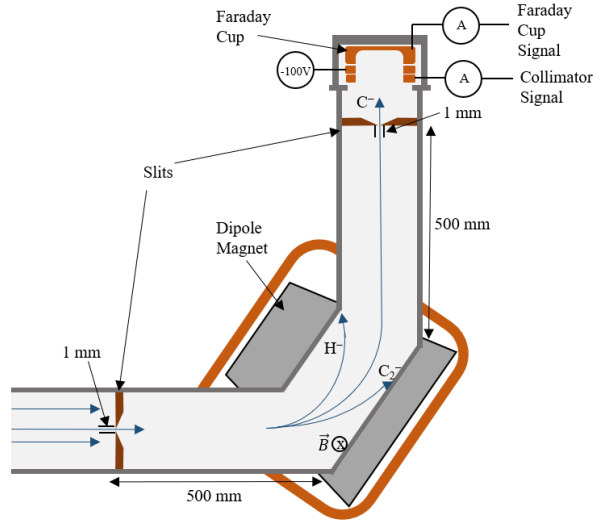
Figure A.9: Schematic of a mass spectrometer using a dipole magnet, two slits and a Faraday cup. The figure presents a beam composed of H^-, C^- and C_2^-.

current will give peaks at currents corresponding to the different species in the beam. From equation A.41, $B \sim \sqrt{\frac{m}{q}}$, the peaks can be identified and the relative composition of the beam can be calculated.

Appendix B

Development, Construction & Validation of the Ion Source Test Facility

As part of the development of a negative carbon ion source, an ion source test stand was fabricated. This work involved the D-Pace [22] team and shall be used by the team for their product development. The author's main contributions in the development of the Ion Source Test Facility (ISTF) were in the installation of the auxiliary system (electrical, cooling, controls, gas) and in the commissioning of the facility with H^-. This appendix will first describe the facility in detail and it will then present the TRIUMF licensed filament-powered volume-cusp H^- ion source [23, 135] as the baseline ion source for the ISTF.

This appendix will also present the diagnostic devices and methods that were used during this Thesis project and confirm they are appropriate for the Thesis topic. These include the baseline ion source equipment read-back parameters as well as the beam diagnostic devices that were part of the initial ISTF design, which includes an emittance scanner and a mass spectrometer. After assessing the diagnostic tools that were available in the baseline system, it was clear additional plasma diagnostic tools would be needed as part of the Thesis work to analyze how the ion source parameters affect the carbon rich plasmas. The design, implementation and testing of a Langmuir probe system and an optical spectroscopy system

197

are presented in this Appendix as important Thesis contributions.

To validate the ISTF, the ion source and the diagnostic devices, the performance of the components of the system was tested with H$^-$ beam. This appendix will present validation measurements of the TRIUMF licensed filament-powered volume-cusp ion source and compare the results to Kuo et al [23]. Then, all of the diagnostic tools presented were validated by operating them with the same ion source, and the performance was analyzed using computational tools. Finally, baseline D$^-$ measurements obtained with the ion source are presented.

B.1 Ion Source Test Facility

All the experiments conducted for this Thesis work were ultimately done at the ISTF. The design, development, construction and validation of the ISTF was necessary to complete prior to undertaking negative carbon ion experiments.

B.1.1 Design & Construction

The ISTF was installed in the testing and quality control area of the Buckley Systems [136] facilities in Auckland, New Zealand. The TRIUMF licensed filament-powered volume-cusp H$^-$ ion source that D-Pace used as the baseline at the ISTF can extract singly-charged negative ion beams with an energy of up to 30 keV. The ISTF was thus designed with a maximum operational voltage of 30 kV. A large Faraday cage was designed to leave room for modifications to the system. A spectrometer system was included to allow the beam composition analysis of beam for particle species with masses up to Fe. Figure B.1 presents a representation of the ISTF.
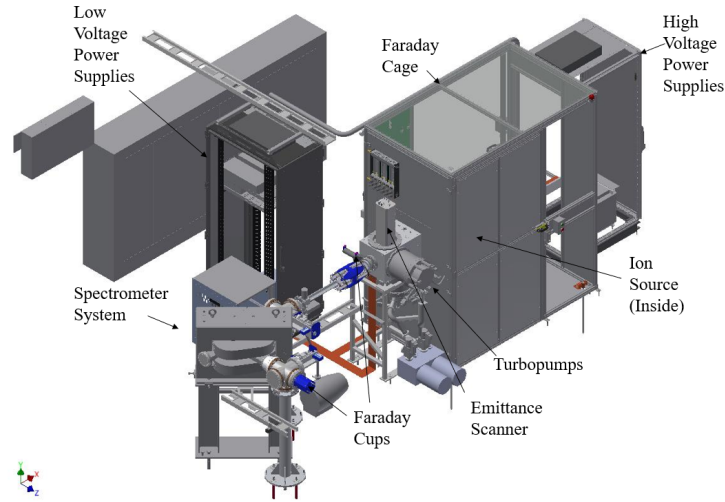
Figure B.1: CAD model of the ISTF showing the beamline and the auxiliary systems. The Faraday cage is on the right side of the figure and the ion source is located in the cage. The figure presents the beamline including the spectrometer system, Faraday cups and an emittance scanner. The CAD model also shows the vacuum system and the power supply racks.

The construction of the system started in July 2015 and the first phase of construction was completed in October 2015. The first phase included the construction and design of the system up to the spectrometer. This included the Faraday cage, the filament-powered ion source along with all of its power supplies and controls, the vacuum system, the cooling water system, the gas system, a fixed Faraday cup and an emittance scanner. A photograph of the ISTF on the first day of construction as well as a photograph of the system after stage 1 is presented in B.2.
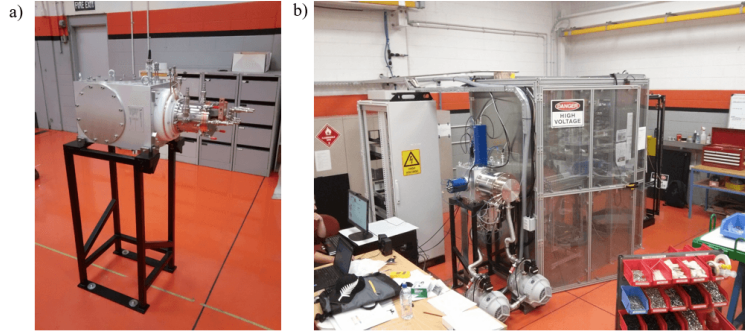
Figure B.2: a) Photograph of the ISTF on the first day of construction and b) Photograph of the ISTF after the completion of stage 1.

The second phase of construction took place during March 2016. The main addition to the system was the spectrometer system, which consists of a 90° bending magnet, two high precision slits and a Faraday cup. A short beamline was also added to connect the ion source vacuum box to the spectrometer system. A photograph of the ISTF after phase 2 is presented in Figure B.3.

Figure B.3: a) Photograph of the ISTF after Phase 2.

The author's specific contributions to this phase of the project included: (i) implementation and development of an arc current control algorithm for the filament-powered ion source, (ii) installation and testing of the safety interlock system, (iii) commissioning of the vacuum system, including simulating the vacuum system pressure as a function of gas flow, (iv) installation of the cooling water system, (v)

installation of the gas system and (vi) commissioning the facility with the TRIUMF licensed filament-powered H⁻ ion source.

B.1.2 Beamline

This section will briefly present the layout of the ISTF's beamline. Detailed information regarding the individual components will be presented in Section 3.3. A schematic of the beamline is presented in Figure B.4.
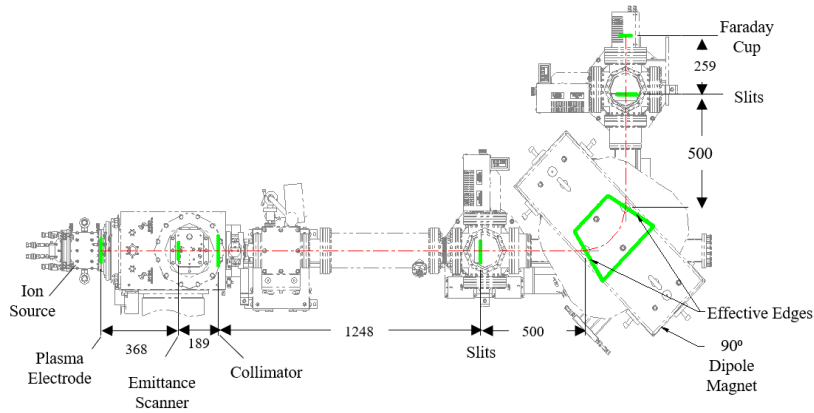
Figure B.4: Schematic of the ISTF beamline.

The baseline ion source at the ISTF is the TRIUMF licensed filament-powered volume-cusp H⁻ ion source. The ion source is biased at a high negative potential (normally 30 kV) and is located in the Faraday cage. The front plate of the ion source serves as the first electrode, and will hereby be denoted as the plasma electrode. The plasma electrode is used as $z = 0$ of the beamline. An emittance scanner is mounted in the y scanning direction in front of the Faraday cup, with the front slit of the scanner located 368 mm downstream of the plasma electrode. A pneumatic Faraday cup is located 480 mm downstream of the plasma electrode. To restrict the beam current to the mass spectrometer, a 3 mm diameter aperture is placed 557 mm from the plasma electrode. The beam then drifts 1248 mm to the entrance slit of the mass spectrometer system. The mass spectrometer is composed of two slits, a 90° dipole magnet and a fixed Faraday cup. The slits are located 500 mm from the effective edges of the dipole magnet, while the Faraday cup is 259

mm downstream of the exit slit. All the distance values quoted have an error of ± 1 mm.

B.1.3 Vacuum System

The vacuum is achieved with two turbo-molecular pumps each with a pumping speed of 1700 L/s for hydrogen. The pumps have a port diameter of 250 mm and are backed by dry scroll pumps. The pumps are located in two distinct regions in the vacuum chamber creating a differential pumping configuration through the ion source's ground electrode aperture. The *upstream* region is the ion source area, and it includes the ion source and its extraction system. The pressure in this region is considerably higher than the rest of the system since this is where the gas is introduced in the system. This is also the region with the most vacuum interfaces, which introduces a higher potential for leaks and has an overall higher outgassing rate. The upstream region is where the bulk of the pumping occurs. The *downstream* region is at a lower pressure since there is no direct gas load in this region. This region includes the beam diagnostic area, housing the Faraday cup, the emittance scanner, and the mass spectrometer. The downstream turbo pump is located on the downstream portion of the vacuum box and there aren't any pumps in the mass spectrometer region, thus the pressure is higher in this region.

The vacuum pressure is monitored by two wide range vacuum gauges which accurately measure vacuum pressures down to $1 \cdot 10^{-9}$ Torr. One is located in the upstream region and the second is in the beam diagnostic area. A schematic of a cross sectional view of the vacuum box is presented in Figure B.5, showing the upstream and downstream regions, without the mass spectrometer.
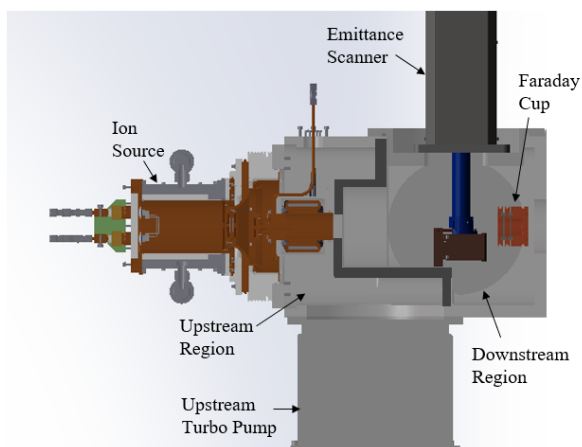
Figure B.5: Schematic of the cross section of the vacuum box and the ion source, showing the upstream and downstream vacuum regions.

Without any gas load, the base vacuum pressure is between $6 \cdot 10^{-7}$ Torr and $1 \cdot 10^{-6}$ Torr in the upstream area, between $7 \cdot 10^{-8}$ Torr and $2 \cdot 10^{-7}$ Torr in the downstream area and between $1 \cdot 10^{-6}$ Torr and $3 \cdot 10^{-6}$ Torr in the mass spectrometer region. When gas is added to the system, the pressure increases in every region, but the increase is most pronounced in the upstream region, where the pressure reads up to $6 \cdot 10^{-5}$ Torr for 32 Standard Cubic Centimeters per Minute (sccm) of H_2 gas injected in the ion source. The pressure in the ion source is not measured, but previous studies show that the pressure in the ion source is between $1 \cdot 10^{-2}$ Torr and $3 \cdot 10^{-2}$ Torr [23].

To obtain an estimate of the pressure in the ion source, a simulation of the vacuum system with Molflow+ was completed [137]. Molflow+ is named for molecular flow, the condition when the molecular mean free path is long compared to geometrical size, so collisions between particles are neglected. Particles travel independently making this physics suitable for Monte Carlo simulations. Gravity is also neglected, and only diffuse gas-surface interactions are considered. Molecular trajectories are assumed rectilinear, and desorption and reflection directions are both computed. Transmission probabilities and other vacuum related properties have been checked against exact computations for ideal structures such as tubes, and its errors are very small at $\sim$0.01% [138].

A number of key physical properties were entered in the program such as: (i) the actual 3D physical geometry, (ii) opacity (probability that a molecule going through a facet will interact with it), (iii) sticking factor (probability that a molecule hitting a facet will be absorbed), (iv) volumetric pumping speed, and (v) outgassing rate. The opacity was set to 1 and the sticking factor was set to 0 on every surface, indicating that particles are reflected off of the surfaces. The outgassing rate of the different surface materials were first estimated from known values from the literature and the system was set running without any gas flow until the pressure in the different areas of the vacuum system were found. The pressures in the model were then compared to actual measurements from the vacuum gauges in the upstream and downstream regions, and the parameters were adjusted until the simulated pressure matches the measured pressure in both regions. It was found that an outgassing rate of $3 \cdot 10^{-7}$ mbar·L/s in upstream region and $5 \cdot 10^{-8}$ mbar·L/s in the downstream region replicated the pressures seen in the system. The higher outgassing rate seen in the upstream region is due to the larger number of o-ring seals in this region. Once this was achieved, a gas load was added to the ion source to simulate the injection of H_2 into the ion source. The gas load was varied to simulate a range of gas flows commonly used in the ion source. Figure B.6 presents a snapshot of the simulation with the particles inside the vacuum chamber as well as the calculated pressure in the ion source as a function of the gas flow in the ion source, as calculated from the Molflow+ model.
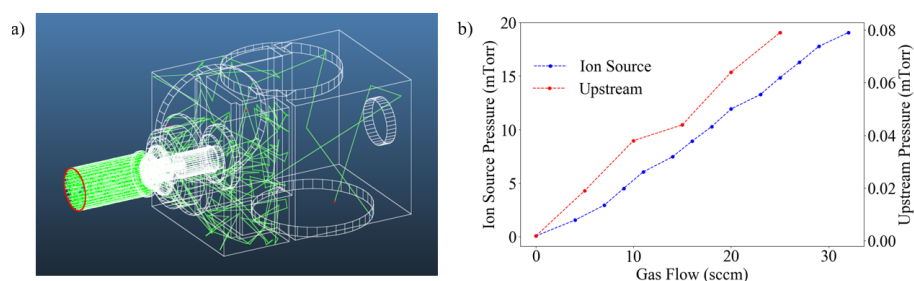
Figure B.6: a) Snapshot of the Molflow+ [137] model used to calculate the pressure in the vacuum system. b) Calculated pressure in the ion source obtained with Molfow+ and pressure measured in the upstream vacuum region as a function of the H_2 gas flow.

The pressure values in the ion source compare well with previous values published in the literature of 10-30 mTorr [23]. The pressure also drops significantly along the beamline as soon as the beam leaves the extraction area. Figure B.7 presents how the pressure varies along the beamline in the vacuum system.
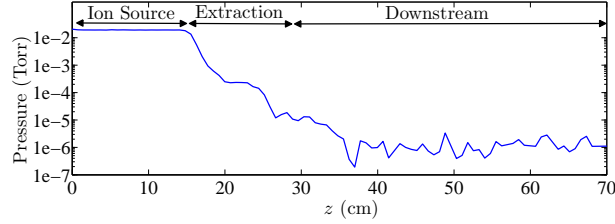
Figure B.7: Simulated pressure along the beamline with a simulated H_2 gas flow of 30 sccm.

B.1.4 Electrical System

The baseline ion source used at the ISTF can extract singly-charged ion beams at a maximum beam energy of 30 keV. The ISTF was thus designed with a floating high voltage platform that has a maximum holding voltage of 30 kV. The electrical infrastructure is divided into two sections, the high voltage and low voltage areas.

The low voltage section is at ground potential. A ± 30 kV power supply capable of producing up to 40 mA of current is in the low voltage cabinet and it biases the high voltage area of the ISTF up to -30 kV. The main Programmable Logic Controller (PLC), which is used to control the ISTF, is located in the low voltage area. The beam diagnostic tools, as well as their power supplies and controls hardware are also located in the low voltage area of the ISTF.

The high voltage area is enclosed in a grounded Faraday cage. The ion source and all of its power supplies and controls are located on the electrically floating platform inside the Faraday cage. A second PLC is located in the Faraday cage and it communicates with the main PLC at ground potential with a fiber optic cable to ensure electrical isolation of the platform. AC power to the high voltage area is done with a 20 kVA isolation transformer with a maximum holding voltage of 40 kV.

B.1.5 Water Cooling

Two separate cooling water systems are used at the ISTF. A De-Ionized (DI) water system was implemented to cool the devices that are at bias potential, such as the ion source body, back plate and its electrodes, and it is also used in the Faraday cups. The DI water system is cooled by a standard cooling water system through a heat exchanger. The DI cooling water system has an entrance pressure of 70 psi and can provide up to 20 L/s of water flow. A standard water cooling system is used for the rest of the components, such as the turbo-molecular vacuum pumps, the spectrometer magnet, the *XY* steering magnet and the emittance scanner. The water is cooled with a cooling tower located outside of the building. The standard cooling water system has an entrance pressure of 90 psi and can provide up to 40 L/s of water flow.

B.2 Filament-Powered Ion Source

D-Pace's baseline ion source at the ISTF is a filament-powered volume-cusp H^- ion source that was licensed from TRIUMF [23, 135]. The ion source was designed to produce more than 15 mA of DC H^- beam at an energy of 30 keV with a normalized 4-RMS emittance of less than 1 mm·mrad.

B.2.1 Plasma Chamber

The cylindrical copper plasma chamber has a diameter of 100 mm and a length of 150 mm. Plasma confinement is done with 10 rows of Sm_2Co_{17} magnets in a Halbach array [139] around the circumference of the plasma chamber. The cusp array configuration is replaced to form a dipole close to the extraction region of the plasma chamber, creating a *virtual dipole*. The permanent magnet configuration used to create the multicusp configuration and the dipole field is presented in Figure B.8.
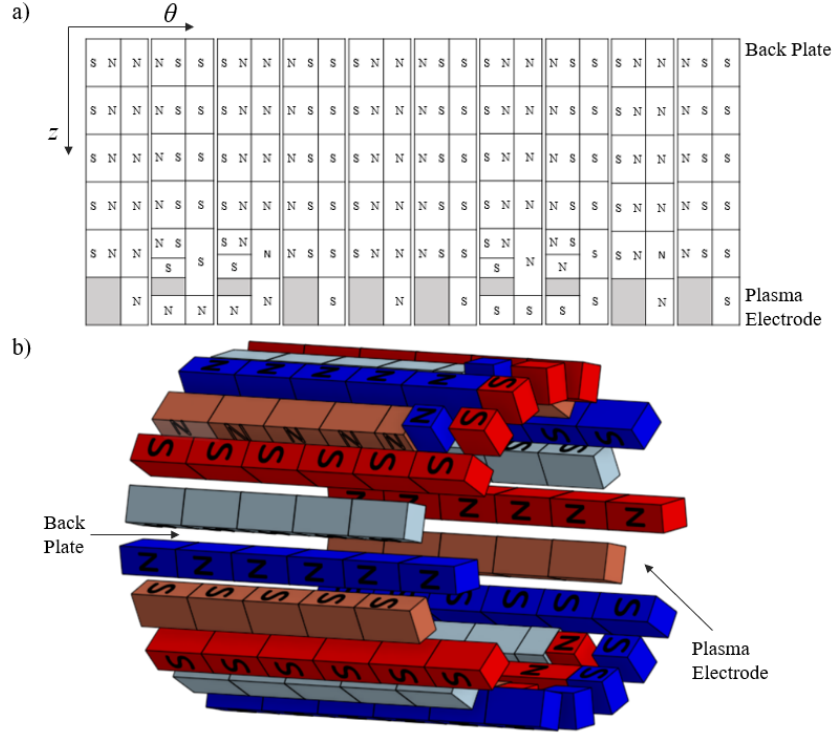
Figure B.8: a) Permanent magnet array around the plasma chamber, the top of the diagram corresponds to the back plate, while the bottom corresponds to the plasma electrode. b) 3D model of the baseline magnetic configuration in the TRIUMF licensed H⁻ ion source.

The back plate of the ion source has 4 rows of alternating North and South facing magnets to add to the plasma confinement in the back of the ion source. The plasma is generated by thermionic emission of four half-circle tantalum filaments located near the center of the back plate of the plasma chamber. The shape of the filaments cancels the magnetic field created by the current circulating through the filaments since the current in the two opposite half circles flow in the same direction. This prevents any $\vec{E} \times \vec{B}$ drift of the electrons in the plasma by ensuring that the center of the plasma chamber is magnetic field free. The filaments are a consumable part of the ion source and they need to be replaced after about 5000 mA·h of operation. A photograph of the filaments is presented in Figure B.9.

Figure B.9: Tantalum filament configuration used in the TRIUMF licensed filament-powered volume-cusp ion source.

The filaments are biased between -80 V and -150 V relative to the ion source body, becoming the cathodes of the plasma chamber. The arc current is the electron current that comes from the filaments and reaches the plasma chamber walls, which acts as the anode. The arc current represents the main power input in the ion source's plasma, with about 4 kW needed to generate a plasma that can produce enough H^- to extract 15 mA. A filament current between 150 A and 250 A is needed to generate a hydrogen plasma, depending on the age of the filaments. The current needed for higher arc currents (>10 A) is lower than what is needed at lower arc currents (<10 A) as the plasma self heats the filaments at higher powers. The current in the filaments has to be actively controlled to keep the arc current constant since the self-heating of the filaments makes the relation between the arc current and the filament current highly non-linear [140]. A schematic of the ion source and the wiring of the filaments and the electrodes is presented in Figure B.10.
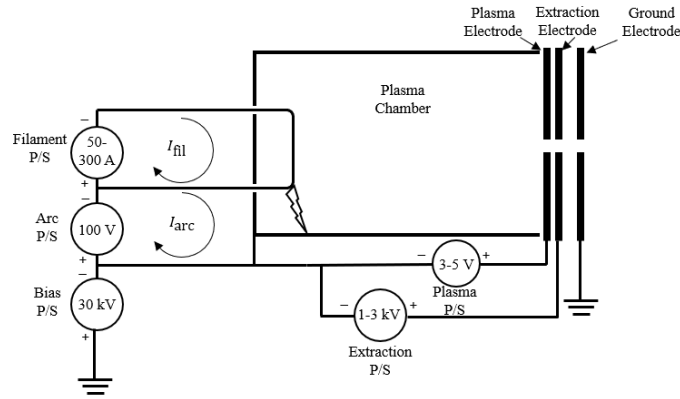
Figure B.10: Schematic of the wiring of the TRIUMF licensed ion source.

B.2.2 Arc Current Stabilization

An important scientific contribution to the ISTF design and implementation was achieved as a part of this Thesis work. This was the development and implementation of an arc current stabilization algorithm, which resulted in a technical publication [140]. For steady operation, it's important to have a stable arc current since it impacts the power into the plasma and is thus closely related to the beam current. However, the arc current is a passive parameter that depends on filament current flowing through it and there's a non-linear relation between the arc current and the filament current. This is caused by the self-heating of the filament by the plasma at higher arc powers. Furthermore, the arc current to filament current relation is highly dependent on the gas flow, gas species, filament aging, plasma confinement, chamber dimensions, etc. The relation between the filament current and the arc current for a new filament and one that has been running for about 450 mA·hours is presented in Figure B.11.
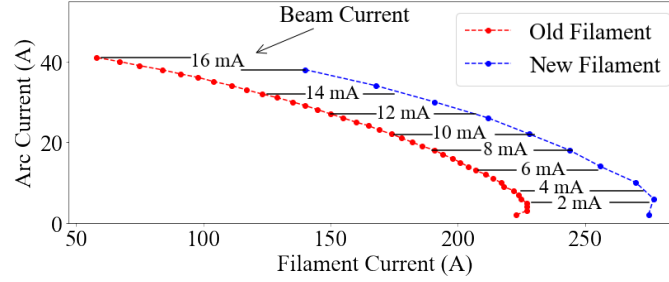
Figure B.11: Relation between the arc current and the filament current for various beam currents for a new filament and one that had been running for about 450 mA·hours. The arc voltage was set at 130 V and the hydrogen gas flow was set at 15 sccm.

An algorithm therefore needs to be developed and implemented to keep the arc current and the beam current stable by controlling the filament current. A Proportional-Integral-Derivative (PID) control algorithm was implemented with the filament current as the controlled variable and the arc current as the feedback variable [140]. The control function can be expressed as

$$I_f(t_i) = I_f(t_{i-1}) + u(t_i), \tag{B.1}$$

where

$$u(t) = K_p e(t) + K_i \int_0^t e(t')dt' + K_d \frac{de(t)}{dt}, \tag{B.2}$$

and where K_p, K_i and K_d are non-negative constant referred to as the proportional, integral and derivative terms and $e(t)$ is the error between the arc current set point and the actual value $(e(t) = I_a(t) - I_{set})$ where I_a is the arc current and I_{set} is the arc current set point. The parameters K_p, K_i and K_d need to be tuned for the specific system.

Since the measurement is discretized, the derivative in Eq. B.2 is approximated by the average error variation between the two closest error points. The integral is approximated by the sum of the errors. In order to eliminate the risk of overcompensating for the integral term, the integral is taken for the last 10 000 points that were recorded by the PLC system. The time interval between consecutive measurements was set at 10 ms, so the integral was taken over 100 s.

Proper tuning of the PID parameters is the key to reducing the arc current error. The control loop is dominated by the proportional term, while the integral term corrects for long term offsets. The derivative term reduces the oscillations around the set point and is usually only needed for fast applications. The three PID tuning parameters serve different purposes; K_p sets the sensitivity to the set point. K_i sets the sensitivity to long term error since the error is integrated over time. K_d compensates for the speed of the convergence, helping reduce the oscillations around the set point.

Since the generation of a plasma with a filament is highly non-linear, the PID parameters depend on the arc current set point. At low arc currents (less than 5 A), the behavior is more predictable and the control algorithm could properly control the arc current with just the proportional term, which was set to $K_p = 50$. At higher arc current set points, it becomes necessary to include the other integral and derivative terms and the proportional term needs to be lowered. For an arc current between 5 A and 20 A, setting $K_p = 30$ and $K_i = 5$ gives good stability. Above 20 A of arc current, an added derivative term helps improve stability along with a lower proportional term. At $I_{\text{set}} = 24.6$ A, the algorithm worked best with $K_p = 15$, $K_i = 10$ and $K_d = 1$.

To evaluate the algorithm, the arc current was set at $I_{\text{arc}} = 24.6$ A. The arc voltage was fixed at 130 V and the H_2 gas flow was at 15 sccm, then the ion source was set running for an hour. The results are presented in Figure B.12.
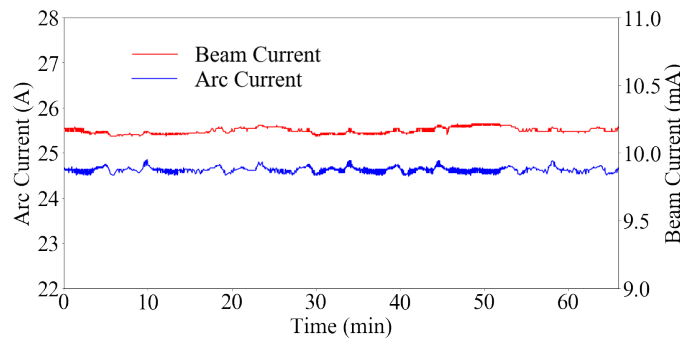
Figure B.12: Variation of the arc current (blue) and of the H^- beam current (red) for $I_{\text{set}} = 24.6$ A. The arc voltage was set at 130 V and the gas flow was set at 15 sccm.

Over 60 minutes of operation, a root mean square error in the arc current of 0.058 A was obtained which yielded an H$^-$ beam current of 10.16 mA with a root mean square error of 0.025 mA on the Faraday cup. The maximum peak-to-peak variation was ±0.76% for the arc current and ±0.45% for the beam current. One will notice that the deviation is larger for the arc current than for the beam current. This is explained by the fact that H$^-$ ion production is a slower process and thus less affected by the electron current to the chamber walls. The results obtained prove that the algorithm developed can efficiently control the arc current and thus the beam extracted out of the ion source.

B.2.3 Extraction System

The TRIUMF licensed ion source has a three electrode extraction system. A schematic of the system is presented in Figure B.13. The first electrode is the aperture forming the front end of the cylindrical plasma chamber, and it's commonly named the plasma electrode. It is biased positively at a few volts above the plasma chamber potential and the baseline ion source has a plasma electrode with a circular aperture with a diameter of 13 mm.
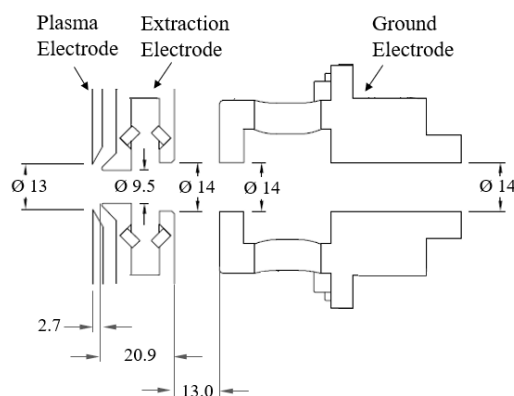
Figure B.13: Schematic of the extraction system of the filament-powered ion source [23].

The second electrode is located 2.7 mm downstream from the plasma electrode, it is called the extraction electrode. It is biased at around 1-3 kV above the ion source potential. Since it's the first electrode outside the plasma chamber, the ex-

212

traction electrode will create the electric field that will shape the plasma meniscus. Thus, the potential on this electrode needs to be tuned as the ion source settings are varied and the plasma densities and temperatures change. The extraction electrode has two apertures separated by 8 mm, the first aperture has a diameter of 9.5 mm and the second aperture has a diameter of 14 mm. Between the two apertures are two magnetic dipoles of opposite polarity, created by two sets of Sm_2Co_{17} magnets. The first dipole is oriented in the same direction as the dipole in the plasma chamber, the second dipole is oriented in the opposite direction. This magnetic field is used to deflect the co-extracted electrons from the beam and the nominal design was set to have the electron dumped between the two apertures of the extraction electrode. This is an important feature of the ion source since it keeps the electrons from reaching ground potential, preventing the ion source's bias power supply to overload with current. The bias power supply at the ISTF can generate a maximum current of 40 mA, and the electron to H^- ratios commonly seen in this ion source are of about 4-5. This equates to about 60-75 mA co-extracted electrons with 15 mA of H^- beam. The extraction electrode's power supply needs to be able to handle this electron current, but the voltage requirements are lower, with a maximum of about 4 kV. The power supply used at the ISTF has a maximum voltage of 7 kV with a maximum current of 150 mA, which is higher than the usual electron current at full power [23]. The magnets in the extraction electrode, along with the rest of the extraction system can be seen in Figure B.14.

The final electrode is the ground electrode, which is at laboratory ground potential. It is located 13 mm from the second aperture of the extraction electrode and it has an aperture diameter of 14 mm. About 100 mm downstream of the ground electrode is an *XY* steering magnet, which is made of two electromagnet dipoles oriented in orthogonal directions to steer the beam in the two transverse directions. Both the *XY* steering magnet and the ground electrode can be seen in Figure B.14.
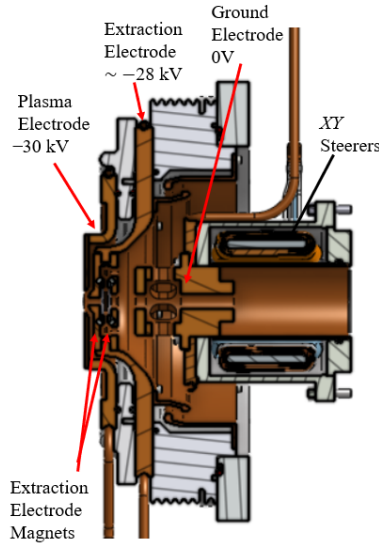
Figure B.14: Schematic of the cross section of the extraction system with the beam.

B.2.4 Ion Source Parameters

When operating the ion source, several parameters can be tuned to vary the beam current and the emittance. Some parameters vary the plasma properties, such as the arc voltage and current, while other parameters vary the properties of the extracted beam, such as the extraction electrode voltage and the *XY* steering currents. Table B.1 lists all of the ion source parameters, their range available and their error bars.

The tuning procedure to maximize the beam on the Faraday cup is as follows. Once the arc current is stable at the desired set point by way of the stability algorithm presented in section B.2.2, the extraction electrode voltage is tuned until a maximum current is read on the Faraday cup. Then, the plasma electrode voltage is tuned to again achieve the maximum. The voltage on the extraction electrode is then again varied to ensure that the beam current obtained is indeed maximum, and if it is varied, the plasma electrode voltage is also tuned a second time. The voltage on the electrodes is tuned until the beam current is maximized. Finally, the *XY* steering magnets are tuned to guarantee that all of the beam is centered.

Parameter	Operating Range	Error Bars
Arc Current	Up to 50 A	± 0.1 A
Arc Voltage	Up to 200 V	± 0.1 V
Filament Current (Auto-Adjusted)	Up to 400 A	± 0.5 A
Filament Voltage (Passive)	Up to 10 V	± 0.1 V
Gas Flow	Up to 32 sccm for H_2	± 0.05 sccm
Bias Voltage	Up to 30 kV	± 0.05 kV
Bias Current (Passive)	Up to 40 mA	± 0.05 mA
Plasma Electrode Voltage	Up to 40 V	± 0.05 V
Plasma Electrode Current (Passive)	Up to 20 A	± 0.05 A
Extraction Electrode Voltage	Up to 8 kV	± 0.01 kV
Extraction Electrode Current (Passive)	Up to 150 mA	± 0.1 mA
XY Steering Current	Up to 5 A	± 0.1 A

Table B.1: Filament ion source parameters and the accuracy with which each parameter can be set. The parameters that are not tunable are labeled as passive.

As the arc power is increased, the voltage on the extraction electrode needs to increase as well since there is a higher H^- and electron density in the plasma which requires a higher electric field to achieve a proper plasma meniscus. The plasma electrode voltage also needs to increase since the increased power will also increase the electron temperature and thus the plasma potential.

Some of the read-backs from the power supplies and control equipment connected to the ion source can be used as diagnostics to obtain information about either the extracted beam or the plasma in the ion source. The TRIUMF licensed filament-powered volume-cusp H^- ion source parameters, their available range and error bars are presented in Table B.1. The effect of the parameters on the ion source performance, as well as the information on the plasma or the beam extracted that can be gained from all of the ion source parameters are presented below.

i. **Arc Current**: The arc current controls the power that's introduced into the plasma. The arc current is a measure of the electron flux off of the filaments, so one expects the arc current to be directly proportional to the electron density in the plasma. Furthermore, the electron temperature is also dependent on the arc current as it directly controls the power in the plasma. Increasing

the arc current usually leads to an increase in H$^-$ beam current, but if the gas flow is not high enough, increasing the arc current will not lead to higher beam currents because the neutral density will be too low.

ii. **Arc Voltage**: Along with the arc current, the arc voltage also controls the power into the plasma chamber. The arc voltage sets the voltage between the filament and the walls of the plasma chamber. It thus sets the energy of the primary electrons emitted from the filaments. Increasing the arc voltage will lead to more ionization, since the ionization of the gas in the ion source is highly dependent on the electron energy, it will also lead to an increase in the electron temperature. Generally, increasing the arc voltage leads to an increase in beam current, but the effect is not as dramatic as with the arc current. The arc voltage is usually set between 80 V and 150 V and not varied.

iii. **Filament Current**: The filament current is controlled by the feedback algorithm that keeps the arc current stable, so it is not set by the user. However, the magnitude of the filament current changes as the filaments age, with a decrease in filament current seen with time.

iv. **Filament Voltage**: The filament voltage is passive, it depends on the filament current, which is controlled by a feedback algorithm.

v. **Gas Flow**: The gas flow directly controls the pressure in the ion source. A higher pressure is needed at higher arc currents since the beam current saturates if the pressure in the ion source is too low. However, for low arc currents, it is advantageous to use a lower gas flow as the higher pressures lead to increased stripping of the H$^-$ ions.

vi. **Bias Voltage**: The bias voltage sets the energy of the beam. The TRIUMF licensed filament-powered volume-cusp ion source was designed to properly extract beams at an energy between 22 keV and 30 keV, thus the bias voltage is usually set between -22 kV and -30 kV to ensure that the H$^-$ is properly extracted. The bias voltage is usually not varied and is set by the beam energy needed for the specific application.

vii. **Bias Current**: The bias current is a passive variable, it is composed of i) the negative ion beam that travels from the ion source to ground potential, ii) the leakage current through the cooling water or through bleed resistors and iii) the back streaming positive ions that travel from ground potential to the ion source. Thus, the bias current increases with the negative ion current and it is commonly about 30% to 50% higher than the negative ion current. If the bias current is much higher than the negative ion current measured on the Faraday cup, this most likely indicates that there is considerable beam loss on the ground electrode.

viii. **Plasma Electrode Voltage**: The plasma electrode voltage is usually set at a few volts above the plasma chamber body. For optimum extraction of H^- ions, the plasma electrode is set close to the plasma potential [141]. This is done to eliminate the potential well that's created by the plasma potential and the potential on the extraction electrode. Thus, the plasma electrode voltage is an estimate of the plasma potential close to the extraction region of the plasma when the plasma electrode voltage is optimized for the extraction of H^-.

ix. **Plasma Electrode Current**: The plasma electrode current is a passive variable that measures the electron current to the plasma electrode. Since the plasma electrode is in the plasma chamber, the plasma electrode current increases with the arc current as there is an extra flux of electrons to the electrode. The plasma electrode current is commonly between 20% to 60% of the value of the arc current. There is a big variability because the plasma electrode current is also dependant on the plasma electrode voltage. A higher voltage leads to a higher current as the potential on the electrode will deplete the plasma from the electrons in this region. This will also lead to a lower co-extracted electron current.

x. **Extraction Electrode Voltage**: The extraction electrode voltage sets the electric field needed to properly extract negative ions from the plasma chamber. The optimum extraction electrode voltage is i) above the space-charge extraction limited region, which is set by the Child-Langmuir law [79] as

seen in Section 1.7.1, and ii) gives the optimum plasma meniscus shape to properly extract the negative ions through the extraction system. Figure B.15 presents simulations of the extraction of negative ions at various extraction electrode voltages.
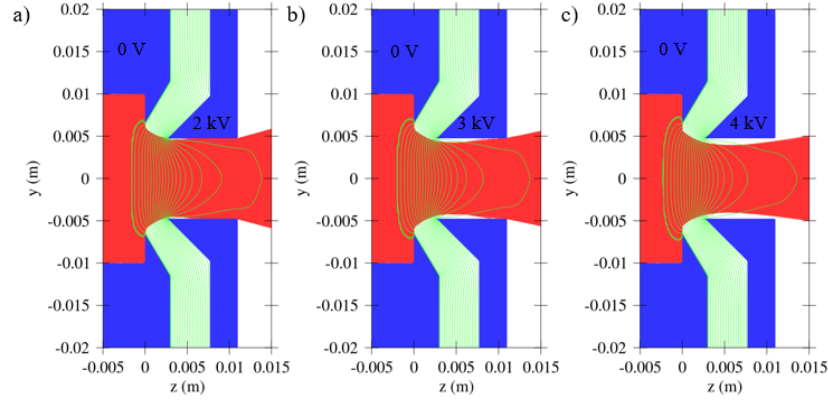
Figure B.15: IBSimu [77] simulation of the extraction of H$^-$ ions through the extraction electrode for an extraction electrode potential of a) 2 kV, b) 3 kV and c) 4 kV. The electrode are presented in blue, the beam is in red and the equipotential lines are in green. A current density of 100 A/m^2 was used.

From Figure B.15, one sees how the extraction electrode shapes the plasma meniscus. A larger extraction electrode voltage leads to a more convex plasma meniscus shape. The optimum plasma meniscus shape depends on the specific extraction system, but the extraction electrode voltage needs to increase to maintain the plasma meniscus shape if there's an increase in the ion density in the plasma.

xi. **Extraction Electrode Current**: The extraction electrode current is an approximation of the co-extracted electron current out of the ion source. There are two set of permanent dipole magnets on the extraction electrode, that deflect the electrons onto the electrode. However, there could be some negative ion beam losses on the electrode, which will also be included on the current seen by the power supply.

xii. **XY Steering Current**: The *XY* steering is used to correct any offset seen by

218

the beam. There is a strong magnetic field in the extraction region which is used to deflect the co-extracted electron out of the beam. The magnetic field integral along the beam path is not equal to zero in the y direction, which will give an offset to the beam in the x direction. Some current on the X steering magnet is also commonly needed.

B.3   Diagnostic Equipment

Along with the read-back of the power supplies controlling the ion source, there are additional beam diagnostic equipment on the baseline ISTF. These devices include an emittance scanner, a Faraday cup and a mass spectrometer system. These devices will be assessed for their appropriateness for the Thesis work and presented in this section.

In order to properly study the plasma in the ion source for the production of negative carbon beams, it was essential to develop special plasma diagnostic tools. It was important, therefore, to develop and implement a Langmuir probe and an Optical Emission Spectroscopy (OES) system as part of this Thesis work. The theory behind these devices, their development, their implementation and validation at the ISTF will be presented here.

B.3.1   Emittance Scanner

The beam quality of the beam extracted out of the ion source is an important parameter to measure since it determines whether the beam can be transported through the beamline. This section will first present how the emittance is measured at the ISTF. Validation emittance and phase space distribution measurements with the TRIUMF licensed H$^-$ ion source will be shown in the following section.

The process of measuring the transverse emittance of a particle beam comes down to measuring the $I(x,x')$ and/or $I(y,y')$ distributions of the beam, as presented in Section 2.11.1. There are different methods that can be used to measure such a distribution, but for this research project, an Allison type emittance scanner, licensed from TRIUMF, was used [142]. A schematic of this type of emittance scanner is presented in Figure B.16. It is composed of two slits separated by parallel, electrically biased, plates. The beam enters the first slit and is deflected by

the electric field created by the plates. For a certain potential on the plates, charged particles with the right entrance divergence angle will be deflected by the electric field created by the plates, fly through the second slit and be detected by the Faraday cup. By scanning the potential on the plates, it is possible to scan the divergence angles of the beam. The process is repeated at various positions along the transverse direction to obtain a 2-D distribution of signal corresponding to the (x, x') phase space. A second emittance scanner in the other transverse direction would then be needed to measure the (y, y') phase space.
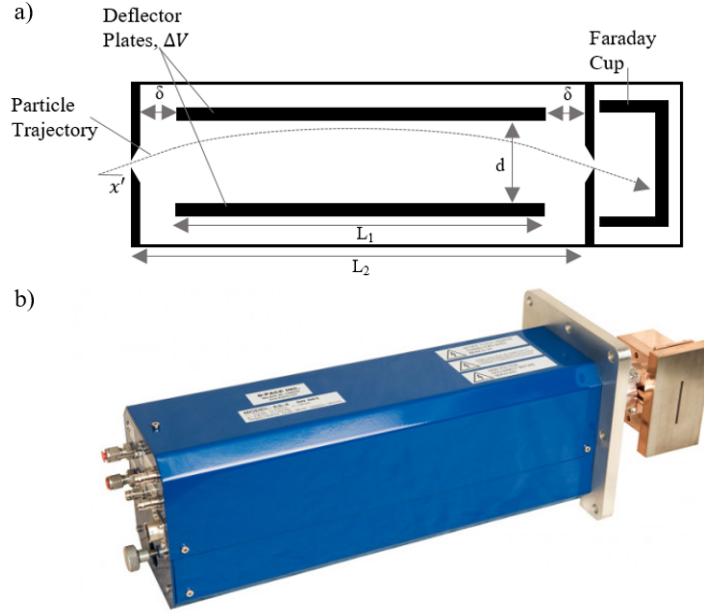
Figure B.16: a)Schematic of an Allison emittance scanner and b) photo of the scanner used.

The divergence of a particle being detected by the Faraday cup for the geometry shown in Figure B.16 and for a potential difference of ΔV on the parallel plates can be calculated [142]. The divergence of a beam with energy $V_0 = \frac{E_k}{q}$ in volts (E_k is the kinetic energy of the beam and q is the absolute value of the charge of the particles in the beam) entering the emittance scanner's Faraday cup is given by

$$x' = \frac{\Delta V}{V_0} \frac{(L_2 - 2\delta)}{4d}. \tag{B.3}$$

The divergence is directly proportional to the voltage on the plates and inversely proportional to the beam energy.

The parameters of the emittance scanner used in this Thesis study are presented in Table B.2.

Parameter	Value
ΔV	1 kV
L_1	76 mm
d	4.0 mm
δ	1.6 mm
$L_2 = L_1 + 2\delta$	79.2 mm

Table B.2: Emittance scanner parameters.

This gives it a maximum deflection angle of $x'_{\text{max}} = 97$ mrad for a beam energy of 30 keV. The emittance scanner has a maximum scanning range of 130 mm, a spatial resolution of 0.1 mm and an angular resolution of 2 mrad for a beam energy of 30 keV. The error in the position and divergence angle measurements will lead to an error in the calculated 4-RMS emittance which was defined as

$$\varepsilon_{\text{RMS}} = \sqrt{\langle x'^2 \rangle \langle x^2 \rangle - \langle xx' \rangle^2} \tag{B.4}$$

in Section 1.11.2. Due to the complexity of the relation between x and x' with the emittance, the propagation of the error can not be calculated accurately. However, the error on the emittance can be estimated by adding the relative error of each measurement. Assuming a full extension of 65 mm the relative error in x is 0.15% while the relative error for a divergence angle of 97 mrad is of 2.1%. Using Equation B.4, the relative error on the emittance is estimated to be 4.4%.

A ring biased at a voltage of -100 V is placed in front of the Faraday cup to prevent secondary electrons to exit the Faraday cup and give a false current reading. The current is read with a pico-ammeter, allowing precise measurement of beam currents from pA to tens of mA.

The emittance scanner is located in the downstream portion of the ion source's vacuum box. The front slit of the emittance scanner is located 368 mm downstream from the plasma electrode. The emittance scanner can be mounted in the x or the y direction, but it was mounted in the y direction for all of the phase space scans and emittance values presented in this Thesis.

The TRIUMF licensed filament-powered volume-cusp H^- ion source, which is the baseline ion source at the ISTF, commonly produces beams with a width of less than 60 mm and a divergence of less than 50 mrad at a beam energy of 30 keV [23]

at the emittance scanner location. The emittance scanner used has an operating range that is larger than this, thus the phase space of the beam extracted out of the ion source will be properly measured by the emittance scanner. The emittance scanner is deemed appropriate for the measurements to be undertaken.

B.3.2 Mass Spectrometer System

Since the purpose of this Thesis project is to study the production of negative carbon ions from volume-cusp ion sources and the beams extracted for this study will contain multiple species, it is important to have a precise beam composition measurement system. This section will present the mass spectrometer system used.

Some high mass ions will be extracted out of the ion source, since some of the gases tested, such as acetylene, are known to polymerize [143]. Thus a high precision spectrometer system was designed for the ISTF with a maximum ion mass separation of 57 a.m.u. The spectrometer system is composed of two high precision slits, a 90° dipole magnet and a Faraday cup. The system was designed with 500 mm between the upstream slit and the entrance dipole pole edge, and 500 mm between the exit dipole edge and the downstream slit. A model of the spectrometer system is presented in Figure B.17.
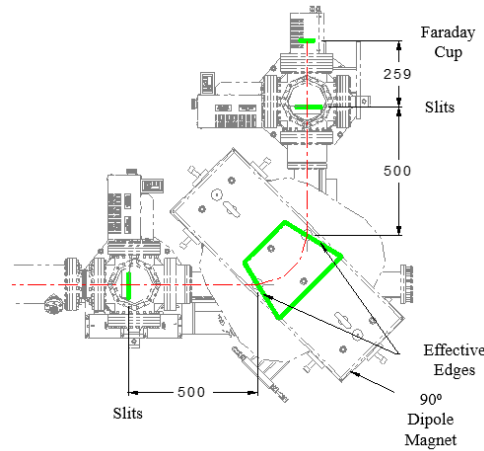
Figure B.17: Model of the spectrometer system showing the slits, dipole magnet and Faraday cup. The pole profile is shown in green and the nominal beam path is shown in red.

The dipole magnet was designed with the parameters in Table B.3.

Parameter	Value
Bend Angle (θ)	90°
Effective Length (L_{eff})	300.0 mm
Effective Bend Radius (R_{eff})	190.99 mm
Entrance Pole Face Angle (α)	31.7°
Exit Pole Face Angle (β)	31.7°
Pole Gap	50 mm
Peak Magnetic Field	1.15 T
Energy Resolution	1:626

Table B.3: Analyze magnet parameters.

With these parameters, the analyzer can bend a beam of masses up to 57 a.m.u. through a bend angle of 90° with a bend radius of 190.99 mm. The pole profile was chosen to be Rogowski [144] so that the effective length is equal to the pole length. A plan view of the model of the poles is presented in Figure B.18.
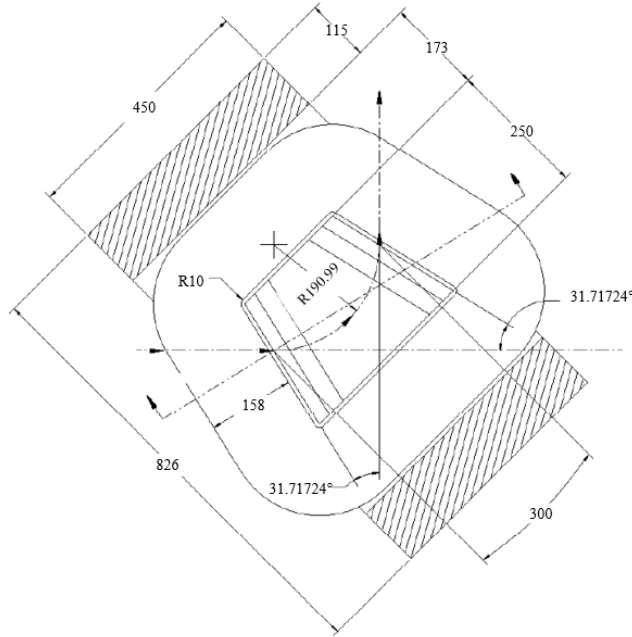
Figure B.18: Plan view cross section of the analyzer magnet model.

To achieve a total species separation between species of mass 56 a.m.u. and 57 a.m.u., the slit widths are set at 1 mm. Since carbon has a mass of 12 a.m.u., the resolution of the mass spectrometer is sufficient to properly measure the C^- and C_2^- ion components from CH^- and C_2H^-. However, the performance of the mass spectrometer magnet will ultimately be dependent on the precision of the machining and the installation of the magnet on the beamline. For the size of the pole, the machining tolerance are of 0.1 mm, which leads to an error on the pole angle of about $0.7°$. Furthermore, the installation of the magnet in the beamline has a tolerance of about 1 mm.

B.3.3 Langmuir Probe

The baseline ISTF does not include any plasma diagnostic tools. It is important to measure the plasma parameters such as the electron temperature and the electron density since the cross section for the negative ion reactions are often highly dependant on the electron temperature. It was thus crucial to develop a Langmuir Probe system as part of this Thesis work to analyse the plasma.

Langmuir probes are used to measure the plasma potential (ϕ_p), the electron density (n_e) and the electron temperature (T_e) in the plasma [145]. A Langmuir probe consists of a metal probe, commonly made of tungsten or tantalum, that is inserted in the plasma. Only the tip of the probe is exposed, the rest of the probe is covered by an insulating material such as ceramic. Since the probe is inserted into the plasma, this is an invasive measurement technique and it is possible that the measurement affects the results obtained. The voltage on the probe is swept and the current is measured.

A typical *I-V* obtained with a Langmuir probe is presented schematically in Figure B.19.
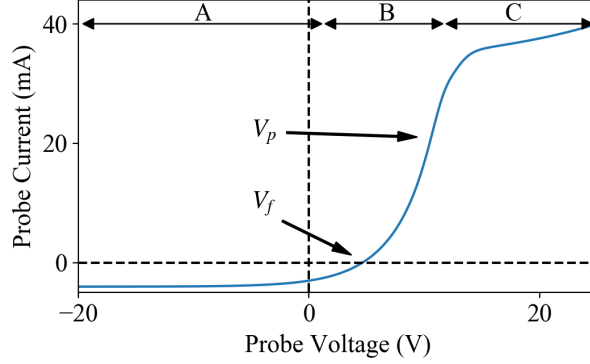
Figure B.19: Schematic of a *I-V* curve for a Langmuir probe.

The curve is separated in three distinct zones. When the probe is biased to a high positive voltage (zone C), the probe collects most electrons in its vicinity and the probe current is saturated. The current on the probe can be described by [145]

$$I_p = \frac{1}{4} e A n_e \left(\frac{8kT_e}{\pi m} \right)^{1/2},$$
(B.5)

where e it the electron charge, A is the probe area, n_e is the electron density, k is the Boltzmann constant, T_e is the electron temperature and m is the electron mass.

When the probe voltage is lowered below the plasma potential, the current falls rapidly as only the electrons with an energy that is higher than the plasma potential will reach the probe (zone B). The plasma potential, V_p, can be found by calculating where the curvature of the *I-V* curve switches from positive to negative. The floating potential, V_f, is defined as the potential where the current on the probe is zero.

The electron energy distribution of most laboratory created plasmas follow a Maxwell-Boltzmann distribution with a temperature of a few electron-volts. So as the probe voltage is varied around the plasma potential, the *I-V* curve of the

226

Langmuir probe can be expressed by the following exponential equation [146]:

$$I = eAn_e \left(\frac{kT_e}{2\pi m} \right)^{1/2} \exp \left(-\frac{e(V_p - V)}{kT_e} \right). \tag{B.6}$$

The electron temperature (T_e) is found by fitting the *I-V* curve of the probe with equation B.6. The electron density (n_e) can be found by measuring the current on the probe at the plasma potential, once the electron temperature has been calculated. From equation B.6, at $V = V_p$,

$$n_e = \frac{I_p}{eA} \left(\frac{2\pi m}{kT_e} \right)^{1/2}, \tag{B.7}$$

where I_p is the current on the probe at the plasma potential.

When the probe is biased a at low negative potential (zone A), only the positive ions in the plasma are collected, so the current measured is negative. Since the ions are not as mobile as the electrons, the ion current will be lower than the electron current.

A Langmuir probe was fabricated with a tantalum wire and a ceramic sleeve to act as an insulator. The outer diameter of the ceramic was of 3.18 mm and the diameter of the tantalum wire was 1.6 mm. The probe was fabricated so that it had an exposed tip length of 5 mm, which creates a collection area of 27.1 mm^2. A second probe was also created with a 90° bend to allow for measurements 30 mm off the central axis of the probe. This second probe also has an exposed probe tip of 5 mm. The probe was inserted in the plasma through the extraction aperture and was electrically connected to an electrical feed-through in the downstream section of the vacuum box. It was then connected to a bipolar power supply, allowing the measurement of the current-voltage characteristics of the probe. The probe was mechanically connected to a metal rod which was inserted in the vacuum chamber via a mechanical feed-through, allowing for the movement of the probe along the central axis of the source. The insertion of the Langmuir probe through the extraction aperture prevented plasma parameters measurements while beam is extracted from the ion source. A schematic of the Langmuir probe system is presented in Figure B.20.
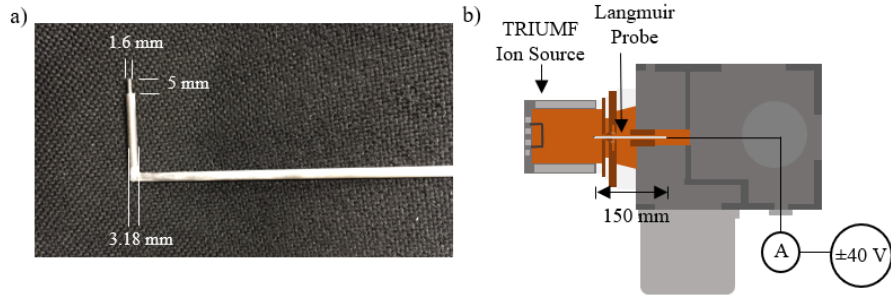
Figure B.20: a) Photograph the 90° Langmuir probe and b) schematic of the Langmuir probe system.

There is an error of ±1 mm in all three spatial dimensions for the position of the probe tip furthermore, the tip has a length of 5 mm which adds an additional error to the plasma measurements location. The power supply connected to the probe can generate ±40 V, which spans the different zones in Figure B.19 and allows for the calculation of the electron density and temperature. The current and voltage on the probe are measured with a multimeter with a current measurement accuracy of 1% and a voltage measurement accuracy of 0.1%.

B.3.4 Optical Emission Spectroscopy

One of the main disadvantages of Langmuir probes is that it is an invasive plasma diagnostic technique, because the probe is inserted directly in the plasma. Furthermore, Langmuir probes do not give any information on the different species in the plasma, which is crucial information for the multiple species that are found in carbon rich plasmas since the injection gases are composed of multiple atoms. For these reasons, it was essential to design and implement an Optical Emission Spectroscopy (OES) system at the ISTF.

OES is a non-invasive plasma diagnostic tool that can be used to obtain various plasma parameters [123]. The technique analyzes light emitted from the plasma, which mostly comes from the transition of electronically excited states from particles in the plasma. The most basic, yet very useful tool of optical spectroscopy is to identify species in the plasma and to compare their relative populations. As a particle transitions from an excited electronic state to a lower energy state, a photon

of energy corresponding to the energy difference between the two states is emitted. The wavelength (λ) of the photon emitted is related to the energy by

$$\lambda = \frac{hc}{E}, \tag{B.8}$$

where h is Planck's constant, c is the speed of light and E is the energy of the photon. The intensity of the signal is directly proportional to the population density of the excited state. One can show that the peak area is directly proportional to the particle density in the plasma [123]. Thus, the relative population of the species in the plasma can be compared by comparing their relative line intensities. This is an important parameter to study for the case of the plasmas studied in this project because these plasmas are composed of multiple species, yet the extraction of one specific ion is to be maximized. Comparing the relative peak intensities of these different species allows for the study of the effect of the ion source parameters on the different populations.

Optical emission spectroscopy can also be used to determine the electron density and the electron temperature in some plasmas. The method consists of adding a small amount of argon to the plasma. The ratio of the spectral lines at 480 nm and 488 nm is used to determine the electron density [147]. The absolute line density of the 750 nm spectral line is used to determine the electron temperature, since its excitation coefficient is well known and is highly dependent on T_e [114]. The temperature of the gas in the plasma can also be determined with optical emission spectroscopy [148]. There will be some Doppler broadening of the emitted emission, and by using a high resolution spectrometer, one can estimate the temperature of the gas by measuring the broadening effect.

One of the main disadvantages of using OES is that the results are averaged over the line of sight of the optical system. For example, if the line of sight of the optical system is through the central axis of a cylindrical plasma chamber, the results will be a weighted average over the entire length of the plasma chamber. If the plasma is non-uniform, such as is the case for volume-cusp H^- ion sources, there will a large variation of the plasma parameters in the plasma. This will increase the error on the measurements made.

An optical emission spectroscopy system was implemented at the ISTF as part

of this Thesis work. Since the ion source's plasma chamber doesn't have any radial view ports, the only option was to use the extraction aperture as the viewing window for the OES system. As discussed in the previous paragraph, this will lead to an increase in the error since the results are averaged over a non-uniform plasma volume.

An optical spectrometer was chosen (Ocean Optics HR 2000+) due to its large bandwidth (200 nm - 1100 nm). The spectrometer has a resolution of about 1 nm, which adequately allows for the proper identification of the major spectral lines, however it is not high enough to measure the Doppler broadening of the different peaks. Light is coupled to the spectrometer through optical fibers. A fiber connects the spectrometer to an optical feed-through and a second optical fiber connects the feed-through to an optical collimator to collect light from the plasma. The collimator is connected to the bottom of the emittance scanner, allowing for it to be moved it in and out of the line of sight of the plasma. There is no beam being extracted when the collimator is in the beamline. A schematic of the setup used is presented in figure B.21.
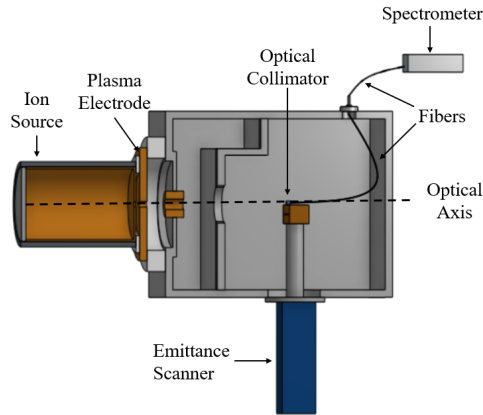

Figure B.21: Schematic of the optical emission spectroscopy setup.

The optical emission system developed is adequate for the purpose of this Thesis work because the resolution of the system is sufficient to accurately identify the main spectral peaks from the plasma and the bandwidth is large enough to identify a large spectrum of peaks.

B.4 Validation Measurements

Once all the components of the ISTF were installed and commissioned, the first experiments performed were to obtain baseline H^- measurements with the TRIUMF licensed ion source. These measurements were critical to validate that the ISTF was completely operational and performs to Kuo et al. [23] original design specifications prior to proceeding to negative carbon experiments. The performance of the ion source as a function of the arc parameters and the gas flow will be presented in this section and is compared to the original measurements made by Kuo et al. [23].

After the ion source system was validated, the ion source was used to verify the performance of the emittance scanner by analyzing the phase space as a function of the different ion source parameters. To properly analyze the phase space scans obtained with the emittance scanner, magnetic field and beam extraction simulations were undertaken. A detailed presentation of the code and the models used as well as the results obtained and their comparison to the measurements are presented. The mass spectrometer system was then validated by measuring the composition of the beam extracted out of the H^- ion source. The following sections present how the plasma electrode potential and the extraction electrode potential affects the extracted H^- beam. Finally, the ion source was used to validate the Langmuir probe and the optical emission spectroscopy system that were developed as part of this Thesis work.

B.4.1 Arc Current and Gas Flow

The main power input to the ion source's plasma is through the arc current. The first ion source measurements were thus to measure the H^- beam current as a function of the arc current for various gas flows. The ion source is designed to output more than 15 mA of H^- beam current, but Kuo et al. [23] showed that the ion source could output up to 18 mA at 5 kW of arc power.

The arc current was varied at various gas flows and the H^- beam current was measured on the Faraday cup located 480 mm downstream of the plasma electrode. For each measurement, the voltage on the extraction and the plasma electrodes is tuned to maximize the beam current on the Faraday cup. The *XY* steering magnets

are also tuned to maximize the beam current. The results are presented in Figure B.22.
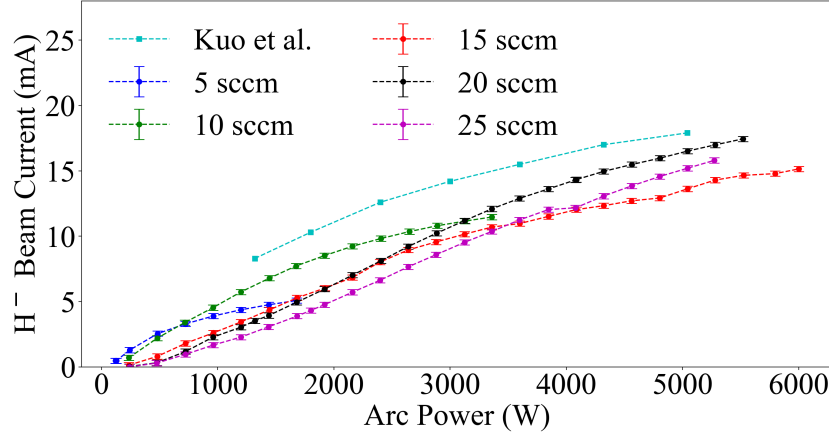

Figure B.22: H^- beam current as a function of the arc power for various H_2 gas flows. The beam energy was set at 30 keV, the arc voltage was set at 120 V, and the plasma and extraction electrode voltages were optimized for every measurement. The Kuo et al. data is taken from [23].

From Figure B.22, the increase in power leads to an increase in beam current until there is saturation of the beam current, and at lower gas flows the saturation occurs at lower powers. The saturation happens at lower arc currents for the lower gas flows since the lower H_2 density in the ion source leads to a lower production of H^- ions in the plasma. At lower arc powers, the beam current is higher at lower gas flows. This effect is explained by a lower stripping rate caused by the lower pressure in the ion source, leading to a higher density of H^- ions in the plasma. As the power increases, the production rate of the H^- increases faster than the total destruction rate, resulting in a higher H^- current.

The data obtained is consistently lower than what was found by Kuo et al. [23]. The beam out of the ion source is divergent and is similar in size to the Faraday cup at the measurement location, so it is believed that the difference seen is due to more beam spill at the ISTF. There is no indication of how the beam current measurements were completed in the measurements presented in [23], it is thus difficult to accurately compare the two measurements. Measuring the beam current

with an additional focusing element between the ground electrode and the Faraday cup, or with a larger Faraday cup, would show whether there is some beam loss due to the high divergence of the beam. This was not done due to cost considerations.

Nevertheless, a maximum H^- beam current of 18 mA was obtained with the TRIUMF licensed filament-powered volume-cusp H^- ion source at the ISTF as part of this Thesis work. The tune details are presented in Table B.4.

Parameter	Value
H^- Beam Current	18.0 ± 0.2 mA
Bias Voltage	30.0 ± 0.1 kV
Bias Current	24.9 ± 0.2 mA
Arc Voltage	120.0 ± 0.1 V
Arc Current	47.5 ± 0.1 A
Extraction Electrode Voltage	3.8 ± 0.1 kV
Extraction Electrode Current	127 ± 1 mA
Plasma Electrode Voltage	3.8 ± 0.1 V
Plasma Electrode Current	21.1 ± 0.1 A
H_2 Gas Flow	19.5 ± 0.2 sccm
Filament Voltage	0.9 V±0.2
Filament Current	35 ± 1 A
X Steer Current	0.8 ± 0.1 A
Y Steer Current	1.6 ± 0.1 A
Upstream Pressure	$4.6\pm0.5 \times 10^{-5}$ Torr
Downstream Pressure	$6.2\pm0.5 \times 10^{-6}$ Torr

Table B.4: 18 mA Tune Details.

Since 18 mA of beam current was obtained, which is the maximum obtained by Kuo et al. [23], the TRIUMF licensed ion source and the ISTF can be confirmed as it meets the design specifications sufficiently for the purpose of this Thesis. The difference seen with arc power is small, and the purpose of this Thesis work was not to replicate the results of Kuo et al. [23] exactly.

The co-extracted electron current is another important ion source parameter since the maximum co-extracted electron current is limited by the current capabilities of the extraction electrode power supply and the co-extracted electron current is an approximate representation of the electron density in the plasma close to the extraction region. Figure B.23 presents the co-extracted electron to H^- beam cur-

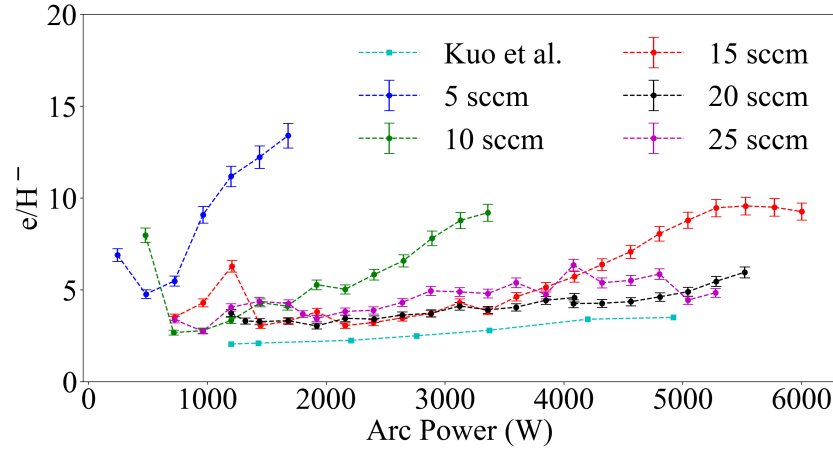rent ratio for the measurements presented in Figure B.22.

Figure B.23: Co-extracted electron to H$^-$ beam current as a function of the arc power for various gas flows. The beam energy was set at 30 keV and the arc voltage was set at 120 V, and the plasma and extraction electrode voltages were optimized for every measurement. The Kuo et al. data is taken from [23].

An electron to H$^-$ ratio of less than 5 is obtained for the ion source operation between 1 kW and 4 kW of arc power and a minimum ratio of 2.67 is found at operation parameters of 720 W of arc power and 10 sccm of gas flow. The ratio is high for low arc powers and higher gas flows, due to the low H$^-$ current yields at these settings. As the arc power increases, the H$^-$ beam current increases and the ratio decreases. The co-extracted electron current is also higher for lower gas flows as the electron density is higher at lower ion source pressures. A low e/H$^-$ ratio is important since the electrons contribute to the space charge between the two first electrodes, which can cause emittance growth.

The data by Kuo et al. [23] is consistently lower than the data obtained, which is partially explained by the lower H$^-$ beam currents that were measured at the ISTF. Nevertheless, the difference between the measurements obtained and those obtained by Kuo et al. [23] is small and the e/H$^-$ ratio achieved is below 10 for most ion source tunes, so the system performs close enough to the specifications for the purpose of this Thesis.

B.4.2 Arc Voltage

As stated in the previous section, the arc voltage is thought to increase the electron temperature in the plasma chamber since it increases the energy of the primary electrons emitted from the filaments. Increasing the arc voltage also increases the arc power into the ion source, so it is expected that an increase in arc voltage will lead to an increase in H^- beam current. Figure B.24 presents the dependence of beam current and the e/H^- on the arc voltage.
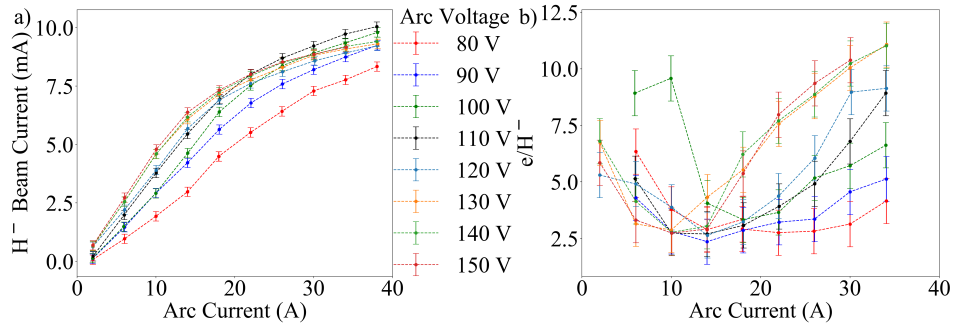

Figure B.24: a) H^- beam current and b) e/H^- ratio as a function of the arc current for various arc voltages. The beam energy was set at 25 keV, the gas flow was set at 15 sccm, and the plasma and extraction electrode voltages were optimized for every measurement.

There is an increase in beam current with arc voltage below 110 V but above this voltage the arc voltage does not have an effect on the H^- beam current. At higher arc currents, the dependence is even less pronounced, since there's beam saturation above a certain arc power, as was seen in Figure B.22. At low arc currents, the lower arc voltages yield considerably higher e/H^- ratios, which is due to lower beam currents observed. But, at higher arc current the effect is reversed which is explained by a higher electron density and/or temperature in the plasma.

From the data, the optimum arc voltage for H^- beam production is above 110 V since beam current yields are not higher above this value.

B.4.3 Emittance Measurements

The following section serves as a validation of the emittance scanner at the ISTF as well as an analysis of the phase space of the beam as a function of the various ion

source parameters. The effect of the emittance on the different ion source parameters is presented and computational tools are used to explain the effects seen. The normalized 4-RMS emittance of the extracted H$^-$ beam from the TRIUMF licensed filament-powered volume-cusp ion source is commonly between 0.4 mm·mrad and 0.6 mm·mrad. Figure B.25 presents the normalized 4-RMS emittance for the measurements presented in Figure B.22.
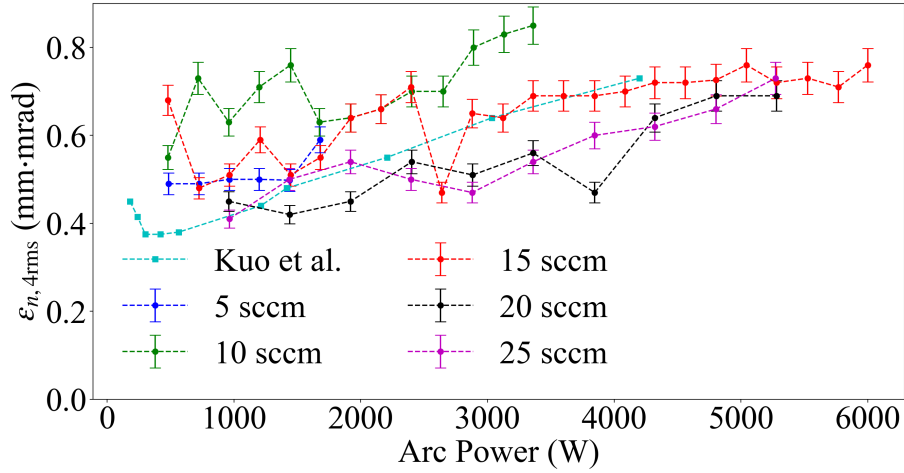

Figure B.25: Normalized 4-RMS emittance of the H$^-$ beam extracted out of the ion source as a function of the arc power for various gas flows. The beam energy was set at 30 keV, the arc voltage was set at 120 V, and the plasma and extraction electrode voltages were optimized for every measurement. The Kuo et al. data is taken from [23].

The arc power doesn't have a large effect on the emittance of the beam, however the emittance is noticeably lower for the higher gas flows. This points to a greater space charge compensation at the higher pressures in the beamline which leads to a lower emittance. The higher pressure causes more ionization of the residual gas in the beamline and thus creates a greater density of positive ions for space charge compensation, as was presented in Section 2.12.2.

The emittance measured by Kuo et al. [23] is similar to what was measured at the ISTF, but it is slightly lower at lower arc powers. This again validates the ISTF since the emittance values are similar to what was obtained by [23].

The effect of the arc voltage on the emittance of the H$^-$ beam extracted out of

the TRIUMF licensed filament-powered volume-cusp ion source is presented next. The normalized 4-RMS emittance for the measurements presented in Figure B.24 are presented in Figure B.26.
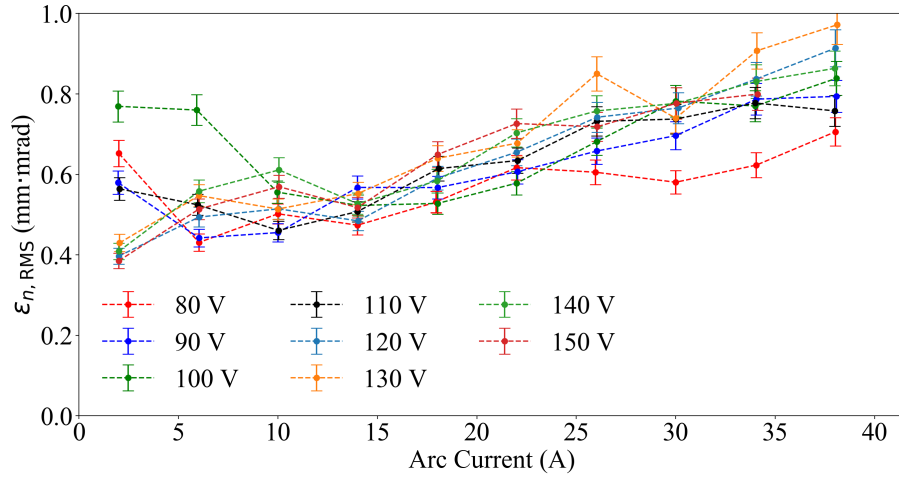

Figure B.26: Normalized 4-RMS emittance of the H$^-$ beam extracted out of the ion source as a function of the arc current for various arc voltages. The beam energy was set at 25 keV, the gas flow was set at 15 sccm and the plasma and extraction electrode voltages were optimized for every measurements.

There is a slight increase in emittance with arc voltage. The hypothesis is that the increase in emittance is not due to an increase in space charge of the beam since higher emittances are not highly correlated to higher beam currents, as was seen in Figure B.25. So, the increase in emittance with arc voltage points to an increase in ion temperature since, as the ions are extracted out of the ion source, they maintain their transverse velocity, creating an increase in emittance. Thus, lower arc voltages are preferred to reduce the emittance of the extracted H$^-$ beam.

From the results presented in Figures B.25 and B.26, the gas flow has the biggest effect on the emittance in the TRIUMF licensed filament-powered volume-cusp ion source. Figure B.27 presents the normalized 4-RMS y emittance as a function of the H$^-$ beam current for various gas flows.
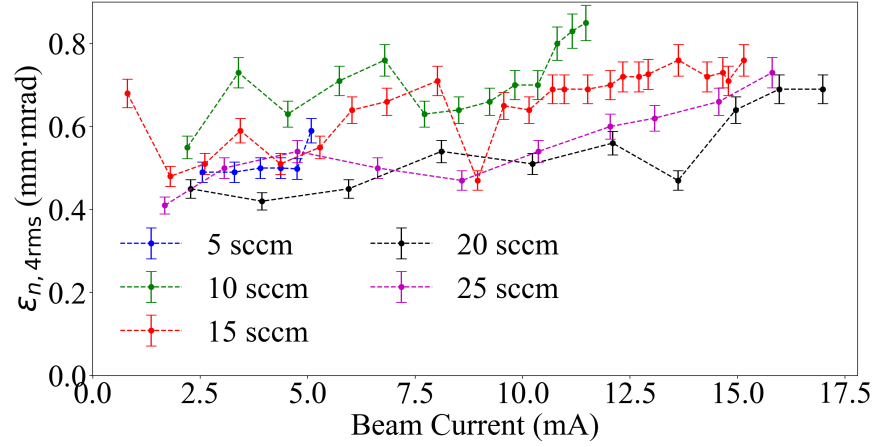
Figure B.27: Normalized 4 RMS y-emittance of the H^- beam extracted out of the ion source measured as a function of the H^- beam current for various gas flows for the data presented in Figure B.25.

From Figure B.27, there's a lot of variation in the emittance values, but the most obvious trend is the reduction of the emittance value with the increased gas flow. To show this, the phase space scan of two 10.3 mA beam, one at 10 sccm and the other at 25 sccm, are plotted in Figure B.28.
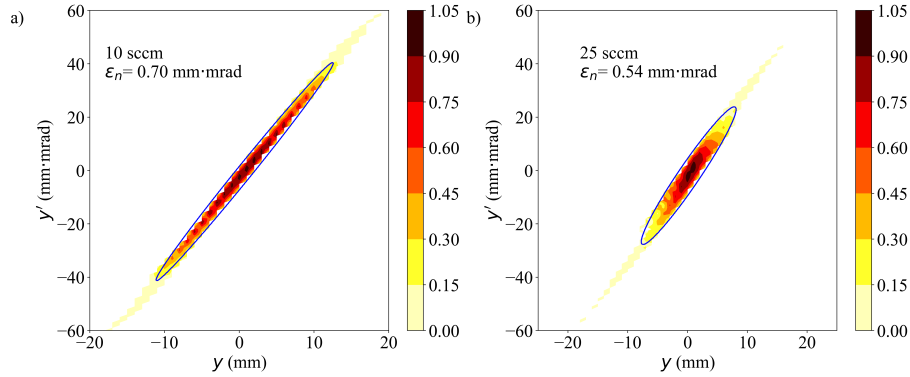

Figure B.28: yy' phase space scans of a) a 10.3 mA beam with the gas flow set at 10 sccm and b) a 10.3 mA beam with the gas flow set at 25 sccm. The calculated normalized 4-RMS emittance value are quoted on the plots and the calculated 4-RMS emittance ellipse is presented in blue.

From Figure B.28, the phase space of the 25 sccm tune has a lower maximum

divergence as well as a smaller beam size, which contributes to a lower emittance value. The different tune parameters are compared in table B.5.

Parameter	10 sccm	25 sccm
Bias Current	13.7±0.1 mA	16.9±0.1 mA
Bias Voltage	30.0±0.1 kV	30.0±0.1 kV
Extraction Electrode Voltage	3.42±0.01 kV	2.85±0.01 kV
Co-extracted Electron Current	71±2 mA	53±2 mA
Plasma Electrode Voltage	4.12±0.01 V	2.66±0.01 V
Plasma Electrode Current	11.11±0.05 A	8.83±0.05 A
Arc Current	22.00±0.06 A	28.00±0.06 A
Arc Voltage	120.0±0.1 V	120.0±0.1 V
H^- Beam Current	10.4±0.1 mA	10.4±0.1 mA
Upstream Pressure	$3.1±0.1 \cdot 10^{-5}$ Torr	$5.3±0.1 \cdot 10^{-5}$ Torr
Downstream Pressure	$2.8±0.1 \cdot 10^{-6}$ Torr	$6.3±0.1 \cdot 10^{-5}$ Torr
Normalized 4-RMS y Emittance	0.92±0.05 mm·mrad	0.70±0.05 mm·mrad

Table B.5: Comparison of the 10 sccm and the 25 sccm ion source tunes.

From Table B.5, other than the different gas flow, the extraction electrode voltage is lower for the 10 sccm tune at 2.85 kV versus 3.40 kV for the 25 sccm tune, but the co-extracted electron current is higher for the 10 sccm tune at 71 mA, compared to 53 mA for the 25 sccm tune. The bias current is also lower for the 10 sccm tune at 13.7 mA compared to 16.9 mA for the 25 sccm. Finally, the plasma electrode voltage was set higher in the 10 sccm tune, at 4.12 V, compared to the 2.66 V for the 25 sccm tune.

The hypothesis is that the higher bias current at 25 sccm comes from a larger H^- density in the plasma but, there are more losses in the beamline, due to the higher pressure associated with the larger gas flow, so that only 10.3 mA of beam is extracted to the Faraday cup. The higher H^- density in the plasma would require a higher voltage on the extraction electrode to have a plasma meniscus shape that is optimized, which would explain the higher voltage used. The higher plasma electrode voltage for the 10 sccm tune is caused by a higher plasma potential as the optimum plasma electrode voltage is set close to the plasma potential. To explain why the phase space varies so much between the two tunes, the extraction system was simulated.

B.4.4 Magnetic Field Simulations

To determine how the different ion source parameters affect the phase space of the extracted beam, particle tracking simulations need to be done. The system needs to be modeled in 3-D since, as was shown in Section B.2.3, the geometry is not radially symmetric because of the magnetic field in the extraction region. Two sets of dipole magnets are located in the extraction electrode and there is a dipole magnetic field in the plasma chamber that extends in the extraction region that will affect how the particles are extracted from the ion source.

It is thus important that the ion source's magnetic field be properly modeled in 3-D. The particle tracking code that will be used [77] doesn't have a finite element algorithm included to calculate the magnetic field. Therefore, Opera [129] was used and the results were imported into the particle tracking code. Opera is a finite elements magneto-static solver that can solve the magnetic field created by electro-magnets and permanent magnets in 3-D. In the case of the TRIUMF licensed ion source, only permanent samarium-cobalt (Sm_2Co_{17}) magnets are used. The geometry was first introduced in the Opera. Only the extraction region is of interest, but the entire ion source was simulated since the dipole field in the plasma chamber extends past the plasma electrode into the extraction region. Figure B.29 presents a cross section of the magnetic field map obtained.
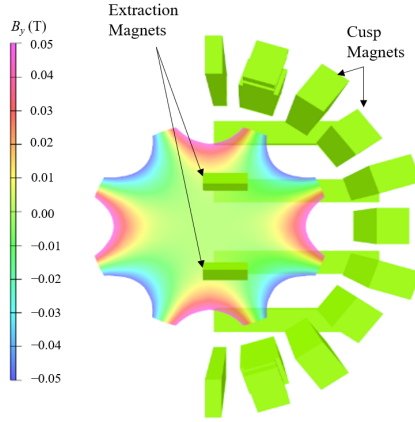
Figure B.29: Cross section of the simulated magnetic field in the plasma chamber. The Sm_2Co_{17} are presented as green rectangular cubes and the magnitude of the y component of the magnetic field is presented by the color map.

To validate the magnetic field values obtained with the Opera simulations, the magnetic field along the ion source's central axis was measured. A Hall probe was mounted on a translation stage and the ion source was removed from the vacuum box and installed on the translation stage. The Hall probe was scanned through the center of the extraction system and into the plasma chamber. The B_y component of the magnetic field was measured since the magnetic dipole and the extraction dipoles are oriented in the y direction. Figure B.30 presents the Hall probe measurements as well as the corresponding Opera simulation values.
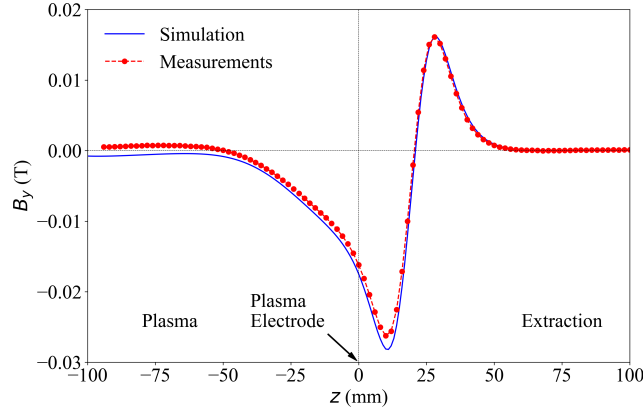
Figure B.30: Comparison between the simulation of the magnetic field on the central axis of the ion source to measurements with a Hall probe. $z = 0$ corresponds to the plasma electrode location.

As can be seen in Figure B.30, the simulation replicate well the shape of the magnetic field in the ion source, but there is a slight offset close to the magnetic field peaks. This is most likely due to slight differences in the magnetic field strength of the different Sm_2Co_{17} magnets. Nevertheless, the agreement between the simulations and the measurement is good enough to use the simulated values in the particle tracking code.

B.4.5   IBSimu

IBSimu [77] is the particle tracking code that was used to model the extraction of particles from the TRIUMF licensed filament-powered volume-cusp H^- ion source. IBSimu is a C++ library, it includes particle tracking, particle extraction from plasmas and electric potential solvers functions, among others. The user needs to write his own simulation code, which includes introducing the geometry along with specifying the meshing used, the potential on the electrodes, the magnetic field, the initial plasma parameters and the initial beam parameters. The code can output the electric potential and fields, the phase spaces at any location, the beam current and beam loss, among many other output parameters.

A negative plasma extraction model, included in the IBSimu library, was used to simulate the extraction of the H^- from the plasma. The model assumes a positive

plasma potential (ϕ_p), a potential of zero close the aperture of the plasma electrode and a positive potential in the extraction area. This creates a potential well that will trap thermal positive ions and will cause fast positive ions to be reflected back into the plasma by the high electric field in the extraction region. The plasma meniscus is the surface with an electrical potential of zero, which equates to the total charge density on this surface to be zero, $\rho_{neg} + \rho_{th} + \rho_f + \rho_e = 0$, where ρ_{neg}, ρ_{th}, ρ_f and ρ_e represent the negative ion, thermal positive ion, fast positive ion and electron densities respectively. The charge density distribution of the thermal ions is assumed to be Maxwellian

$$\rho_{th} = \rho_{th0} \exp\left(-\frac{e\phi}{kT_p}\right),\tag{B.9}$$

where ρ_{th0} is the space charge density at the meniscus and T_p is the ion temperature. The charge density distribution of the fast positive ions is described by

$$\rho_f = \rho_{f0}\left(1 - \text{erf}\left(\frac{\phi}{\phi_p}\right)\right),\tag{B.10}$$

where ρ_{f0} is the charge density at the meniscus and erf is the error function.

With the charge density distributions above and the required negative ion and electron current densities, the code solves the Poisson equation and then tracks the particles through the system using a fourth order Runge-Kutta algorithm [149]. Additional input parameters that must be included in the model include the initial drift energy of the negative ions (E_0) and T_t which is the negative ion temperature in the plasma. Table B.6 presents the parameters used for these simulations.

Parameter	Value
Initial Drift Energy (E_0)	2 eV
Ion Temperature (T_t)	0.5 eV
Relative Density of Fast Positive Ions (R_f)	0.1
Thermal Positive Ion Temperature (T_p)	0.5 eV

Table B.6: Parameters used in the IBSimu simulations.

The initial guess for the parameters used were based on educated guesses from Langmuir probe measurements in a similar ion source [150] and the final value was chosen by iterating the parameters and comparing the results with phase space mea-

surements. Additional parameters, such as the initial particle density, the plasma potential and the voltage on the extraction electrode were set according to Table B.5.

Once the particles are tracked through the system, a space charge map is created by measuring the current through each of the system's mesh cube. The code then re-solves the Poisson equation while including this space charge map. The particles are then tracked through the system a second time and a new space charge map is obtained and the process is repeated until the beam's trajectory converges to a solution. This ensures that the space charge effect is properly included in the simulation.

Figure B.31 presents the *xz* and *yz* cross sections of the IBSimu simulations using the parameters from the 25 sccm tune from table B.5 and the parameters of table B.6. The beam current density was adjusted to have a total of 16.9 mA through the system and on the ground electrode, as this is the bias current measured. The difference between the bias current and the measured beam current is due to the neutralization of some of the H^- ions along the beamline and the back scattering flow of positive ions back into the ion source. This is an important source of error as the actual negative ion current cannot be measured because the current of back streaming positive ions nor the neutralization percentage of the beam are not known.
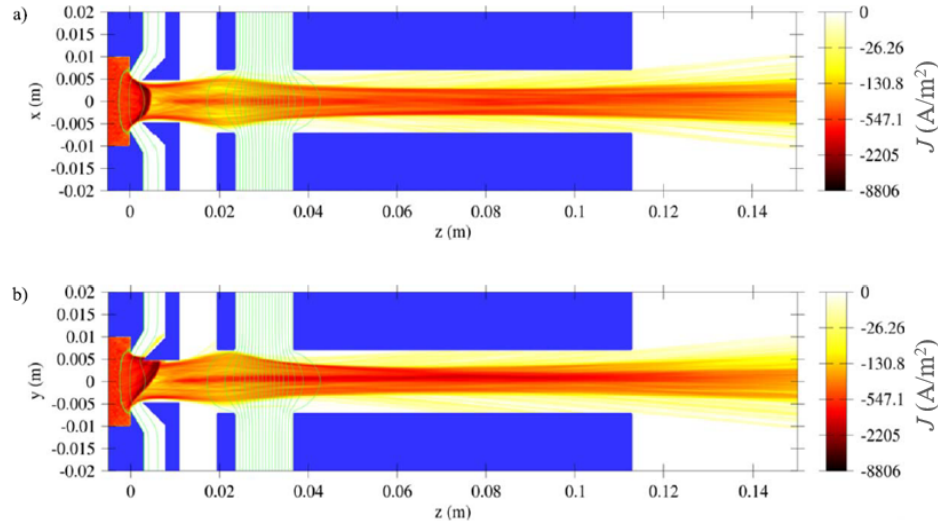
Figure B.31: a) *zx* and b) *zy* cross sections of the IBSimu simulations with the plasma parameters of the 25 sccm tune. The electrodes are represented in blue and the 1 kV equipotential lines are plotted in green with the 1 V, 2 V and 4 V lines added. The beam density is presented with the colormap.

From Figure B.31, the first important finding of the IBSimu simulations is that the electrons are dumped on the front of the extraction electrode and even on the plasma electrode at low extraction electrode voltages, instead of between the two apertures of the extraction electrode, as was first thought. This is due to the dipole magnetic field in the plasma extending past the plasma electrode and into the extraction region of the ion source, deflecting the electrons before they reach the extraction electrode. One can also see from the simulations how all the electrons are dumped on the extraction electrode, with none of the electrons making their way to ground potential, which would be added to the bias current seen. The simulation was also run to include secondary electrons from the collision of H^- ions with the electrodes. From this exercise, one notices that all of the electrons were trapped at the extraction electrode due to the large magnetic field in this region. Again, showing that the bias current seen is not due to any electrons escaping the ion source.

From Figure B.31, there is a large curvature of the plasma meniscus, which

is due to the protrusion on the front of the extraction electrode and to the smaller extraction electrode aperture than the plasma electrode aperture. This geometry creates a strong electric field at the plasma electrode aperture, which creates the large curve seen on the plasma meniscus. The beam extracted from the plasma is thus highly focused because of this meniscus shape. The large focusing force on the beam as it is extracted from the plasma causes the beam size to increase between the two apertures of the extraction electrode, leading to some slight beam loss on the second extraction electrode aperture. Furthermore, there is also some beam loss on the ground electrode.

As described earlier, the larger bias current seen is partially due to beam neutralization along the beamline and the back streaming of positive ions into the ion source. The presence of positive ions in the beamline will influence the space charge seen by the beam. This is thus a source of error for the model since the neutralization effect of the positive ions was not included in the simulations. Figure B.32 presents the xx' and yy' phase space plots for the simulation of the 25 sccm beam that was presented in Figure B.31. The phase space plots were obtained at $z = 368$ mm, which is the location of the front slit of the emittance scanner at the ISTF if $z = 0$ at the plasma electrode.
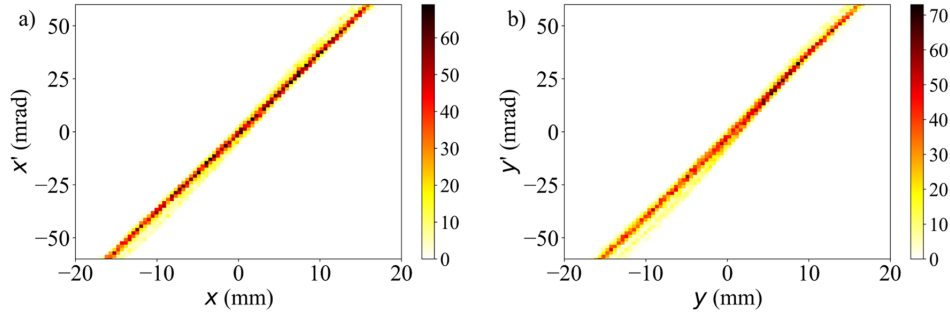

Figure B.32: a) xx' and b) yy' phase space simulations with the plasma parameters of the 25 sccm tune without any space charge compensation.

As can be seen in Figure B.32, the phase space obtained resembles the 10 sccm tune shown in Figure B.28, more than the 25 sccm tune. Varying the different variable parameters presented in Table B.6 doesn't lead to the 0.22 mm·mrad reduction in emittance that was seen with the phase space scan done at the ISTF. To remediate

246

this, space charge compensation was added to the beam after the ground electrode since there is likely some gas ionization forming positive ions in this region. To do this, the space charge value in IBSimu was multiplied by a compensation factor after each beam tracking iteration. It was found that a space charge compensation factor of 80% gave a phase space profile that best compares with measurements made at the ISTF. Figure B.33 compares the measured yy' phase space for the 25 sccm tune to the best match that could be obtained with the IBSimu simulations.
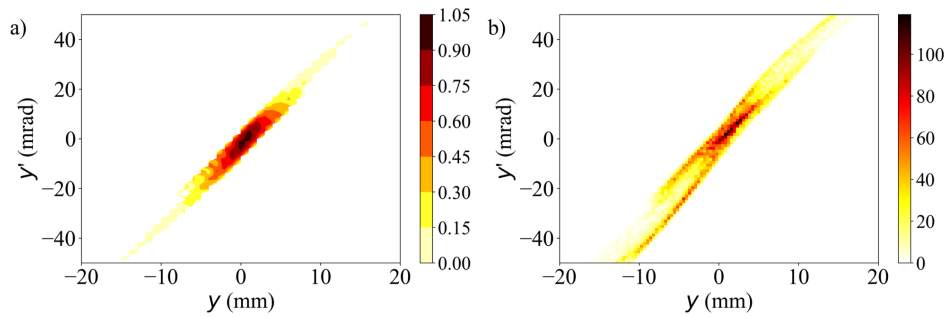

Figure B.33: a) yy' phase space scan obtained of a 10.3 mA H$^-$ beam with a 25 sccm gas flow. b) Simulation of the extraction of the beam with the parameters of table B.6 and a space charge compensation of 80%.

From Figure B.33, there is still a substantial difference between the two scans but there is a clear improvement when comparing to Figure B.32. The experimental beam is more collimated and the peak is much narrower than what is obtained in the simulations. However, one can clearly see how introducing space charge compensation to the simulation transformed the phase space. Furthermore, it partially explains the difference between the 10 sccm tune and the 25 sccm tune since the pressure was higher for the 25 sccm tune, hence a large positive ion density is expected in the vacuum at the higher pressure and thus a greater space charge compensation effect is also expected.

For the 10 sccm phase space scan, the space charge compensation factor will be lower since the pressure is about 2.5 times lower with this tune and this can be seen in Figure B.28 where the beam is more divergent and the emittance is higher. A space charge compensation factor of 40% was found to give the best match with the experimental scan. The results are presented in Figure B.34.
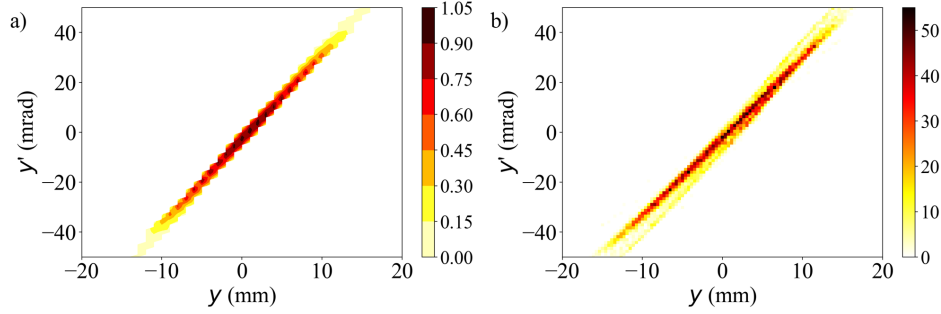
247

Figure B.34: a) *yy'* phase space scan obtained of a 10.3 mA H⁻ beam with a 10 sccm gas flow. b) Simulation of the extraction of the beam with the parameters of table B.6 and a space charge compensation of 40%.

Again, from Figure B.34, the beam is more divergent in the IBSimu simulations than what was seen when measuring the phase space at the ISTF. There are multiple source of error that could contribute to this, the main one being the effect of back streaming positive ions, as well as the neutralization of the H⁻ which are not accounted for in the simulations. Furthermore, most of the plasma parameters used for the simulations are based on educated guesses, which is an additional source of error.

From the analysis presented in this section, one can conclude that IBSimu can be used to simulate the extraction of negative ion beams. It was found that the main parameter that influences the phase space of the beam is space charge compensation, and this is confirmed by the fact that the largest change in emittance seen at the ISTF was when the gas flow was varied.

B.4.6 Plasma Electrode

The plasma electrode plays a crucial role in volume-cusp H⁻ ion sources. It is electrically isolated from the rest of the plasma chamber and it's commonly biased at a few volts above the main plasma chamber potential. The optimum plasma electrode potential is commonly close to the plasma potential [44], so the optimum plasma electrode voltage approximates the plasma potential in the TRIUMF licensed volume-cusp ion source.

The plasma electrode affects the H⁻ beam current and the co-extracted elec-

trons in two ways [44]. First, it reduces the electron density in the extraction area of the plasma. Since it's biased positively, the electric field created by the electrode will induce a flow of electrons towards it. The electrons are much more mobile in the plasma than the H^- ions, so the flow of H^- ions to the electrode will be much lower than the flow of electrons resulting in a decrease in the electron density as the electrode voltage is increased. Second, when the plasma electrode is biased near the plasma potential, the potential barrier between the bulk of the plasma and the extraction area is reduced which will allow for a greater flow of H^- ions through the aperture. The net result of an optimum plasma electrode voltage is an increase in the H^- current and a reduction in the co-extracted electron current. Figure B.35 presents the effect of the plasma electrode voltage on the H^- beam current and the co-extracted electron current.
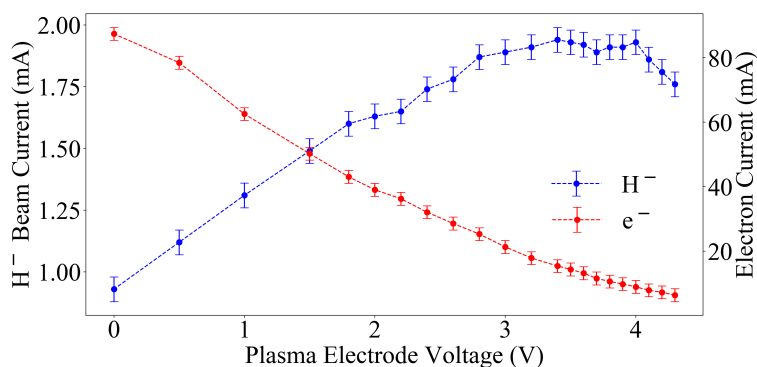

Figure B.35: H^- beam current and co-extracted electron current as a function of the plasma electrode voltage. The beam energy was set at 30 keV, the arc voltage was set at 120 V, the arc current was set at 4 A, the gas flow was set at 10 sccm and the extraction electrode voltage was optimized for every measurement.

There is a clear reduction in the co-extracted electron current as the voltage is increased, and there is a maximum in H^- beam current when the plasma electrode is biased at about 3.5 V. This is on the same order of magnitude of the plasma potential of the TRIUMF licensed filament-powered volume-cusp ion source at this operational setting, by using the analysis of Section 2.3.3. The results presented in Figure B.35 confirm the theory presented at the beginning of this section as the

249

two effects expected were seen.

When the ion source is tuned, the optimum plasma electrode voltage is found by carefully varying the potential on the electrode to find the maximum H^- seen in Figure B.35. Figure B.36 presents the optimum plasma electrode voltage as a function of the arc current for various gas flows. The optimum extraction electrode voltage is also presented for the various measurement points. The optimum extraction electrode voltage sets the optimum plasma meniscus shape for the given H^- and electron densities in the plasma.
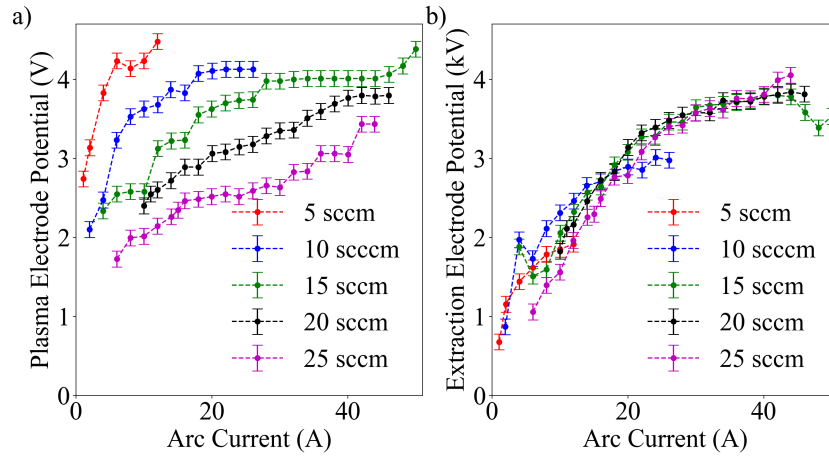

Figure B.36: a) Optimum plasma electrode voltage and b) extraction electrode voltage as a function of the arc current for various gas flows. The arc voltage was set at 120 V and the bias voltage was at 30 kV for every measurement.

As can be seen in Figure B.36, the optimum plasma electrode increases with the arc current for every gas flow. From Section 2.3 of the Chapter 2, it was shown that the plasma potential is directly proportional to the electron potential, so the increase in the optimum plasma electrode voltage with arc current shows that increasing the arc current leads to an increase in the electron temperature in the plasma. Furthermore, there is a decrease in the optimum plasma electrode voltage with the gas flow, which shows the decrease in the electron temperature with gas flow.

In Figure B.36b, the optimum extraction electrode voltage is not highly depen-

dant on the gas flow but shows a strong dependence on arc current. The extraction electrode voltage is adjusted to ensure that the plasma meniscus has the optimum shape, and this will be highly dependent on the ion density in the plasma. As the arc current increases, so does the ion density and the beam current until there is saturation, as was seen in Figure B.22. A similar result with the optimum extraction electrode voltage was seen in Figure B.36. From Figure B.36b, one can see that the higher gas flows require a slightly smaller extraction electrode voltage, and this is due to the lower electron densities seen at higher gas flows, which is consistent with the lower plasma electrode voltage.

B.4.7 Perveance

Extraction limited extraction of an ion source happens when the extracted current is limited by the space charge of the beam [151]. Under such a condition, the beam current has a $\frac{3}{2}$ power dependence on the extraction voltage. If one assumes that the particles are extracted with zero velocity and from a flat surface, the relation between beam current and voltage is given by $I_{\text{tot}} = PV^{\frac{3}{2}}$, where I_{tot} was defined in Section 2.7.1 and the perveance P is

$$ P = \frac{4\varepsilon_0}{9} \sqrt{\frac{2q}{m}} \frac{\pi a^2}{d^2}, \tag{B.11} $$

with a the radius of the plasma electrode aperture and d is the distance between the plasma and extraction electrodes. The relation between the current and the voltage will be given by $I = fPV^{\frac{3}{2}}$, where $f \approx 0.49$ for most spherical geometry systems [152]. For the TRIUMF ion source, the perveance would be about $P = 7.7 \cdot 10^{-7}$ A/V$^{\frac{3}{2}}$.

Figure B.37 presents the total current as a function of the extraction electrode voltage for various arc powers measured with the TRIUMF licensed ion source.
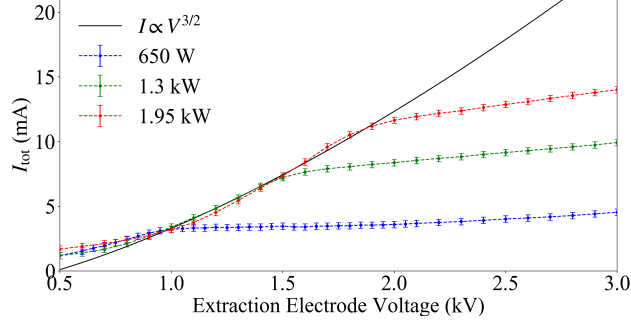
Figure B.37: Total beam current as a function of the extraction electrode voltage for three different arc powers. The fitted curve is of the equation of the perveance. The bias voltage was set at 25 kV, the arc voltage was set at 130 V, the plasma electrode was set at 2.5 V and the gas flow was set at 15 sccm.

The ion source is extraction current limited and has a 3/2 power dependence below a certain extraction electrode voltage, but then saturates and becomes production limited above this voltage. The transition voltage is also higher for higher arc power as there is a higher H^- and electron density at higher arc powers.

The perveance obtained with the fit presented in Figure B.37 is equal to $P = 1.56 \cdot 10^{-7} A/V^{\frac{3}{2}}$, while the theoretical perveance for the geometry is of $P = 7.7 \cdot 10^{-7} A/V^{\frac{3}{2}}$. The difference between the measured result and the theoretical one can be attributed to the fact that there is H^- beam loss onto the extraction electrode which is not accounted for in I_{tot} and would shift the curves up and give a higher perveance value. Finally, the model assumes that the particles are extracted without any initial velocity, which is most likely false in the TRIUMF ion source since the first electrode has a potential of a few volts, which would accelerate the particles to a few eVs before they reach the beginning of the extraction. The initial velocity of the particles explains the offset in $V_{ext} = 0$ seen in the experimental data in Figure B.37.

B.4.8 H⁻ Beam Composition

To validate the mass spectrometer system, the beam composition of the TRIUMF licensed filament-powered volume-cusp H⁻ ion source was analyzed. The beam current through the system was restricted by a 3 mm aperture diameter collimator 557 mm downstream of the plasma electrode to prevent damage on the uncooled spectrometer slits, so the beam current measured on the fixed Faraday cup at the end of the spectrometer system will be orders of magnitude lower than the total beam current measured close to the ion source. The spectrometer slits were set at 1 mm. The results are presented in Figure B.38.
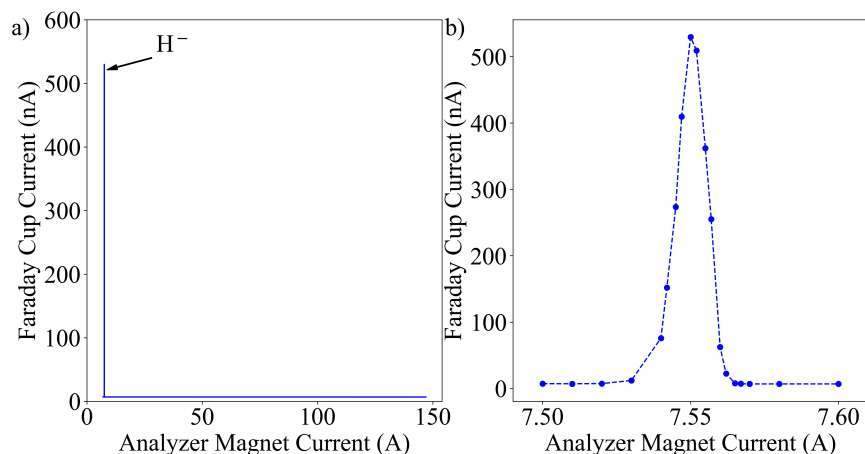

Figure B.38: Spectrometer scan of the beam extracted out of the TRIUMF licensed H⁻ ion source. A beam of 1.2 mA was extracted with 2 A of arc current, 120 V of arc voltage and 5 sccm of gas flow.

As can be seen in Figure B.38, the only beam species measured was H⁻. The hydrogen gas used in the ion source has a purity of 99.999% so the concentration of impurities in the plasma chamber is low. Furthermore, few negative ions are extracted from plasmas due to the fragile nature of negative ions. Thus, the only negative ions that are extracted from the ion source are H⁻.

The Full Width at Half Maximum (FWHM) of the H⁻ peak obtained is about 0.013 A of analyzer magnet current. Assuming a linear relation between the magnet current and the magnetic field, the analyzer magnet current would be 56.5 A for a species with a mass of 56 a.m.u. and 57.0 A for a species with a mass of

57 a.m.u.. Thus, both beams would be properly resolved as the FWHM is much smaller than the difference in analyzer magnet current. These results validate the mass spectrometer system design.

B.4.9   Langmuir Probe Measurements

The Langmuir probe system developed was first tested with the TRIUMF licensed filament-powered volume-cusp H^- ion source. The experimental configuration presented in Figure B.20b was used. The probe was placed in the plasma so that the probe tip was located 20 mm from the plasma electrode on the ion source's central axis, allowing for plasma properties measurements in the *cold* plasma region. A typical *I-V* curve obtained with the Langmuir probe in the hydrogen plasma is presented in Figure B.39.
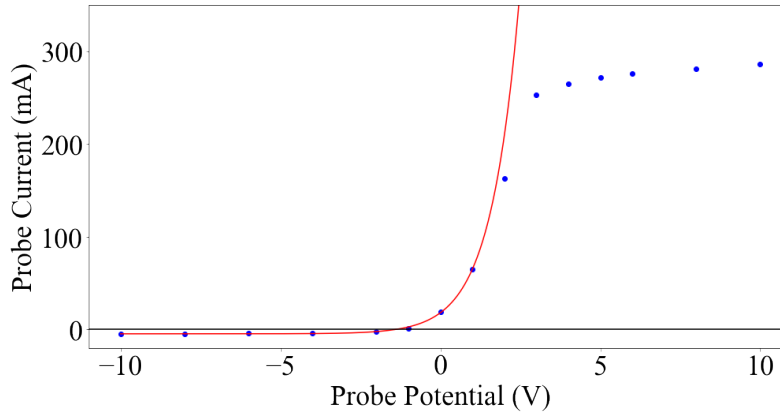

Figure B.39: *I-V* curve obtained with the probe tip 20 mm from the plasma electrode and exponential fit applied to the data. The arc current was set at 2 A, the arc voltage was set at 120 V and the plasma electrode voltage was set at 0 V.

The three main regions of Figure B.19 can be distinguished in the *I-V* curve of Figure B.39. At low negative voltages, the negative current corresponds to positive ions collected by the probe. When the voltage is increased, electrons with sufficient energy can make it past the potential barrier to reach the probe. This leads to an exponential increase in probe current as the probe voltage is increased further. Eventually the potential barrier falls to zero and all the electrons drifting towards

the probe will be collected. At higher voltages, the electrons will be attracted to the probe and the probe current eventually saturates. By fitting an exponential function to the first half of the curve the electron temperature is obtained, and by measuring the current at the plasma potential, the electron density and temperature in the region are calculated. These measurements validate the Langmuir probe system as the measured electron temperatures and densities were in the expected ranges.

Figure B.40 presents the electron density and temperature as a function of the arc power with the probe tip located on the central axis, 20 mm from the plasma electrode. The error bars on the electron temperature are obtained with the 95% confidence interval when fitting the *I-V* curve with an exponential function. The error bars on the electron density are obtained by assuming ± 0.1 mA on the current measurements and the 95% confidence interval on the electron temperature.
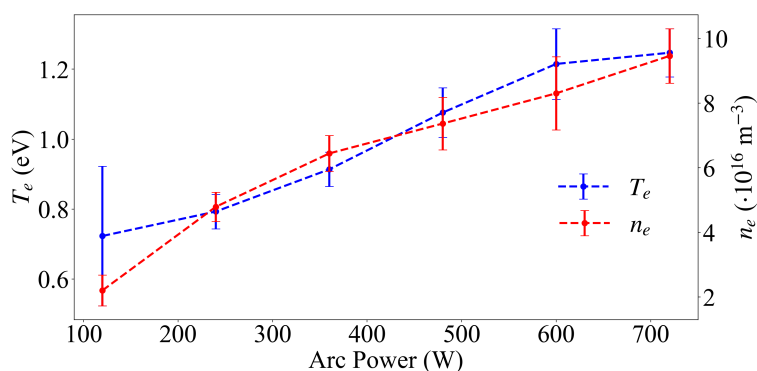

Figure B.40: Electron density and temperature as a function of the arc power measured with the Langmuir probe on the central axis, 20 mm from the plasma electrode. The arc voltage was set at 120 V, the gas flow was set at 10 sccm and the plasma electrode voltage was set at 0 V.

The linear increase in both the electron density and temperature is explained by the increase in power delivered to the plasma, which leads to more ionization and faster electrons. The increase of the electron temperature with the arc power was predicted in Figure B.36, where the optimum plasma electrode was analyzed as a function of the arc current for various gas flows. The theory predicts that the optimum plasma electrode voltage is close to the plasma potential [112], and it was shown that the plasma potential is directly proportional to the electron temperature

in Section 1.3.3. 2.3. Thus, the increase in the electron temperature with the arc power confirms that the increase in the optimum plasma electrode voltage with the arc current is due to an increase in the electron temperature. The analysis was repeated as a function of gas flow, the results are presented in Figure B.41.
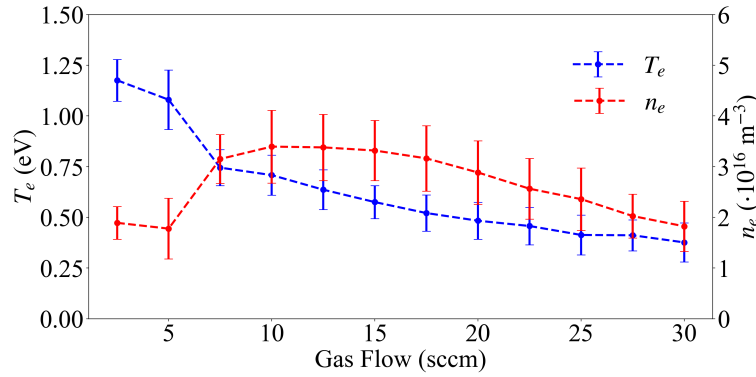

Figure B.41: Electron density and temperature as a function of the gas flow measured with the Langmuir probe on the central axis, 20 mm from the plasma electrode. The arc voltage was set at 120 V, the arc current was set at 1 A and the plasma electrode voltage was set at 0 V.

As seen in Figure B.41, the main effect of the increase in pressure in the ion source is to decrease the electron temperature. This is due to the increased collisions rate caused by the increased pressure in the plasma chamber, which distributes the power to more particles and reduces the mean electron energy. The effect on the electron density is minimal, although there is a slight decrease with the increase in pressure. The hypothesis is that this is explained by the reduction in electron temperature which leads to a decrease in the ionization rate. The reduction of the electron temperature with an increase in gas flow was predicted in Figure B.36 where the optimum plasma electrode voltage decreases with the increased gas flow, since the optimum plasma electrode voltage is proportional to the electron temperature. The dependence of the plasma parameters with distance along the central axis is presented in Figure B.42.
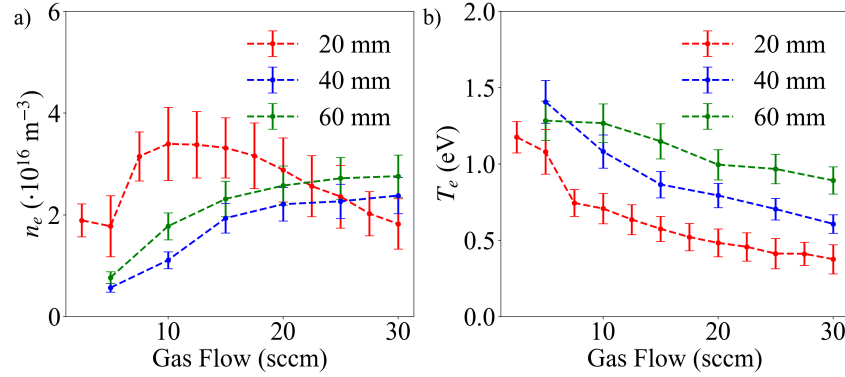
Figure B.42: a) Electron density and b) electron temperature as a function of the gas flow measured with the Langmuir probe on the central axis, at three different positions. The arc voltage was set at 120 V, the arc current was set at 1 A and the plasma electrode voltage was set at 0 V.

The decrease in electron temperature with the increased distance from the plasma electrode is expected since there's a magnetic filter close to the plasma electrode that filters out the fast electrons from the plasma. It was also expected that the electron density would be lower closer to the plasma electrode, however this is not the case as there is little variation in the electron density as a function of the distance from the plasma electrode. Electron tracking simulations in the plasma chamber will have to be done to determine how the magnetic field affects the electron density close to the plasma electrode.

The measurements performed with the Langmuir probe confirm the proper functioning of the device. Furthermore, the results of these measurements allowed for the explanation of the behavior seen in Figure B.36 as well as give insight into the plasma in the TRIUMF licensed ion source, which had never been reported in the literature.

B.4.10 Optical Emission Spectroscopy Measurements

To validate the optical emission spectroscopy system, the system was tested with the TRIUMF licensed filament-powered volume-cusp H^- ion source in the configuration presented in Figure B.21. To reduce saturation on the detector, the in-

tegration time of the spectrometer had to be set close to its minimum of 1 ms for arc powers of more than 400 W. Neutral density filters could be used to reduce the intensity of the signal coming through the collimator. A typical spectrum obtained with the TRIUMF licensed filament-powered volume-cusp H^- ion source is presented in Figure B.43.
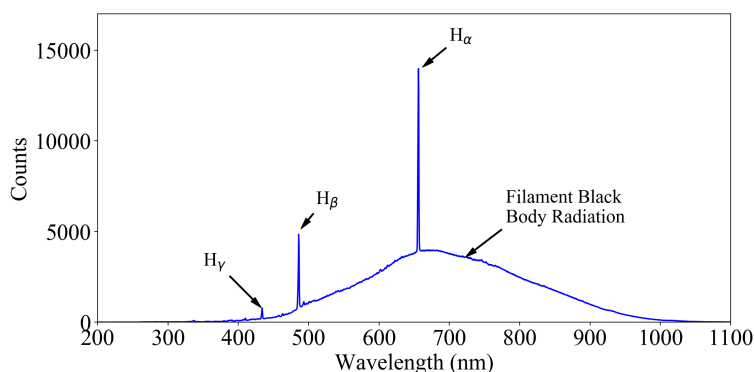

Figure B.43: Optical emission spectrum obtained with the TRIUMF licensed filament-powered volume-cusp H^- ion source. The arc current was set at 2 A, the arc voltage was set at 120 V and the gas flow was set at 15 sccm.

From Figure B.43, three of the Balmer lines of hydrogen can be distinguished: H_α at 656 nm, H_β at 486 nm and H_γ at 434 nm [153]. The Balmer lines stem from the electronic transition of the radial quantum number n of hydrogen. H_α corresponds to transition $3 \rightarrow 2$, H_β is for $4 \rightarrow 2$, while H_γ is for $5 \rightarrow 2$. A broad spectrum that stems from the blackbody radiation of the hot filaments is also clearly seen. These measurements validate the optical emission spectroscopy system as the different excitation lines of Hydrogen could be properly identified.

B.5 D^- Measurements

The TRIUMF licensed filament-powered volume-cusp ion source is designed to also extract D^- ions. Deuterium is an isotope of hydrogen, its nucleus has an extra neutron, so the isotope has twice the mass of hydrogen. The electron affinity of deuterium is very close to Hydrogen's at 0.754 eV [154], and the volume production of D^- is thought to be the same as hydrogen [155].

The performance of the ion source with deuterium will be presented, as it was done as a baseline measurement during the validation of the ISTF. Figure B.44 presents the D^- beam current obtained as a function of arc current for various gas flows.
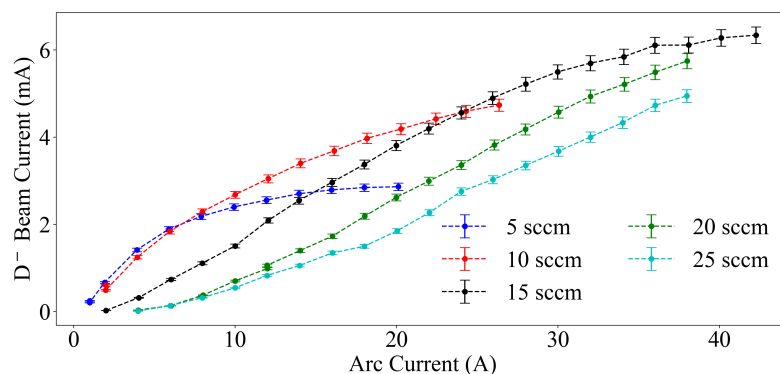

Figure B.44: D^- beam current as a function of the arc current for various deuterium gas flow rates. The arc voltage was set to 120 V and the bias voltage was set to 30 kV.

More than 6 mA of D^- can be extracted from the ion source which is about a third of what was extracted for H^-. Lower extracted D^- ion currents are commonly seen in H^- ion sources [156–158]. The electron to D^- ratio was higher than the electron to H^- ratio, as presented in Figure B.45.
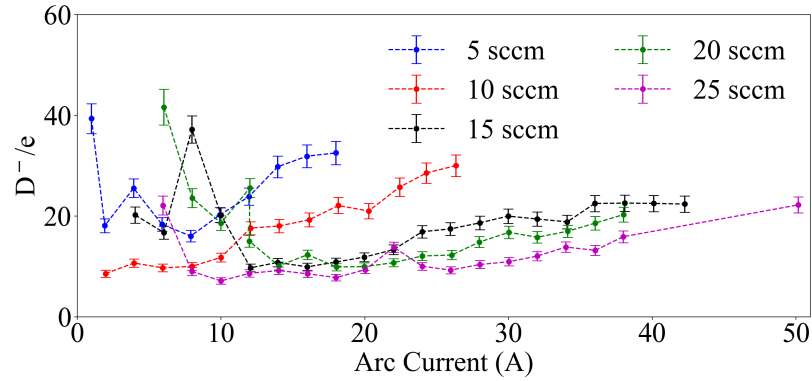
Figure B.45: e to D$^-$ ratio as a function of the arc current for various deuterium gas flow rates. The arc voltage was set to 120 V and the bias voltage was set to 30 kV.

The electron to D$^-$ ratio is much higher that what is seen with hydrogen and this is due to the lower mobility of the deuterium ions, compared to hydrogen. This leads to a lower flux of D$^-$ to the ion source's aperture, while the electron density will remain relatively constant when comparing deuterium and hydrogen plasmas. Higher e/D$^-$ ratios than e/H$^-$ ratios are also commonly seen in H$^-$ ion sources [156].

Finally, the normalized 4-RMS emittance as a function of the arc current for various gas flows is presented in Figure B.46.
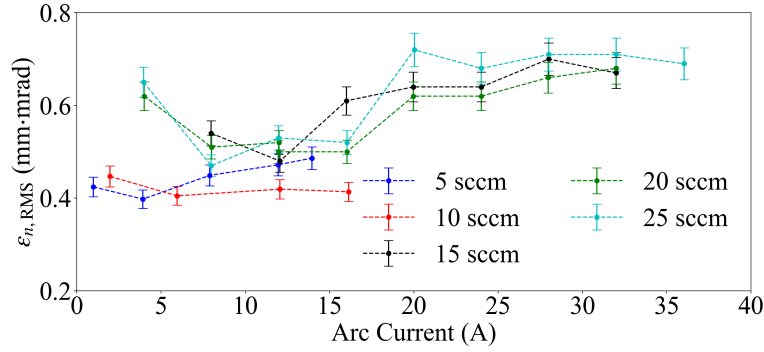
Figure B.46: Normalized 4-RMS emittance as a function of the arc current for various deuterium gas flow rates. The arc voltage was set to 120 V and the bias voltage was set to 30 kV.

Unlike the case with H^-, the emittance value is lower for the lower gas flows (5 sccm and 10 sccm) than it is for the higher gas flows.

B.6 Conclusion

The goal of this appendix was to present the equipment used to perform this Thesis work as well as to show the baseline measurement study that was done to confirm the design of the system. The first task that needed to be accomplished for this Thesis work was to design, build and validate an ion source test stand. The Ion Source Test Facility was thus commissioned in two phases and it was completed in March 2016. The first validation measurements of the facility were done with the TRIUMF licensed H^- filament-powered volume-cusp ion source. Up to 18 mA of H^- was extracted from the ion source and the performance matches Kuo et al. to a sufficient degree.